Investigation of Superlattices and Deep Impurities of Narrow Gap Semiconductors by Magneto-Optical Methods

by Satoshi SHIMOMURA

1987

DISSERTATION IN PHYSICS

THE OSAKA UNIVERSITY

GRADUATE SCHOOL OF SCIENCE

TOYONAKA, OSAKA

Investigation of Superlattices and Deep Impurities of Narrow Gap Semiconductors by Magneto-Optical Methods

by Satoshi SHIMOMURA

1987 OSAKA UNIVERSITY

ABSTRACT

Studies on PbTe/$Pb_{0.8}Sn_{0.2}Te$ superlattices and $Pb_{1-x}Sn_xTe$ doped with indium are carried out by magnetoplasma spectroscopy.

The superlattices, with periodicities of 220Å/30Å, 240Å/60Å, 260Å/150Å, 220Å/220Å, 300Å/190Å, 180Å/230Å, and 34Å/41Å ($PbTe/Pb_{0.8}Sn_{0.2}Te$), are investigated. The characterization of the superlattice structure has been performed by examining the satellite intensity of X-ray diffraction. From the dependence of resonance magnetic field on the magnetic field direction, the band edge structures of the superlattices are determined. For superlattices(260Å/150Å, 240Å/60Å, 220Å/30Å) with small interdiffusion, the cyclotron masses are calculated by the envelope function approximation method. The measured and calculated cyclotron masses agree well with each other. On the other hand, for superlattices with large interdiffusion, difference of subbands in the same valley in the <111> direction yields two dimensional electron system and three dimensional electron system, though electrons belong to the same valley.

For the $Pb_{1-x}Sn_xTe$ doped with indium, mechanism of photoexcitation and relaxation of carriers is investigated. From the magnetoplasma spectra using strip-line method, the temperature dependence of carrier density is obtained by calculations to reproduce the measured spectra. It is found that carrier density almost does not change in the temperature range (4.2K-15K), while it rapidly decreases above 15K. Similar temperature dependences are observed for samples with various tin composition(0.21-

0.35). The temperature dependence is discussed in the double capture model. It is also found that the band edge masses of $Pb_{1-x}Sn_xTe$ doped with In are much heavier than those of undoped $Pb_{1-x}Sn_xTe$.

From these investigations, it is found that experimental results are consistent with the model in which the band discontinuities between PbTe and $Pb_{1-x}Sn_xTe$ are determined by taking the In pinning level as the energy origin.

ACKNOWLEDGEMENTS

I want to express my deepest gratitude to my adviser Prof. K. Murase for introducing me to the field of superlattices and deep impurities of IV-VI compound semiconductors. I will never forget his enthusiastic interest and encouragement during the course of this study, as well as his always precise and clever advice. I would like to express my sincere thanks to him for his kind reading of this manuscript.

I am also grateful to Dr. S. Takaoka not only for several fruitful discussions about the subject of this thesis but also for teaching me many excellent experimental techniques.

I am also indebted to Prof. H. Fujiyasu, Dr. A. Ishida and Mr. Matsuura for stimulating discussions and preparing superlattice samples. If it had not been for their help, I could not have obtained high quality superlattices.

I would like to thank Prof. M. Yamanaka, Dr. Y. Tsunawaki, Dr. K. Muro, and Dr. H. Nakata for their advice of constructing the optical pumping laser system. I express my gratitude to Mr. Aoyagi and Mr. Mishima, of the Technical Center of Osaka Univ., for making of carbon dioxide laser tubes.

I am grateful to Mr. K. Moritoki and Mr. Y. Urakawa for their cooperations in the construction of the laser systems and magnetoplasma experiments. I also thank to Mr. F. Nihei for his help in magnetoresistance experiments. I wish to thank to Mr. H. Takahashi for preparing samples of In doped PbSnTe and for

his support in magnetoplasma reflection experiments.

Appreciation should also be expressed to Prof. S. Ishida, Dr. S. Sugai and Dr. K. Inoue for their encouragements. Particularly, the suggestion of Dr. K. Inoue for the dynamics based on the configurational coordinate model helps my interpretation for the experimental results of PbSnTe doped with In.

I wishes also to thank the Yukawa foundation for the award of a fellowship for the last half year.

CONTENTS

$Pb_{1-x}Sn_xTe/In$

§1 INTRODUCTION

§1-1 PbTe/$Pb_{1-x}Sn_xTe$ superlattice

In recent years it has become possible to design even an electronic structure of semiconductor by periodically alternating thin films (a few - a few hundred Å) of two different materials periodically, that is, by making a supperlattice[1]. Since the superlattice has a periodic structure composed of two different materials, the Brillouin zone is divided into minizones by $k=n\pi/d$, where k: the wave vector of the superlattice direction, n: an integer, d: the superlattice periodicity. As a result, narrow allowed bands and forbidden gaps are formed in the host material conduction band. Hence the superlattice has different electronic properties from those of the host materials.

Important parameters to determine the electronic properties of a superlattice are the layer thicknesses and the energy gaps of the host materials. In addition, one more very important parameter is the band discontinuity between the two host materials. The discontinuity of conduction band edge, ΔE_c is defined by

$$\Delta E_c = E_{cB} - E_{cA}, \qquad (1.1.1)$$

where E_{cA} and E_{cB} are the conduction band edge energies of the host materials A and B, respectively. Determining ΔE_c simultaneously gives the discontinuity of valence band edge, ΔE_v by the equation

$$\Delta E_V = \Delta E_C + Eg_A - Eg_B, \qquad (1.1.2)$$

where Eg_A and Eg_B are the energy gaps of the host materials A and B, respectively. The differences of these discontinuities extremely change the electronic properties.

When $\Delta Ec>0$ and $\Delta Ev<0$(type I), electrons and holes are confined in the layers of the host material A. The transition probability of electrons across the energy gap is large(see Fig. 1-1-1 (a)). A $GaAs/Ga_{1-x}Al_xAs$ superlattice[1-13] corresponds to this case and is used as a quantum well laser device[4,11] for this reason. On the other hand, when $\Delta Ec>0$ and $\Delta Ev>0$(type I')[14], electrons are confined in the layers of the host material A and holes are confined in the layers of the host material B(see Fig. 1-1-1 (b)). In an extreme case(type II), the conduction band edge of the host material A is below the valence band edge of the host material B (see Fig. 1-1-1 (c)). The GaSb/InAs superlattice[15-22] belongs to this case, and shows semimetal-semiconductor transitions with decreasing layer thicknesses.

To explain these electronic properties of the superlattice, electronic structures have been calculated. The calculation methods are classified into two types. One is the calculation based on the first principle[18], and it is suitable for the superlattices composed of thin layers, e.g., atomic monolayer superlattices[6]. The other is based on the effective mass theory[23], and it is preferable for thicker layer superlattices. Particularly an envelope function approximation[24-30], which

belongs to the effective mass theory, has succeeded in explaining metal-insulator transitions of the GaSb/InAs superlattice[26].

Since superlattices were proposed in 1970 by Esaki and Tsu[1] to obtain high speed switching devices having negative resistance, $Ga_{1-x}Al_xAs/GaAs$, InAs/GaSb, Ge/Si, Ge/GaAs, InSb/PbTe, InSb/CdTe, ZnSe/ZnTe, PbTe/CdTe ,$PbTe/Pb_{1-x}Sn_xTe$ superlattice, etc. have been prepared and their electronic structures have been investigated. These samples have been prepared by various methods; molecular beam epitaxy (MBE)[5,15], metal-organic chemical vapor deposition(MO-CVD)[31], laser deposition[32], hot wall epitaxy[33,34], and so on. Especially MBE is widely used for III-V compound superlattice, because this method makes it possible to control the growth of each material by atomic monolayer unit.

The IV-VI compound semiconductors have narrow energy gaps and their band edge structures are described the two band model whose formalism is practically the same as Dirac's equation[35,36]. Hence IV-VI compound superlattices have been attracting great interest in fundamental electronic properties and application to infrared lasers and detectors[37-39]. In IV-VI compound superlattices, $PbTe/Pb_{1-x}Sn_xTe$ superlattice was prepared for the first time by Kinoshita and Fujiyasu[33], using hot wall epitaxy method. Since then PbTe/SnTe[40], $Pb_{1-x}Eu_xTe/PbTe$[41,42], $PbSe/Pb_{1-x}Sn_xSe$[14], nipi PbTe[43,44] superlattices have been investigated.

In particular, $PbTe/Pb_{1-x}Sn_xTe$ superlattices have been wide-

ly investigated[14,29,30,33,34,40,43,45-49], because of their high mobilities. Kinoshita and Fujiyasu analyzed the band edge structure using absorption due to interband transition, and measured Shubnikov-de Haas oscillations[33,47]. Fantner et al. revealed by X-ray diffraction that lattice mismatch between PbTe and $Pb_{1-x}Sn_xTe$ is accommodated with uniform strain of each layer[50]. Measurements of cyclotron resonance showed that the PbTe layers form well potentials in the conduction band[14]. But Pascher et al. concluded from g-value measurement that electrons and holes are confined in the $Pb_{1-x}Sn_xTe$[49]. In addition to these experimental results, the model based on deep levels of In in $Pb_{1-x}Sn_xTe$ suggests that the superlattice belongs to type I'[14], but the tight binding calculation suggests that it belongs to type I[29]. Thus contradictory experimental results and models exist.

So far, IV-VI compound superlattices forming 2D-electron systems have been investigated intensively. But superlattices are originally characterized by widely spread miniband due to tunnelling of electrons through barrier layers. One of our purposes is to show that miniband spread with decreasing thickness of the barrier layer. Another is to examine a consistency between experimental results and envelope function calculations. The third purpose is to determine the band discontinuities between PbTe and $Pb_{1-x}Sn_xTe$.

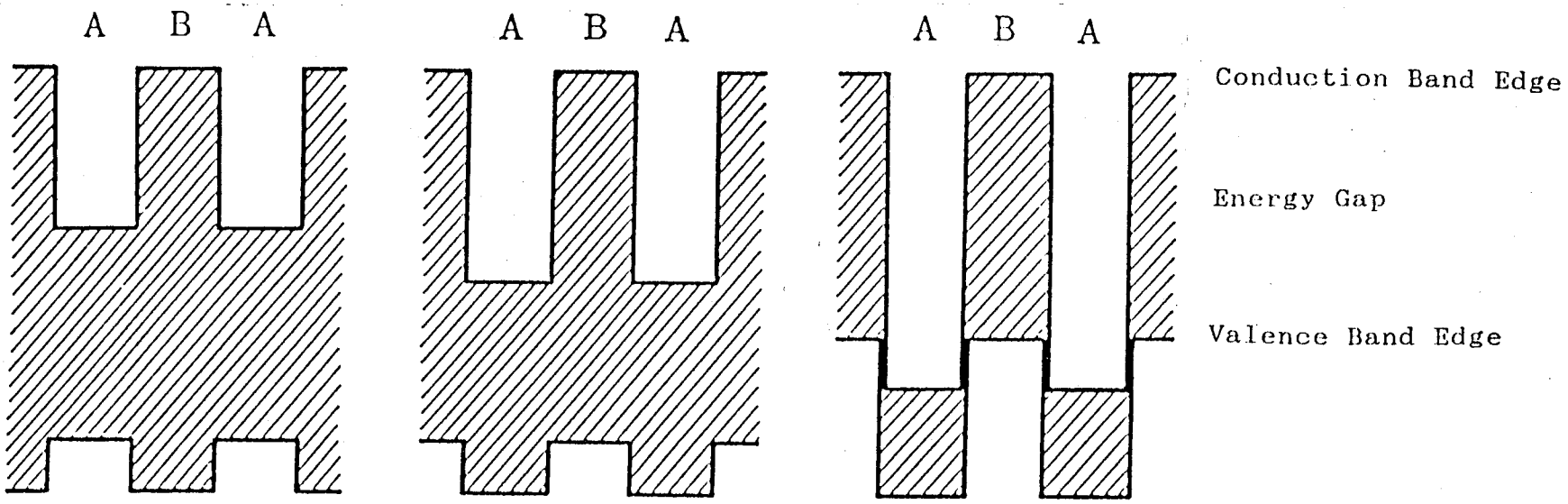

FIG. 1-1-1 Types of superlattices. The differences of Band Edge discontinuities yield various types of superlattice.

§1-2 In-doped $Pb_{1-x}Sn_xTe$

Aluminum, Ga, In, and Tl atoms, belonging to third column in the periodic table, show respectively different characters in IV-VI narrow gap semiconductors. Usually, the same group atoms act with same dopant behavior; for Si, group V atoms, that is, P, As, and Sb atoms make shallow donor levels. However, Al, Ga atoms are strong donor dopants and In atoms are weak donor dopants in PbTe, while Tl impurities behave as strong acceptors. The carrier concentration in PbTe saturates to a constant value independent of the impurity concentration at high impurity doping[50,51]. For n-type dopants, the saturation carrier concentration in $Pb_{1-x}Sn_xTe$ decreases with increasing tin compositions; on the other hand for p-type dopants the saturation carrier concentration increase with increasing tin composition[51]. In particular, $Pb_{1-x}Sn_xTe$ doped with In shows metal-insulator-metal transitions with increasing tin composition[52,53](see Figs. 1-2-1 and 1-2-2). Thus the levels of In impurities in $Pb_{1-x}Sn_xTe$ move from above the conduction band bottom to below the valence band top with increasing tin compositions. Pressure (0-18kbar) also causes similar metal-insulator transitions for $Pb_{1-x}Sn_xTe$ doped with In as shown in Fig. 1-2-3). Moreover In impurities emit or capture electrons and pin the Fermi energy. Even though the density of states at band edge changes by applying high magnetic field.(0-3T), the Fermi energy does not change[54,55]. In order to explain these curious experi-

mental results, a double electron capture model is suggested[56]. In the model, In atom in $Pb_{1-x}Sn_xTe$ takes three charged states, $(4s)^0$, $(4s)^1$, and $(4s)^2$, and electrons occupied at In impurity levels largely couple with the lattice surrounding the In atoms (large electron-phonon coupling). Introducing large electron phonon coupling makes In impurities prefer doubly electron captured states and non electron captured states to singly captured states(as discussed in section 9-1). There was single electron capture model in which the In impurity state was of s-type. However, the dependence of carrier concentration on temperature and impurity concentration suggests that the singly occupied model is improbable[57]. There was another model that the In forms a very narrow impurity band composed of two states per impurity atom. This model is also doubtful because it does not take into account the Coulomb interaction between two electrons captured by the same impurity. Moreover, the impurity conduction cannot be observed[57]. Diminishing of photoluminescence intensity due to interband transition and long relaxation of photoconduction support the existence of large electron phonon coupling[58].

Recently a kinetic mechanism of the photoconduction draws attentions of many researchers[59-61]. The photoconduction of $Pb_{1-x}Sn_xTe$ doped with In is remarkably strong below 20K. Negative photoconduction[56,61] and persistent photoconduction[62] are also observed. The photoconduction is sensitive to temperature and excitation light spectra. Our main purpose is to clarify the mechanism of photo-conduction and to give quantitative interpre-

tation for the Anderson's negative U model.

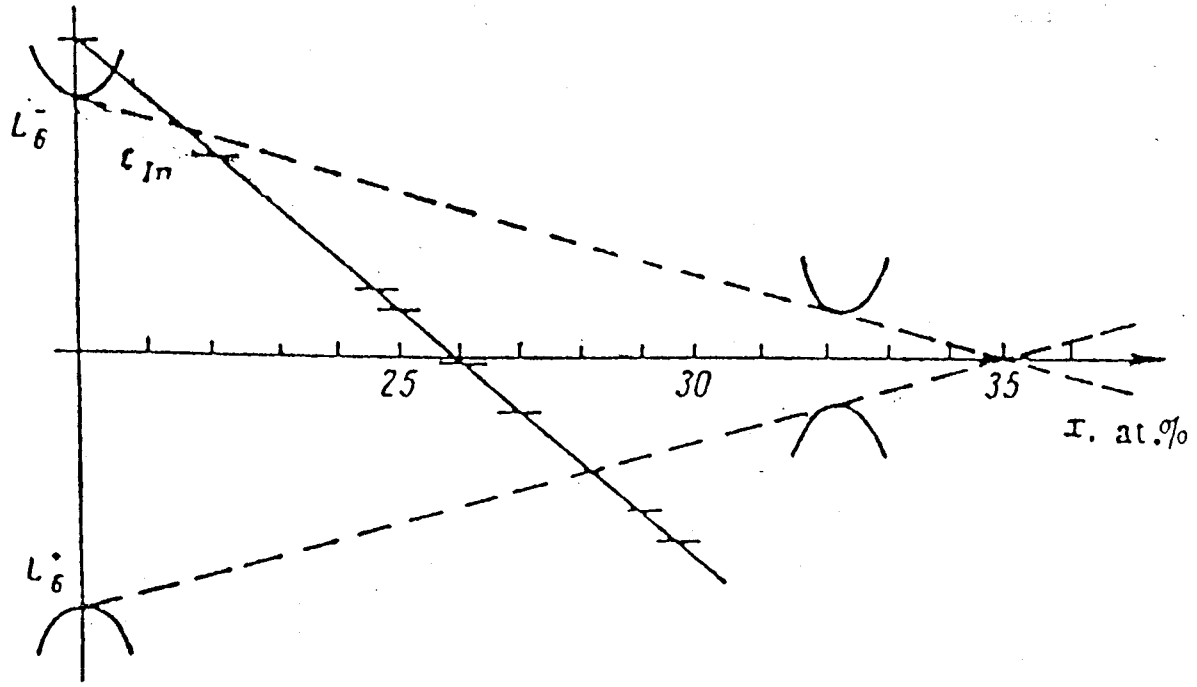

FIG. 1-2-1 Tin composition dependence of pinning Fermi level of $Pb_{1-x}Sn_xTe$ doped with 0.5 at.% In(after Akimov et al. ref.63).

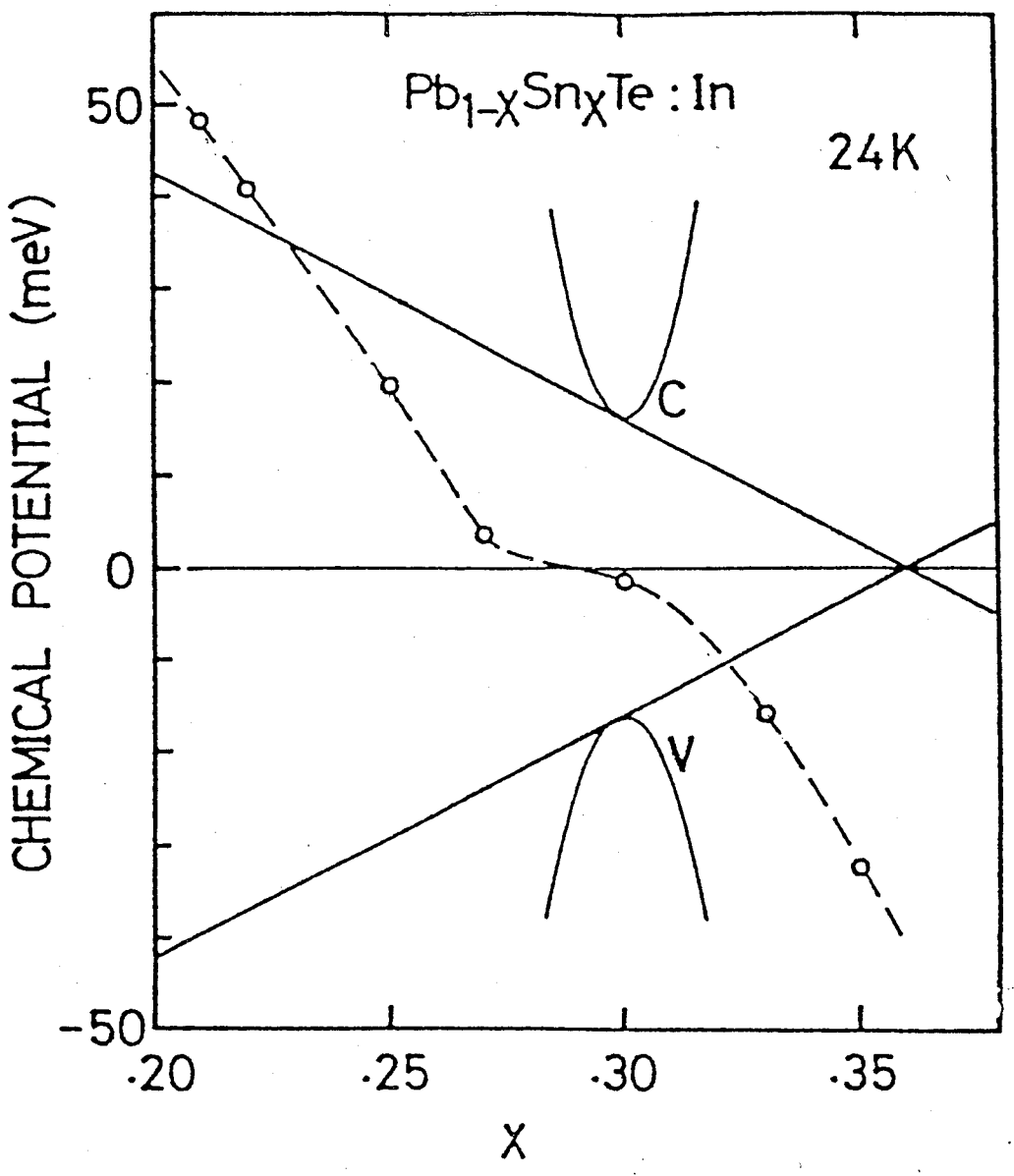

FIG. 1-2-2 Tin composition dependence of pinning Fermi level of $Pb_{1-x}Sn_xTe$ doped with In by isothermal anealing(after Takaoka et al. ref.54)

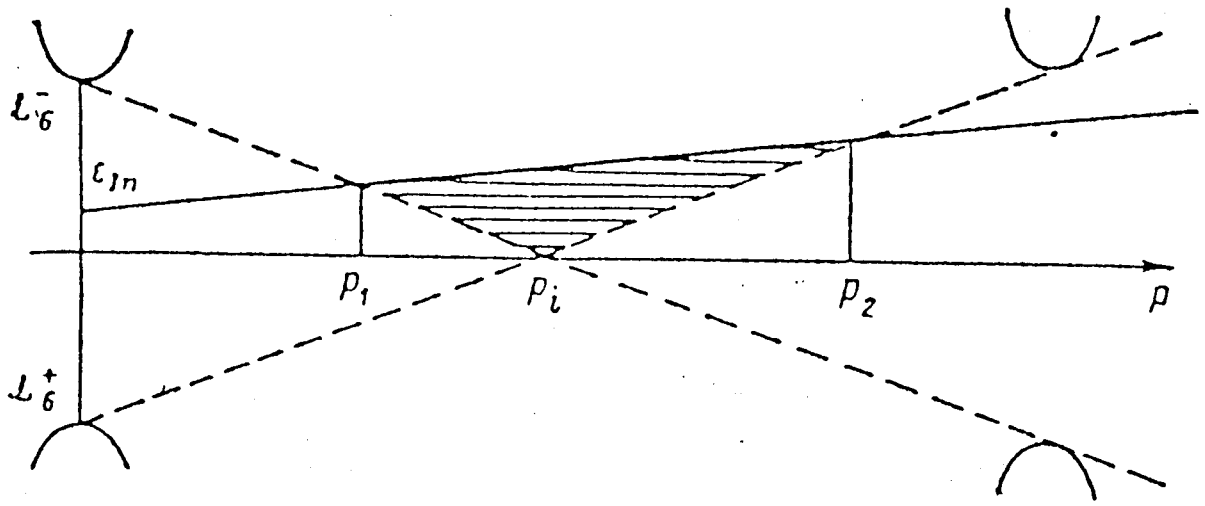

FIG. 1-2-3 Pressure dependence of pinning Fermi level of $Pb_{0.75}Sn_{0.25}Te$ doped with 0.5 at.% In(by Akimov et al.ref.63).

§1-3 The relation between investigations of PbTe/$Pb_{1-x}Sn_xTe$ superlattices and In doped $Pb_{1-x}Sn_xTe$

These two investigations seems to be independent of each other but they are closely related in band discontinuities between PbTe and $Pb_{1-x}Sn_xTe$. It is difficult to determine the discontinuities from the first principle, because very precise calculations are needed due to the very narrow energy gaps (<180meV) of these compounds. There is another method to determine the discontinuity. This method utilizes the deep impurity level of In as the energy origin. Indium atoms in $Pb_{1-x}Sn_xTe$ enter at the metallic atom sites. Since In are surrounded by Te atoms and electrons captured by In atoms are strongly localized, In levels are determined by the interaction between In atoms and Te atoms. Therefore In levels are supposed not to be affected by tin composition. Investigation of In levels is important for study of superlattices[14].

Section 2 describes the band model in $Pb_{1-x}Sn_xTe$ and the k·p perturbation theory.

For superlattices, in Section 3, we describe the envelope function approximation to calculate superlattice electronic structures. The magnetoplasma theory is presented for analysis of spectra in Section 4. Laser construction and experimental procedure(for PbTe/$Pb_{1-x}Sn_xTe$) are described in Section 5. Strain effect and X-ray analysis are given in Section 6. Experimental

results are presented in Section 7. Section 8 presents discussion of superlattices.

For In-doped $Pb_{1-x}Sn_xTe$, Section 9 contains Anderson's negative U model. Magnetoplasma dielectric constant is given in Section 10. Experimental procedure(for $Pb_{1-x}Sn_xTe$/In) is given in Section 11. The experimental results are given in Section 12. The discussion is given in Section 13. Summary is given in Section 14.

§2 BAND STRUCTURES OF PbTe, SnTe, AND $Pb_{1-x}Sn_xTe$

The energy band structures of IV-VI compounds have been investigated with great interest to understand their physical properties: the narrow band gap, the band inversion, the phase transition[64-66], the Knight shift[67], etc. In this section, we survey the overall band feature and describe the band edge structure by $\mathbf{k}\cdot\mathbf{p}$ perturbation theory. This perturbation theory is important to derive the envelope function approximation for the band calculation of superlattices.

§2-1 Full band structure of PbTe and SnTe

A number of band structures of IV-VI compounds have already been calculated, using various methods[67-78]. In the compounds, especially lead chalcogenides, relativistic effects are very important. They are becoming more accurate using recent precise measurements of XPS and UPS[79,80], Knight shift, and effective masses.

Figure 2-1-1 shows the band structure of PbTe calculated by Martinez et al. using an empirical pseudopotential method (E.P.M.)[78]. The lowest band has a character of s-bonding and mainly comes from 5s electrons of Te. The second lowest band has a character of s-antibonding and mainly comes from 6s electrons of PbTe. The third, fourth, and fifth lowest bands have characters of p-bonding and mainly come from p-electrons of Te. The

sixth, seventh, and eighth lowest bands have anti-bonding characters and mainly come from p-electrons of Pb. The very small minimum energy gap(0.2eV) lies between the fifth and sixth lowest bands, and the valence band maxima and the conduction band minima are found at the L-points in the Brillouin zone.

Figure 2-1-2 shows the band structure of SnTe calculated by Bernick and Kleinman using EPM[76]. Its feature resembles that to PbTe except for inversion of the levels at L-points. Figure 2-1-3 shows the first Brillouin zone and Fermi surface of PbTe and SnTe.

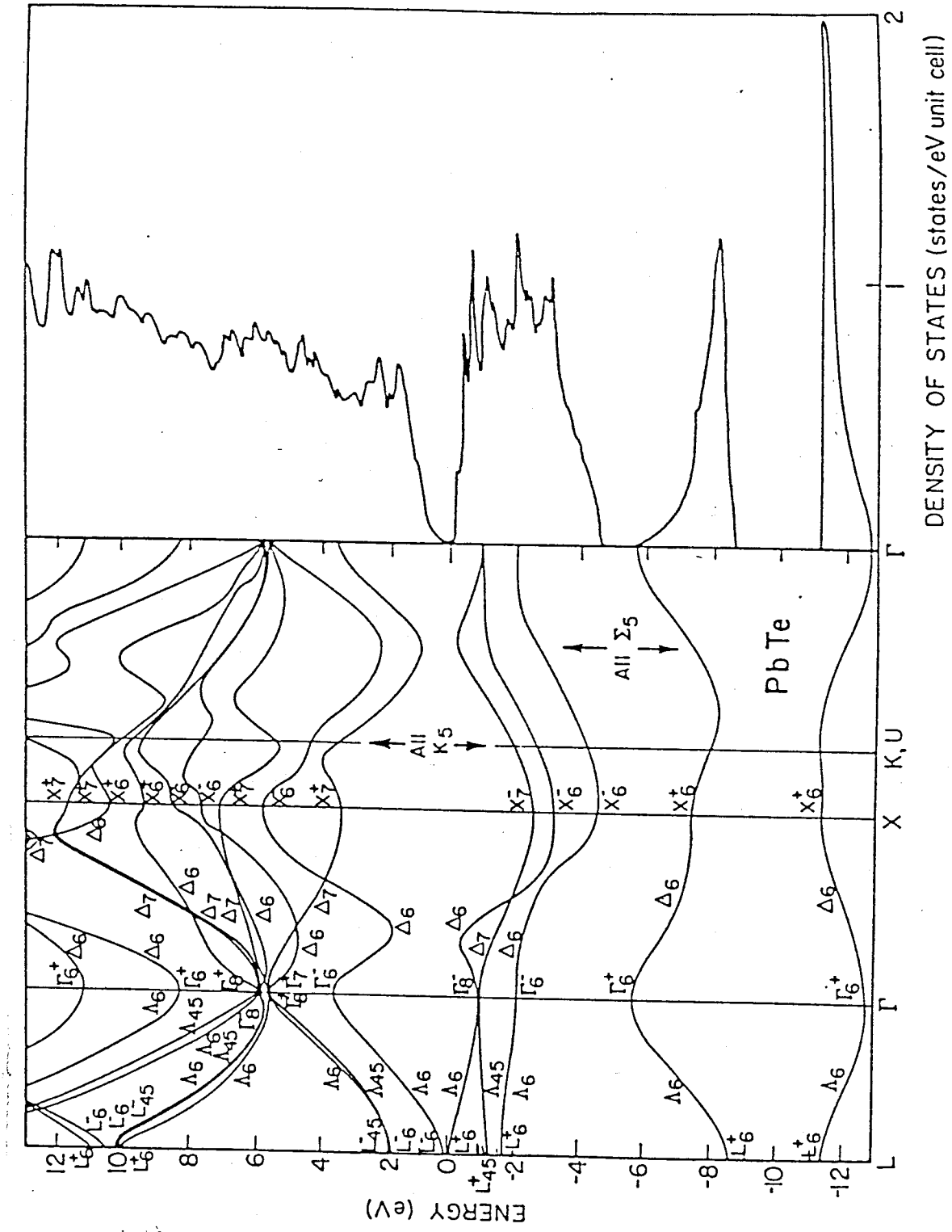

FIG. 2-1-1 Band structure of PbTe(after Martinez et al. ref.78).

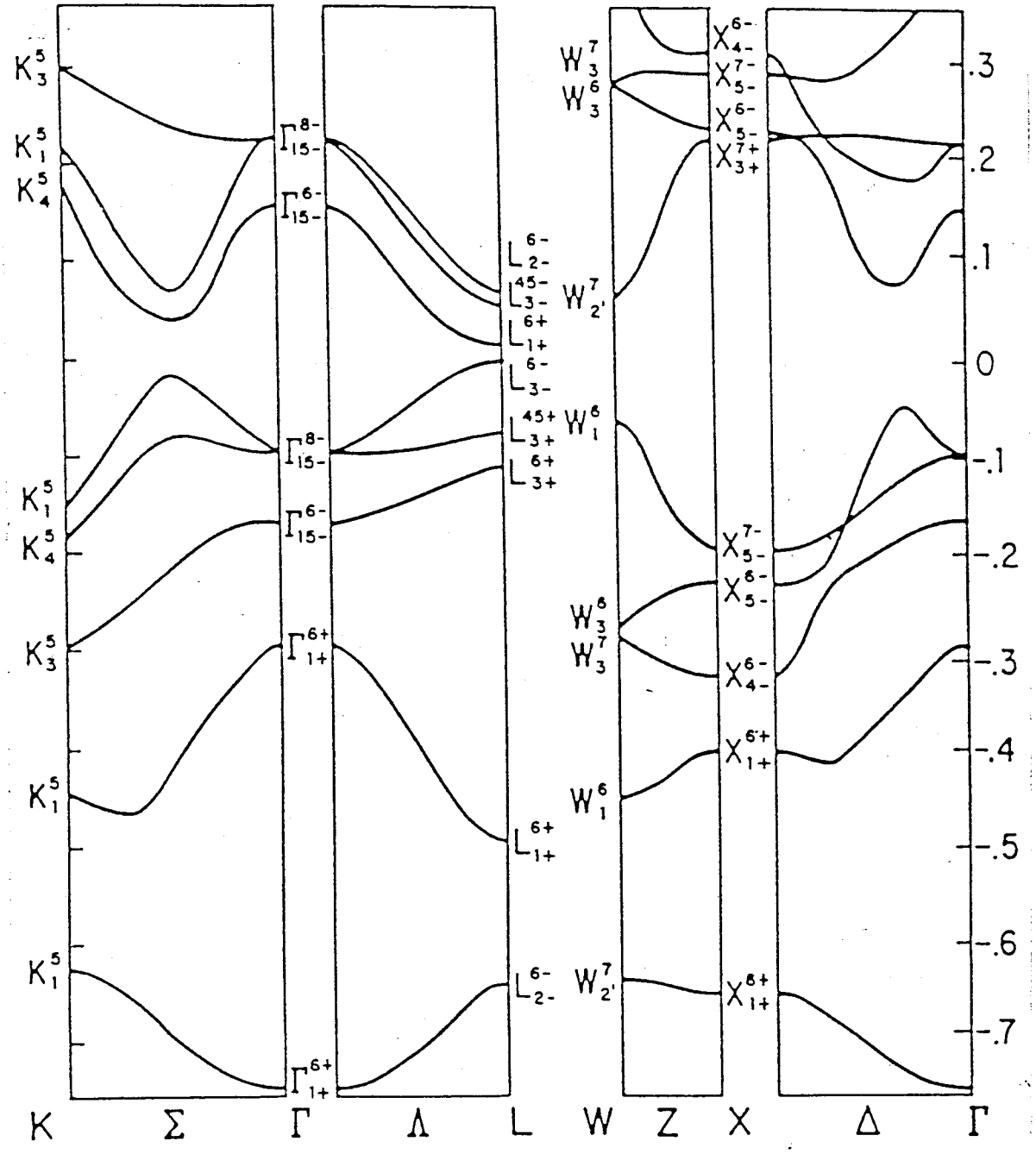

FIG. 2-1-2 Band structure of SnTe after Bernik et al.(Energy in Ry, ref.76).

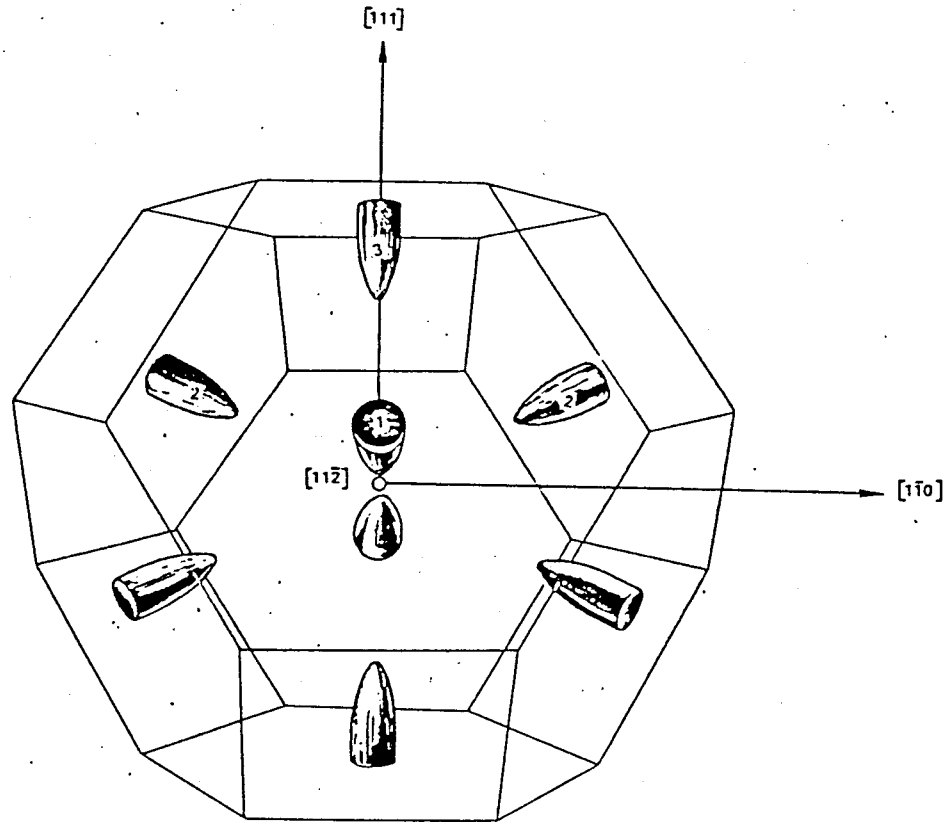

FIG. 2-1-3 First Brillouin zone of PbTe and SnTe and Fermi surface.

§2-2 Band edge structure and k·p theory

Although full band structures are valid for recognizing XPS or UPS results, only properties at L-point of them is needed to describe band edge structures. Since our substantial interests are transport properties and magnetic level near the Fermi level, we must know the band edge structure. For describing band edge structures k·p theories are useful[81-87]. In particular, for pseudobinary system, e.g., PbTe-SnTe, k·p theories are helpful because band parameter can be easily obtained. Moreover k·p theories develop as envelope function approximation to calculate band edge structure of superlattice. Full band structure has established and gives the sequence of energy levels at L-point and symmetry of their wave functions to formalize k·p perturbation theory.

For PbTe, reading from Fig. 2-1-1 and Fig. 2-1-2 gives the energy levels at L-point as follows.

L-point level	Energy(eV)	
	PbTe	SnTe
other higher levels	>10.0	
$L_6^-(L_{61}^-)$	2.0	0.98
L_{45}^-	1.9	0.75
$L_6^-(L_{62}^-)$	0.2	0.0
$L_6^+(L_{61}^+)$	0.0	0.26
L_{45}^+	-1.2	-1.03
$L_6^+(L_{62}^+)$	-1.7	-1.46
other lower levels	<-8.5	<-5.0

(reading directly Figs. 2-1-1 and 2-1-2)

We can see that that band edge symmetry is L_{61}^+ for the valence band and L_{62}^- for the conduction band in PbTe. These are reversed in SnTe. The energy difference of valence band maxima and conduction band minima is very small. Because the other levels at L-points are far from the two band, the two band model based on k·p perturbation theory is valid. Even when more precise approach is needed, it is sufficient to take into account the other four band contributions. To acquire momentum matrix elements, Mitchell and Wallis started from single group basis functions belonging to the Hamiltonian without spin-orbit interaction[84]. They transformed single group basis functions into double group basis functions, and they diagonalized the Hamiltonian taking into account spin-orbit interaction. the Hamiltonian is given by

$$\mathcal{H} = -\frac{\hbar^2}{2m}\frac{\partial^2}{\partial r^2} + V(r) + \frac{1}{8(mc)^2}\nabla^2 V(r) + \frac{1}{2(mc)^2}[p\cdot\sigma\times\nabla V(r)]. \quad (2.2.1)$$

They could decrease the number of momentum matrix element parameter down to seven by this procedure. Figure 2-2-1 shows the procedure and gives the notation and symmetry of basis wave functions at L-point. In these notation, + and - denote even and odd parities, respectively; α and β are a Kramers degeneracy pair; the X, Y, and Z coordinate axes are taken in [$\bar{1}\bar{1}$2], [1$\bar{1}$0], and [111] crystallographic directions, respectively; θ^+ and θ^- are mixing parameter of spin-orbit interaction. Using the basis functions $L_{61}^{+}\alpha$, $L_{61}^{+}\beta$, $L_{62}^{-}\alpha$, and $L_{62}^{-}\beta$ gives the 4×4 k·p Hamiltonian:

$$
\mathcal{H} = \begin{array}{c}
\begin{matrix} L_{62}^{-}\,\alpha & L_{62}^{-}\,\beta & L_{61}^{+}\,\alpha & L_{61}^{+}\,\beta \end{matrix} \\
\begin{pmatrix}
\frac{E_g}{2} & 0 & \frac{\hbar}{m_0} P_{/\!/} k_z & \frac{\hbar}{m_0} P_{\perp} k_- \\
0 & \frac{E_g}{2} & \frac{\hbar}{m_0} P_{\perp} k_+ & -\frac{\hbar}{m_0} P_{/\!/} k_z \\
\frac{\hbar}{m_0} P_{/\!/} k_z & \frac{\hbar}{m_0} P_{\perp} k_- & -\frac{E_g}{2} & 0 \\
\frac{\hbar}{m_0} P_{\perp} k_+ & -\frac{\hbar}{m_0} P_{/\!/} k_z & 0 & -\frac{E_g}{2}
\end{pmatrix}
\end{array} , \qquad (2.2.2)
$$

where P// and P⊥ are the longitudinal and transverse momentum matrix elements; k_+ and k_- are defined by k_x+ik_y, and k_x-ik_y; the operator p is composed of momentum part and spin-orbit term

$$p = \frac{\hbar}{i}\nabla + \frac{\hbar}{4mc^2}\sigma\times\nabla V \ . \qquad (2.2.3)$$

From Eq. (2.2.2) the energy dispersion is given by

$$(\frac{Eg}{2} - E)(\frac{Eg}{2} + E) = \frac{\hbar^2}{m_o^2}\left\{P_\perp^2(k_x^2+k_y^2)+P_L^2k_z^2\right\}. \qquad (2.2.4)$$

Taking into account contributions from the other bands of six bands leads to the 4×4 Hamiltonian operator

$$
\mathcal{H} = \begin{pmatrix}
 & L_{62}^{-}\,\alpha & L_{62}^{-}\,\beta & L_{61}^{+}\,\alpha & L_{61}^{+}\,\beta \\
L_{62}^{-}\,\alpha & \frac{E_g}{2} + \frac{\hbar^2 k_\perp^2}{2 m_t^-} + \frac{\hbar^2 k_z^2}{2 m_\ell^-} & 0 & \frac{\hbar}{m_0} P_{/\!/} k_z & \frac{\hbar}{m_0} P_\perp k_- \\
L_{62}^{-}\,\beta & 0 & \frac{E_g}{2} + \frac{\hbar^2 k_\perp^2}{2 m_t^-} + \frac{\hbar^2 k_z^2}{2 m_\ell^-} & \frac{\hbar}{m_0} P_\perp k_+ & -\frac{\hbar}{m_0} P_{/\!/} k_z \\
L_{61}^{+}\,\alpha & \frac{\hbar}{m_0} P_{/\!/} k_z & \frac{\hbar}{m_0} P_\perp k_- & -\frac{E_g}{2} - \frac{\hbar^2 k_\perp^2}{2 m_t^+} - \frac{\hbar^2 k_z^2}{2 m_\ell^+} & 0 \\
L_{61}^{+}\,\beta & \frac{\hbar}{m_0} P_\perp k_+ & -\frac{\hbar}{m_0} P_{/\!/} k_z & 0 & -\frac{E_g}{2} - \frac{\hbar^2 k_\perp^2}{2 m_t^+} - \frac{\hbar^2 k_z^2}{2 m_\ell^+}
\end{pmatrix} . \qquad (2.2.5)
$$

It is called the six band Hamiltonian. From Eq.(2.2.5) the energy dispersion is given by

$$\left(\frac{Eg}{2} + \frac{\hbar^2 k_\perp^2}{2m_t^-} + \frac{\hbar^2 k_{/\!/}^2}{2m_l^-} - E\right)\left(\frac{Eg}{2} + \frac{\hbar^2 k_\perp^2}{2m_t^+} + \frac{\hbar^2 k_{/\!/}^2}{2m_l^+} + E\right)$$

$$= \frac{\hbar^2}{m_o^2}\left(P_\perp^2 k_{/\!/}^2 + P_L^2 k_z^2\right) . \qquad (2.2.6)$$

From Eq.(2.2.6) the band edge masses are given by

$$\frac{1}{m_{tc}} = \frac{2P_\perp^2}{Egm_o^2} + \frac{1}{m_t^-} , \qquad \frac{1}{m_{lc}} = \frac{2P_{/\!/}^2}{Egm_o^2} + \frac{1}{m_l^-} ,$$

$$\frac{1}{m_{tv}} = \frac{2P_\perp^2}{Egm_o^2} + \frac{1}{m_t^+} , \text{ and } \frac{1}{m_{tv}} = \frac{2P_\perp^2}{Egm_o^2} + \frac{1}{m_t^+} . \qquad (2.2.7)$$

Figure 2-2-3 shows the energy levels of L-points in $Pb_{1-x}Sn_xTe$ versus Sn composition. The Sn composition dependence of energy gap determined experimentally is shown in Fig. 2-2-4.

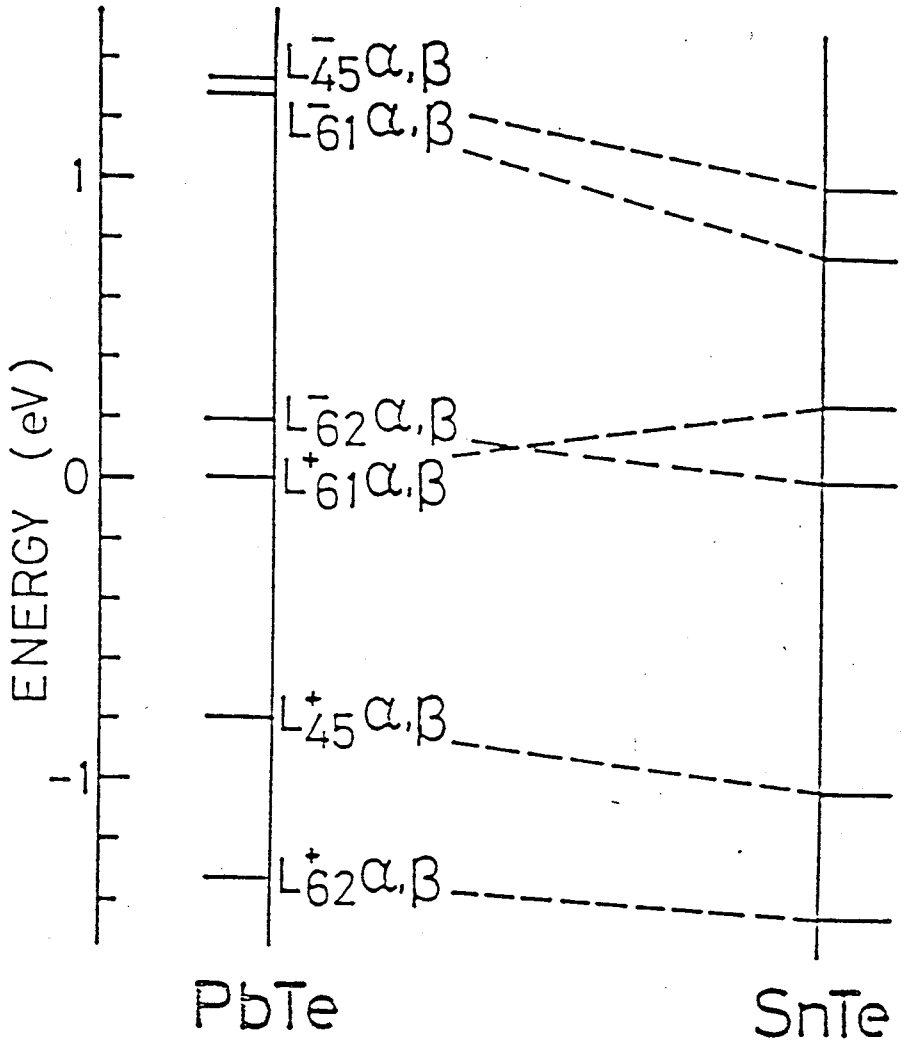

FIG. 2-2-1 Level ordering at L-points in PbTe and SnTe.

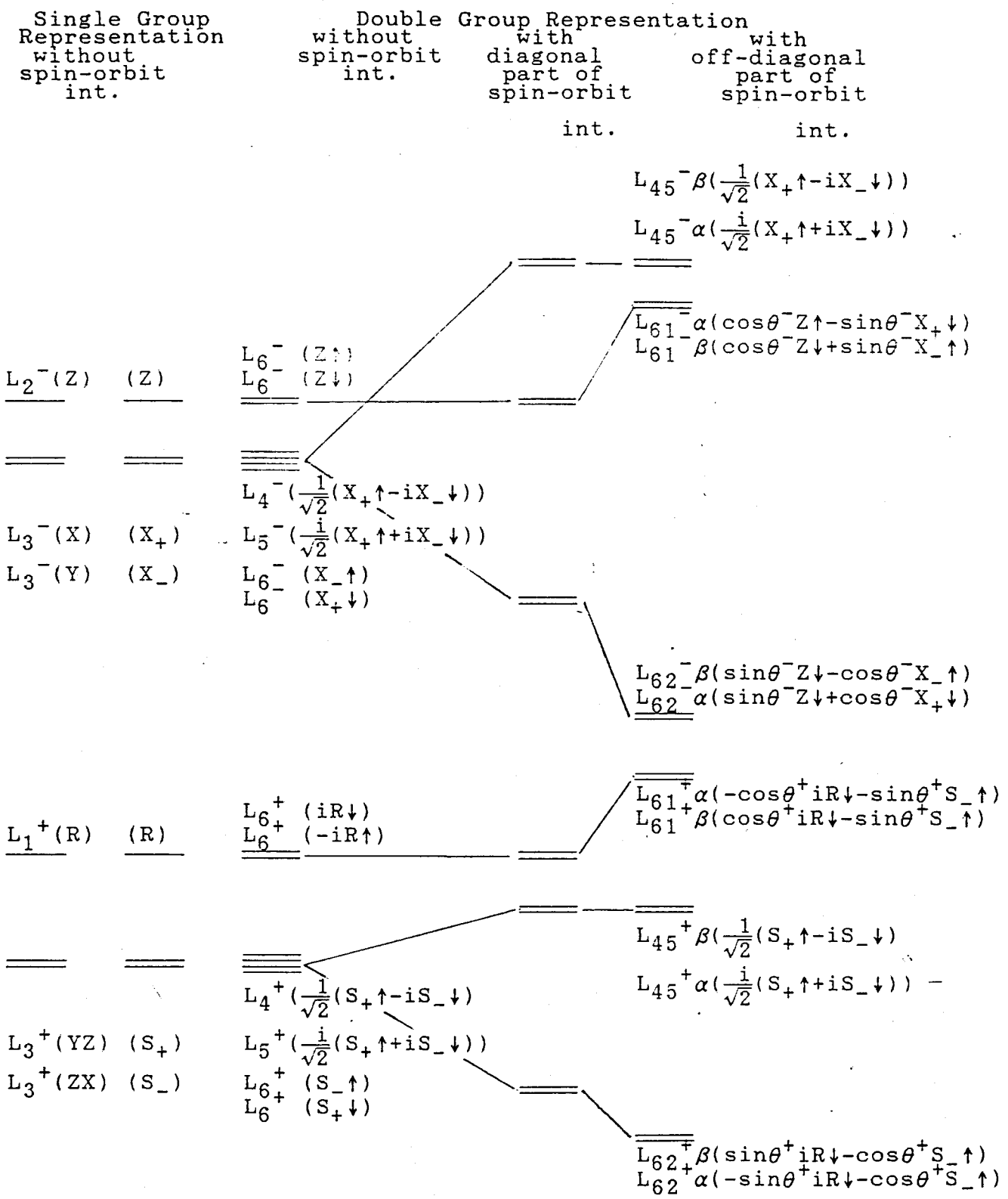

FIG. 2-2-2 Level at L-points and symmetry notations of wave functions(ref.84).

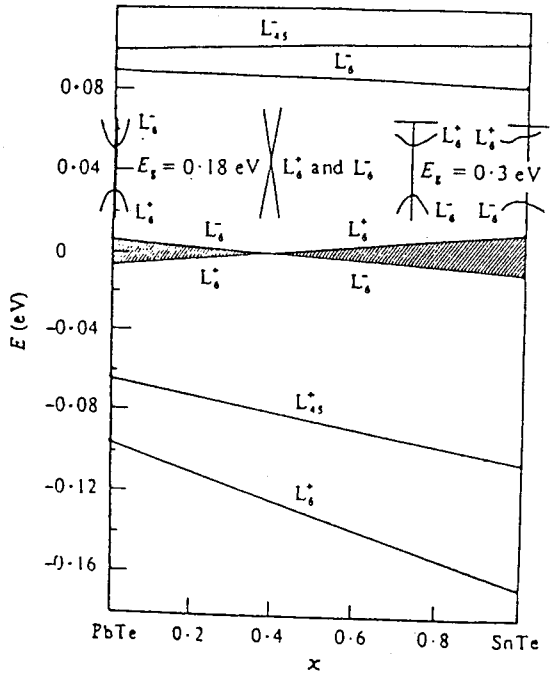

FIG. 2-2-3 Tin composition dependence of energy levels of L-points in $Pb_{1-x}Sn_xTe$. The shaded area shows energy forbidden band(ref.85).

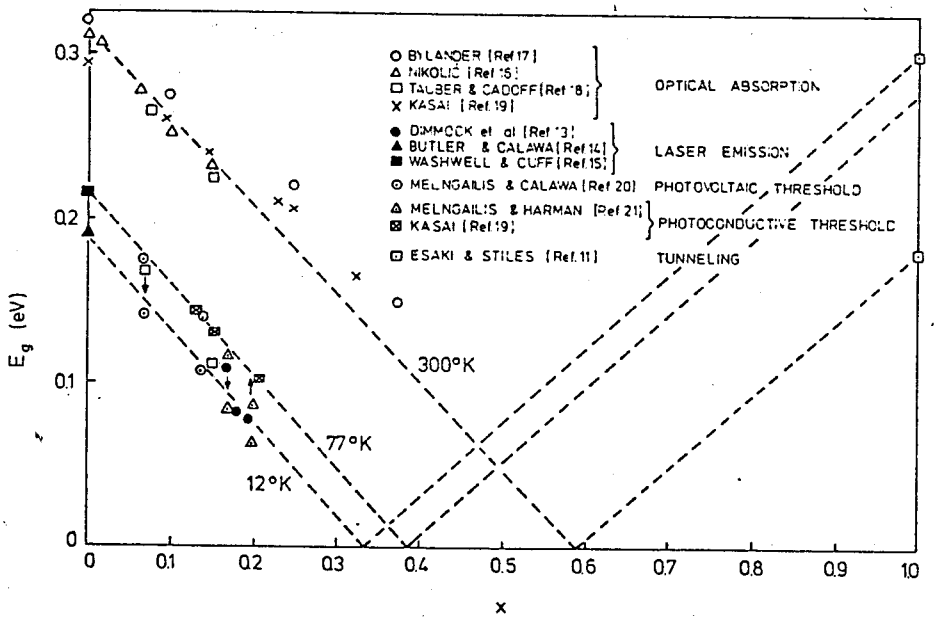

FIG. 2-2-4 Tin composition dependence of energy gap of $Pb_{1-x}Sn_xTe$ obtained from laser emission, optical absorption coefficient, photovoltaic threshold, photoconductive threshold and tunneling(ref.88).

§3 ELECTRONIC STRUCTURE IN PbTe/$Pb_{1-x}Sn_xTe$ SUPERLATTICES

Electronic structures of superlattices are mainly determined by band discontinuities and layer thicknesses. In this section, the problem of the band discontinuities is reviewed. Next, to describe the electronic structure, the energy dispersion relation based on the envelope function approximation is given.

§3-1 Band discontinuities

As stated in introduction, band discontinuities between the two host materials are very important parameters to determine the electronic properties of superlattices. The discontinuity of conduction band edge, ΔE_c is defined by

$$\Delta E_c = \chi_A - \chi_B \ ,$$

and the discontinuity of valence band edge, ΔE_v is defined by

$$\Delta E_v = \chi_A + Eg_A - (\chi_B + Eg_B),$$

where Eg_A and Eg_B are the energy gaps of host materials A and B respectively; χ_A and χ_B are the electron affinity of the host materials A and B. The differences of these discontinuities extremely change the electronic properties.

Band discontinuities would be obtained by taking the difference of electron affinities between the two materials. But electron affinity of each material is not an accurate quantity because it is dependent on crystal face directions and chemical properties of crystal surface(this effect is like the effect of

charge double layer in metals). Since the interface charge transfer must be taken into account, even this definition is doubtful. A large number of attempts to obtain the discontinuities are made experimentally and theoretically, but it is difficult to determine the discontinuities in energy within 10meV. It has been long since many people[90] cast doubt on the discontinuities(85% 15% law in GaAs/$Ga_{1-x}Al_xAs$ superlattices) determined by Dingle[89] using energy of sublevels.

In recent years Bauer and Margaritondo have obtained the band discontinuities by synchrotron radiation in a accuracy range of a few tens meV[91]. Harrison has compared the discontinuities obtained from calculation of semiempirical tight binding model, with experimental ones and he obtained an astonishing coincidence between them[92,93]. Another empirical approach is a method using deep level impurity states, which have the character of bare atoms[94].

In PbTe/$Pb_{1-x}Sn_xTe$ the problem of the band discontinuities is controversial because there are two contradictory experimental results. One result shows PbTe/$Pb_{1-x}Sn_xTe$ superlattices(x=0.22) are the type I' by measuring the cyclotron mass of PbTe[14]. The other result claims that PbTe/$Pb_{1-x}Sn_xTe$ superlattices (x=0.12) are the type I from measuring g-value of $Pb_{1-x}Sn_xTe$ by the four wave mixing technique[29,49]. Two contradictory models are proposed beside these results; based on deep levels on In impurities(see Fig. 3-1-1), it has been predicted that the PbTe superlattice belongs to the type I'[14], while based on tight binding

calculation(see Fig. 3-1-2), it has been suggested that superlattices belong to the type I[49].

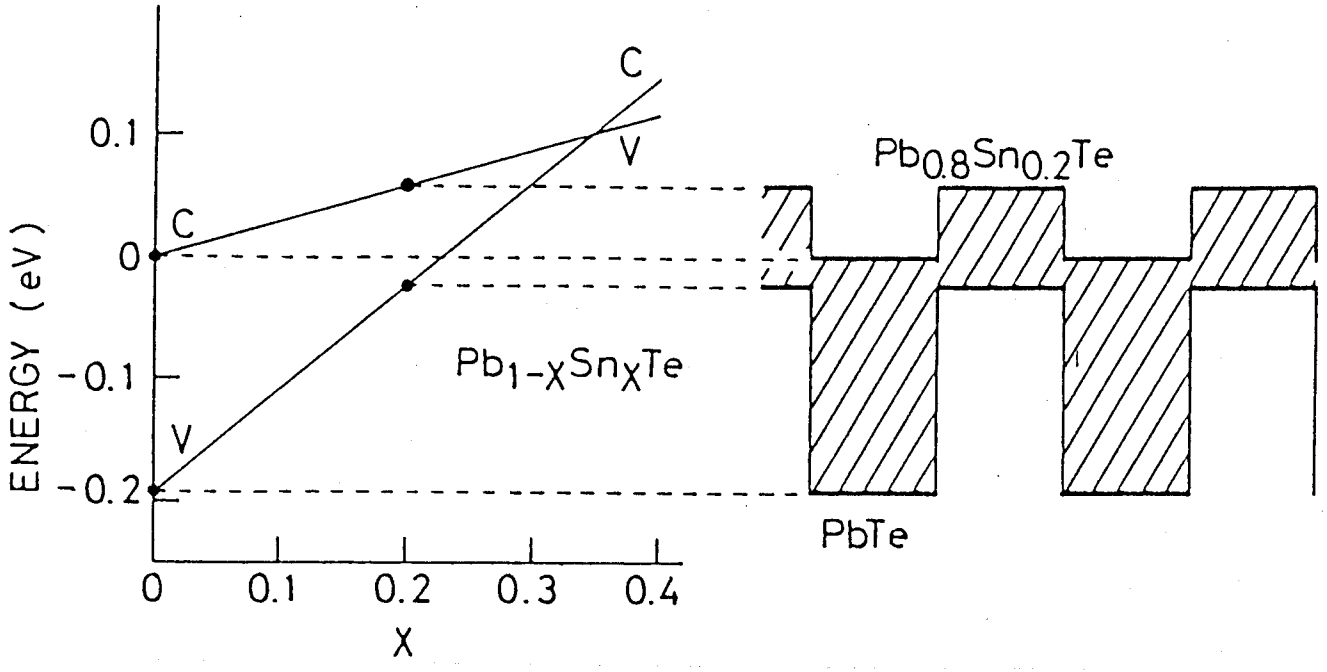

FIG. 3-1-1 Band discontinuity model in which the pinning level of deep impurity indium atoms in $Pb_{1-x}Sn_xTe$ is taken as the energy origin(by Murase et al. ref.25). In this case $PbTe/Pb_{0.8}Sn_{0.2}Te$ superlattices belong to Type I'.

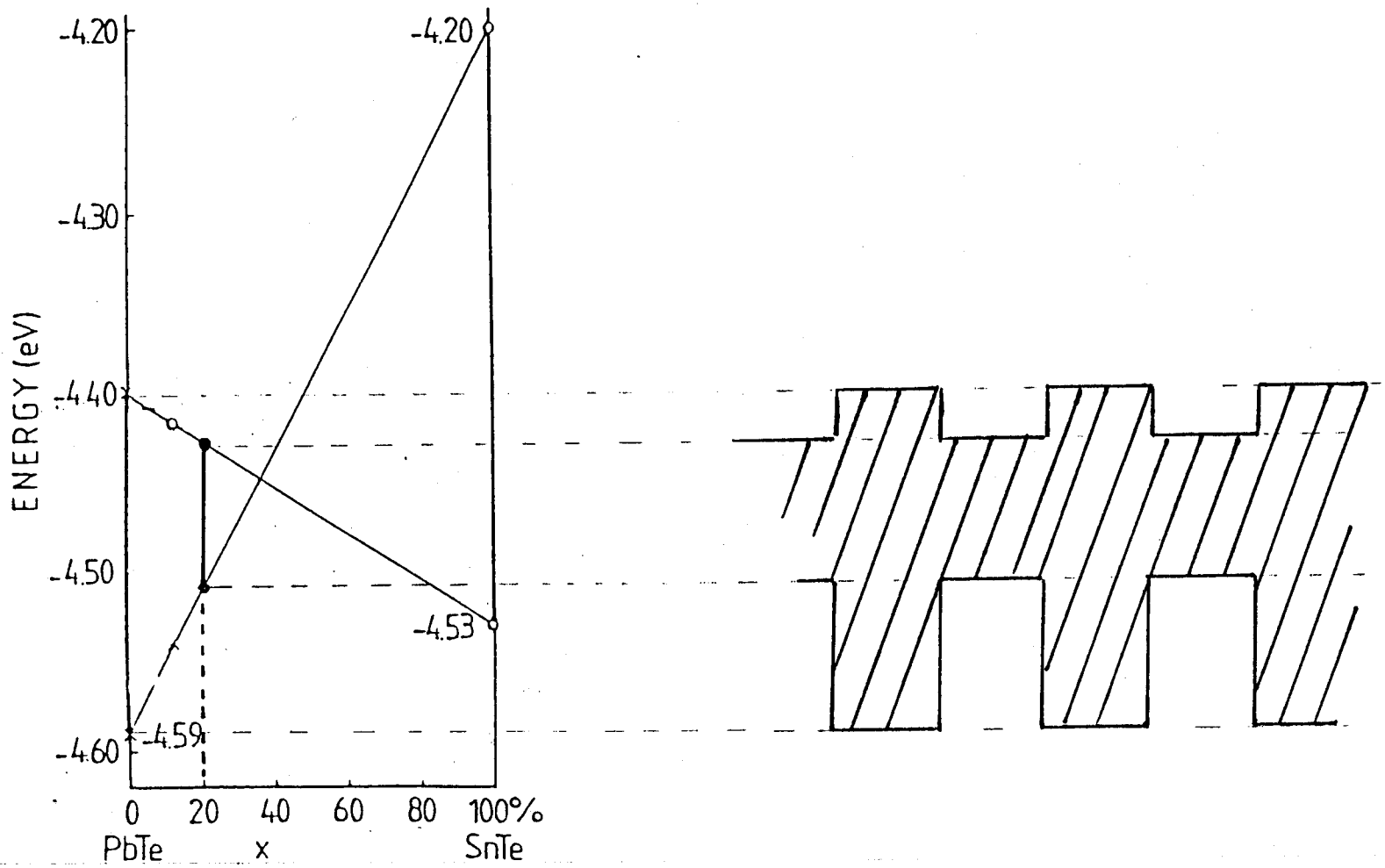

FIG. 3-1-2 Band discontinuity model based on LCAO calculation (by Kriechbaum et al. ref.29). In this case PbTe/$Pb_{0.8}Sn_{0.2}Te$ superlattices belong to Type I.

3-2 Envelope function approximation

The envelope function approximation is an suitable method to obtain the energy dispersions of superlattices consisting of relatively thick layers[24-26,29]. Well-known Kronig-Penny model can not take into account the nonparabolic effects due to the two bands. Moreover Kronig-Penny model does not give the boundary condition of the wave functions at the interfaces between two materials with deferent effective masses. In the envelope function approximation, these effects are taken into account naturally. Suppose that the wave function for a superlattice PbTe/$Pb_{1-x}Sn_xTe$ takes the form

$$\Phi(r) = \begin{cases} \sum_{j=1,2,3,4} F_j(r)u_j^A(r) & \text{at } r \text{ in A} \\ \sum_{j=1,2,3,4} F_j(r)u_j^B(r) & \text{at } r \text{ in B} \end{cases} , \qquad (3.2.1)$$

where $F_j(r)$'s are slowly varying envelope functions; $u_1(r)$, $u_2(r)$, $u_3(r)$, and $u_4(r)$ are the wave functions at the L-point in the Brillouin zone, $L_{62}^-\alpha$, $L_{62}^-\beta$, $L_{61}^+\alpha$, and $L_{61}^+\beta$ (those are defined in Fig. 2-2-2; the superscripts, A and B denote belonging to PbTe and $Pb_{1-x}Sn_xTe$. This assumption for the wave function is justified when the electron energy considered is near band edge energy.

Consider an ideal interface between two semiconductors at the plane $z=z_o$. We make two assumption to derive the matching relation of $F_j(r)$ at the interface.

1) The four basis functions $u_j(r)[j=1,2,3,4]$ in each

material are linearly independent functions of x and y at $z=z_o$.

2) For all x and y at $z=z_o$,

$$\frac{\partial}{\partial z}u_j^A(r) = \frac{\partial}{\partial z}u_j^B(r) . \qquad (3.2.2)$$

The assumption 1) is right because each wave function of x and y does not belong to the same basis function of an irreducible representation of the two-dimensional group of the surface. The assumption 2) is should be examined by a numerical calculation. We define $u_j(r)$ as follows:

$$u_j(r) = \begin{cases} u_j^A(r) \text{ at } r \text{ in } A \\ u_j^B(r) \text{ at } r \text{ in } B \end{cases} . \qquad (3.2.3)$$

Operating the Hamiltonian $\mathcal{H}$ to $\Phi(r)$ leads to

$$\mathcal{H}\Phi = E\Phi, \qquad (3.2.4)$$

or

$$\sum_{j=1,2,3,4} \left\{ -[\frac{\hbar^2}{2m_o}\nabla^2 F_j(r)]u_j(r) - \frac{\hbar}{m_o}\nabla F_j(r)\cdot p u_j(r) + F_j(r)\mathcal{H}u_j(r) \right\} = E\Phi. \qquad (3.2.5)$$

Since $F_j(r)$'s are slowly varying functions, $\nabla^2 F_j(r)$'s are negligible. Multiplying both sides of Eq.(3.2.5) through by $u_1(r)$ and integrating over unit cell at **a**, we obtain

$$\sum_{j=1,2,3,4} \left\{ -\frac{\hbar}{m_o} \nabla F_j(a) \cdot \langle u_1 | p | u_j \rangle + F_j(a) \langle u_1 | \mathcal{H} | u_j \rangle \right\} = E \sum_{j=1,2,3,4} F_j(a) \langle u_1 | u_j \rangle ,$$

(3.2.6)

where we use the fact that since $F_j(r)$'s are slowly varying wave functions, they are regarded constant in the range of unit cell. Finally using normalization properties of $u_j(r)$'s, we obtain simultaneous differential equations for $F_j(r)$'s.

$$\begin{pmatrix} \frac{Eg^-(r)}{2} & 0 & \frac{\hbar}{m_o} P_{//} k_z & \frac{\hbar}{m_o} P_{\perp} k_- \\ 0 & \frac{Eg^-(r)}{2} & \frac{\hbar}{m_o} P_{//} k_+ & -\frac{\hbar}{m_o} P_{//} k_z \\ \frac{\hbar}{m_o} P_{//} k_+ & \frac{\hbar}{m_o} P_{\perp} k_- & \frac{Eg^+(r)}{2} & 0 \\ \frac{\hbar}{m_o} P_{\perp} k_- & -\frac{\hbar}{m_o} P_{//} k_z & 0 & \frac{Eg^+(r)}{2} \end{pmatrix} \begin{pmatrix} F_1(r) \\ F_2(r) \\ F_3(r) \\ F_4(r) \end{pmatrix} = E \begin{pmatrix} F_1(r) \\ F_2(r) \\ F_3(r) \\ F_4(r) \end{pmatrix},$$

(3.2.7)

where $Eg^-(r)$ and $Eg^+(r)$ denote, respectively,

$$Eg^-(r) = \begin{cases} Eg_A^- & \text{(at r in A)} \\ Eg_B^- & \text{(at r in B)} \end{cases}$$

and

$$Eg^+(r) = \begin{cases} Eg_A^+ & \text{(at r in A)} \\ Eg_A^+ & \text{(at r in B);} \end{cases} \qquad (3.2.8)$$

while k_+ and k_- denote

$$k_+ = k_x + ik_y \tag{3.2.9}$$

and

$$k_- = k_x - ik_y, \tag{3.2.10}$$

respectively, with

$$k_x = \frac{\hbar}{i}\frac{\partial}{\partial x}\ , \quad k_y = \frac{\hbar}{i}\frac{\partial}{\partial y}\ , \quad k_z = \frac{\hbar}{i}\frac{\partial}{\partial z}\ . \tag{3.2.11}$$

Using Pauli Matrices σ_x, σ_y, and σ_z, we can rewrite Eq.(3.2.7) as

$$\begin{bmatrix} (Eg^-(r)-E)I & \frac{\hbar}{m_o}\left\{P\perp(\sigma_x k_x+\sigma_y k_y)+P/\!/\sigma_z k_z\right\} \\ \frac{\hbar}{m_o}\left\{P\perp(\sigma_x k_x+\sigma_y k_y)+P/\!/\sigma_z k_z\right\} & (Eg^+(r)-E)I \end{bmatrix} \begin{bmatrix} f_1(r) \\ f_2(r) \\ f_3(r) \\ f_4(r) \end{bmatrix} = 0 \ , \tag{3.2.12}$$

where I is the 2×2 unit matrix. Projecting $f_3(r)$ and $f_4(r)$ onto $f_1(r)$ and $f_2(r)$, we obtain

$$\left[(Eg^-(r)-E)I - \frac{\hbar}{m_o}\left\{P\perp(\sigma_x k_x+\sigma_y k_y)+P/\!/\sigma_z k_z\right\}\frac{1}{Eg^+(r)-E}\frac{\hbar}{m_o}\left\{P\perp(\sigma_x k_x+\sigma_y k_y)+P/\!/\sigma_z k_z\right\}\right] \cdot \begin{bmatrix} f_1(r) \\ f_2(r) \end{bmatrix} = 0 \ . \tag{3.2.13}$$

We impose the Bloch condition on $f_1(r)$ and $f_2(r)$:

$$\begin{pmatrix} f_1(x,y,z+d) \\ f_2(x,y,z+d) \end{pmatrix} = \exp(iqd) \begin{pmatrix} f_1(x,y,z) \\ f_2(x,y,z) \end{pmatrix}. \tag{3.2.14}$$

At the A-B interface, we integrate Eq.(3.2.13) across the boundary. We obtain the condition that

$$\frac{1}{Eg^+(r)-E} \frac{\hbar}{m_0}\left\{P_\perp(\sigma_x k_x+\sigma_y k_y)+P_{/\!/}\sigma_z k_z\right\}\Big] \begin{pmatrix} f_1(r) \\ f_2(r) \end{pmatrix} \tag{3.2.14}$$

is continued at the interface. From this matching condition, we obtain the energy dispersion relation:

$$\cos(qd)=\cos(k_A d_A)\cos(k_B d_B) - \frac{1}{2}\xi\sin(k_A d_A)\sin(k_B d_B) \tag{3.2.15}$$

with

$$\xi= \frac{(Eg_A^+-E)^2 P_{/\!/}^2 k_B^2+(Eg_B^+-E)^2 P_L^2 k_A^2+(Eg_B^+-Eg_A^+)^2 P_\perp^2 (k_x^2+k_y^2)}{(Eg_A^+ - E)(Eg_A^+ - E)P_{/\!/}^2 k_A k_B}. \tag{3.2.16}$$

§4 MAGNETOPLASMA THEORY

In this section, we derive the formal expressions for power transport and power dissipation that accompany the propagation of electro-magnetic radiation in material media under static magnetic field[95]. From the expression, the dielectric tensor of $Pb_{1-x}Sn_xTe$ is given.

§4-1 General theory

The starting point is Maxwell's equations (in CGS units)

$$\nabla \times E = -\frac{1}{c}\frac{\partial B}{\partial t} \tag{4.1.1}$$

and

$$\nabla \times H = \frac{1}{c}\frac{\partial D}{\partial t} + \frac{4\pi}{c} j, \tag{4.1.2}$$

with the constitutive equations relating the fields to the flux vectors

$$D = \varepsilon_1 E \tag{4.1.3}$$

and

$$B = \mu H, \tag{4.1.4}$$

as well as the equation relating the conductivity tensor to current density vector by Ohm's law including the static magnetic field effect

$$j = \sigma E, \tag{4.1.5}$$

where $\mathbf{j}(\mathbf{r},t)$ is the current density; σ is the conductivity tensor; $\mathbf{E}(\mathbf{r},t)$ and $\mathbf{H}(\mathbf{r},t)$ are the electric and magnetic field vectors, respectively; $\mathbf{D}(\mathbf{r},t)$ and $\mathbf{B}(\mathbf{r},t)$ are the electric and magnetic flux vectors; ε and μ are the electric and magnetic permiativity tensors of the material. Since IV-VI compounds do not contain transition metals, we can put

$$\mu = \mathbf{I}, \tag{4.1.6}$$

where I is the unit tensor. Substituting Eqs.(4.1.3), (4.1.4), (4.1.5), and (4.1.6) into Eqs.(4.1.1) and (4.1.2) leads to

$$\nabla\times\mathbf{E} = -\frac{1}{c}\frac{\partial}{\partial t}\mathbf{H} \tag{4.1.7}$$

and

$$\nabla\times\mathbf{H} = \frac{1}{c}\frac{\partial}{\partial t}\varepsilon\mathbf{E} + \frac{4\pi}{c}\sigma\mathbf{E} \ . \tag{4.1.8}$$

Taking rotation of Eq.(4.1.7), and using Eq.(4.1.8), we obtain

$$\nabla\times(\nabla\times\mathbf{E}) = -\frac{1}{c^2}\frac{\partial^2}{\partial t^2}\mathbf{E} + \frac{4\pi}{c}\sigma\frac{\partial}{\partial t}\mathbf{E} \ . \tag{4.1.9}$$

Since our main interest is in harmonic time variations, we postulate a solution in the form of

$$\mathbf{E} = \mathbf{E}_o\exp[i(\mathbf{q}\cdot\mathbf{r}-\omega t)] \ , \tag{4.1.10}$$

where $\mathbf{E}_o\exp(i\mathbf{q}\cdot\mathbf{r})$ is the complex field amplitude at r; ω is the circular (radian) frequency; q is the complex wave number vector. Substitution of this equation into Eq.(4.1.9) gives

$$q\times(q\times E_o) = -(\frac{\omega}{c})^2(\varepsilon_l+\frac{4\pi}{i\omega}\sigma)E_o. \qquad (4.1.11)$$

Here we define a generalized dielectric tensor for the phonon and magnetoplasma coupled system

$$\varepsilon = \varepsilon_l + \frac{4\pi}{i\omega}\sigma. \qquad (4.1.12)$$

If we postulate a solution in the form of

$$E = E_o\exp[i(qz-\omega t)]; \qquad (4.1.13)$$

then Eq.(4.1.11) becomes

$$\begin{bmatrix} \varepsilon_{xx} - (\frac{\omega}{c})^2q^2 & \varepsilon_{xy} & \varepsilon_{xz} \\ \varepsilon_{yx} & \varepsilon_{yy} - (\frac{\omega}{c})^2q^2 & \varepsilon_{yz} \\ \varepsilon_{zx} & \varepsilon_{zy} & \varepsilon_{zz} \end{bmatrix} \begin{bmatrix} E_x \\ E_y \\ E_z \end{bmatrix} = 0. \qquad (4.1.14)$$

Projecting E_z onto the E_x and the E_y leads to

$$\begin{bmatrix} \varepsilon_{xx} - \frac{\varepsilon_{xz}\varepsilon_{zx}}{\varepsilon_{zz}} & \varepsilon_{xy} - \frac{\varepsilon_{xz}\varepsilon_{zy}}{\varepsilon_{zz}} \\ \varepsilon_{yx} - \frac{\varepsilon_{yz}\varepsilon_{zx}}{\varepsilon_{zz}} & \varepsilon_{yy} - \frac{\varepsilon_{yz}\varepsilon_{zy}}{\varepsilon_{zz}} \end{bmatrix} \begin{bmatrix} E_x \\ E_y \end{bmatrix} = (\frac{\omega}{c})^2q^2 \begin{bmatrix} E_x \\ E_y \end{bmatrix}. \qquad (4.1.15)$$

According to fundamental linear algebra, we obtain two effective

dielectric constants

$$\varepsilon = (\frac{\omega}{c})^2 q^2 \qquad (4.1.16)$$

as the two eigenvalues of the matrix,

$$\begin{bmatrix} \varepsilon_{xx} - \frac{\varepsilon_{xz}\varepsilon_{zx}}{\varepsilon_{zz}} & \varepsilon_{xy} - \frac{\varepsilon_{xz}\varepsilon_{zy}}{\varepsilon_{zz}} \\ \varepsilon_{yx} - \frac{\varepsilon_{yz}\varepsilon_{zx}}{\varepsilon_{zz}} & \varepsilon_{yy} - \frac{\varepsilon_{yz}\varepsilon_{zy}}{\varepsilon_{zz}} \end{bmatrix}. \qquad (4.1.17)$$

Substituting the eigenvalues back into Eq.(4.1.15) gives their eigen modes of electro-magnetic field amplitude. Using Eq.(4.1.18) leads to

$$E_z = - \frac{\varepsilon_{zx}}{\varepsilon_{zz}} E_x - \frac{\varepsilon_{zy}}{\varepsilon_{zz}} E_y. \qquad (4.1.18)$$

If $E_z \neq 0$, electro-magnetic radiation involves longitudinal electric field.

§4-2 Dielectric function due to lattice

The dielectric function ε_1 due to optical phonon is a tensor in crystal but we can treat it as scalar when the crystal has cubic symmetry. According to derivation used by Born and Huang, we start with the equation of the ionic motion in the long wave limit (the wavelength of the electromagnetic field is much larger than the lattice constant)

$$\frac{d^2}{dt^2}u + \Gamma\cdot\frac{d}{dt}u + \omega_{TO}{}^2 u = \frac{e^*}{M}E \ , \qquad (4.2.1)$$

where $u = u_+ - u_-$; u_+ and u_- are is the displacement vectors of the cation and the anion from their equilibrium position, respectively; Γ is relaxation time ; $\omega_{TO}{}^2$ is restoring force constant; e^* is the effective charge of the ions; M is the reduced mass of anion and cation; E is the external field. Actually the field acting on ions is not E but the Lorentz field. Since the polarization vector is proportional to the displacement vector u, this effect only renormalizes (e^*/M). The electric field E is in a sinusoidal time variation

$$E = E_o\exp(-i\omega t), \qquad (4.2.2)$$

so that we postulate a solution in the form of

$$u = u_o\exp(-i\omega t). \qquad (4.2.3)$$

Substituting the last equation into Eq.(4.2.1) gives

$$(-\omega^2 + i\Gamma\omega + \omega_{TO}{}^2)u = \frac{e^*}{M}E. \qquad (4.2.4)$$

Using the relations

$$P = Ne^{*}u, \tag{4.2.5}$$

$$\varepsilon_1 E = \varepsilon_\infty E + 4\pi P, \tag{4.2.6}$$

and

$$\omega_{LO}^{2} - \omega_{TO}^{2} = \frac{4\pi Ne^{*2}}{M}, \tag{4.2.7}$$

Eq.(4.2.4) results in

$$\varepsilon_1 = \varepsilon_\infty\left(1 + \frac{\omega_{LO}^{2} - \omega_{TO}^{2}}{\omega_{TO}^{2} - \omega^{2} - i\Gamma\omega}\right), \tag{4.2.8}$$

where N is the number of ion pairs per unit volume; P is the polarization vector; ε_Γ is the dielectric constant at high frequency.

§4-3 Magnetoplasma conductivity tensor

In this section we consider the conductivity tensor of electron or hole gas medium on which static magnetic field is imposed. To save manipulations, Einstein's promise is used for the tensor. Hence we must take summation with respect to the suffix which emerges twice in the same term. Consider the motion of the electron with mass m_{ij} under the static magnetic field H_i and the oscilatory time varying electric field E_i. Using Drude model, we can get the equation of the motion of the electron with the velocity v_i:

$$m_o m_{ij} \frac{dv_j}{dt} = -m_o m_{ij} \Gamma_{el} v_j + e(E + \frac{1}{c} \epsilon_{ijk} v_j H_k) \quad , \quad (4.3.1)$$

where ϵ_{ijk} is the component of the antisymmetric tensor; Γ_{el} is a reciprocal of the relaxation time of electrons. Postulate a solution in the form of

$$E_i = \tilde{E}_i \exp(-i\omega t) \qquad (4.3.2)$$

and

$$v_i = \tilde{v}_i \exp(-i\omega t).$$

Substitution of these equations into Eq.(4.3.1) gives

$$\left\{ m_o m_{ij}(-i\omega + \Gamma_{el}) + \frac{e}{c} \epsilon_{ijk} H_k \right\} v_j = eE_i. \qquad (4.3.3)$$

Using the relation

$$j_i = \sigma_{ij} E_j = nev_i \quad , \qquad (4.3.4)$$

the conductivity tensor becomes

$$\sigma_{ij} = \frac{ne^2}{m_o}\cdot\frac{1}{-i\omega+\Gamma_{el}}\left\{m_{ij} + \frac{1}{-i\omega+\Gamma_{el}}\cdot\frac{e}{m_o c}\epsilon_{ijk}H_k\right\}^{-1}, \quad (4.3.5)$$

where n is the carrier density of electrons. Solving the inverse matrix in the last equation, we obtain

$$\begin{aligned}\sigma_{ij} = &- \frac{ine^2}{m_o}\cdot\frac{1}{(\omega+i\Gamma_{el}+\omega_c)}\left\{m^{-1}{}_{ij} - \frac{m_c{}^2}{\det(m_{ij})}\hat{H}_i\hat{H}_j + \frac{1}{i}\epsilon_{ijk}m_{kl}\hat{H}_l\right\} \\ &- \frac{ine^2}{m_o}\cdot\frac{1}{(\omega+i\Gamma_{el}-\omega_c)}\left\{m^{-1}{}_{ij} - \frac{m_c{}^2}{\det(m_{ij})}\hat{H}_i\hat{H}_j - \frac{1}{i}\epsilon_{ijk}m_{kl}\hat{H}_l\right\} \\ &- \frac{ine^2}{m_o}\cdot\frac{1}{(\omega+i\Gamma_{el})}\left\{\frac{m_c{}^2}{\det(m_{ij})}\hat{H}_i\hat{H}_j\right\},\end{aligned} \quad (4.3.6)$$

where m_c, ω_c, and $\hat{H}_i$ are defined by

$$m_c = (\det(m_{ij})/(m_{ij}\hat{H}_i\hat{H}_j))^{1/2}, \quad (4.3.7)$$

$$\omega_c = \frac{eH}{m_o m_c c}, \quad (4.3.8)$$

with

$$\hat{H}_i = H_i/(H_iH_i). \quad (4.3.9)$$

§4-4 Magnetoplasma dielectric tensor of IV-VI compounds in Faraday configuration (q//H//<111>)

Since IV-VI compounds are grown epitaxially on a (111) cleaved surface of BaF_2, we need the dielectric tensor in the condition that q//H//<111>(Faraday configuration) and q//<111> H//<$\bar{1}\bar{1}$2>(Voigt configuration). We name four valleys as follows:

<111> valley a,

<$\bar{1}\bar{1}$1> valley b,

<1$\bar{1}\bar{1}$> valley c,

and

<$\bar{1}$1$\bar{1}$> valley d

(see Fig. 4-4-1).

We take the Cartesian Coordinates as follows:

x <$\bar{1}\bar{1}$2>,

y <1$\bar{1}$0>,

and

z <111>.

Derive the dielectric tensor in Faraday configuration:

H // z

and

q // z.

From Eq.(4.3.7), cyclotron masses of a, b, c, and d valley, m_{ca}, m_{cb}, m_{cc}, and m_{cd} are given by

$$m_{ca} = m_{ta},$$

$$m_{cb} = \left\{ m_{tb}^2 m_{lb} / \left(\frac{8}{9} m_{tb} + \frac{1}{9} m_{lb} \right) \right\}^{1/2},$$

and

$$m_{cc} = m_{cd} = m_{cb},$$

(4.4.1)

respectively. From Eq.(4.3.8), the cyclotron frequencies of a, b, d, and d valleys, ω_{ca}, ω_{cb}, ω_{cc}, and ω_{cd} are given by

$$\omega_{ca} = \frac{eH}{m_o m_{ca} c},$$

$$\omega_{cb} = \frac{eH}{m_o m_{cb} c},$$

and

$$\omega_{cc} = \omega_{cd} = \omega_{cb},$$

(4.4.2)

respectively. Using Eqs.(4.1.12), (4.2.8), and (4.3.6), we obtain the components of the dielectric tensor

$$\varepsilon_{xx} = \varepsilon_l - \frac{4\pi n_a e^2}{m_o} \cdot \left\{ \frac{1}{2\omega(\omega + i\Gamma_{el} + \omega_{ca})} + \frac{1}{2\omega(\omega + i\Gamma_{el} - \omega_{ca})} \right\} \frac{1}{m_{ta}}$$

$$- \frac{12\pi n_b e^2}{m_o} \cdot \left\{ \frac{1}{2\omega(\omega + i\Gamma_{el} + \omega_{cb})} + \frac{1}{2\omega(\omega + i\Gamma_{el} - \omega_{cb})} \right\} \frac{1}{9} \left\{ \frac{5}{m_{tb}} + \frac{4}{m_{lb}} \right\},$$

$$\varepsilon_{xy} = - \frac{4\pi n_a e^2}{m_o} \cdot \left\{ \frac{1/i}{2\omega(\omega + i\Gamma_{el} + \omega_{ca})} - \frac{1/i}{2\omega(\omega + i\Gamma_{el} - \omega_{ca})} \right\} \frac{1}{m_{ta}}$$

$$-\frac{12\pi n_b e^2}{m_o}\cdot\left\{\frac{1/i}{2\omega(\omega+i\Gamma_{el}+\omega_{cb})}-\frac{1/i}{2\omega(\omega+i\Gamma_{el}-\omega_{cb})}\right\}\frac{(8m_{tb}+m_{lb})m_{cb}}{9m_{tb}^{2}m_{lb}},$$

$$\varepsilon_{yx} = -\varepsilon_{xy},$$

$$\varepsilon_{yy} = \varepsilon_{xx},$$

$$\varepsilon_{yz} = \varepsilon_{zy} = 0,$$

and

$$\varepsilon_{zz}=\varepsilon_1-\frac{4\pi n_a e^2}{m_o}\cdot\frac{1}{\omega(\omega+i\Gamma_{el})}\cdot\left\{\frac{1}{m_{la}}+3\left(\frac{8}{9}m_{tb}+\frac{1}{9}m_{lb}\right)^{-1}\right\}$$

$$-\frac{12\pi n_b e^2}{m_o}\cdot\left\{\frac{1}{2\omega(\omega+i\Gamma_{el}+\omega_{cb})}+\frac{1}{2\omega(\omega+i\Gamma_{el}-\omega_{cb})}\right\}$$

$$\cdot\left\{\left(\frac{8}{9m_{tb}}+\frac{1}{9m_{lb}}\right)-\left(\frac{8}{9}m_{tb}+\frac{1}{9}m_{lb}\right)^{-1}\right\},$$

(4.4.3)

Taking eigenvalue of Eq.(4.1.17), we obtain the effective dielectric constant of the cyclotron active mode,

$$\varepsilon_{CRA}=\varepsilon_{xx}-i\varepsilon_{xy}$$

$$=\varepsilon_1-\frac{4\pi n_a e^2}{m_o}\cdot\frac{1}{\omega(\omega+i\Gamma_{el}-\omega_{ca})}\cdot\frac{1}{m_{ta}}$$

$$-\frac{12\pi n_b e^2}{m_o}\cdot\frac{1}{\omega(\omega+i\Gamma_{el}-\omega_{cb})}\cdot\frac{1}{2}\left\{\frac{1}{9}\left(\frac{5}{m_{tb}}+\frac{4}{m_{lb}}\right)+\frac{(8m_{tb}+m_{lb})m_{cb}}{9m_{tb}^{2}m_{lb}}\right\}$$

$$-\frac{12\pi n_b e^2}{m_o}\cdot\frac{1}{\omega(\omega+i\Gamma_{el}+\omega_{cb})}\cdot\frac{1}{2}\left\{\frac{1}{9}\left(\frac{5}{m_{tb}}+\frac{4}{m_{lb}}\right)-\frac{(8m_{tb}+m_{lb})m_{cb}}{9m_{tb}^2 m_{lb}}\right\} \tag{4.4.4}$$

and the effective dielectric constant of the cyclotron inactive mode,

$$\begin{aligned}\varepsilon_{CRI} &= \varepsilon_{xx}+i\varepsilon_{xy}\\ &= \varepsilon_1-\frac{4\pi n_a e^2}{m_o}\cdot\frac{1}{\omega(\omega+i\Gamma_{el}+\omega_{ca})}\cdot\frac{1}{m_{ta}}\\ &\quad -\frac{12\pi n_b e^2}{m_o}\cdot\frac{1}{\omega(\omega+i\Gamma_{el}+\omega_{cb})}\cdot\frac{1}{2}\left\{\frac{1}{9}\left(\frac{5}{m_{tb}}+\frac{4}{m_{lb}}\right)+\frac{(8m_{tb}+m_{lb})m_{cb}}{9m_{tb}^2 m_{lb}}\right\}\\ &\quad -\frac{12\pi n_b e^2}{m_o}\cdot\frac{1}{\omega(\omega+i\Gamma_{el}-\omega_{cb})}\cdot\frac{1}{2}\left\{\frac{1}{9}\left(\frac{5}{m_{tb}}+\frac{4}{m_{lb}}\right)-\frac{(8m_{tb}+m_{lb})m_{cb}}{9m_{tb}^2 m_{lb}}\right\}.\end{aligned} \tag{4.4.5}$$

Under the lossless limit situation, poles of ε_{CRA} and ε_{CRI} correspond to the dips in the magnetoplasma transmission spectra. 0's give the peaks in the spectra. 'Contour map' of ε_{CRA} and ε_{CRI} is given in Fig. 4-4-2. The effective dielectric constants ε_{CRA} and ε_{CRI}, and transmission versus magnetic field are shown in Fig. 4-4-3.

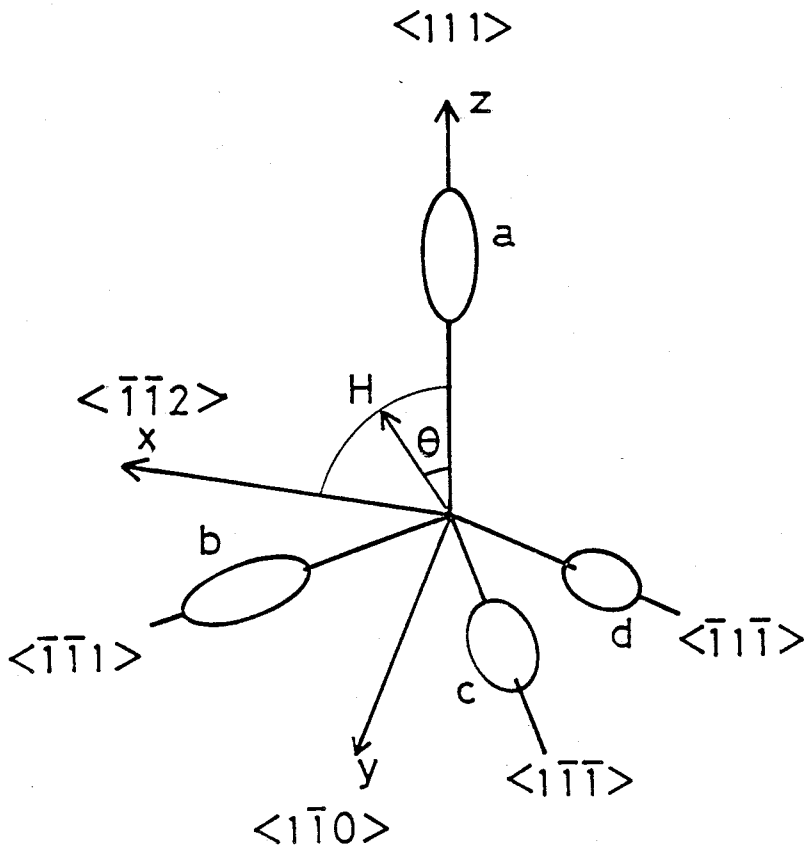

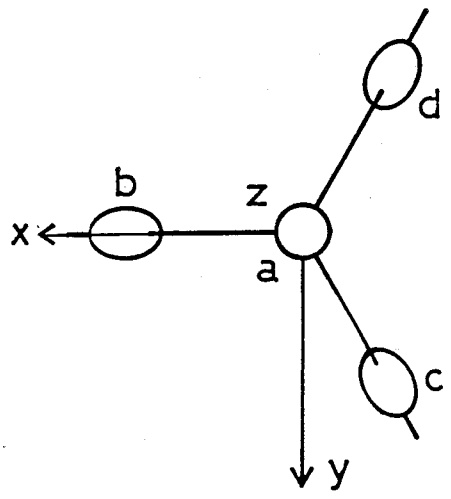

FIG. 4-4-1 Definition of Cartesian coordinates and the valleys of $Pb_{1-x}Sn_xTe$.

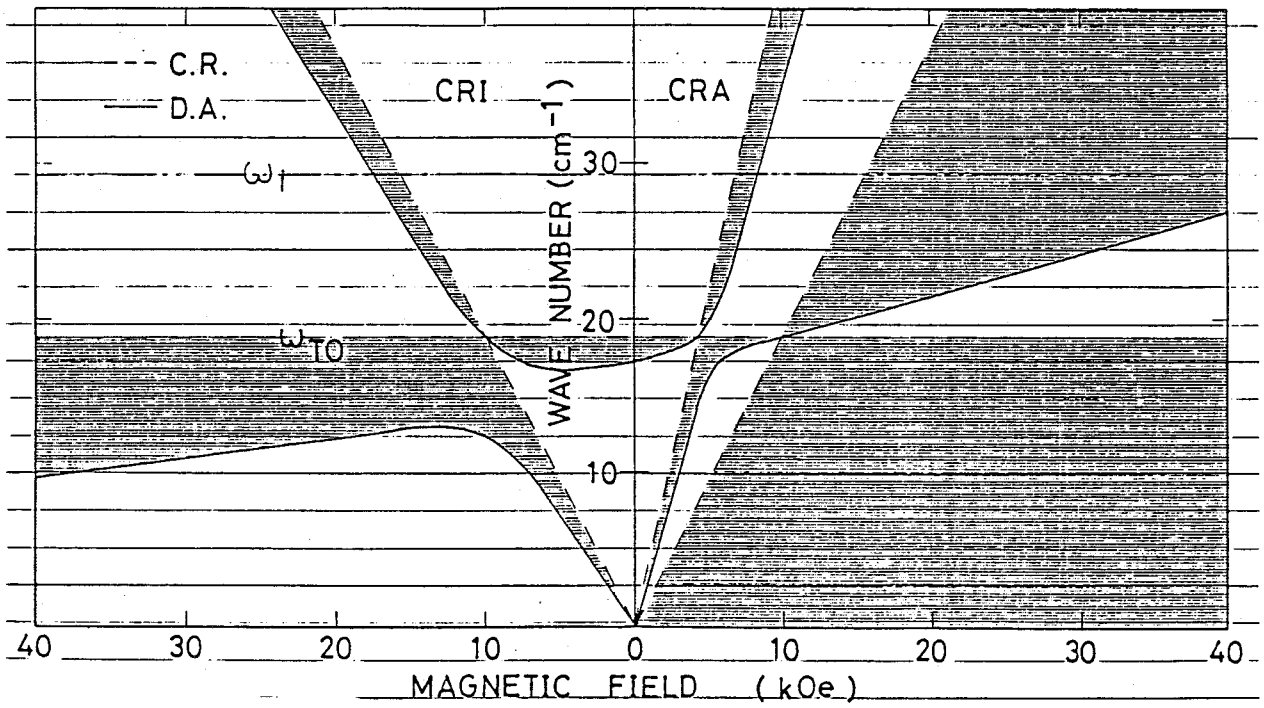

FIG. 4-4-2 Contour map of ε_{CRA} and ε_{CRI} for the Faraday configuration with H//<111>. The solid and broken lines show the location of the dielectric anomalies and poles, respectively. Shaded areas represent regions of negative ε, where reflectivity is unity. The parameters used in calculation are: $m_t = 0.0218m_o$, K = 11, $n = 2.0\times10^{17}cm^{-3}$, $\omega_{TO} = 18.8cm^{-1}$, $\omega_{LO} = 114cm^{-1}$ and $\varepsilon_\infty = 34$.

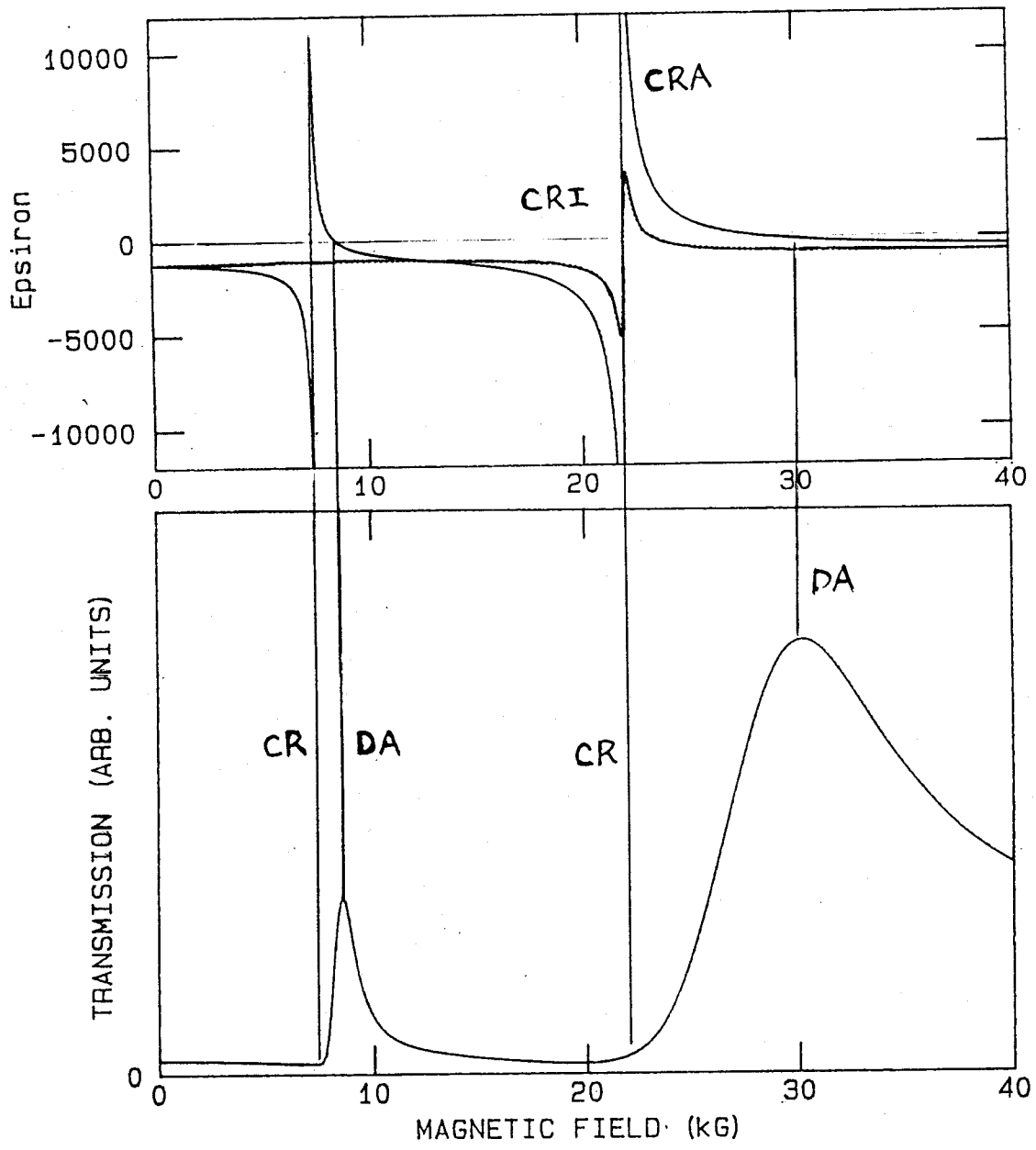

FIG. 4-4-3 Real parts of dielectric constant ε_{CRA} and ε_{CRI}, and Transmissivity.

§4-5 Magnetoplasma dielectric tensor of IV-VI compounds in Voigt configuration (q//<111> and H//<$\bar{1}\bar{1}$2>)

Let us derive the dielectric tensor in Voigt configuration:

$$H \,//\, x$$

and

$$q \,//\, z.$$

From Eq.(4.3.7), cyclotron masses of a, b, c, and d valleys, m_{ca}, m_{cb}, m_{cc}, and m_{cd} are given by

$$m_{ca} = \sqrt{m_{ta}m_{la}},$$

$$m_{cb} = \left\{m_{tb}^{\,2}m_{lb}/(\tfrac{1}{9}m_{tb} + \tfrac{8}{9}m_{lb})\right\}^{1/2},$$

$$m_{cc} = \left\{m_{tb}^{\,2}m_{lb}/(\tfrac{7}{9}m_{tb} + \tfrac{2}{9}m_{lb})\right\}^{1/2},$$

and

$$m_{cd} = m_{cc},$$

(4.5.1)

respectively. From Eq.(4.3.8), cyclotron frequency of a, b, c, and d valleys, ω_{ca}, ω_{cb}, ω_{cc}, and ω_{cd}, are given by

$$\omega_{ca} = \frac{eH}{m_o m_{ca}c},$$

$$\omega_{cb} = \frac{eH}{m_o m_{cb}c},$$

$$\omega_{cc} = \frac{eH}{m_o m_{cc}c},$$

and

$$\omega_{cd} = \omega_{cc} \cdot \tag{4.5.2}$$

Using Eqs.(4.1.12), (4.2.8), and (4.3.6), we obtain the components of the dielectric tensor

$$\varepsilon_{xx}=\varepsilon_1$$

$$-\frac{4\pi n_a e^2}{m_o}\cdot\frac{1}{1(\omega+i\Gamma_{el})}\cdot\left\{\frac{1}{m_{ta}}+\left(\frac{1}{9}m_{tb}+\frac{8}{9}m_{lb}\right)^{-1}+2\cdot\left(\frac{7}{9}m_{tb}+\frac{2}{9}m_{lb}\right)^{-1}\right\}$$

$$-\frac{4\pi n_b e^2}{m_o}\cdot\left\{\frac{1}{2\omega(\omega+i\Gamma_{el}+\omega_{cb})}+\frac{1}{2\omega(\omega+i\Gamma_{el}-\omega_{cb})}\right\}$$

$$\cdot\left\{\left(\frac{1}{9m_{tb}}+\frac{8}{9m_{lb}}\right)-\left(\frac{1}{9}m_{tb}+\frac{8}{9}m_{lb}\right)^{-1}\right\}$$

$$-\frac{8\pi n_b e^2}{m_o}\cdot\left\{\frac{1}{2\omega(\omega+i\Gamma_{el}+\omega_{cc})}+\frac{1}{2\omega(\omega+i\Gamma_{el}-\omega_{cc})}\right\}$$

$$\cdot\left\{\left(\frac{7}{9m_{tb}}+\frac{2}{9m_{lb}}\right)-\left(\frac{7}{9}m_{tb}+\frac{2}{9}m_{lb}\right)^{-1}\right\} ,$$

$$\varepsilon_{yy}=\varepsilon_1-\frac{4\pi n_a e^2}{m_o}\cdot\left\{\frac{1}{2\omega(\omega+i\Gamma_{el}+\omega_{ca})}+\frac{1}{2\omega(\omega+i\Gamma_{el}-\omega_{ca})}\right\}\frac{1}{m_{ta}}$$

$$-\frac{4\pi n_b e^2}{m_o}\cdot\left\{\frac{1}{2\omega(\omega+i\Gamma_{el}+\omega_{cb})}+\frac{1}{2\omega(\omega+i\Gamma_{el}-\omega_{cb})}\right\}\frac{1}{m_{tb}}$$

$$-\frac{8\pi n_b e^2}{m_o}\cdot\left\{\frac{1}{2\omega(\omega+i\Gamma_{el}+\omega_{cc})}+\frac{1}{2\omega(\omega+i\Gamma_{el}-\omega_{cc})}\right\}\frac{1}{3}\left\{\frac{1}{m_{tb}}+\frac{2}{m_{lb}}\right\} ,$$

$$\varepsilon_{zz}=\varepsilon_l-\frac{4\pi n_a e^2}{m_o}\cdot\left\{\frac{1}{2\omega(\omega+i\Gamma_{el}+\omega_{ca})}+\frac{1}{2\omega(\omega+i\Gamma_{el}-\omega_{ca})}\right\}\frac{1}{m_{la}}$$

$$-\frac{4\pi n_b e^2}{m_o}\cdot\left\{\frac{1}{2\omega(\omega+i\Gamma_{el}+\omega_{cb})}+\frac{1}{2\omega(\omega+i\Gamma_{el}-\omega_{cb})}\right\}\frac{1}{9}\left\{\frac{8}{m_{tb}}+\frac{1}{m_{lb}}\right\}$$

$$-\frac{8\pi n_b e^2}{m_o}\cdot\left\{\frac{1}{2\omega(\omega+i\Gamma_{el}+\omega_{cc})}+\frac{1}{2\omega(\omega+i\Gamma_{el}-\omega_{cc})}\right\}\frac{1}{9}\left\{\frac{8}{m_{tb}}+\frac{1}{m_{lb}}\right\}\ ,$$

$$\varepsilon_{xy}=-\frac{4\pi n_b e^2}{m_o}\cdot\left\{\frac{1/i}{2\omega(\omega+i\Gamma_{el}+\omega_{cb})}-\frac{1/i}{2\omega(\omega+i\Gamma_{el}-\omega_{cb})}\right\}\frac{2\sqrt{2}(m_{tb}-m_{lb})m_{cb}}{9m_{tb}^2m_{lb}}$$

$$=-\frac{8\pi n_b e^2}{m_o}\cdot\left\{\frac{1/i}{2\omega(\omega+i\Gamma_{el}+\omega_{cb})}-\frac{1/i}{2\omega(\omega+i\Gamma_{el}-\omega_{cb})}\right\}\frac{-\sqrt{2}(m_{tb}-m_{lb})m_{cb}}{9m_{tb}^2m_{lb}}\ ,$$

$$\varepsilon_{yz}=-\frac{4\pi n_a e^2}{m_o}\cdot\left\{\frac{1/i}{2\omega(\omega+i\Gamma_{el}+\omega_{ca})}-\frac{1/i}{2\omega(\omega+i\Gamma_{el}-\omega_{ca})}\right\}\frac{1}{m_{ca}}$$

$$=-\frac{4\pi n_b e^2}{m_o}\cdot\left\{\frac{1/i}{2\omega(\omega+i\Gamma_{el}+\omega_{cb})}-\frac{1/i}{2\omega(\omega+i\Gamma_{el}-\omega_{cb})}\right\}\frac{(m_{tb}+8m_{lb})m_{cb}}{9m_{tb}^2m_{lb}}$$

$$=-\frac{8\pi n_b e^2}{m_o}\cdot\left\{\frac{1/i}{2\omega(\omega+i\Gamma_{el}+\omega_{cb})}-\frac{1/i}{2\omega(\omega+i\Gamma_{el}-\omega_{cb})}\right\}\frac{(7m_{tb}+2m_{lb})m_{cb}}{9m_{tb}^2m_{lb}}\ ,$$

$$\varepsilon_{zx}=-\frac{4\pi n_b e^2}{m_o}\cdot\left\{\frac{1}{2\omega(\omega+i\Gamma_{el}+\omega_{cb})}+\frac{1}{2\omega(\omega+i\Gamma_{el}-\omega_{cb})}\right\}\frac{2\sqrt{2}}{9}\left\{\frac{1}{m_{tb}}-\frac{1}{m_{lb}}\right\}$$

$$-\frac{8\pi n_b e^2}{m_o}\cdot\left\{\frac{1}{2\omega(\omega+i\Gamma_{el}+\omega_{cc})}+\frac{1}{2\omega(\omega+i\Gamma_{el}-\omega_{cc})}\right\}\frac{-\sqrt{2}}{9}\left\{\frac{1}{m_{tb}}-\frac{1}{m_{lb}}\right\}\ ,$$

$$\varepsilon_{yx}=-\varepsilon_{xy}\ ,$$

$$\varepsilon_{zy}=-\varepsilon_{yz}\ ,$$

and

$$\varepsilon_{xz}=-\varepsilon_{zx}\ .$$

(4.5.3)

§5 EXPERIMENTAL PROCEDURE

§5-1 The Construction of submillimeter laser system

For magnetoplasma spectroscopy, a powerful and stable submillimeter light source is essential. Optically pumped gas lasers are representatives of the light sources, because they widely cover the wavelength region from 13μm to 2mm[97-99]. We have constructed an optically pumped laser system for stable light sources and easy driving. First we describe mechanism and improvement of a CO_2 laser system for pumping light source. Second we report mechanism of laser action and construction in a submillimeter laser system. third we report a feed back system to acquire a stable output power.

§5-1-1 CO_2 laser for pumping

The carbon dioxide laser is the molecular laser whose wave length output is λ=10.6 and 9.6μm[100]. The CO_2 laser generates high power(about 30W C.W.) using only compact system because it possesses a high overall working efficiency. This is one of the reasons the CO_2 laser is used for excitation of optically pumped laser.

The CO_2 laser is one of the molecular gas lasers which utilize the internal vibration and rotation levels. Laser medium contains N_2 and He in addition to CO_2. The mechanism of laser

action is shown in Fig.5-1-2. First nitrogens are excited from ground states to first excited states(which belong to stretching vibration modes) by a plasma discharge. Second nitrogen vibration energy preferentially transfers to the ground state CO_2 molecule by collision, that is, CO_2 is excited from ground state to the (0 0 1) state, where a set of three integers(n_1,n_2,n_3) denote the energy level of the CO_2 molecule; n_1, n_2, n_3 are the quantum numbers that correspond to the symmetric stretching, bending, and asymmetric stretching modes, respectively(see Fig. 5-1-2). (Actually there are a large fraction of CO_2 molecules directly excited by electron impact, and the excited molecules cascade down the energy ladder from their original level of excitation to (0 0 1) state.) The laser oscillation occurs using transition from (0 0 1) state to (1 0 0) and from (0 0 1) to (0 2 0). The transition from (0 0 1) to (1 0 0) states corresponds to 10.6μm line. The transition from (0 0 1) to (0 2 0) corresponds to 9.6μm line.

Figure 5-1-3 shows the optically pumping laser laser system. Very high stability is required in power and frequency of CO_2 laser light because absorption lines of CH_3OH, CHOOH etc. are very narrow. The factors determining the stability is as follows.

1) stability of cavity length
2) stability of flowing gas pressure
3) stability of an electric power supplier
4) stability of optical alignment

On the first factor, the cavity length is affected by atmospheric

temperature because most of materials expand with increasing temperature. To eliminate this factor we use neoseram whose thermal expansion coefficient is -1.0×10^{-7};neoseram bar with length 2m shrink by 2μm with increasing temperature by 10 degrees (we used before invar whose thermal coefficient is 1.0×10^{-6}). The second and third factors are related to each other, because increase of gas pressure causes decrease of the electrical conductance. We eliminate these factors using high quality needle valve. On the fourth factor, the stability of optical alignment depends on the performance of an isolation from vibration generated by rotary pumps and man walking. We perform the isolation by introducing air damper under optical bench of pumping laser system. In addition to the above improvements, we develop the feed back system to stabilize the power.

§5-1-2 FIR laser

Since Chang and Bridges have developed the submillimeter wave laser action in CH_3F molecules excited by P(20) CO_2-laser line at 9.6μm branch[101], new lines in the region from 13μm to 2mm have been discovered using various molecules.

To get light source in the range from 13μm to 2mm, molecules, e.g. CH_3OH , CHOOH are used. The CO_2 laser light excites molecules in the FIR laser tube from ground state to vibrationally excited states. The excitation inverts population between rotational energy levels. Since the molecules have permanent

electric dipole, laser action arises using these rotational levels.

In laying out FIR laser, we have taken care of easiness of optical alignment. Main feature is introducing a cavity box for optical instrument to build up optical resonator(see Fig. 5-1-2). This improvement enables us to use this system not only as an open cavity resonator but also closed cavity resonator (wave guide) by setting up copper cylinder instead of glassy one.

§5-1-3 Feed back system by PID control

We have achieved further improvement for stabilizing output power of FIR laser. The fluctuation of the power is primarily caused by the drift of the frequency of the CO_2 laser, because absorption line is too narrow to coincide with CO_2 laser line. The drift of the frequency is due to a change of the resonator length. For the CO_2 laser with the free spectral range of 80MHz, 1μm change of the resonator length corresponds to 16MHz drift of the frequency. Various methods to stabilize the power and frequency have been reported[102-104]. The control mechanism adopted for our laser system is as follows. First set output power of FIR laser at 90% maximum power by controlling resonator length of CO_2 laser. Next carry out PID feedback using linear relation between the increment of resonator length and the increment of power.

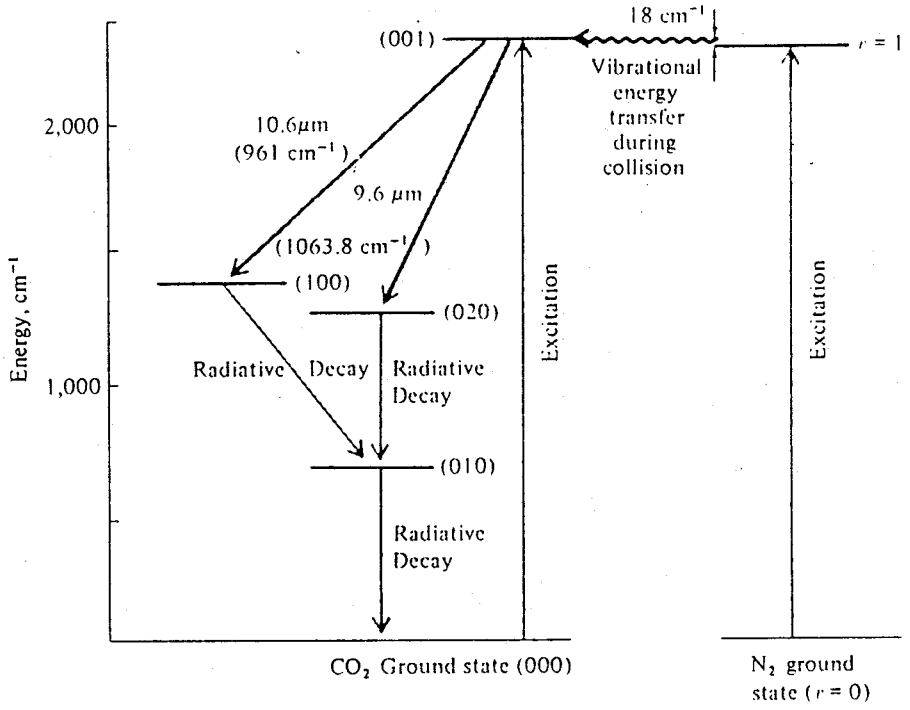

FIG. 5-1-1 The mechanism of excitation and emission of the CO_2 laser.

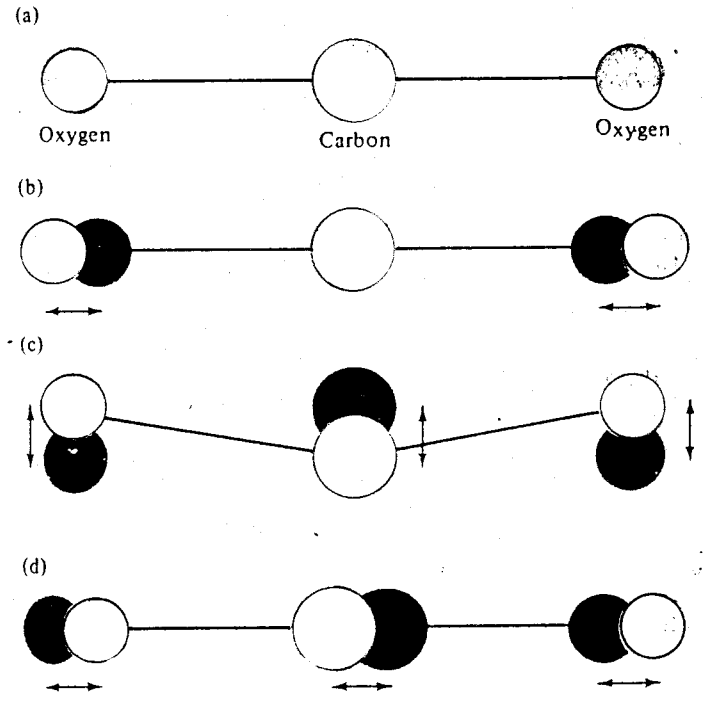

FIG. 5-1-2 (a)Unexcited CO_2 molecule. (b), (c), and(d)The three modes of vibration of the CO_2 molecule(ref. 100).

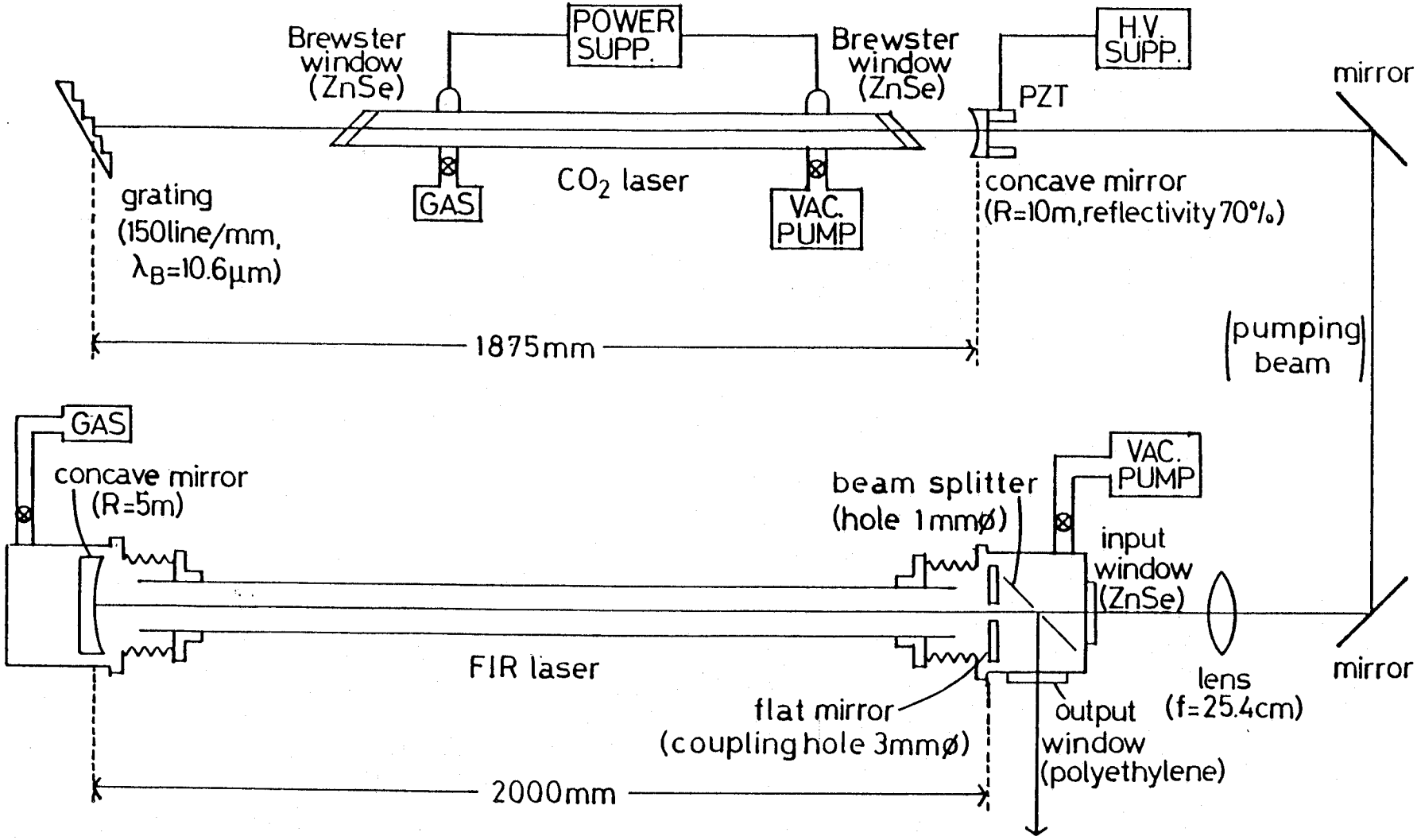

FIG. 5-1-3 Submillimeter laser system.

§5-2 Signal detection and experimental arrangements

Figure 5-2-1 shows the apparatus for the magnetoplasma spectroscopy. Submillimeter light emitted from a laser is chopped at 450Hz with duty ratio of 1:1 and guided into cryostat by a light pipe(inner diameter 6-10 mm). The light transmitting through a sample is detected by changes of conductance of an InSb photodetector[105]. Magnetic field(0~5T) applies to the sample by a superconducting magnet. The changes of conductance is transformed into voltage signals and amplified by a pre-amplifier. The voltage signals is transmitted into DC voltage by lock-in-amplifier and memorized by a computor. The sample holder for measuring magnetoplasma transmission is shown in Fig. 5-2-2. The sample is mounted on the aluminum film with a 5mm×5mm square hole by G.E.wax. To avoid even very small leak of light beside the sample, which distorts the transmission spectra, the greatest possible care must be paid due to superimposing and resulting interference, since transmissivity of PbTe with thickness of 4μm is only about 0.1%.

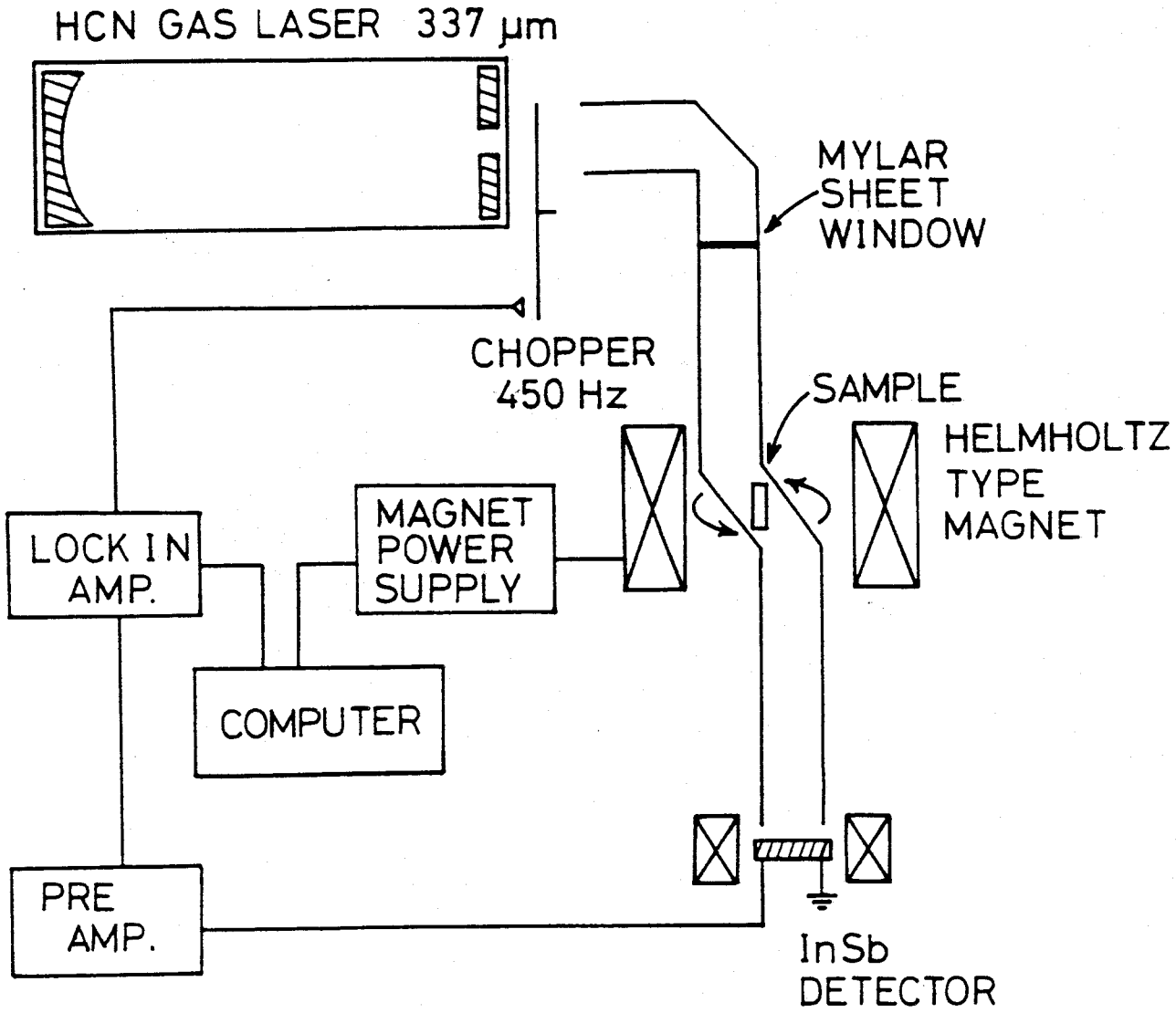

FIG. 5-2-1 System for magnetoplasma spectroscopy.

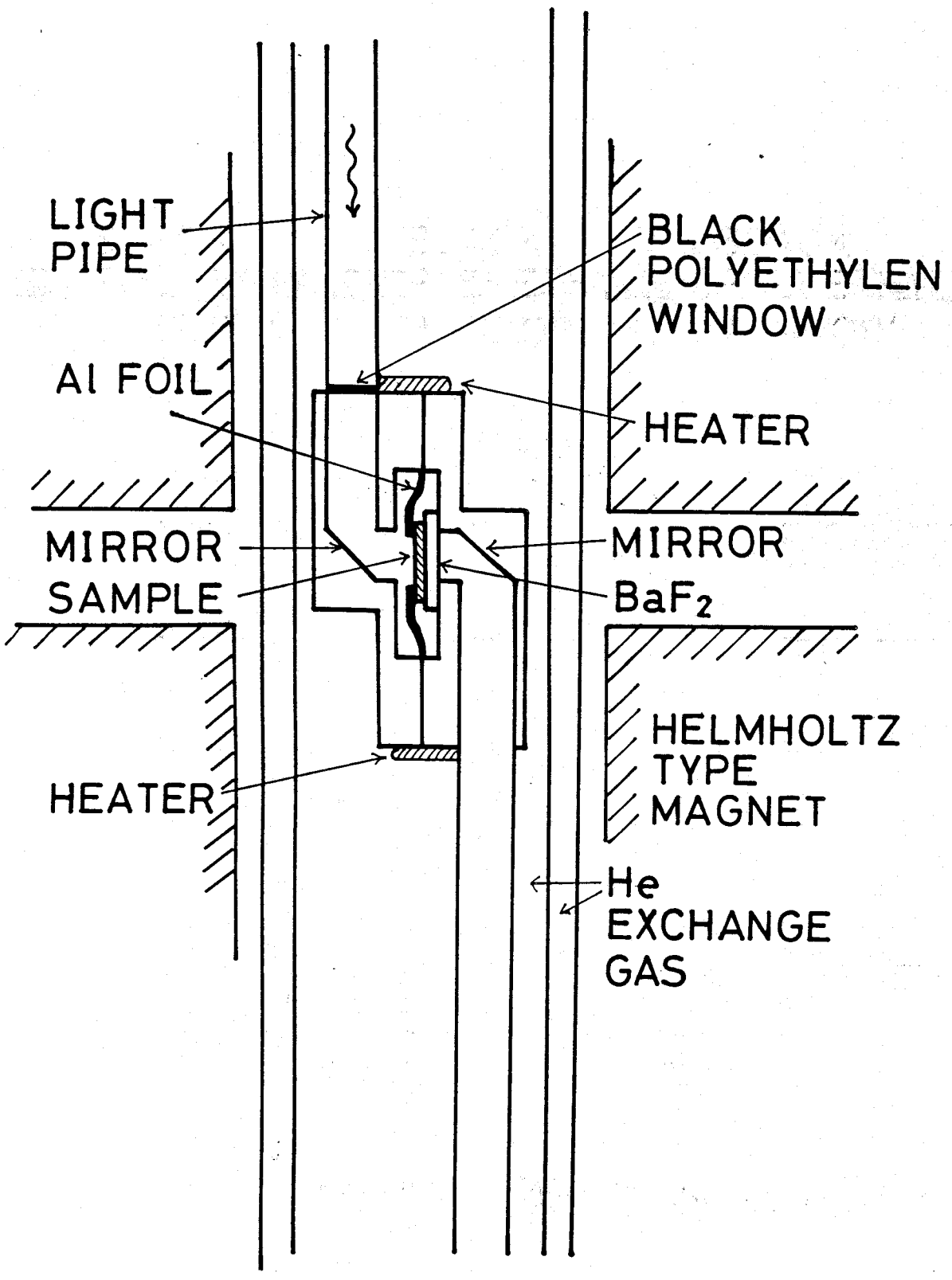

FIG. 5-2-2 Sample holder for measuring magnetoplasma transmission spectra.

§6 SAMPLE PREPARATION AND CHARACTERIZATION

§6-1 Lattice Mismatch and Strain Effect

The lattice constants of PbTe and $Pb_{0.8}Sn_{0.2}Te$ are 6.460 and 6.430Å and the lattice mismatch between them is 0.46%[106]. The lattice mismatch is accommodated by matching the lattice constant in the direction perpendicular to growth direction across the interface[50,107-110]. As a result, a large strain is yielded in each layers of the superlattice. The strain effect is important because the strain causes valley splitting and changes the intensity of the satellite in the X-ray diffraction pattern of the superlattice. In this section we discuss the strain of the superlattice.

The spacing $d_0(\alpha)$ without the strain between the αth metal layer and the nearest neighbor telluride layer is given by

$$d_0(\alpha) = \frac{1}{2\sqrt{3}}\, a(x(\alpha)), \qquad (6.1.1)$$

where $x(\alpha)$ is the tin composition of the αth metal layer and $a(x)$ is the lattice constant of $Pb_{1-x}Sn_xTe$. After deformation by matching the lattice constant, $d_0(\alpha)$ changes into $d_1(\alpha)$ by the strains along the growth direction and the space $d_0(\alpha)$ perpendicular to the growth direction change into d_t. The strains along the growth direction and perpendicular to the growth direction, $e_{//}(\alpha)$ and $e_{\perp}(\alpha)$, are defined by

$$e_{/\!/}(\alpha) = \frac{d_1(\alpha) - d_o(\alpha)}{d_o(\alpha)} \qquad (6.1.2)$$

and

$$e_{\perp}(\alpha) = \frac{d_t - d_o(\alpha)}{d_o(\alpha)}, \qquad (6.1.3)$$

respectively. The strain energy $U(\alpha)$ of the αth layer is given by

$$U(\alpha) = \frac{1}{6}(C_{11}(\alpha)e_{/\!/}(\alpha)e_{/\!/}(\alpha) + C_{1t}(\alpha)e_{/\!/}(\alpha)e_{\perp}(\alpha) + C_{tt}(\alpha)e_{\perp}(\alpha)e_{\perp}(\alpha)) \quad , \qquad (6.1.4)$$

where $C_{11}(\alpha)$, $C_{1t}(\alpha)$, and $C_{tt}(\alpha)$ are defined by the elastic stiffness constants C_{ij}^{PbTe} and C_{ij}^{SnTe}[11] as follows:

$$C_{11}(\alpha) = (C_{11}^{PbTe} + 2C_{12}^{PbTe} + 4C_{44}^{PbTe})(1-x(\alpha)) + (C_{11}^{SnTe} + 2C_{12}^{SnTe} + 4C_{44}^{SnTe})x(\alpha) \quad , (6.1.5)$$

$$C_{1t}(\alpha) = 4(C_{11}^{PbTe} + 2C_{12}^{PbTe} - 2C_{44}^{PbTe})(1-x(\alpha)) + 4(C_{11}^{SnTe} + 2C_{12}^{SnTe} - 2C_{44}^{SnTe})x(\alpha) \quad , (6.1.6)$$

and

$$C_{tt}(\alpha) = 4(C_{11}^{PbTe} + 2C_{12}^{PbTe} + C_{44}^{PbTe})(1-x(\alpha)) + 4(C_{11}^{SnTe} + 2C_{12}^{SnTe} + C_{44}^{SnTe})x(\alpha) \quad . (6.1.7)$$

Impose the condition that there is no stress along the growth direction of the superlattice; namely,

$$\frac{\partial U(\alpha)}{\partial d_1(\alpha)} = 0 \qquad (6.1.8)$$

and

$$e_{/\!/}(\alpha) = - \frac{C_{1t}(\alpha)}{2C_{11}(\alpha)} e_{\perp}(\alpha) \ . \qquad (6.1.9)$$

Substituting this into Eq.(6.1.4), the total energy of strain, U is given by

$$U = \sum_{\alpha} - \left\{ C_{tt}(\alpha) - \frac{C_{1t}(\alpha)^2}{4C_{11}(\alpha)} \right\} e_{\perp}(\alpha)^2 \ . \qquad (6.1.10)$$

Impose the condition that the total energy is minimized in equilibrium state

$$\frac{\partial U}{\partial d_t} = 0. \qquad (6.1.11)$$

From the last condition, we get

$$d_t = \sum_{\alpha} \frac{G(\alpha)}{d_o(\alpha)} \Big/ \sum_{\alpha} \frac{G(\alpha)}{d_o(\alpha)^2} \qquad (6.1.12)$$

and

$$d_1(\alpha) = d_o(\alpha) + (d_t - d_o(\alpha))P(\alpha), \qquad (6.1.13)$$

where $G(\alpha)$ and $P(\alpha)$ are defined by

$$G(\alpha) = C_{tt}(\alpha) - \frac{C_{1t}(\alpha)^2}{4C_{11}(\alpha)} \qquad (6.1.14)$$

and

$$P(\alpha) = - \frac{C_{1t}(\alpha)}{2C_{11}(\alpha)}, \qquad (6.1.15)$$

respectively. So far, we are taking into account interdiffusion between PbTe layers and $Pb_{1-x}Sn_xTe$ layers by (α). When there is no interdiffusion,

$$d_t = \left(\frac{L_A G_A}{d_A^2} + \frac{L_B G_B}{d_B^2} \right) / \left(\frac{L_A G_A}{d_A^3} + \frac{L_B G_B}{d_B^3} \right), \qquad (6.1.16)$$

$$d_{1A} = d_{oA} + (d_t - d_{oA}) P_A \qquad (6.1.17)$$

and

$$d_{1B} = d_{oB} + (d_t - d_{oB}) P_B, \qquad (6.1.18)$$

where L_A and L_B are the layer thicknesses of the PbTe layer and $Pb_{1-x}Sn_xTe$ layer, respectively.

TABLE 6-1-1 Lattice constant and stiffness constant

		lattice constant(Å)	P	G
A	$Pb_{0.8}Sn_{0.2}Te$	6.430	-1.08	0.892
B	PbTe	6.460	-1.08	0.916
	BaF_2	6.187		

lattice mismatch 0.46% between PbTe and $Pb_{0.8}Sn_{0.2}Te$

lattice mismatch 4.2% between PbTe and BaF_2

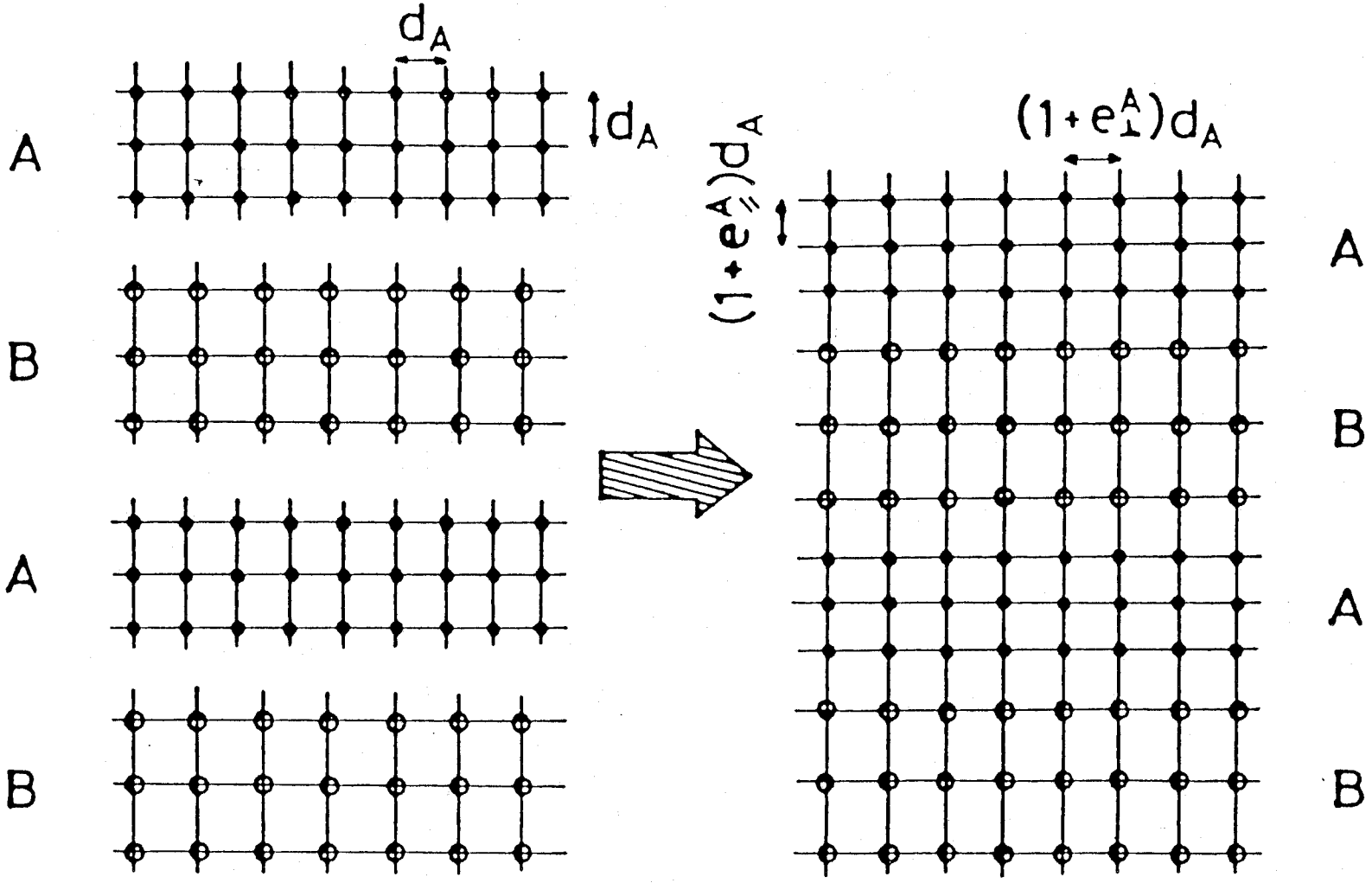

FIG. 6-1-1 Accommodation of lattice mismatch by inner layer strain.

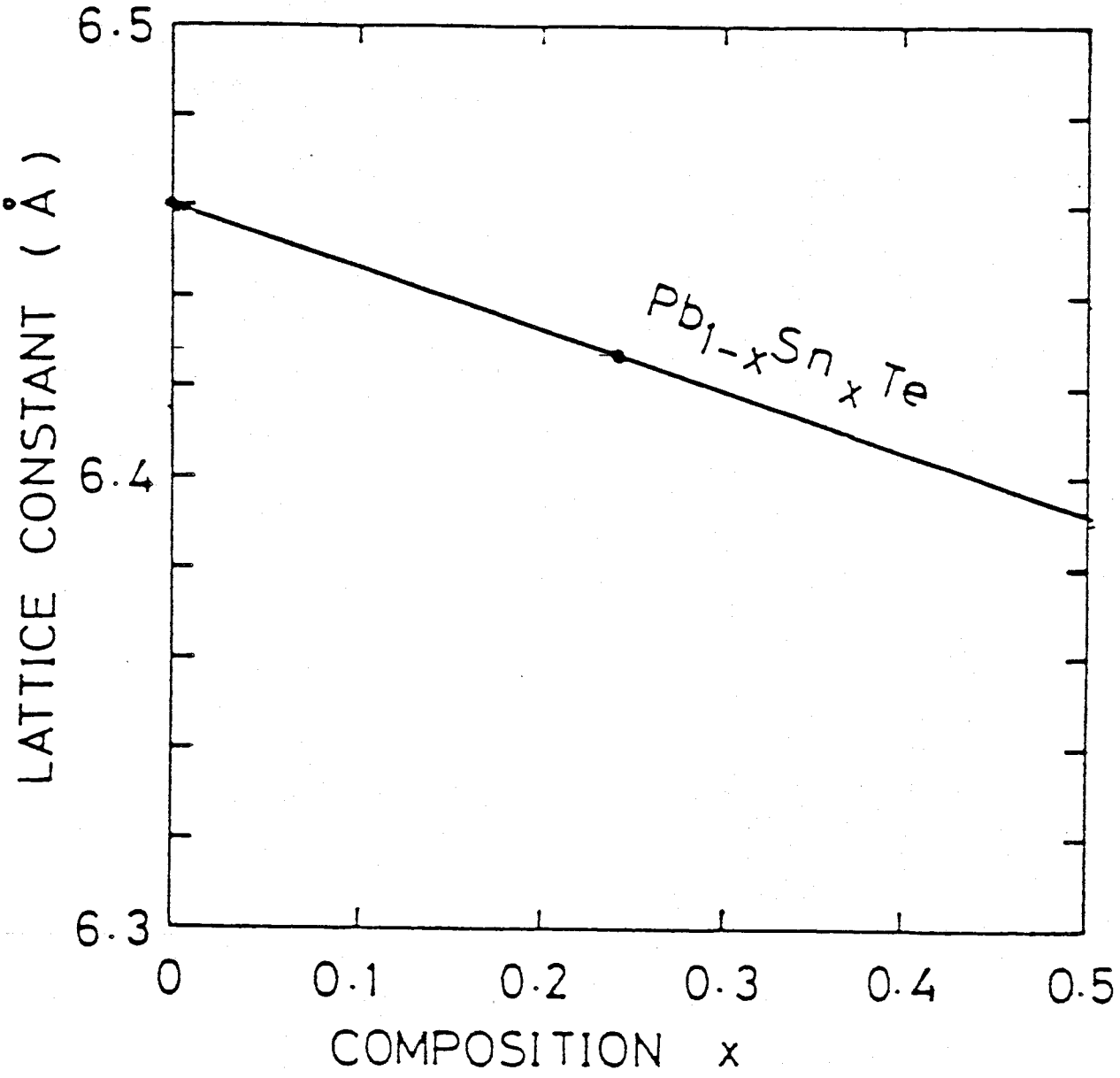

FIG. 6-1-2 Tin composition dependence of lattice constant of $Pb_{1-x}Sn_xTe$(ref. 106).

§6-2 X-ray Diffraction of Superlattices

X-ray difraction is a powerful method to determine the structural characterization of superlattices[50,109-110]. Let us consider X-ray diffraction intensity of a PbTe/$Pb_{1-x}Sn_xTe$ superlattice. The superlattice consists of N periods and each period has 2M atomic layers. For the superlattice with <111> growth direction, metallic atom layer and Te atom layer are grown alternately. When x-ray is incident with the angle θ with respect to the superlattice interface, the amplitude A of X-ray difracted with the same angle θ is given by summation of amplitude of reflected X-ray from the αth atomic layer:

$$A = \sum_{\alpha=0}^{2NM-1} f(\alpha)\exp[i\Delta k * ds(\alpha)] \ , \qquad (6.2.1)$$

with

$$f(\alpha)=\begin{cases} f_{Pb}(\theta)(1-x(\alpha))+f_{Sn}(\theta)x(\alpha) & (\alpha = \text{odd number}) \\ f_{Te}(\theta) & (\alpha = \text{even number}) \end{cases} \qquad (6.2.2)$$

$$ds(\alpha)= \sum_{\beta=1}^{\alpha} d(\beta) \ ,$$

where $f_{Pb}(\theta)$, $f_{Sn}(\theta)$ and $f_{Te}(\theta)$ are atomic scattering factors of Pb, Sn and Te, respectively; $d(\alpha)$ is the distance between $(\alpha-1)$th and αth atomic layer. The amplitude A becomes

$$A = \sum_{n=0}^{N-1} \exp[i\Delta k * ND] \sum_{\alpha=0}^{2M-1} f(\alpha)\exp[i\Delta k * ds(\alpha)]$$

$$= N\exp(i\Delta k * ND/2)\delta(\Delta k - \frac{2n\pi}{D}) \sum_{\alpha=0}^{2M-1} f(\alpha)\exp[i\Delta k * ds(\alpha)], \quad (6.2.3)$$

where D is the thickness of one period; ν is integer; $\delta(x)$ is defined by

$$\delta(x) = \begin{cases} 1 & (x = 0) \\ 0 & (x \neq 1) . \end{cases}$$

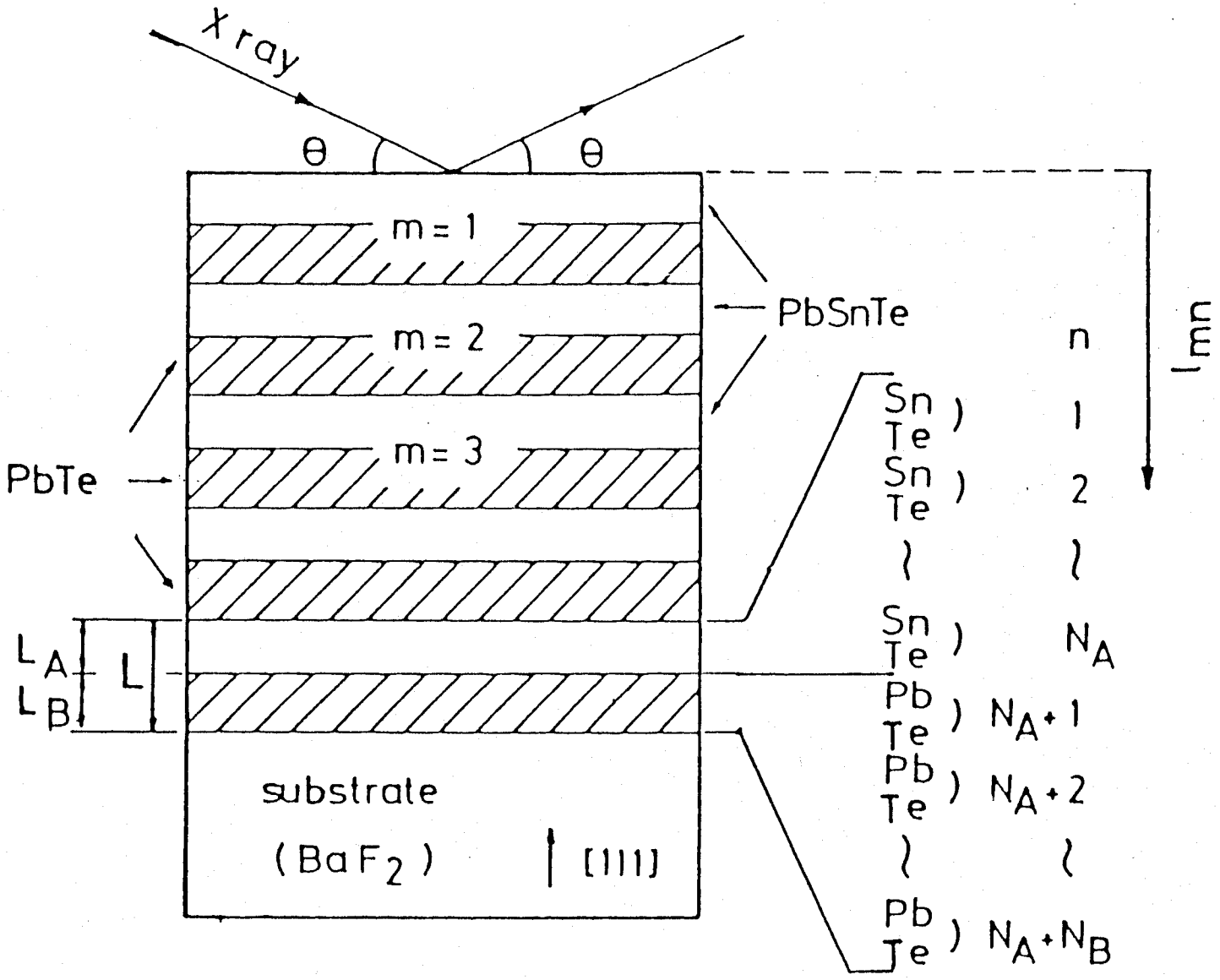

FIG. 6-2-1 θ-2θ method of X-ray diffraction.

§6-3 Sample preparation by hot wall epitaxy

Samples have been prepare by flip-flop hot wall epitaxy system in 1×10^{-7} torr(see Fig. 6-3-1)[112]. Crystal growth has been performed in almost closed tube so that 1×10^{-7} torr is sufficiently high vacuum. Hot wall epitaxy Vapor pressure in hot wall epitaxy method is much high($10^{-4}\sim10^{-3}$ Torr) than that in molecular beam epitaxy. Typical source temperature is 520°C and a substrate temperature is 250°C. Growth rate is about 8Å/sec. Carrier concentration has been controlled by Te reservoir temperature.

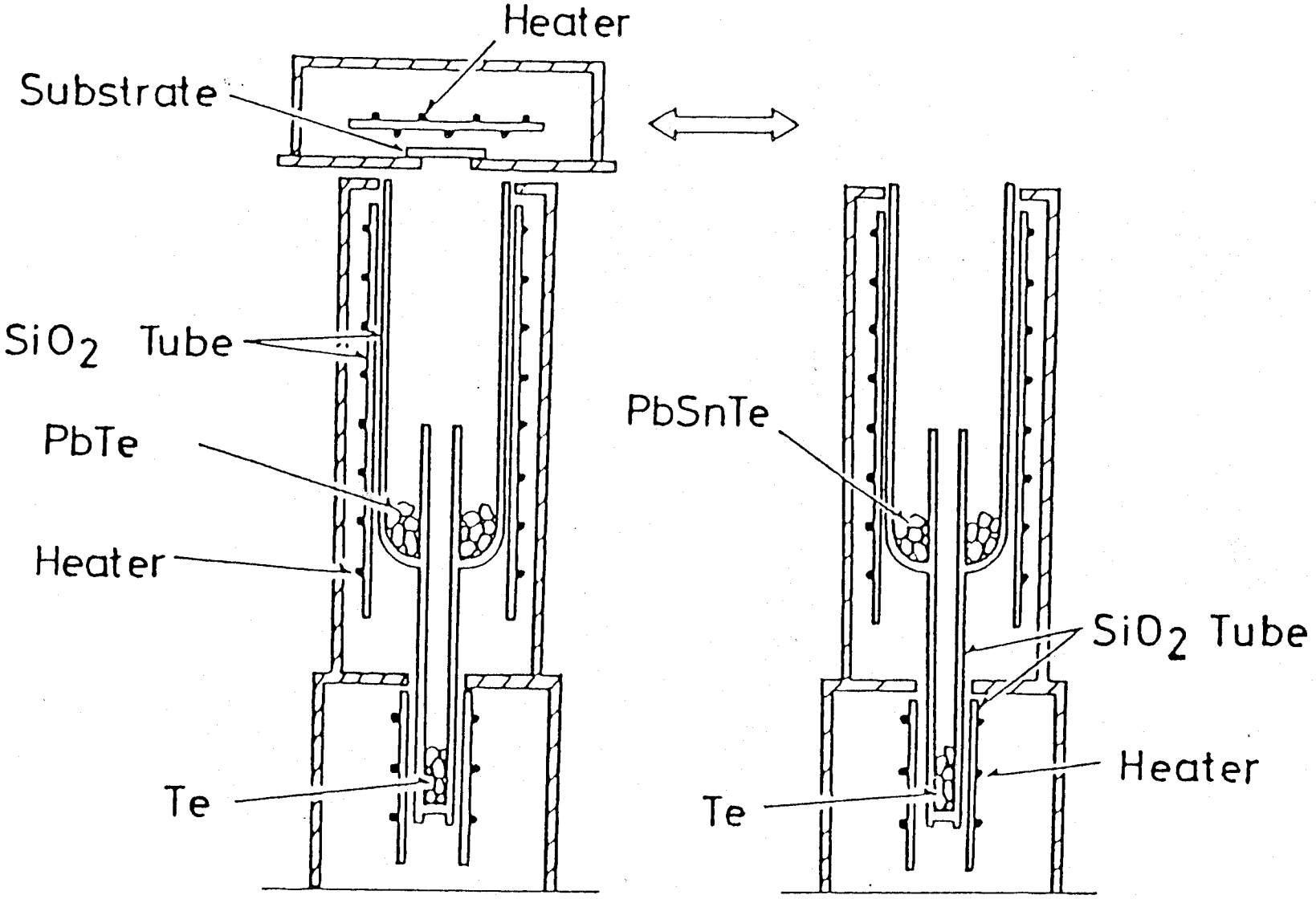

FIG. 6-3-1 Hot wall epitaxy system for preparing PbTe/$Pb_{1-x}Sn_xTe$ superlattices(ref.112).

§7 EXPERIMENTAL RESULTS AND ANALYSES FOR VARIOUS SUPERLATTICES

To observe minibands of superlattices, barrier layers must be enough narrow for electrons to tunnel through the barrier layers. If $Pb_{0.8}Sn_{0.2}Te$ layers act as barriers, electrons with an energy about the middle of energy gap penetrate into the barrier layers by 145Å in the case of the singlet valley, where the <111> direction is taken as a superlattice growth direction. In the case of the triplet valleys the penetration depth is 44Å, since the mass along the superlattice direction is almost equal to m_t. (see Table 7-0-1). We prepared superlattices with barrier layer thicknesses in the range from 30Å to 200Å as shown in Table 7-0-2.

It is also important to check the interdiffusion of Pb and Sn atoms across the interfaces because the interdiffusion changes the potential shape for electrons and holes. Layer thicknesses and interdiffusion lengths are determined by using satellite intensity and spacing of X-ray diffraction pattern. The X-ray through monochromator from Cu target contains only characteristic lines of $k\alpha_1(\lambda=1.5405Å)$ and $k\alpha_2(\lambda=1.5443Å)$ with intensity ratio of 2:1. Carrier densities of the superlattices are determined by Hall measurements. These characterization data are listed in Table 7-0-2. Electronic properties of superlattices are specified by the superlattice structure and carrier density. We will discuss properties of the superlattices individually. Sections 7-1, 7-2, 7-3, and 7-4 give the analysis of cyclotron resonance

for superlattices with small interdiffusion. The samples analysed in these four sections have the PbTe layers with almost the same thickness(200^{o}A). The $Pb_{0.8}Sn_{0.2}Te$ layer thicknesses is 30, 60, 150, 220^{o}A, respectively. From the four sections we will get the barrier layer thickness dependence of the electronic properties in the superlattices. The magneto-plasma spectra of superlattice with large interdiffusion are given in section 7-5 and 7-6. In section 7-7, the cyclotron resonance data of the superlattice consist of very thin layer are presented. Over all discussion is given in section 8.

TABLE 7-0-1 Energy gap and effective mass

	E_g(meV)at 4.2K	$m_t(m_o)$	$m_l(m_o)$
PbTe	184	0.023	0.242
$Pb_{0.8}Sn_{0.2}Te$	76	0.0095	0.100

$$E\left(1 + \frac{E}{E_g}\right) = \frac{\hbar^2 kx^2}{2m_t} + \frac{\hbar^2 ky^2}{2m_t} + \frac{\hbar^2 kz^2}{2m_l}$$

penetration depth of electron in $Pb_{0.8}Sn_{0.2}Te$, dx and dz

$E = -38(meV)$, $m_t = 0.0095m_o$, $dx = 145\mathring{A}$

$m_l = 0.1000m_o$, $dz = 44\mathring{A}$

TABLE 7-0-2 SAMPLE CHARACTERISTICS

sample name	layer thickness PbTe (Å)	layer thickness PbSnTe(Å)	inter-diffsion length(Å)	total layer number	carrier density ($1/cm^3$)	mobility at 4.2K ($cm^2/V \cdot s$)
#1	220	30	<10	175	1.2×10^{17}	17000
#2	240	60	<10	160	1.1×10^{17}	260000
#3	260	150	<30	135	3.9×10^{17}	220000
#4	220	220	<10	100	-	-
#5	300	190	95	100	2.1×10^{17}	130000
#6	180	230	70	100	1.5×10^{17}	13400
#7	34	41	<16	600	1.5×10^{17}	90000

§7-1 PbTe/$Pb_{1-x}Sn_xTe$ 220Å/30Å Superlattice(#1)

From the X-ray diffraction pattern(see Fig. 7-1-1), PbTe and $Pb_{1-x}Sn_xTe$ layer thicknesses, 220Å and 30Å, are obtained. Total thickness is 4.48μm. Interdiffusion length is below 10Å. To obtain more precise interdiffusion length, we must detect intensity of further satellites. Because higher harmonics become increasingly important as tin composition profile approaches the square shape. Actually they are very weak. Figure 7-1-2 shows Sn composition profile at interdiffusion length 10Å(worst case). Figure 7-1-3 shows an energy diagram based on the model that the indium level are taken as the energy origin. Figs. 7-1-4 and 7-1-5 show the dependence of the magnetoplasma transmission spectra on magnetic field direction. Dip A is the cyclotron resonance of the singlet valley. Peak B is the dielectric anomaly. There is no triplet valley signal due to valley splitting caused by tensile strain from BaF_2. This tensile strain arise on account of the difference of thermal expansion coefficient between the superlattice film and the BaF_2 substrate when a sample is cooled down from room temperature to 4.2K. Figure 7-1-6 shows resonance magnetic field versus magnetic field directions. The solid line in Fig. 7-1-6 are calculated resonance magnetic field based on the envelope function approximation method. In this calculation, potential is taken as the square shape. This is good approximation from the above X-ray analysis. Band discontinuities are defined by

$$Ec(x) = 300x(meV)$$

and

$$Ev(x) = -184 + 243x(meV)$$

from the model in which the indium level in $Pb_{1-x}Sn_xTe$ is used as reference level(see Fig. 3-1-1). For $PbTe/Pb_{0.8}Sn_{0.2}$, the band discontinuity of the conduction band is 60meV. The valley splitting effect due to the internal strain to accommodate the lattice mismach must be taken into account. The deformation parameters in ref. are used(listed below).

$$D_d^c = -1.09 \ (eV)$$

$$D_d^v = -2.23 \ (eV)$$

$$D_u^c = 2.07 \ (eV)$$

$$D_u^v = 2.62 \ (eV)$$

From cross section of the Fermi surface, S_k, cyclotron mass, m_c, is derived by using

$$m_c = \frac{\hbar^2}{2\pi} \cdot \frac{dS_k}{dE} \ , \qquad (7.1.1)$$

where E is the energy at the Fermi surface. From this calculation, calculated carrier density and area of cross section of the Fermi surface are almost coincident with measured ones (see Table 7-1-1). Band parameters in calculation are given in Fig. 7-1-7. The band edge energy suffers from the effect of internal strains at the PbTe layer and $Pb_{0.8}Sn_{0.2}Te$ layer to accommodate the lattice mismatch. The effect of tensile strain due to the BaF_2 substrate is taken into account as a valley splitting to maintain consistency between measured Fermi surface and carrier density

and calculated ones. The energy dispersion curves are shown in Figs. 7-1-8 and 7-1-9. For the singlet valley, the first and second subbands are not dispersive along the q(<111> superlattice direction). In other words, energy gaps between the first and second subbands at q=0, and between the second and third subbands at $q=\pi/d$ are wide. The Fermi level locates slightly above the third subband edge(short and long dashed line in Fig. 7-1-8). Thus the Fermi surfaces of the first and second subbands have cylindrical shapes and are 2-dimensional. The third subband is dispersive but the number of carriers is quite small to detect the cyclotron resonance Table 7-1-1). For the triplet valleys, dispersion of subbands along q is large. However carriers do no exist in the triplet valleys, we could not examine this dispersion.

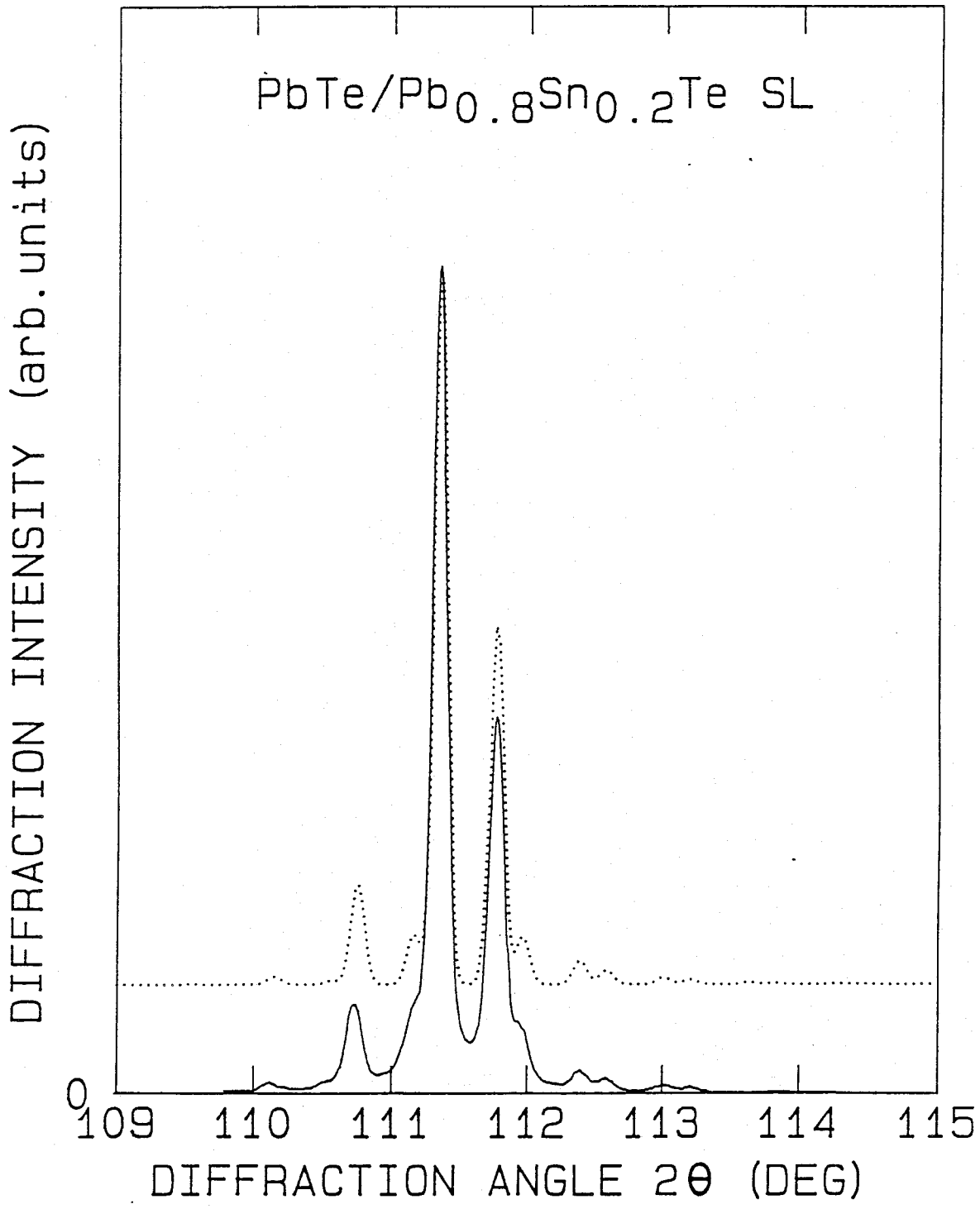

FIG. 7-1-1 Measured(solid line) and calculated(dotted line) X-ray diffraction patterns for the sample #1. Calculated line is shifted intentionally to avoid overlapping. Diffraction is around (444) reflection. From the calculation, the thicknesses of 220Å(60 PbTe layers) and 30Å(9 $Pb_{0.8}Sn_{0.2}Te$ layers) are obtained. The interdiffusion length is below 10Å.

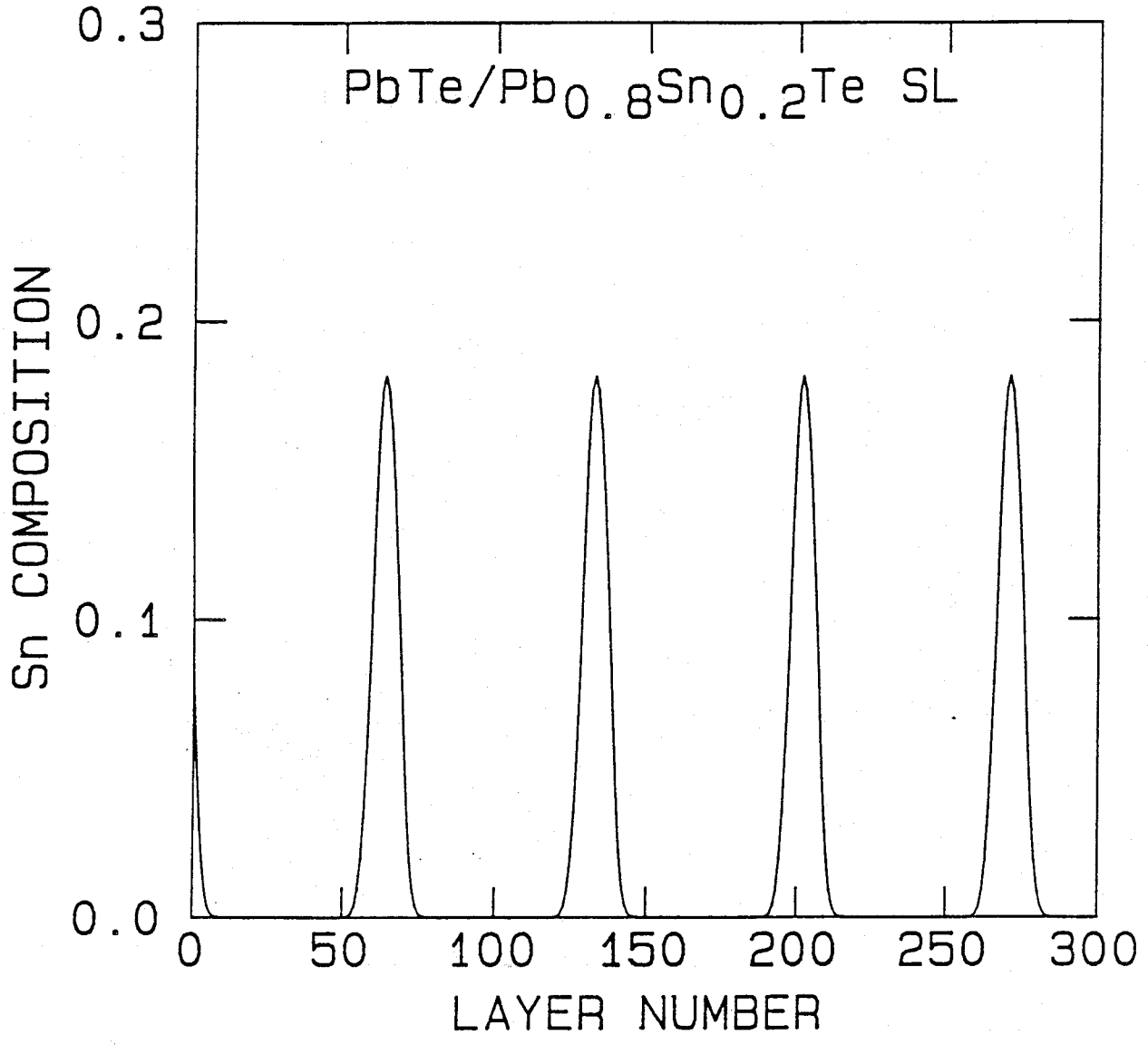

FIG. 7-1-2 Tin composition profile versus metallic atom layer numbers for the sample #1(220Å/30Å). The thickness of 100 molecular layers corresponds to 373Å.

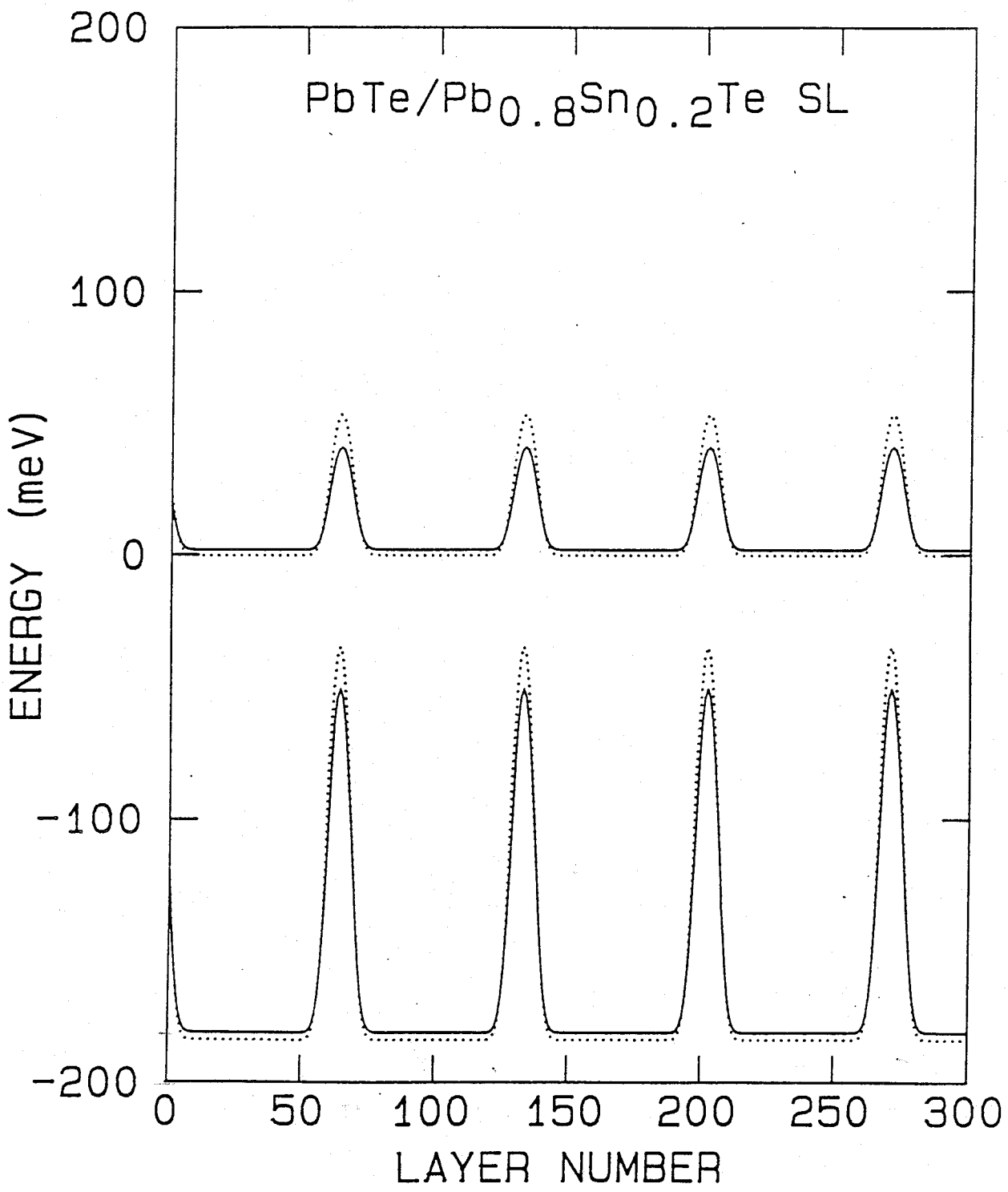

FIG. 7-1-3 Energy band diagrams of the singlet valley(solid lines) and triplet valleys(dotted lines) versus metallic atom layer numbers for the sample #1(220Å/30Å). The thickness of 100 molecular layers corresponds to 373Å. Energy bands shift by internal strain to accommodate the lattice mismatch between PbTe and $Pb_{0.8}Sn_{0.2}Te$ layers.

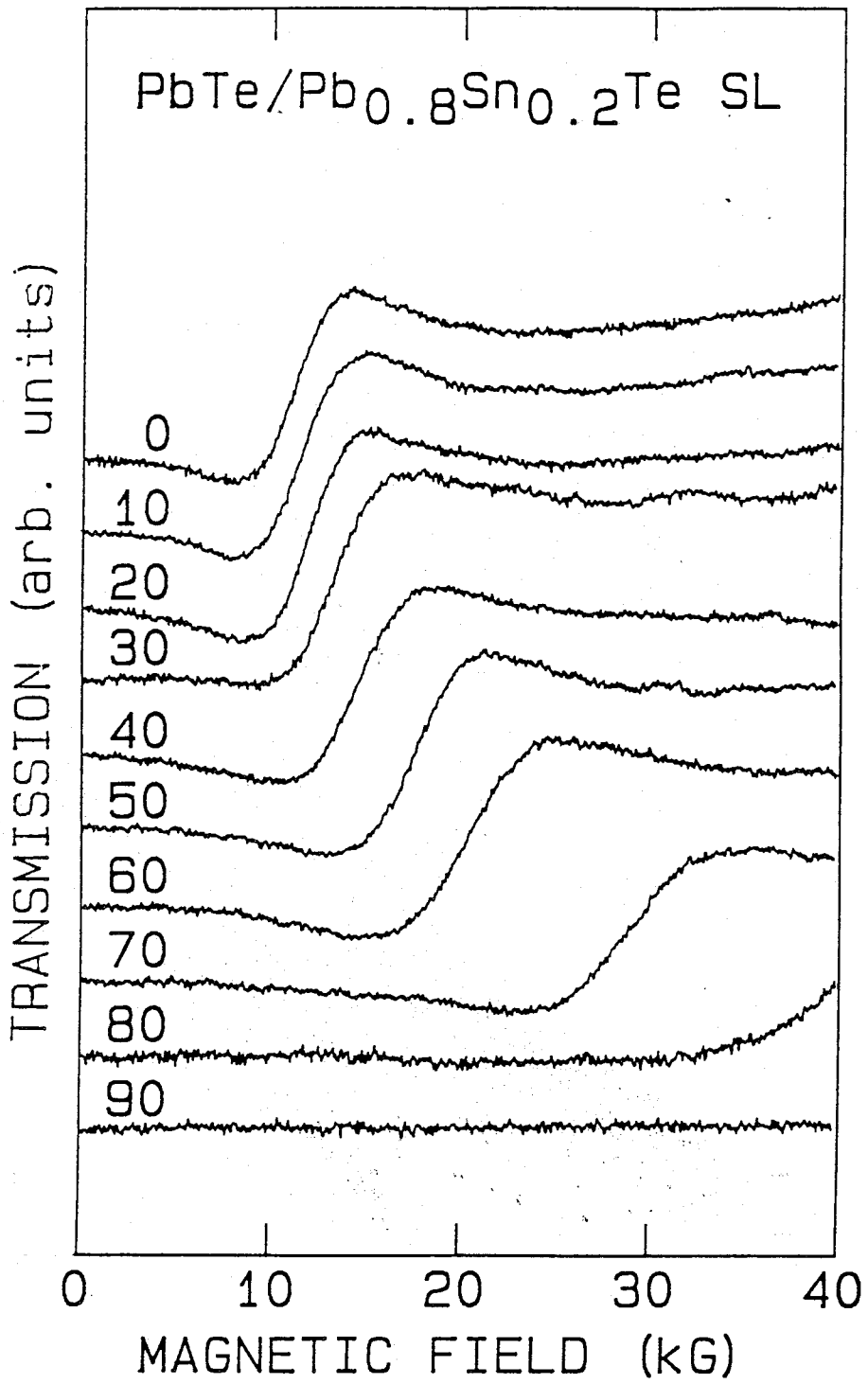

FIG. 7-1-4 Magnetoplasma transmission spectra with 307μm laser light at 4.2K for the sample #1(220Å/30Å). The magnetic field direction is changed from 0 deg along <111>(Faraday configuration)to 90 deg along <$\bar{1}\bar{1}$2>(Voigt configuration).

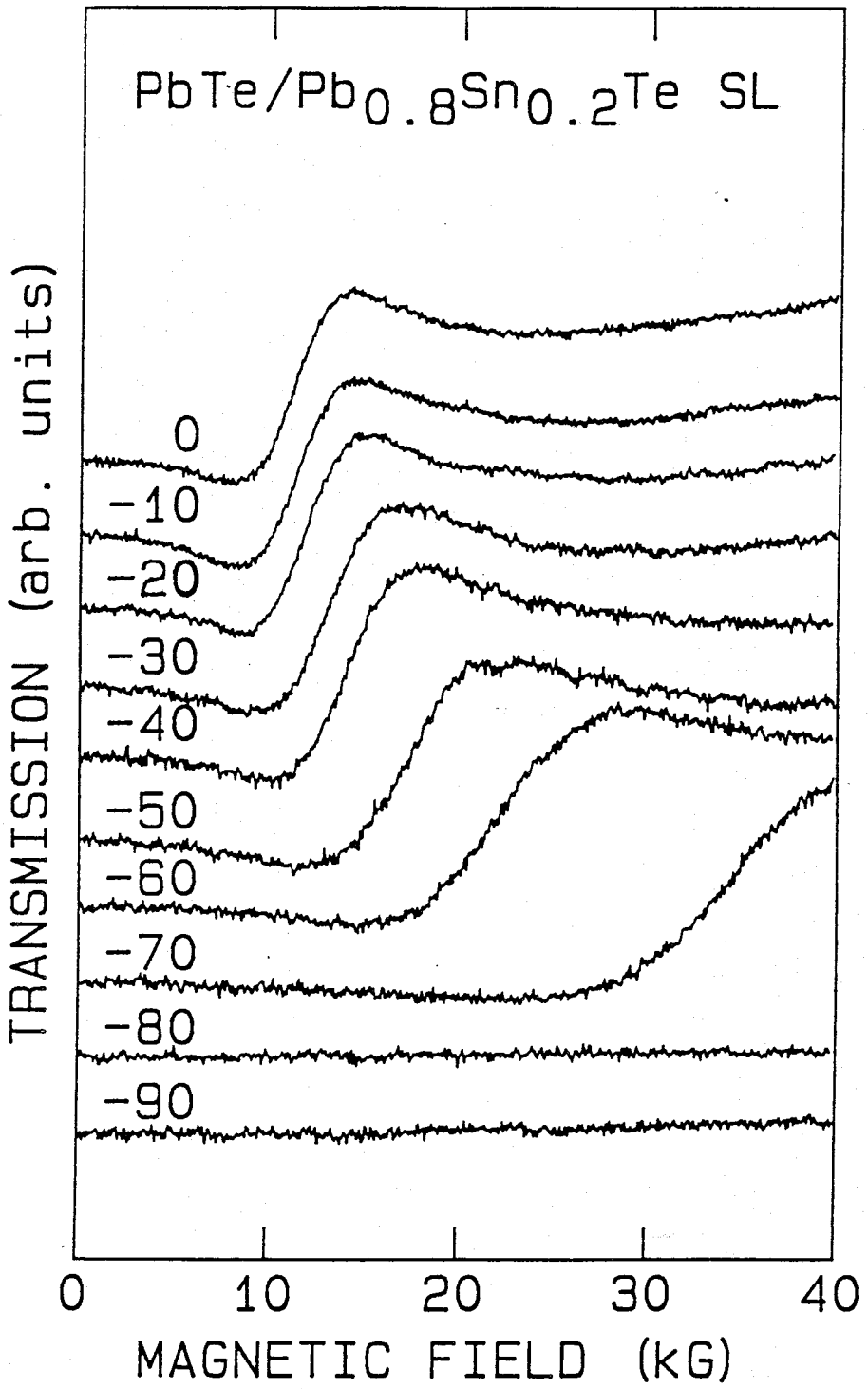

FIG. 7-1-5 Magnetoplasma transmission spectra with 337μm laser light at 4.2K for the sample #1(220Å/30Å). The magnetic field direction is changed from 0 deg along <111>(Faraday configuration) to -90 deg along <11$\bar{2}$>(Voigt configuration).

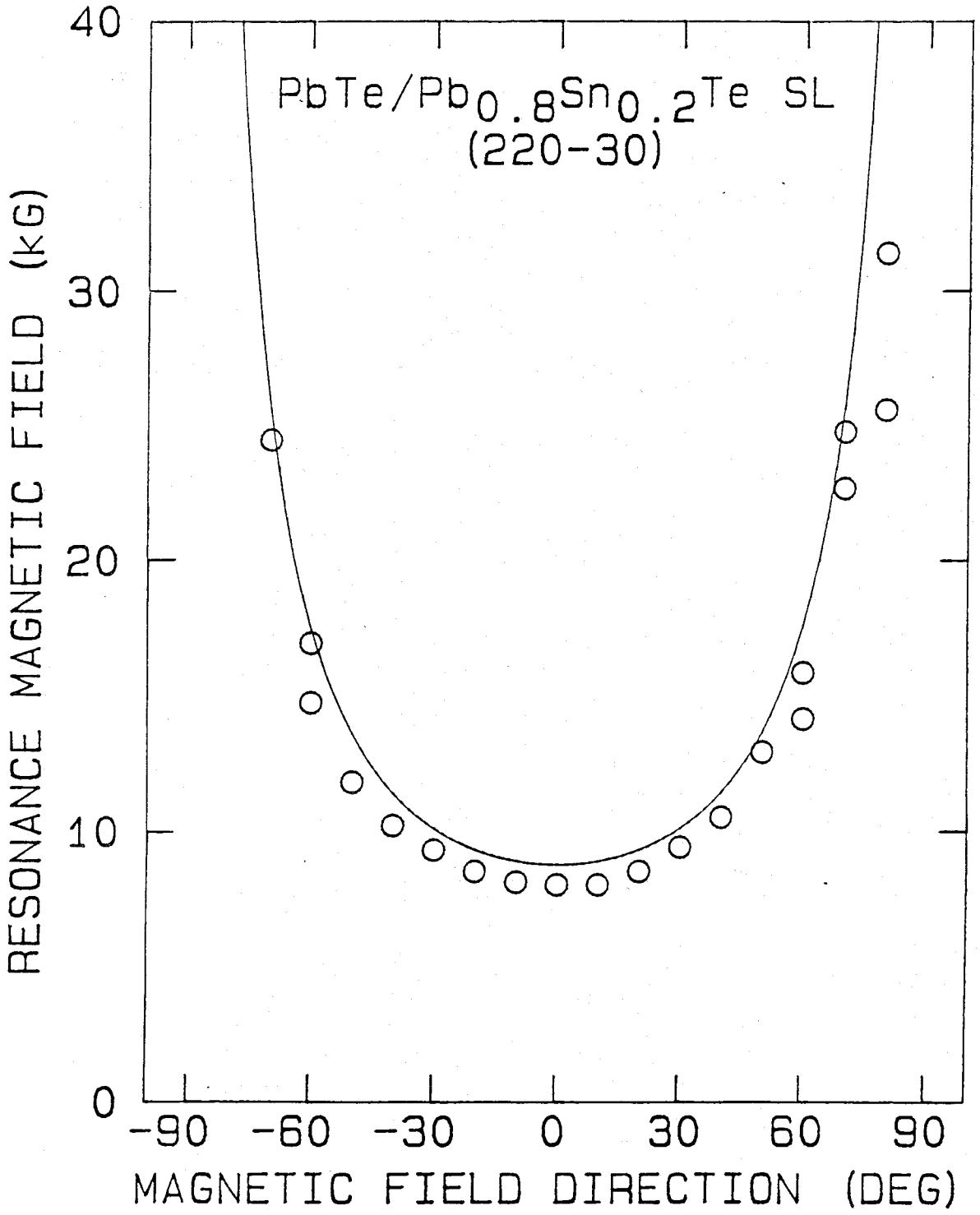

FIG. 7-1-6 Dip position as a function of the magnetic field directions for the sample #1(220Å/30Å). Solid line is the cyclotron resonance field obtained from calculation based on the envelope function approximation.

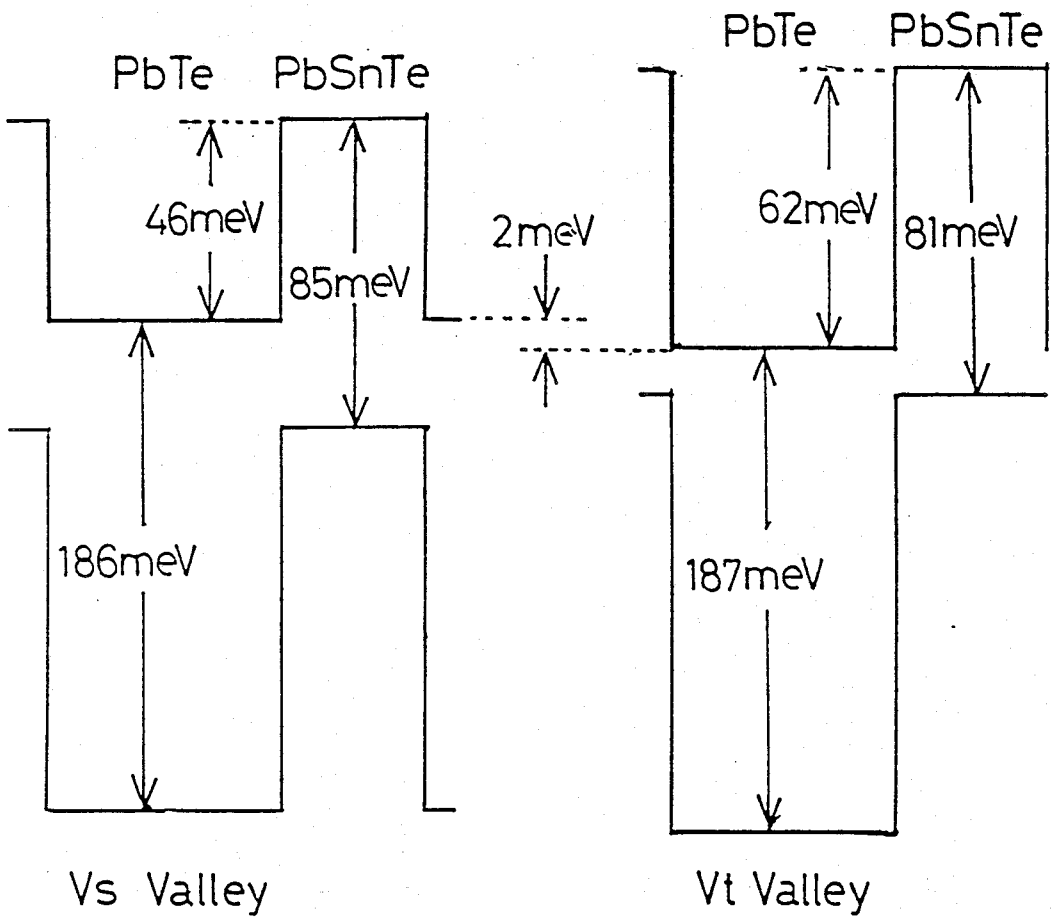

FIG. 7-1-7 Band parameters used in the calculation based on the envelope function approximation for the sample #1(220Å/30Å).

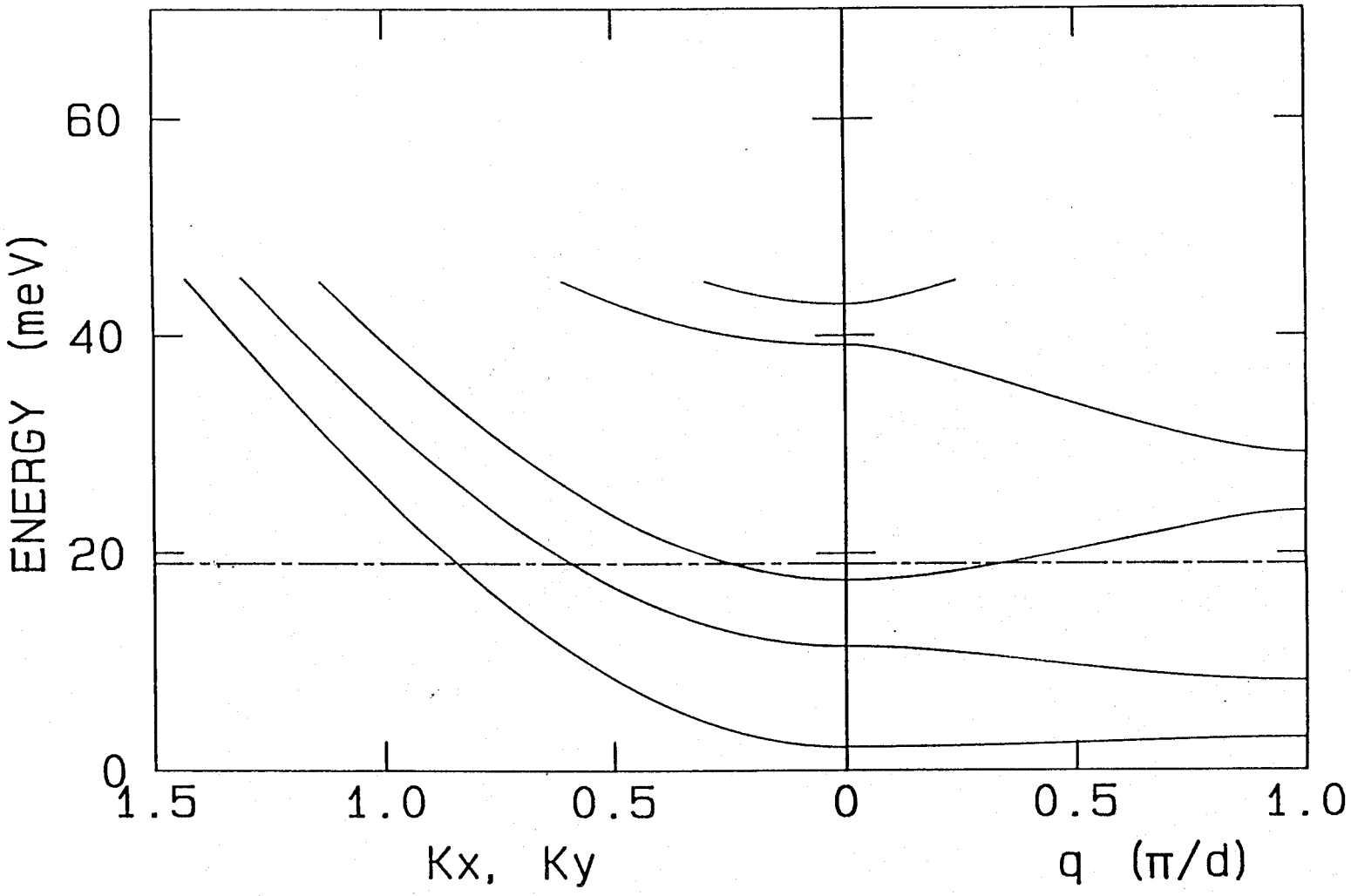

FIG. 7-1-8 Energy dispersion of the singlet valley for the sample #1(220Å/30Å) obtained from the envelope function approximation. The dashed and dotted line indicates the Fermi level.

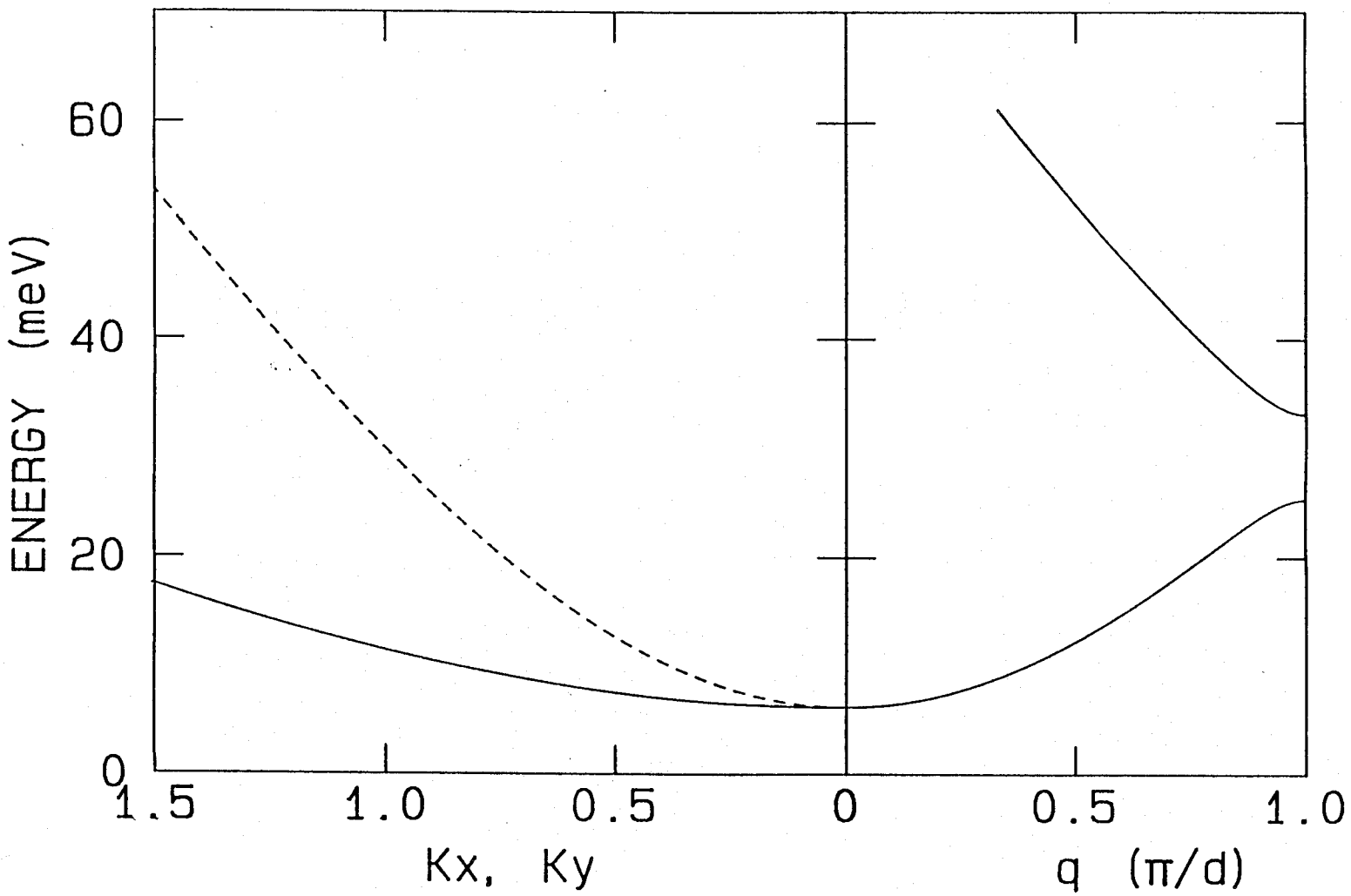

FIG. 7-1-9 Energy dispersion of the triplet valleys for the sample #1(220Å/30Å) obtained from the envelope function approximation. The dashed and dotted line indicates the Fermi level.

TABLE 7-1-1 Period of Shubnikov de-Haas and parameter obtained from the envelope function approximation for #1(220Å/30Å)

Valley and Sublevel	Δ(1/B) (T^{-1}) SdH	S_k(10^{-4}Å^{-2}) SdH	EFA center	EFA edge	n(×10^{16}cm^{-3}) HALL	EFA	Resonance Field(kG) CR	EFA center	EFA edge
Vs 1	0.28	3.4	3.51	3.40		7.0	8.0	8.8	8.8
Vs 2	0.47	2.0	1.72	2.22		4.0	8.0	8.9	8.4
Vs 3			0.29			0.1			
				total	12	11.1			

S_k:cross section of the Fermi surface at center:k_z=0, edge:k_z=π/D

§7-2 PbTe/$Pb_{1-x}Sn_xTe$ 240Å/60Å Superlattice(#2)

From the X-ray diffraction pattern(see Fig. 7-2-1), PbTe and $Pb_{1-x}Sn_xTe$ layer thicknesses, 240Å and 60Å are obtained. Total thickness is 4.67μm. Interdiffusion length is below 10Å. To analyze more precise interdiffusion length, we must detect intensity of further satellites for the same reason in section 7-1. Figure 7-2-2 shows the Sn composition profile with an interdiffusion length 10Å(worst case). Figure 7-2-3 shows energy diagram based on the model that the indium level is taken as the energy origin. In this case, the square well potential approximation is good even in a worst case for interdiffusion. The mobility of 260000 $cm^2/V\cdot s$ is extremely high in this sample. Figures 7-2-4 and 7-2-5 show the dependence of the magnetoplasma transmission spectra on magnetic field directions. Dips A and B come from cyclotron resonance of the singlet valley(valley A) and valley B of the triplet valleys, respectively. Dip C is cyclotron resonance due to valleys C and D of the triplet valleys. Valleys A, B, C, and D are denoted by valleys directed $\langle 111\rangle$, $\langle 1\bar{1}\bar{1}\rangle$, $\langle \bar{1}1\bar{1}\rangle$ and $\langle \bar{1}\bar{1}1\rangle$, respectively. Electrons belonging to the singlet valley are 2-dimensional but the electrons belonging to the triplet valleys are 3-dimensional. Figure 7-2-6 shows resonance magnetic field versus magnetic field directions. The solid line in Fig. 7-2-6 are calculated resonance magnetic field based on the envelope function approximation. Procedure of calculation is the same as section 7-1. Calculated carrier density and area of cross

section of the Fermi surface almost reproduce experimental ones (see Table 7-2-1). Band parameters in calculation are given in Fig. 7-2-7. The energy dispersion curves are shown in Figs. 7-2-8 and 7-2-9.

For the singlet valley, dispersion of the first and second subbands is almost constant as function of q. Fermi level is slightly above the second subband edge. Hence the electron system of the singlet valley is 2-dimensional. For the triplet valleys, even the first subbands are dispersive as shown in Fig. 7-2-9. The Fermi level locates in the first subband. The shape of the Fermi surface is almost spheroidal and the dependence of resonance magnetic field is 3-dimensional.

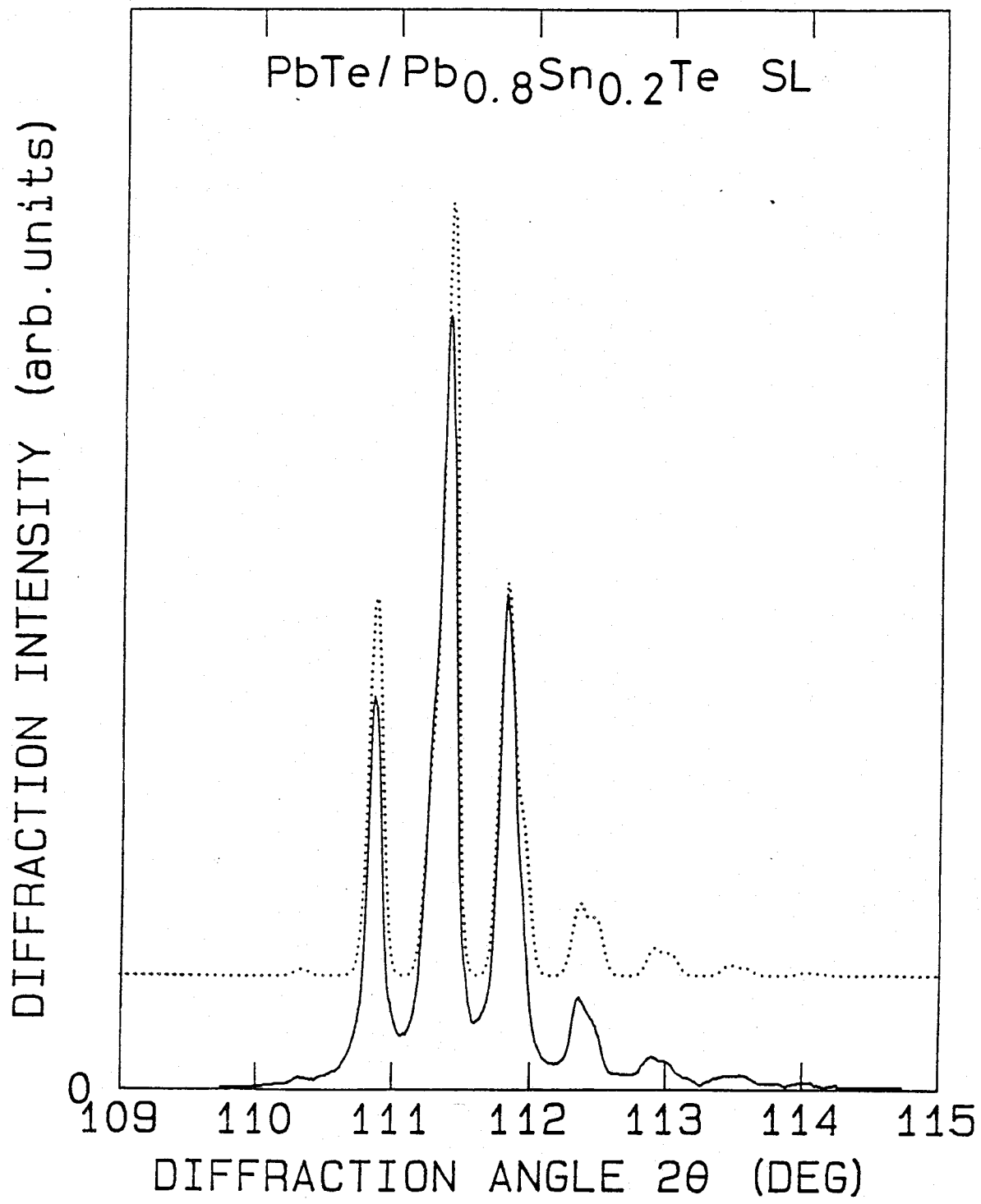

FIG. 7-2-1 Measured(solid line) and calculated(dotted line) X-ray diffraction patterns of the sample #2. Diffraction is around (444) reflection. From the calculation, the thicknesses of 240Å(63 PbTe layers) and 60Å(15 $Pb_{0.8}Sn_{0.2}Te$ layers) are obtained. The interdiffusion length is below 10Å.

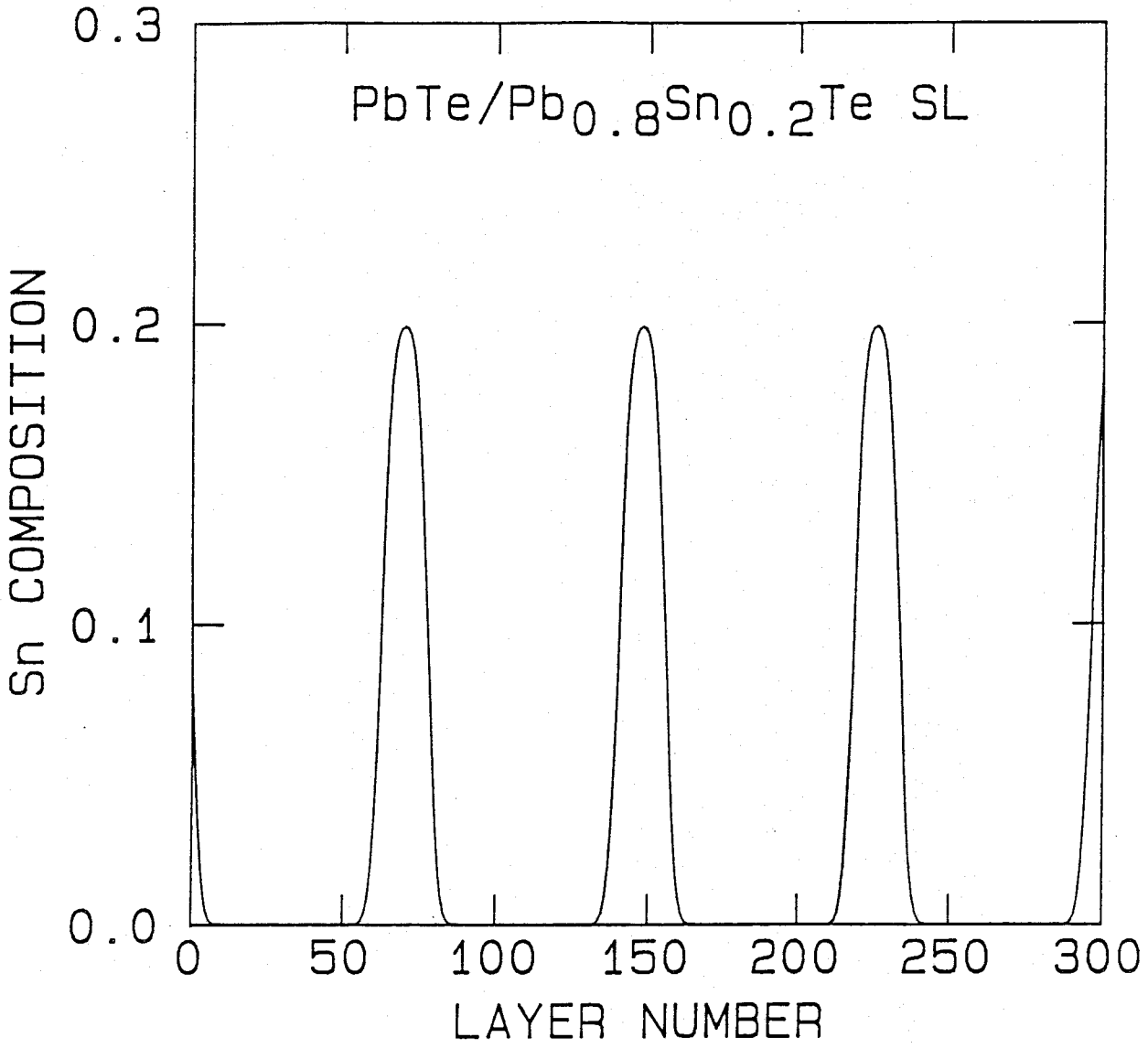

FIG. 7-2-2 Tin composition profile versus metallic atom layer numbers for the sample #2(240Å/60Å). The thickness of 100 molecular layers corresponds to 373Å.

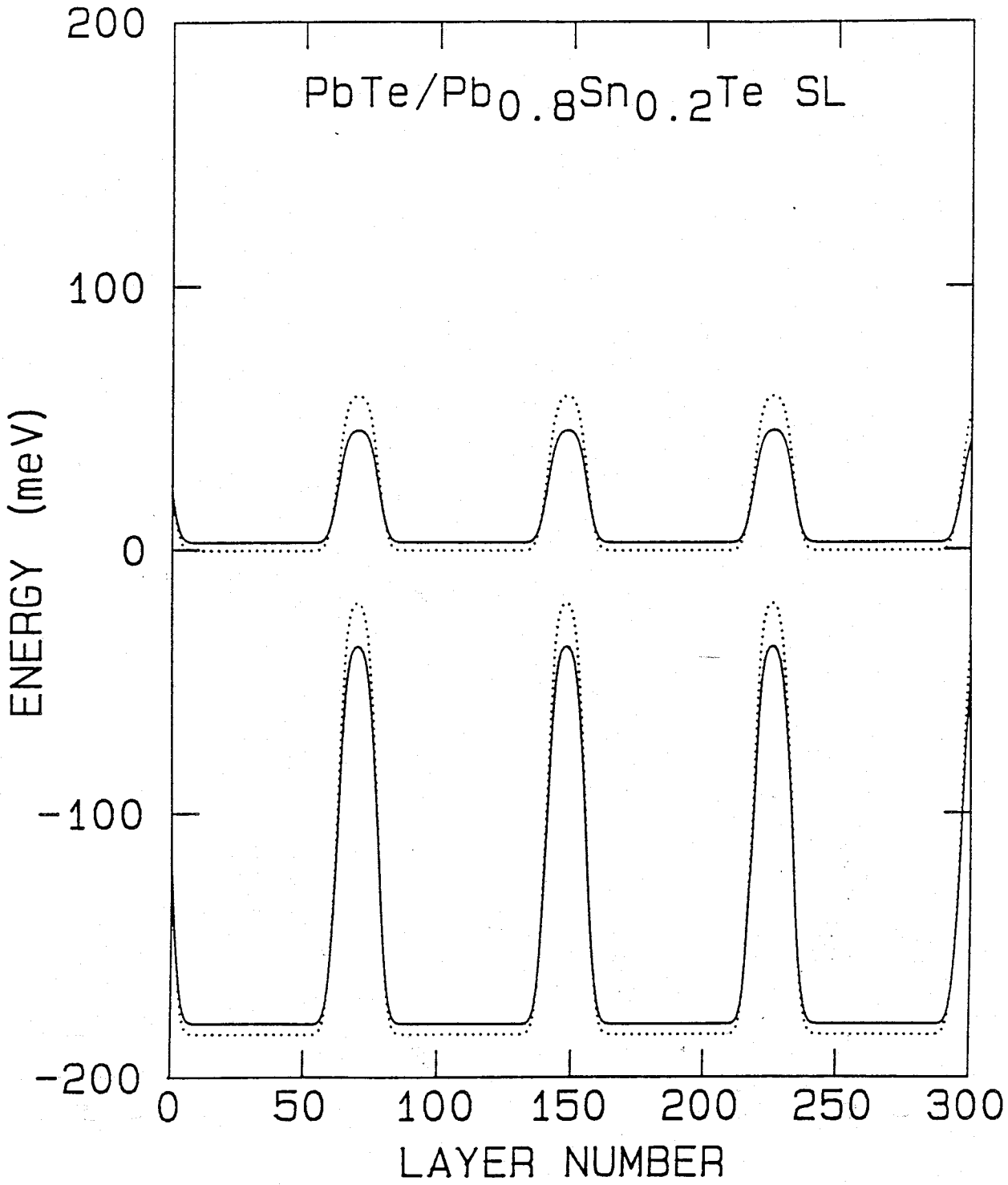

FIG. 7-2-3 Energy band diagrams of the singlet valley(solid lines) and triplet valleys(dotted lines) versus metallic atom layer numbers for the sample #2(240Å/60Å). The thickness of 100 molecular layers corresponds to 373Å. Energy bands shift by internal strain to accommodate the lattice mismatch between PbTe and $Pb_{0.8}Sn_{0.2}Te$ layers.

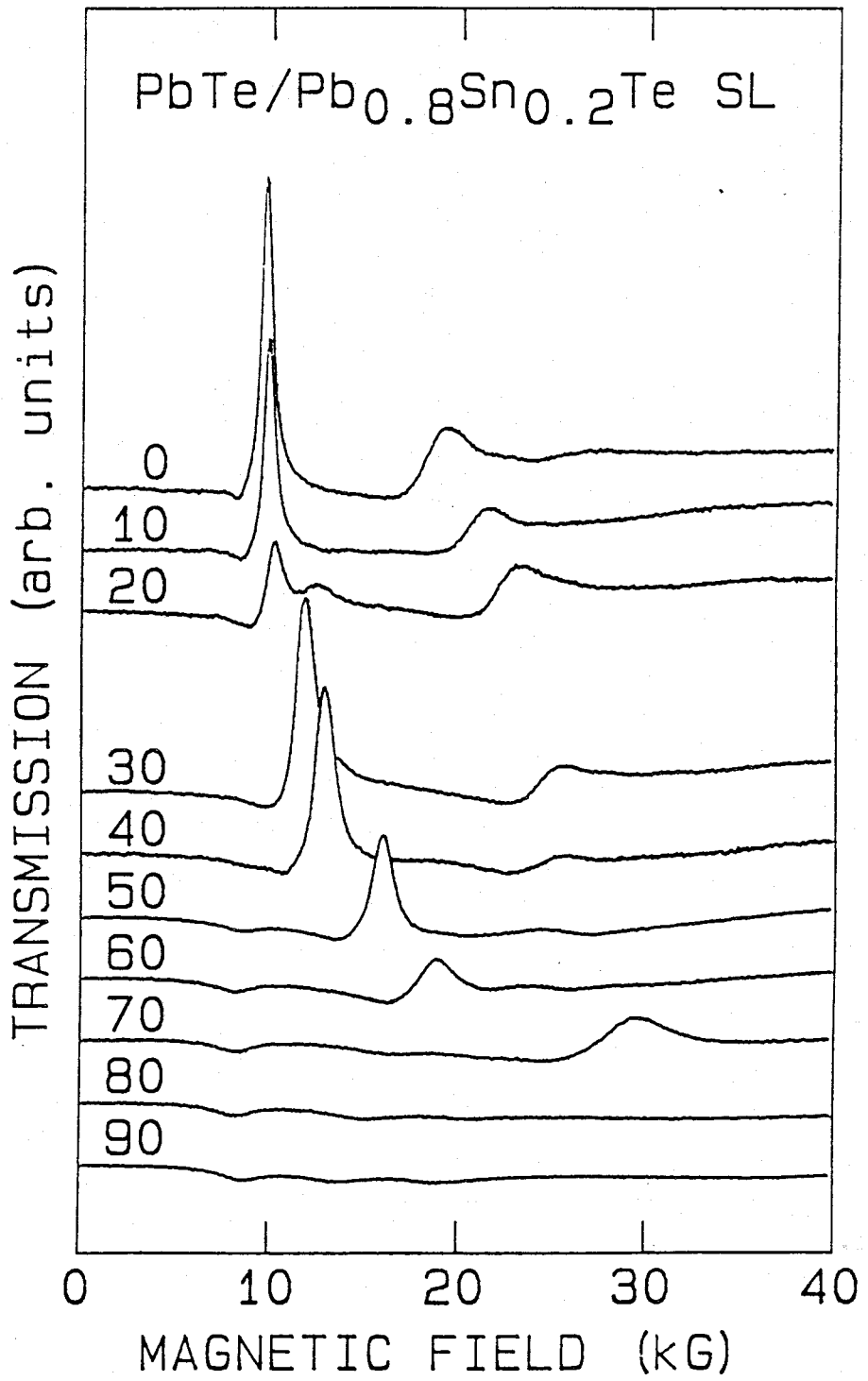

FIG. 7-2-4 Magnetoplasma transmission spectra with 337μm laser light at 4.2K for the sample #2(240Å/60Å). The magnetic field direction is changed from 0 deg along <111>(Faraday configuration) to 90 deg along <$\bar{1}\bar{1}$2>(Voigt configuration).

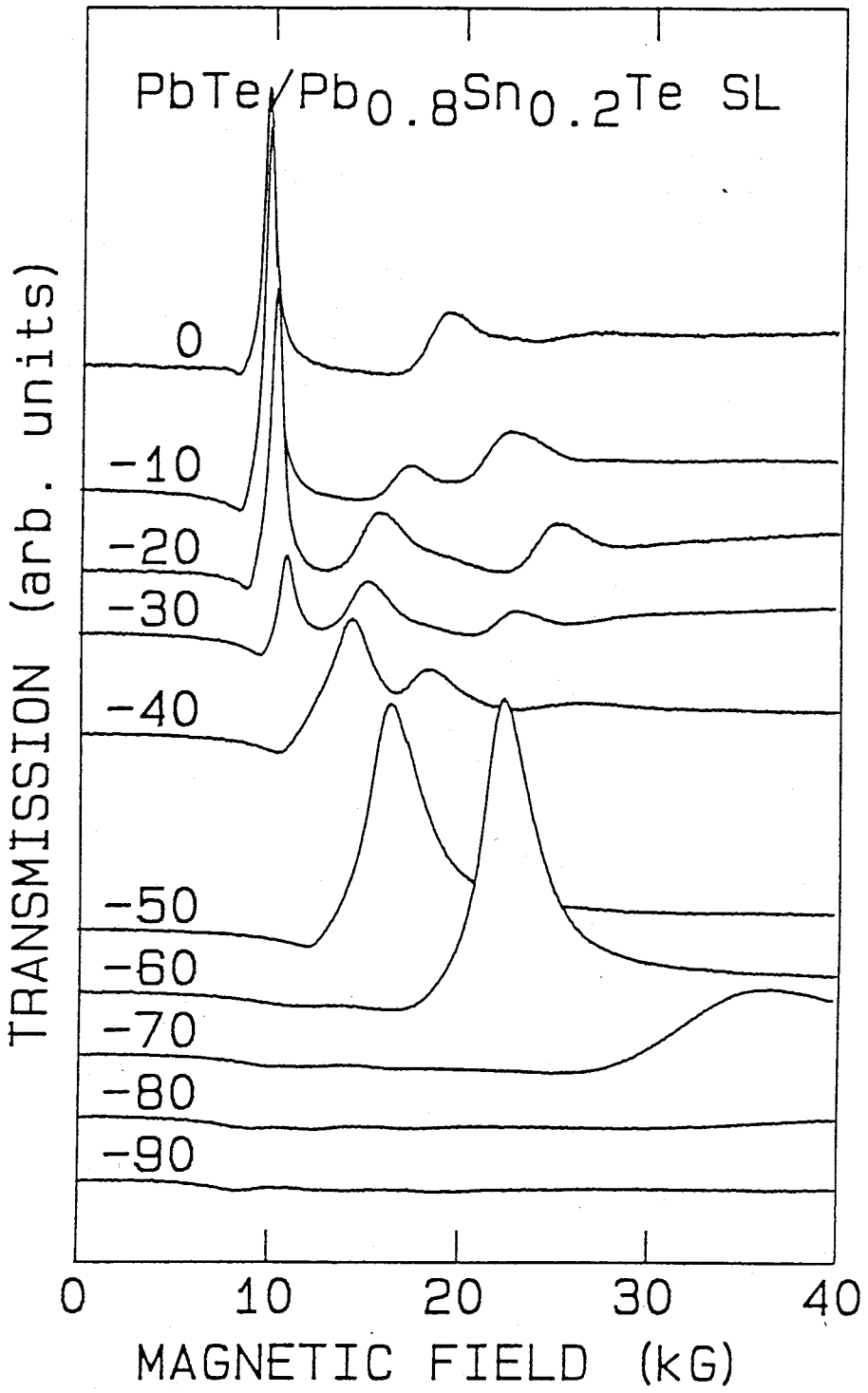

FIG. 7-2-5 Magnetoplasma transmission spectra with 337μm laser light at 4.2K for the sample #2(240Å/60Å). The magnetic field direction is changed from 0 deg along <111>(Faraday configuration) to -90 deg along <11$\bar{2}$>(Voigt configuration).

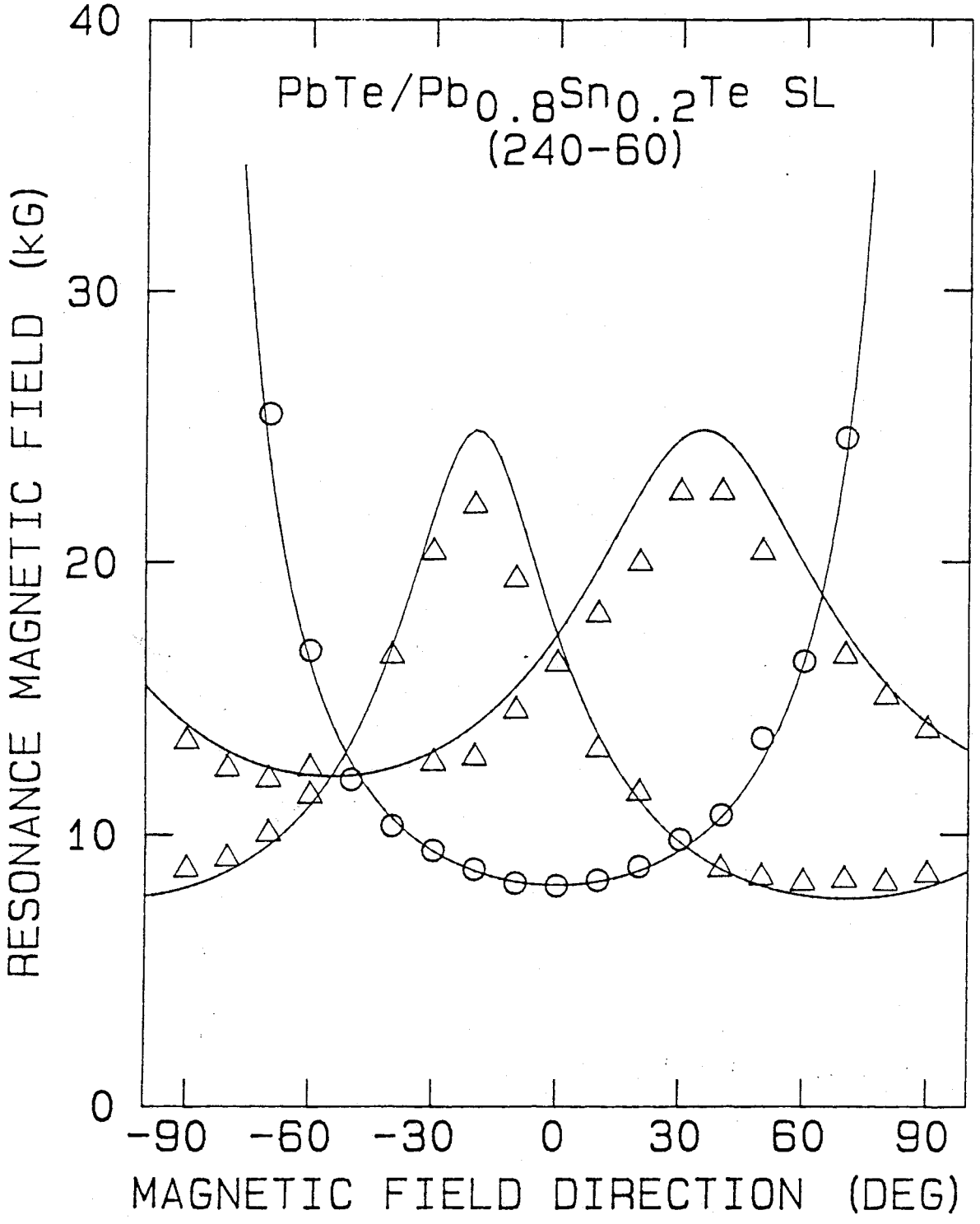

FIG. 7-2-6 Dip position as a function of the magnetic field direction for the sample #2(240Å/60Å). Solid lines are the cyclotron resonance field obtained from calculation based on the envelope function approximation.

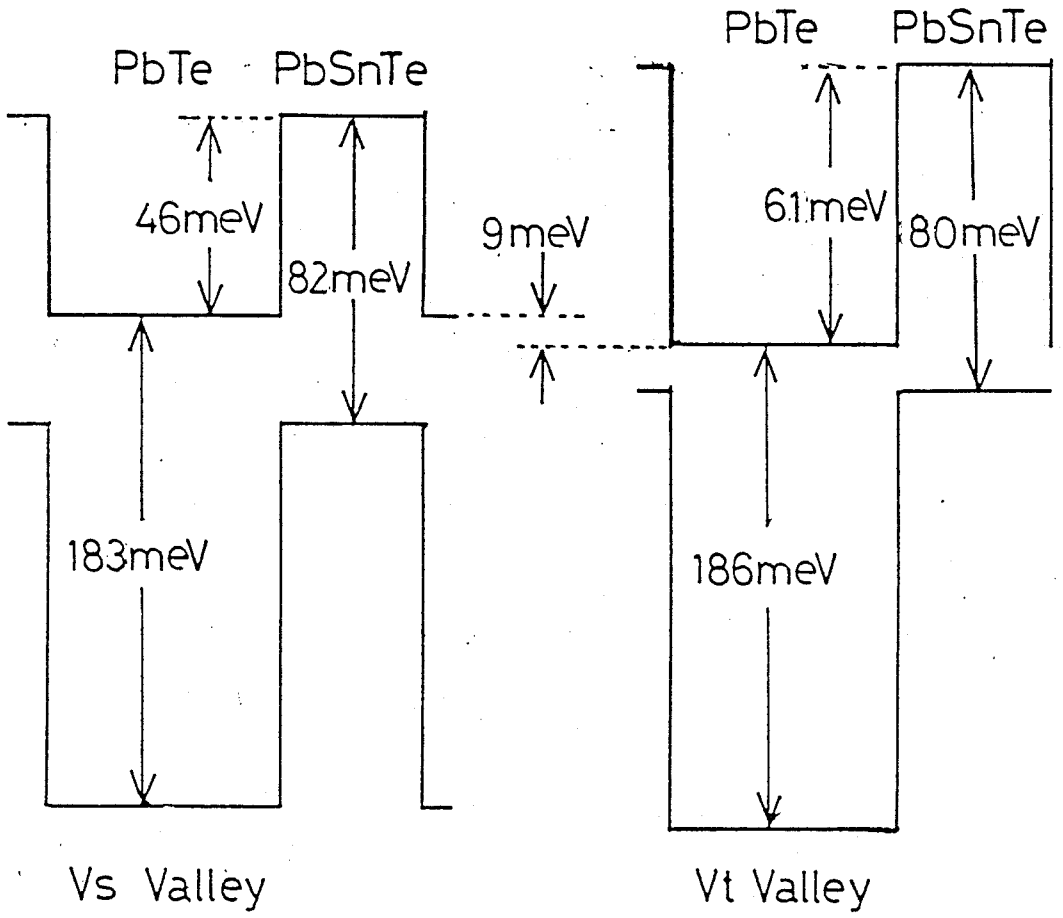

FIG. 7-2-7 Band parameters used in the calculation based on the envelope function approximation for the sample #2(240Å/60Å).

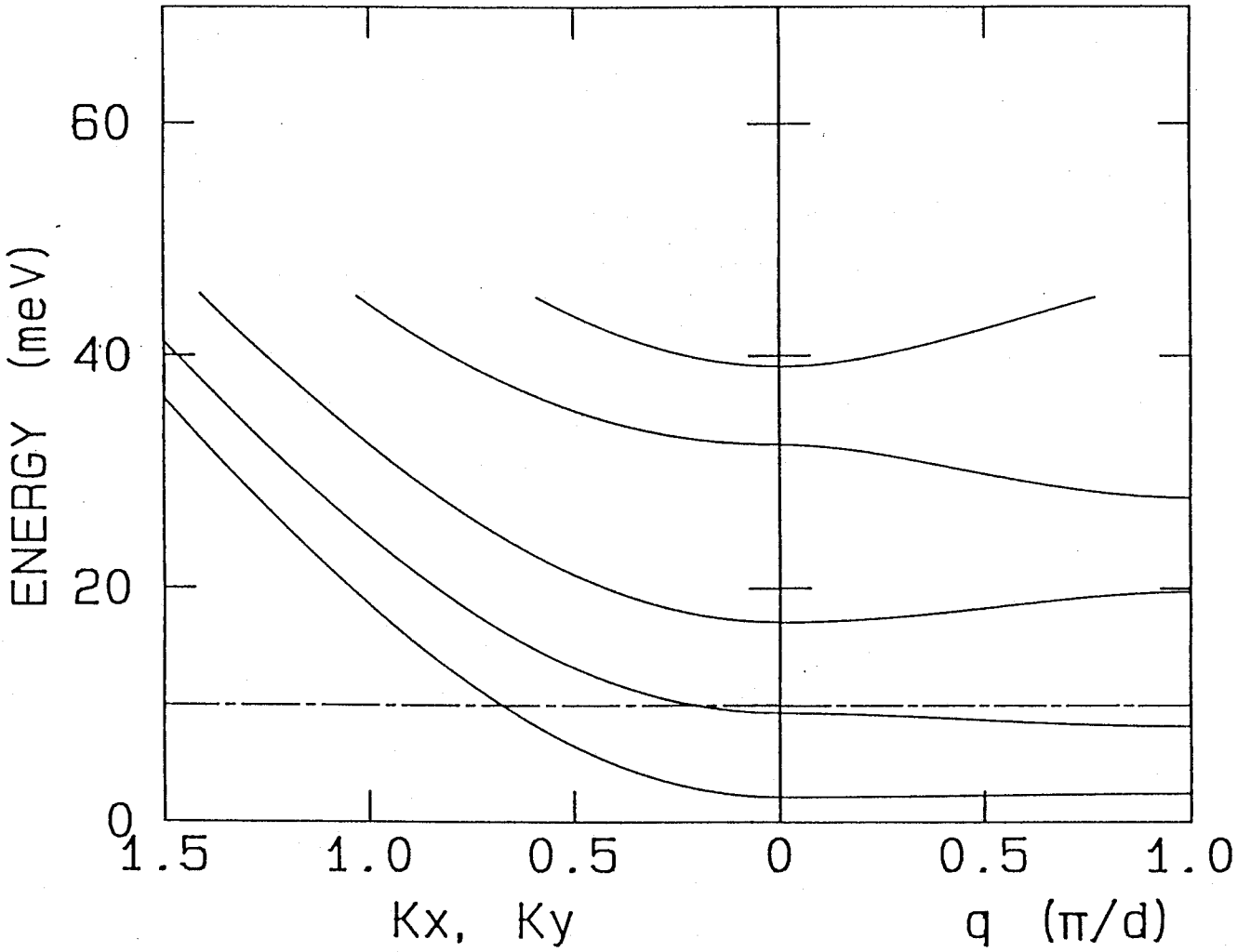

FIG. 7-2-8 Energy dispersion of the singlet valley for the sample #2(240Å/60Å) obtained from the envelope function approximation. The dashed and dotted line indicates the Fermi level.

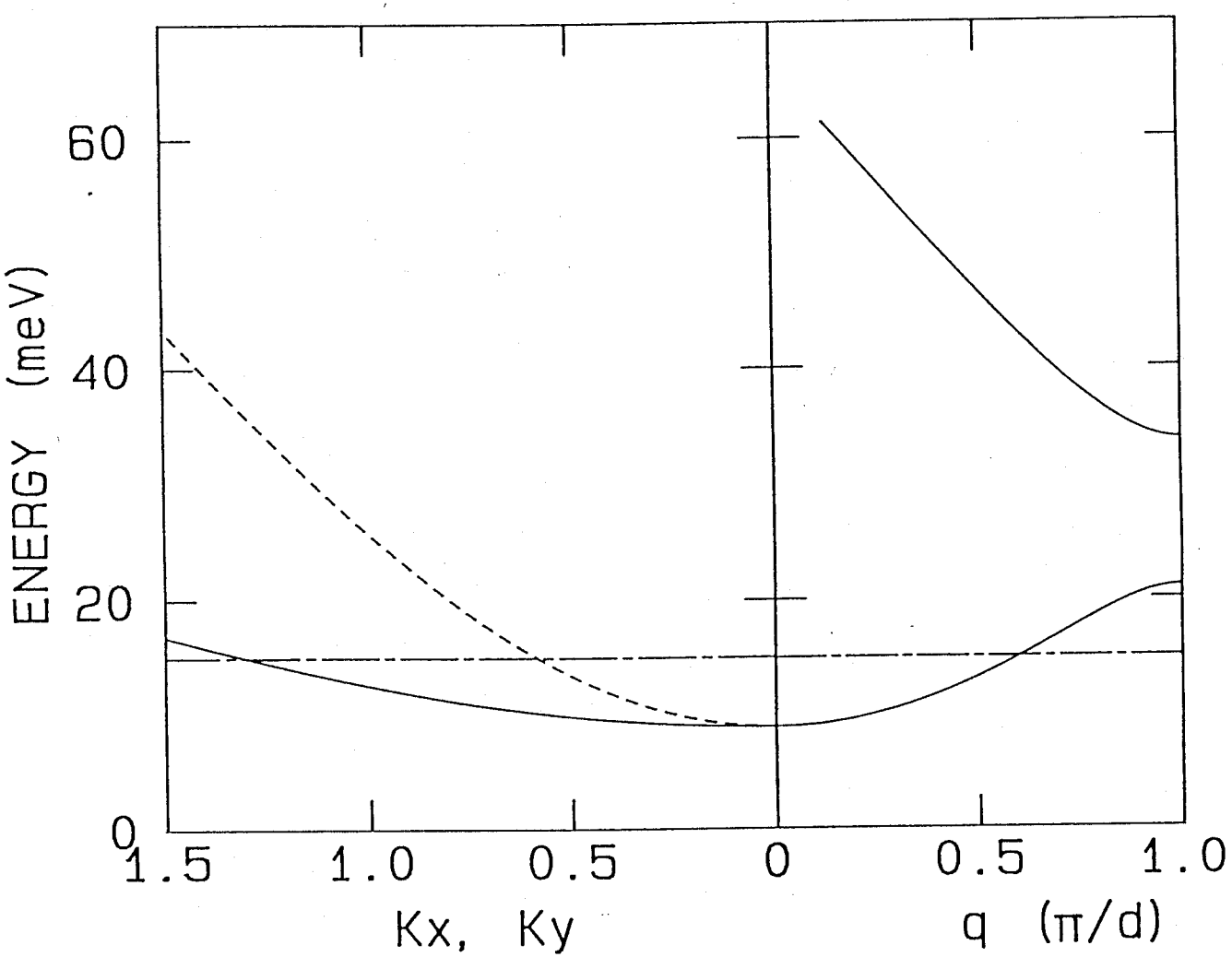

FIG. 7-2-9 Energy dispersion of the triplet valleys for the sample #2(240Å/60Å) obtained from the envelope function approximation. The dashed and dotted line indicates the Fermi level.

TABLE 7-2-1 Period of Shubnikov de-Haas and parameter obtained from the envelope function approximation for #2(240Å/60Å)

Valley and Sublevel	Δ(1/B) (T^{-1}) SdH	S_k(10^{-4}Å^{-2}) SdH	EFA center	EFA edge	n(×10^{16}cm^{-3}) HALL	EFA	Resonance Field(kG) CR	EFA center	EFA edge
Vs 1	0.67	1.4	1.57	1.53		2.6	8.1	8.0	8.1
Vs 2			0.14	0.36		0.4		8.4	7.9
Vt 1	0.33	2.9	2.61			2.5	16.2	17.4	
				total	11	10.7			

S_k:cross section of the Fermi surface at center:k_z=0, edge:k_z=π/D

§7-3 PbTe/$Pb_{1-x}Sn_xTe$ 260Å/150Å Superlattice(#3)

From the X-ray diffraction pattern(see Fig. 7-3-1), PbTe and $Pb_{1-x}Sn_xTe$ layer thicknesses, 260Å and 150Å are obtained. Total thickness is 5.48μm. Interdiffusion length is below 30Å. To determine more precise interdiffusion length, we must measure intensity of far satellites for the same reason in section 7-1. Tin composition profile are shown in Fig. 7-3-2 at interdiffusion length 30Å(worst case). Figure 7-3-3 shows energy diagram based on the model that the indium level is taken as the energy origin. In this case, the square well potential approximation is safely used. The carrier mobility of 220000 $cm^2/V\cdot s$ is very high. Figures 7-3-4 and 7-3-5 show the dependence of the magnetoplasma transmission spectra on magnetic field direction. The electrons belonging to the singlet and triplet valleys are 2-dimensional because magnetic field direction dependence is $1/\cos\theta$. Figure 7-3-6 shows resonance magnetic field versus magnetic field directions. The solid lines in Fig. 7-3-6 are calculated resonance magnetic field based on the envelope function approximation. Calculation are made by the same procedure in section 7-1. The caluculated carrier density and area of cross section of the Fermi surface well agree with measured ones as shown in Table 7-3-1. Calculated band parameters in calculation are given in Fig. 7-3-7. The energy dispersion curves are shown in Figs. 7-3-8 and 7-3-9. For the singlet valley, dispersion curves of the first, second, third, and forth subbands are almost constant for

q. Electrons in the singlet valley indicate 2-dimensional properties because the Fermi level is above the third subband(Kx=0,Ky=0) and the Fermi surfaces of these subbands are spheroidal. For the triplet valleys, the dispersion of the first subband is small. Since the Fermi level locate in the gap between the first and second subbands, the triplet valley's electrons act 2-dimensional electron.

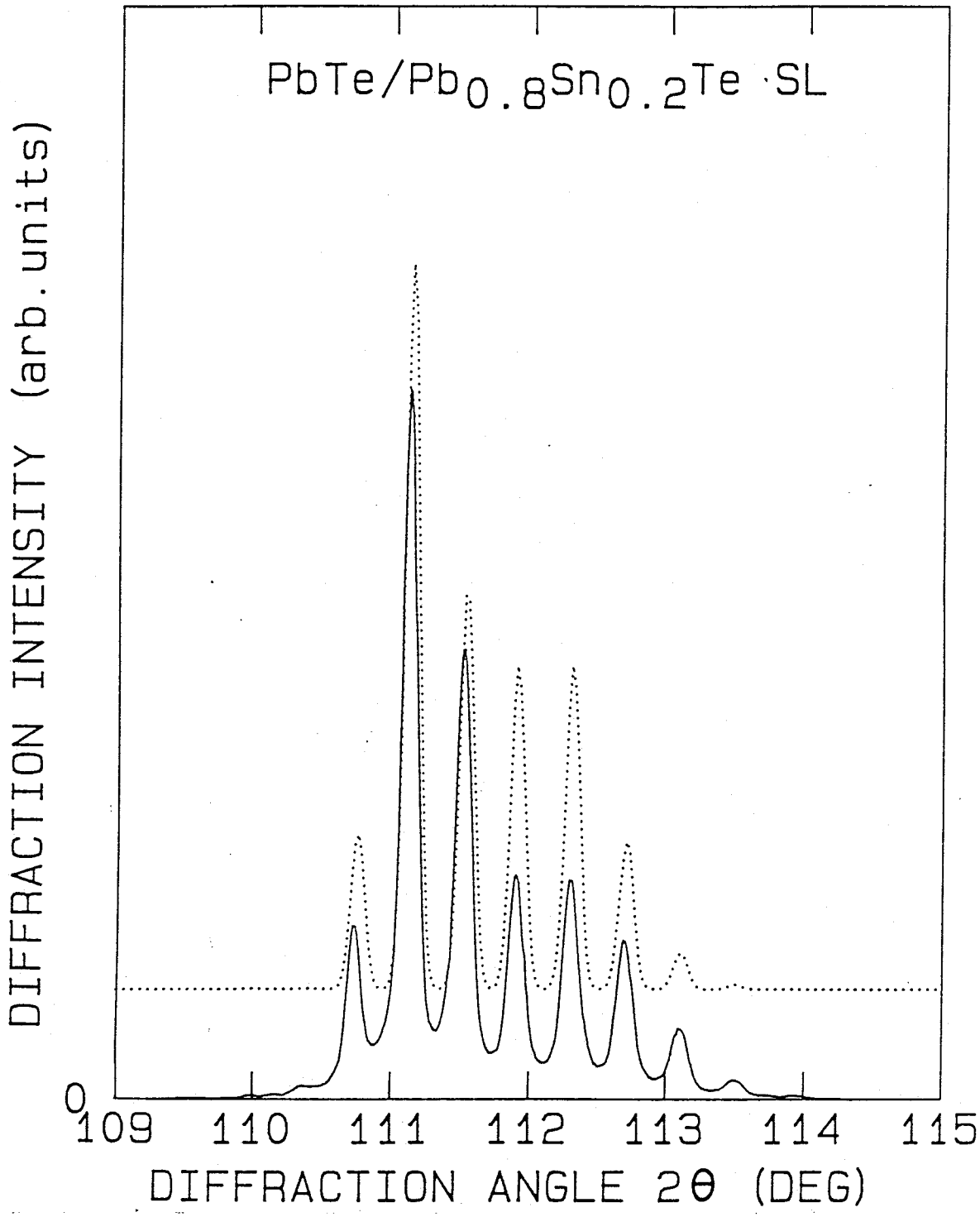

FIG. 7-3-1 Measured(solid line) and calculated(dotted line) X-ray diffraction patterns of the sample #3. Diffraction is around (444) reflection. From the calculation, the thicknesses of 260Å(70 PbTe layers) and 150Å(39 $Pb_{0.8}Sn_{0.2}Te$ layers) are obtained. The interdiffusion length is below 30Å.

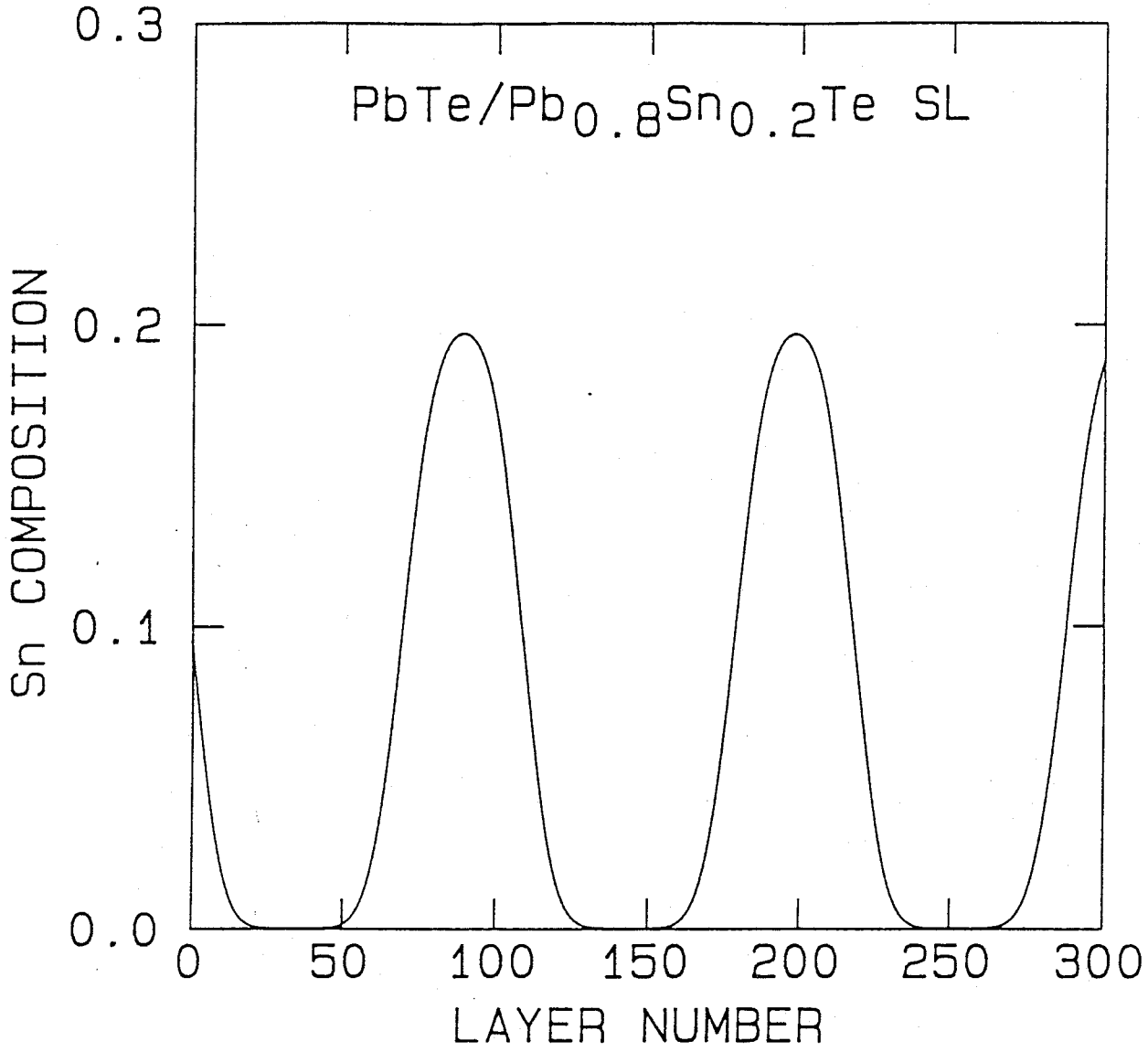

FIG. 7-3-2 Tin composition profile versus metallic atom layer numbers for the sample #3(260Å/150Å). The thickness of 100 molecular layers corresponds to 373Å.

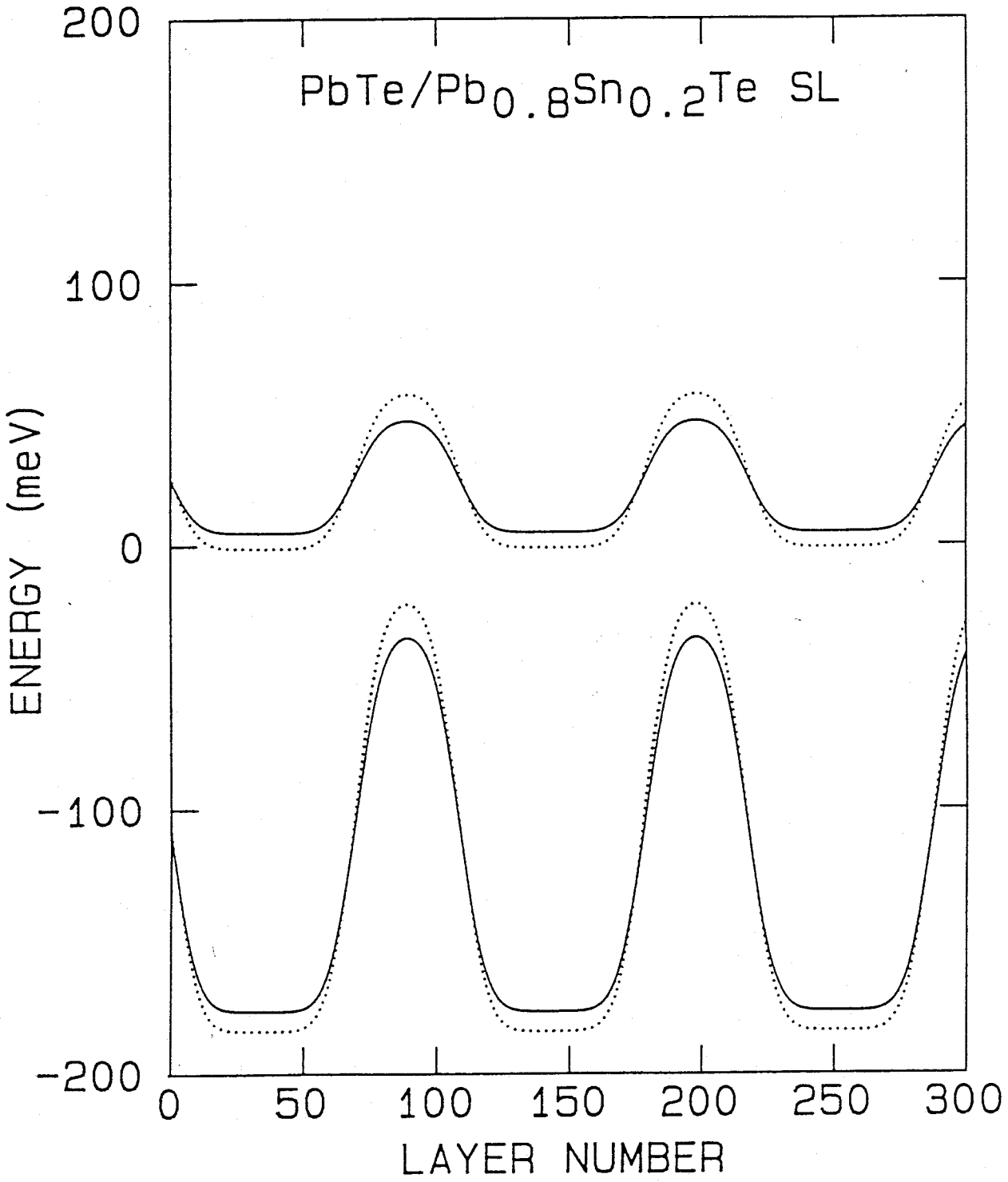

FIG. 7-3-3 Energy band diagrams of the singlet valley(solid lines) and triplet valleys(dotted lines) versus metallic atom layer numbers for the sample #3(260Å/150Å). The thickness of 100 molecular layers corresponds to 373Å. Energy bands shift by internal strain to accommodate the lattice mismatch between PbTe and $Pb_{0.8}Sn_{0.2}Te$ layers.

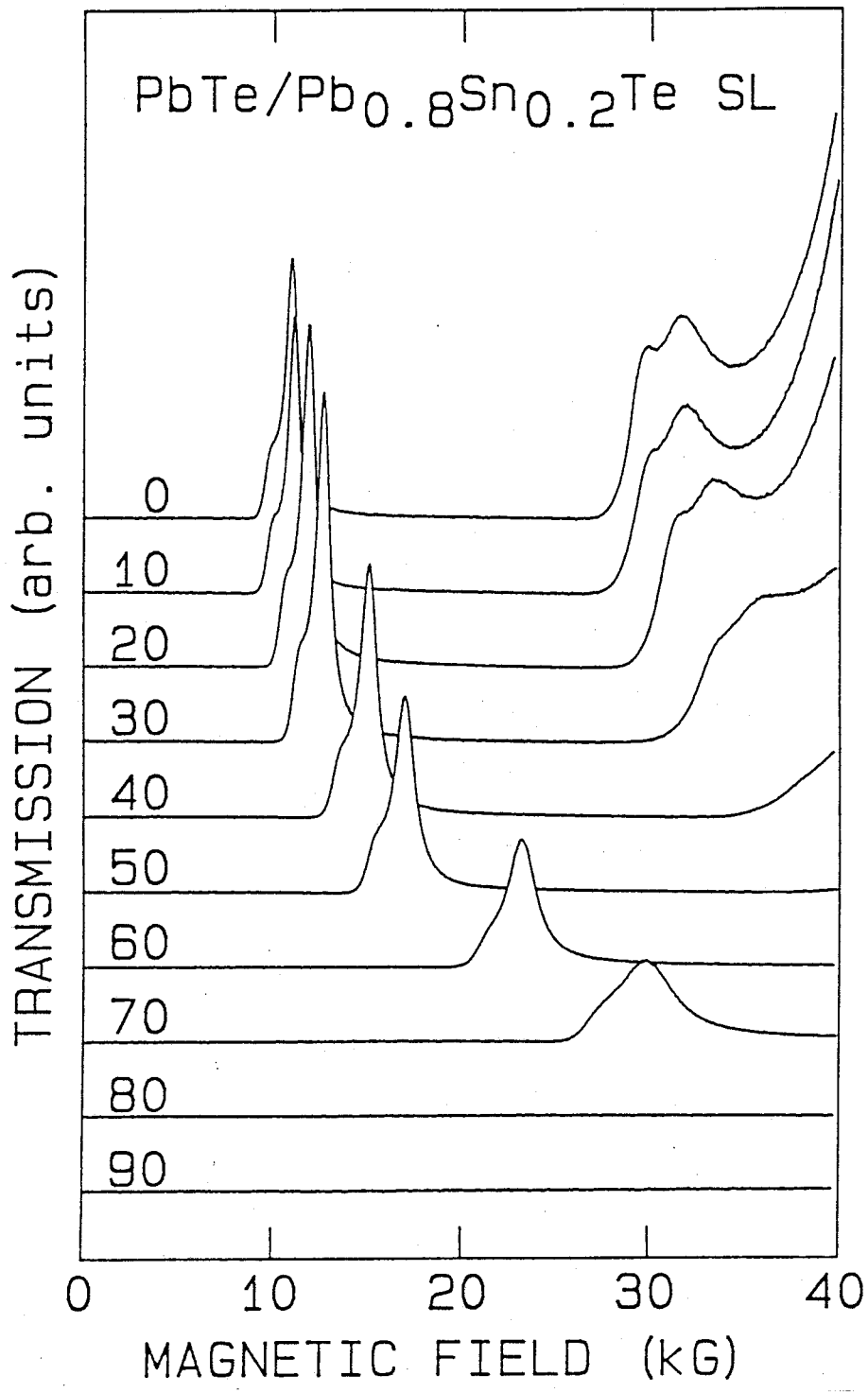

FIG. 7-3-4 Magnetoplasma transmission spectra with 337μm laser light at 4.2K for the sample #3(260Å/150Å). The magnetic field direction is changed from 0 deg along <111>(Faraday configuration) to 90 deg along <$\bar{1}\bar{1}$2>(Voigt configuration).

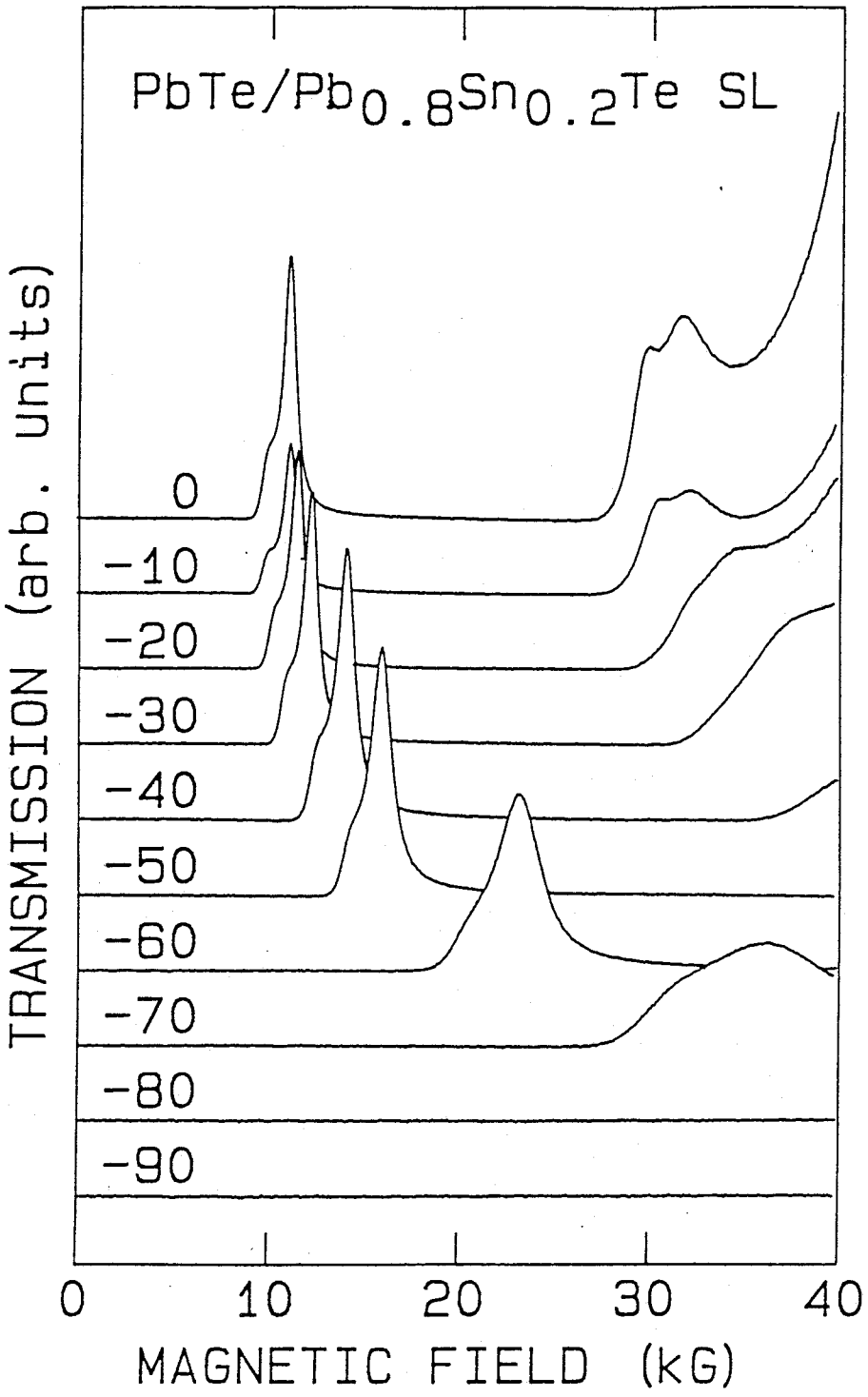

FIG. 7-3-5 Magnetoplasma transmission spectra with 337μm laser light at 4.2K for the sample #3(260Å/150Å). The magnetic field direction is changed from 0 deg along <111>(Faraday configuration) to at -90 deg along <11$\bar{2}$>(Voigt configuration).

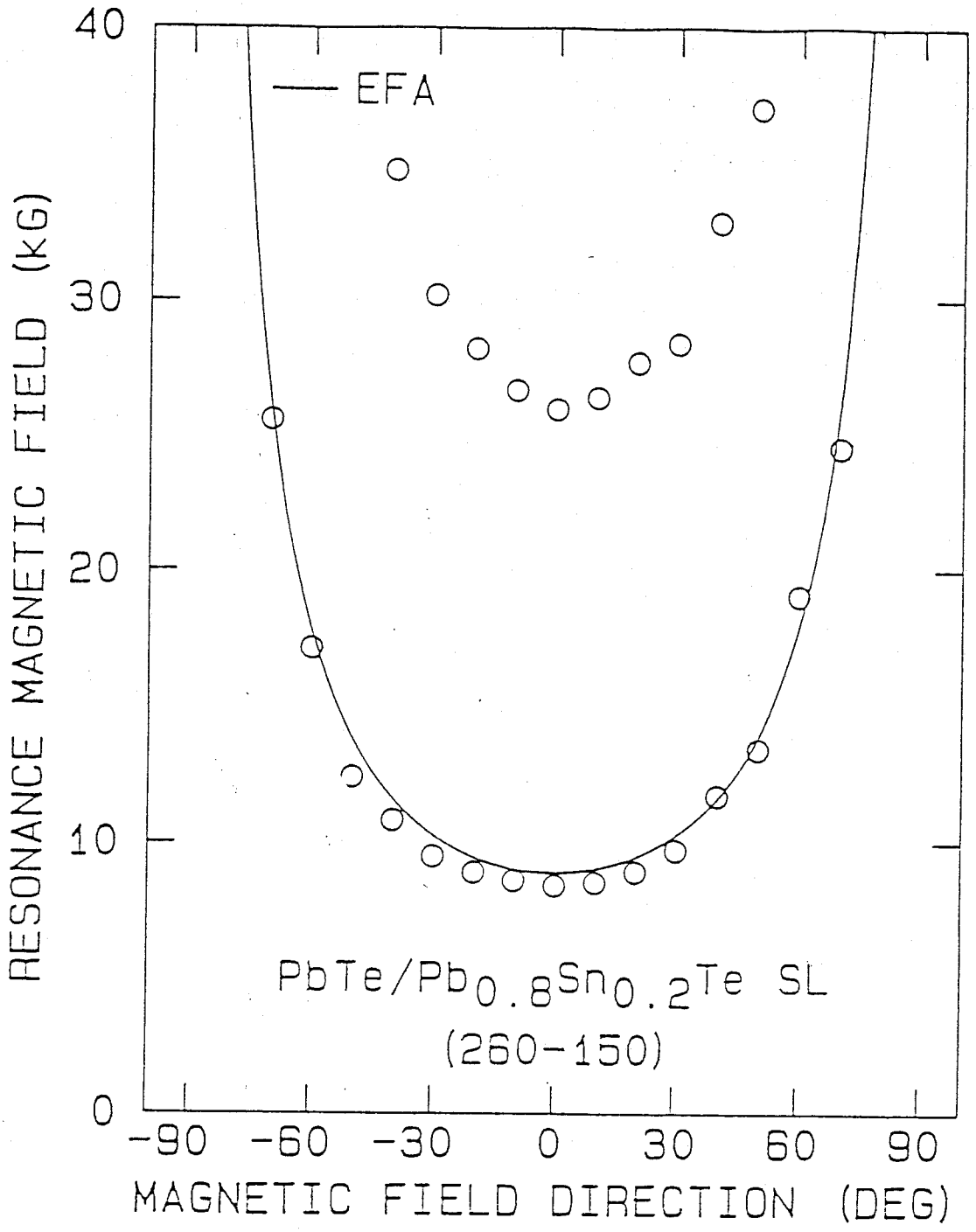

FIG. 7-3-6 Dip position as a function of the magnetic field direction for the sample #3(260Å/150Å). Solid lines are the cyclotron resonance field obtained from calculation based on the envelope function approximation.

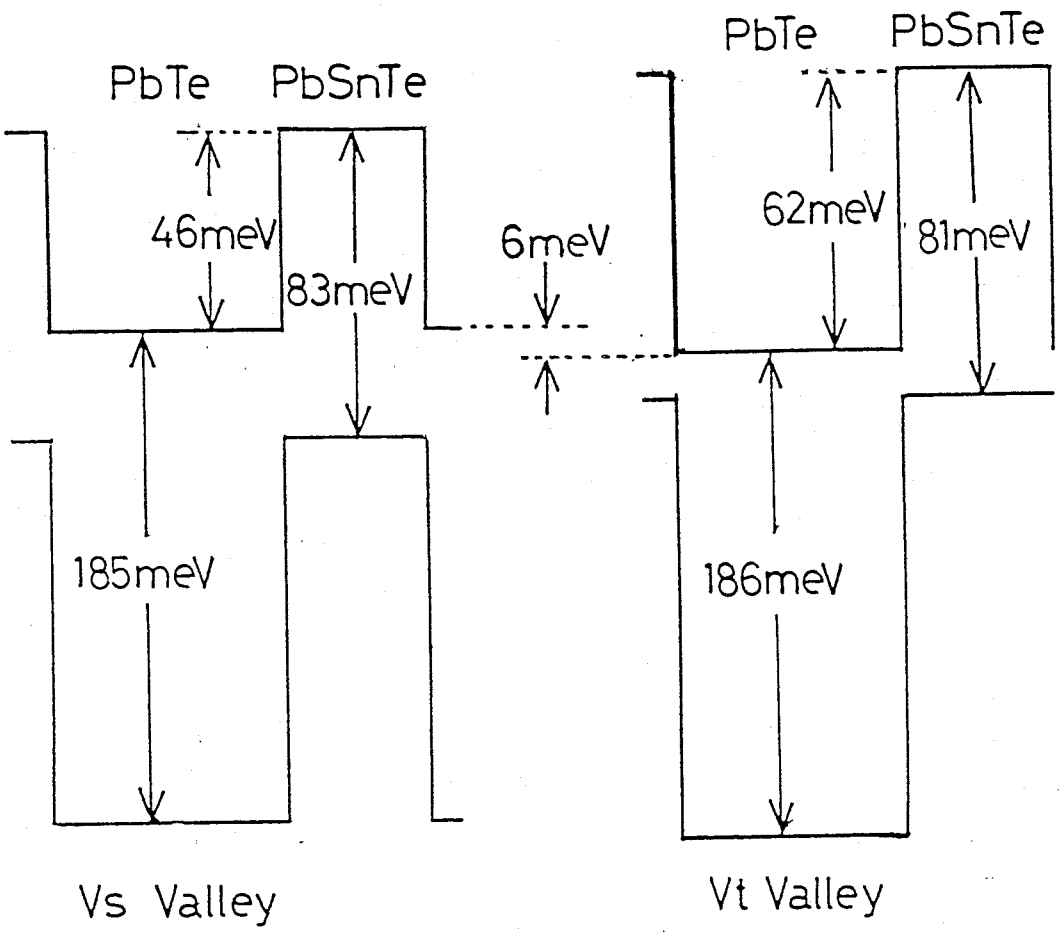

FIG. 7-3-7 Band parameters used in the calculation based on the envelope function approximation for the sample #3(260Å/150Å).

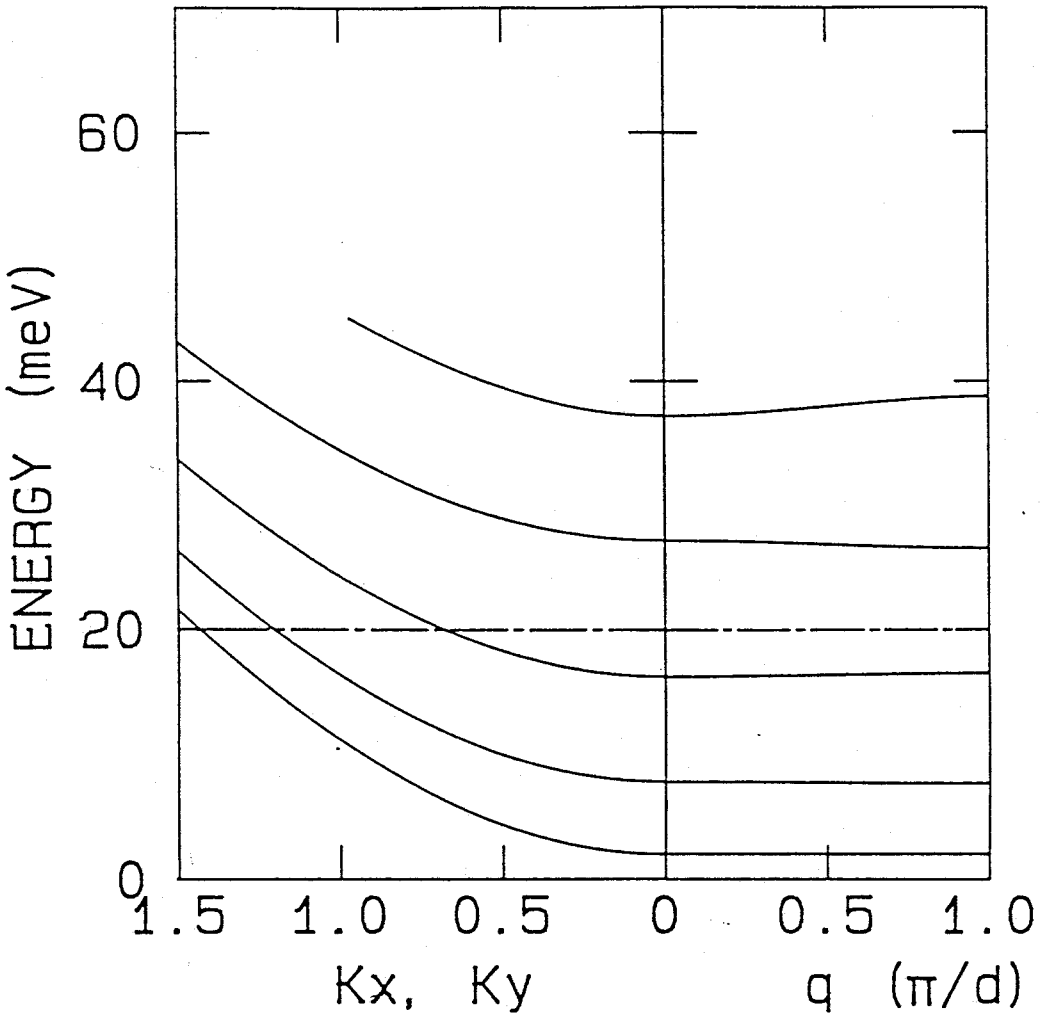

FIG. 7-3-8 Energy dispersion of the singlet valley for the sample #3(260Å/150Å) obtained from the envelope function approximation. The dashed and dotted line indicates the Fermi level.

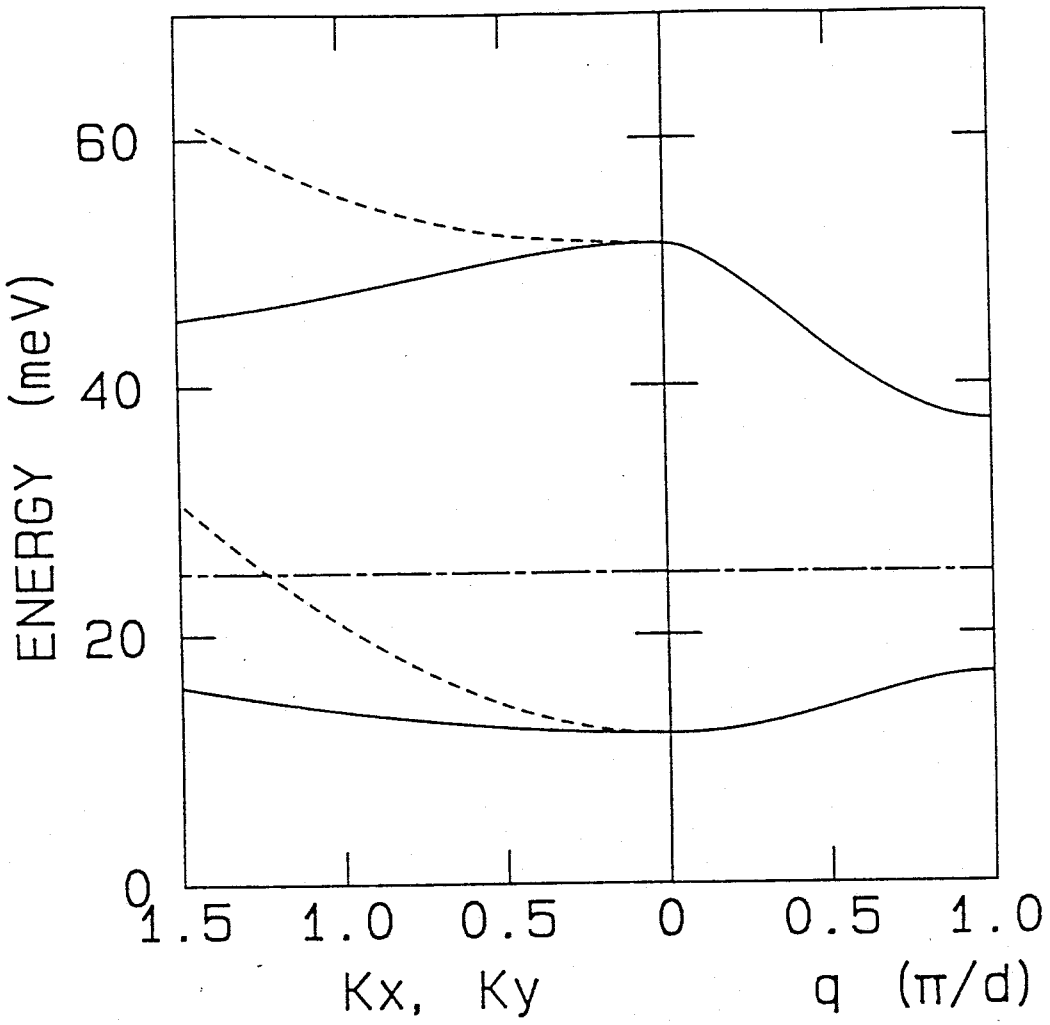

FIG. 7-3-9 Energy dispersion of the triplet valleys for the sample #3(260Å/150Å) obtained from the envelope function approximation. The dashed and dotted line indicates the Fermi level.

TABLE 7-3-1 Period of Shubnikov de-Haas and parameter obtained from the envelope function approximation for #3(260Å/150Å)

Valley and Sublevel	Δ(1/B) (T^{-1}) SdH	S_k(10^{-4}Å^{-2}) SdH	EFA center	EFA edge	n(×10^{16}cm^{-3}) HALL	EFA	Resonance Field(kG) CR	EFA center	EFA edge
Vs 1	0.25	3.8	3.78	3.78		4.7	8.42	8.8	9.0
Vs 2	0.33	2.9	2.67	2.67		3.3		8.9	8.8
Vs 3	0.75	1.3	0.85	0.82		1.0		8.8	8.8
Vt 1	0.11	8.6	8.61			10.0	26.0	28.4	28.8
	0.81	11.7							
				total	39	39.1			

S_k:cross section of the Fermi surface at center:k_z=0, edge:k_z=π/D

§7-4 PbTe/$Pb_{1-x}Sn_xTe$ 220Å/220Å Superlattice(#4)

PbTe and $Pb_{1-x}Sn_xTe$ layer thicknesses, 220Å and 220Å are obtained to reproduce the measured X-ray diffraction pattern(see Fig. 7-4-1). Total thickness is 4.32μm. Interdiffusion length is below 10Å. To measure more precise interdiffusion length, we must detect intensity of further satellites because of the same reason in section 7-1. But they are too weak to measure. Figure 7-4-2 shows Sn composition profile at interdiffusion length 30Å(worst case). Carrier concentration could not be determined probably due to coexistence of two types of carriers. Figure 7-4-3 shows energy diagram based on the model that the indium level is taken as the energy origin. In this case, the square well potential approximation is safe. Figures 7-4-4 and 7-4-5 show the dependence of the magnetoplasma transmission spectra on magnetic field direction. The electrons belonging to the singlet and triplet valleys are 2-dimensional. The envelope function calculation was not carried out because the carrier density and the cross section area of the Fermi surface due to existence of two type of carriers(n/p). But analysis of section 7-3 suggests that calculated dispersion curve in this superlattice should be almost constant as a function of q.

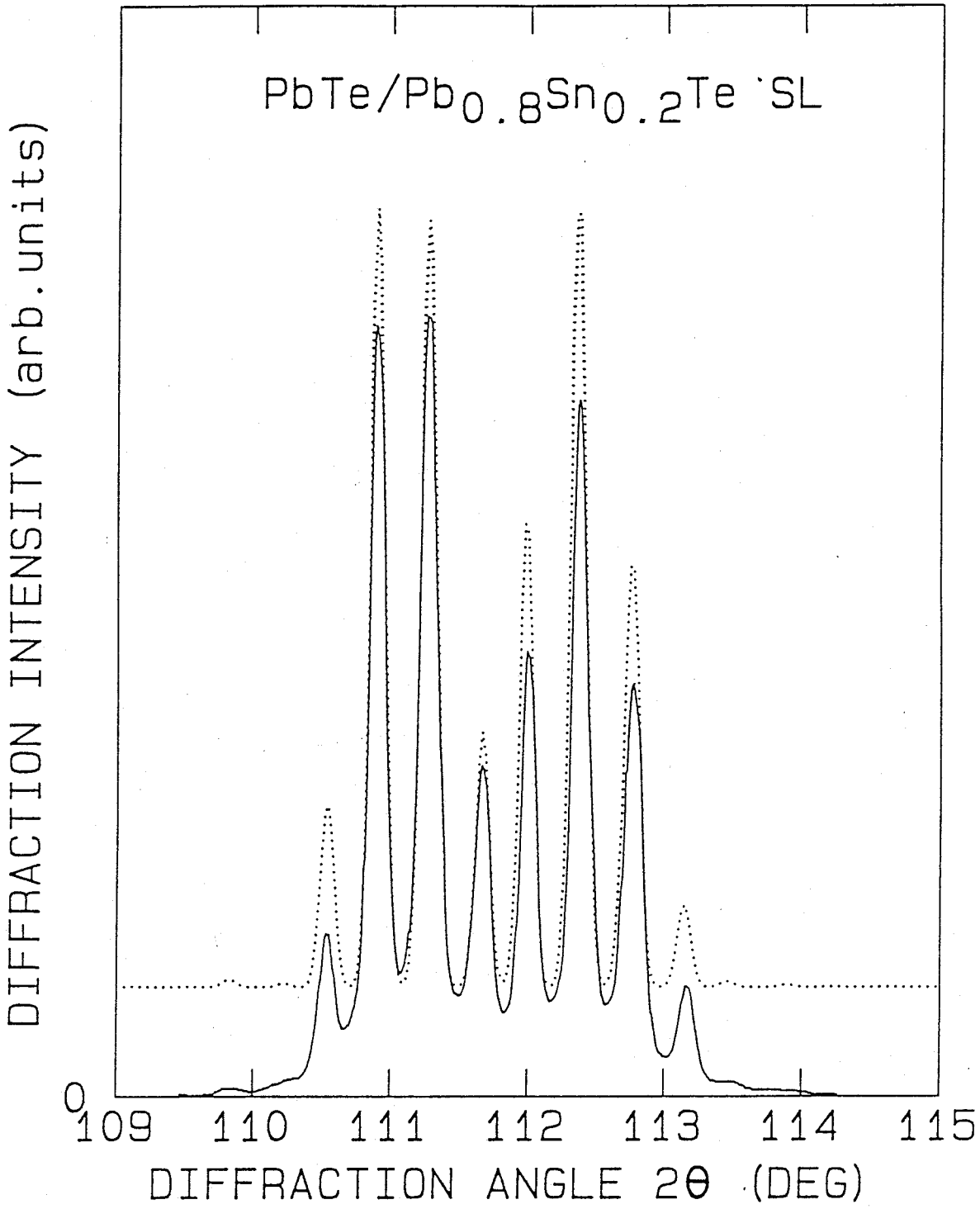

FIG. 7-4-1 Measured(solid line) and calculated(dotted line) X-ray diffraction patterns of the sample #4. Diffraction is around (444) reflection. From the calculation, the thicknesses of 220Å(58 PbTe layers) and 220Å(58 $Pb_{0.8}Sn_{0.2}Te$ layers) are obtained. The interdiffusion length is below 10Å.

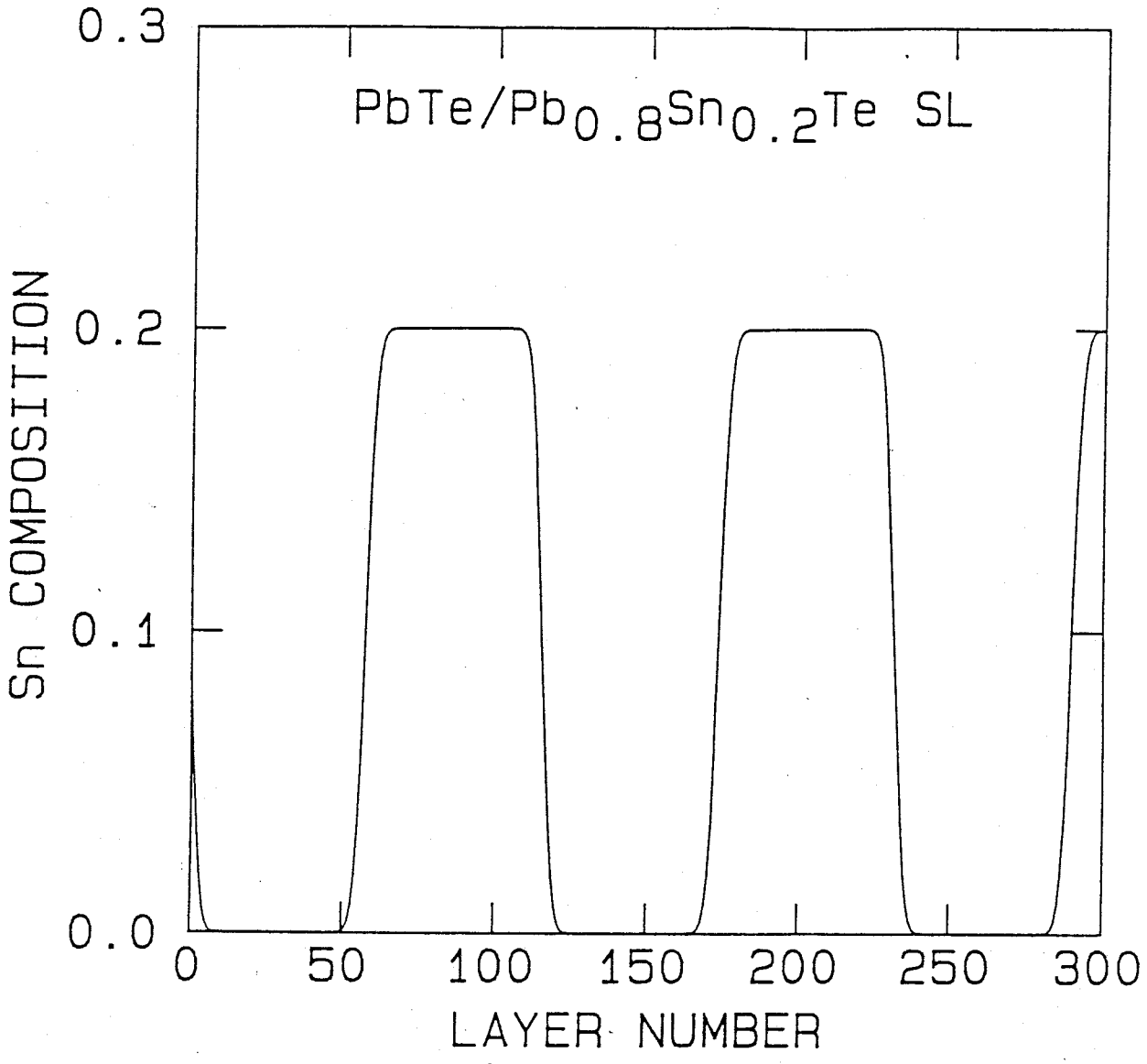

FIG. 7-4-2 Tin composition profile versus metallic atom layer numbers for the sample #4(220Å/220Å). The thickness of 100 molecular layers corresponds to 373Å.

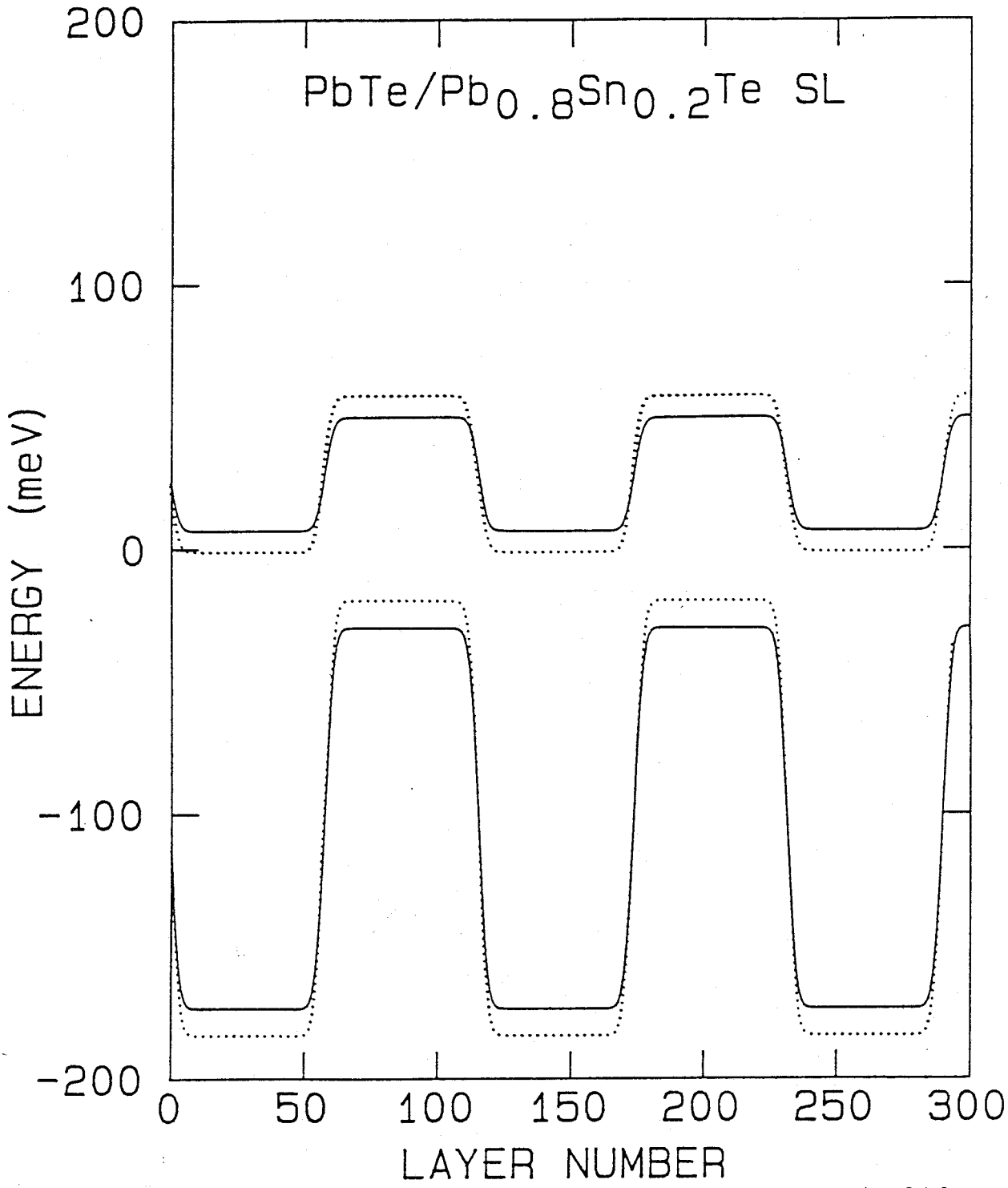

FIG. 7-4-3 Energy band diagrams of the singlet valley(solid lines) and triplet valleys(dotted lines) versus metallic atom layer numbers for the sample #4(220Å/220Å). The thickness of 100 molecular layers corresponds to 373Å. Energy bands shift by internal strain to accommodate the lattice mismatch between PbTe and $Pb_{0.8}Sn_{0.2}Te$ layers.

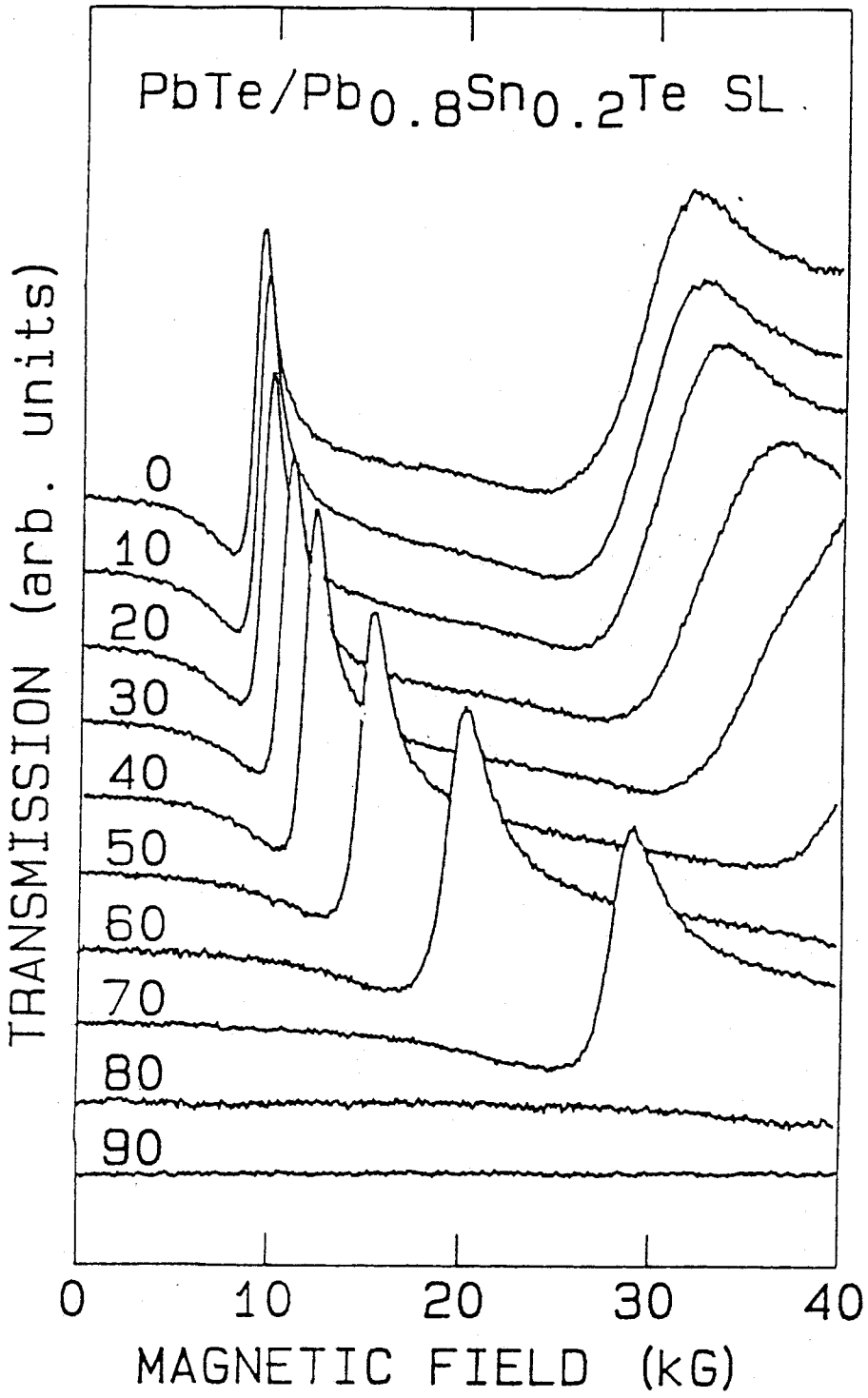

FIG. 7-4-4 Magnetoplasma transmission spectra with 337μm laser light at 4.2K for the sample #4(220Å/220Å). The magnetic field direction is changed from 0 deg along <111>(Faraday configuration) to 90 deg along <$\bar{1}\bar{1}$2>(Voigt configuration).

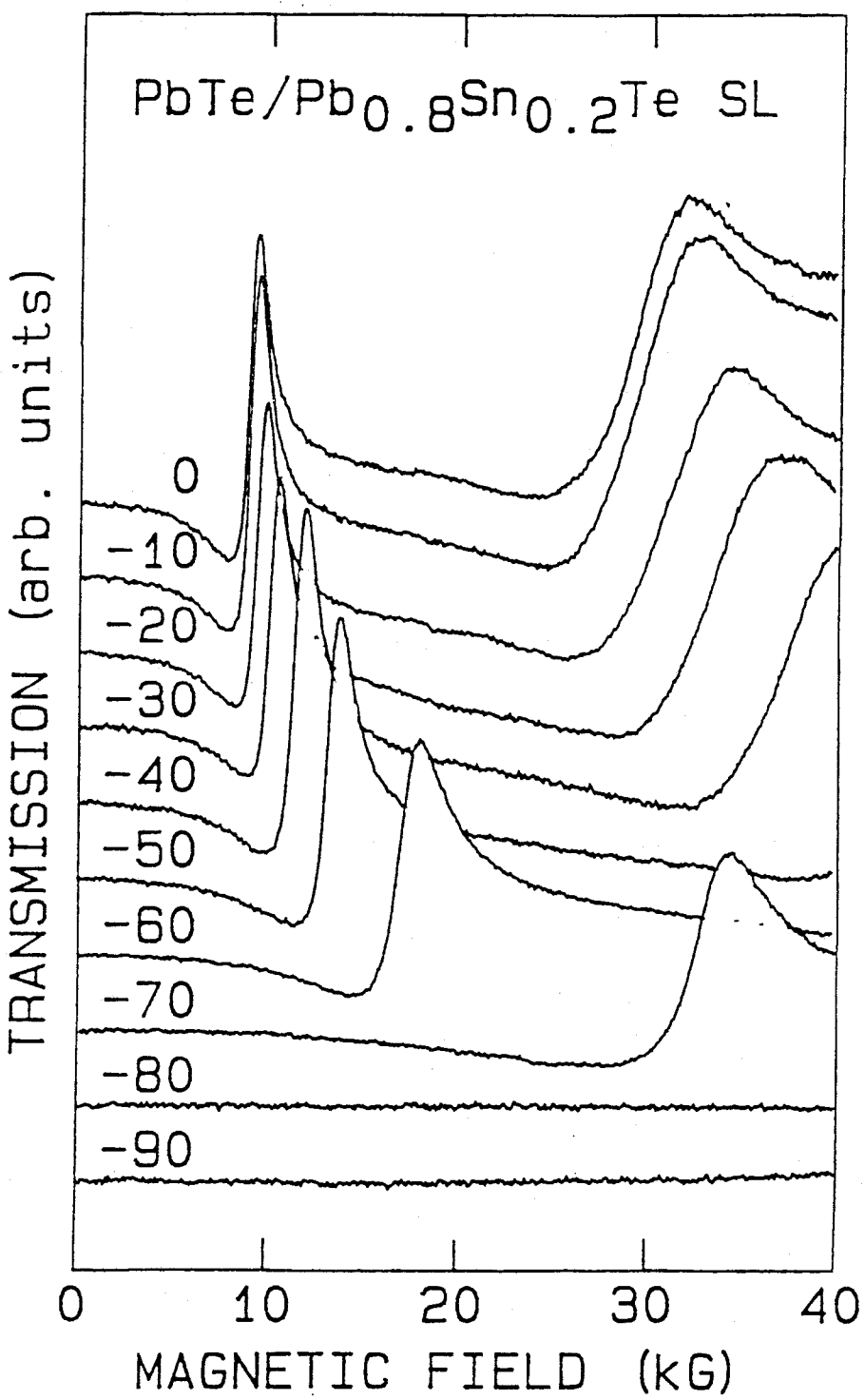

FIG. 7-4-5 Magnetoplasma transmission spectra with 337μm laser light at 4.2K for the sample 8603065A(220Å/220Å). The magnetic field direction is changed from 0 deg along <111>(Faraday configuration) to -90 deg along <11$\bar{2}$>(Voigt configuration).

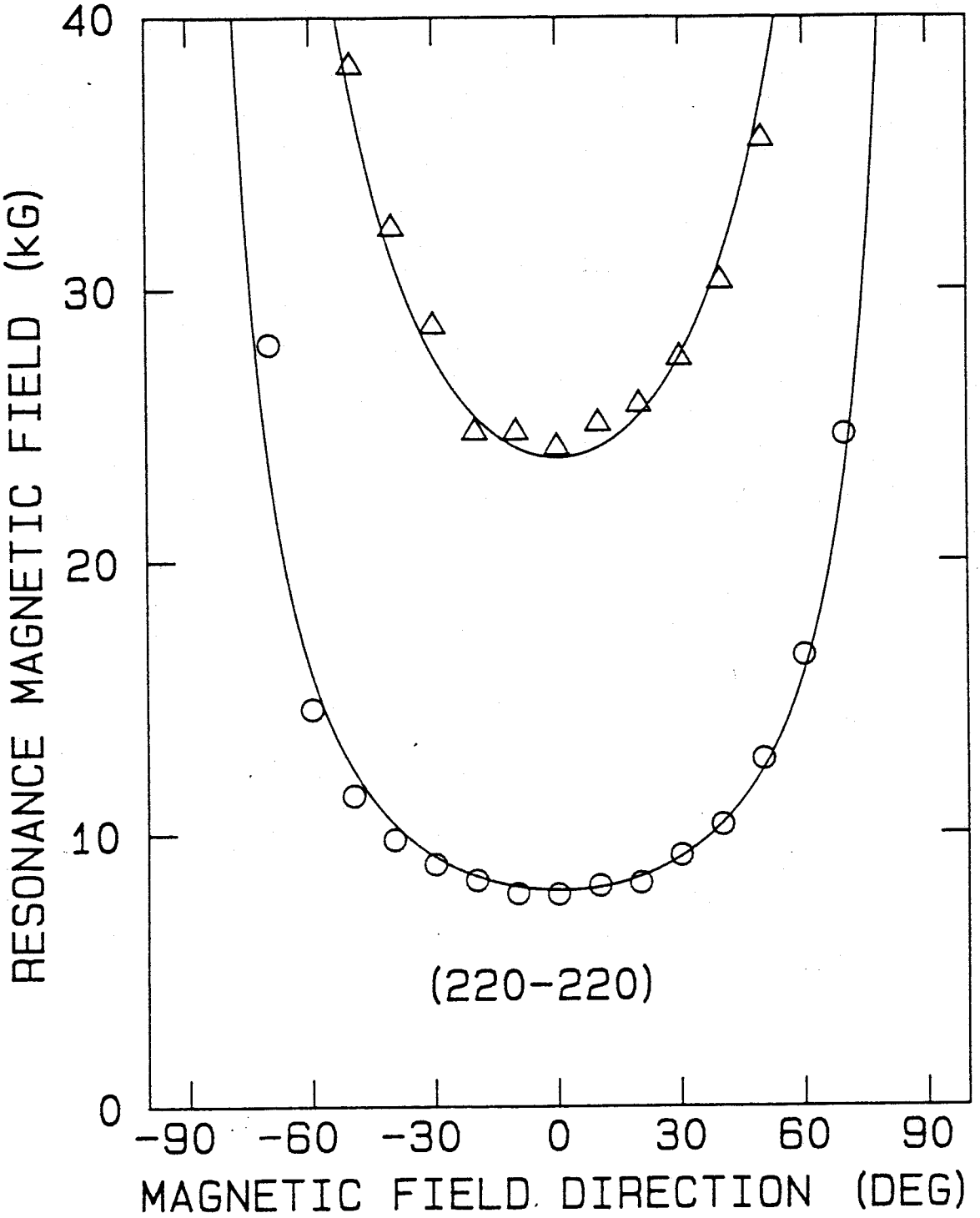

FIG. 7-4-6 Dip position as a function of the magnetic field direction for the sample #4(220Å/220Å). Solid lines are the cyclotron resonance field having $1/\cos(\theta)$.

§7-5 PbTe/$Pb_{1-x}Sn_xTe$ 300Å/190Å Superlattice(#5)

From the X-ray diffraction pattern(see Fig. 7-5-1), PbTe and $Pb_{1-x}Sn_xTe$ layer thicknesses, 300Å and 190Å are obtained. Total thickness is 4.84μm. Interdiffusion length is very large 95Å. Sn composition profile at interdiffusion length 95Å. Figure 7-5-3 shows energy diagram based on the model that indium level are taken as the energy origin. The carrier mobility of 130000 $cm^2/V\cdot s$ is very high. Figures 7-5-4 and 7-5-5 show the dependence of the magnetoplasma transmission spectra on magnetic field direction. The electrons belonging to the triplet valleys are 2-dimensional. but the electrons belonging to the singlet valley are divided into 2-dimensional and 3-dimensional one. This difference comes from large interdiffusion. Large interdiffusion makes the potential shallow, where higher subbands have large dispersion. Internal strain due to lattice mismatch between PbTe and $Pb_{0.8}Sn_{0.2}Te$ layers decreases potential deference(compare solid line and dotted line in Fig. 7-5-6). Thus, for the singlet valley, the first subband Fermi surface is cylindrical but second subband is spheroidal. For the triplet valleys only electrons belonging to the first subband exist and its Fermi surface is cylindrical. The envelope function calculation was not carried out. In this case, equations for obtaining the energy dispersion curve are differential ones. It is interesting physically to calculate the interdiffusion dependence of subband dispersion.

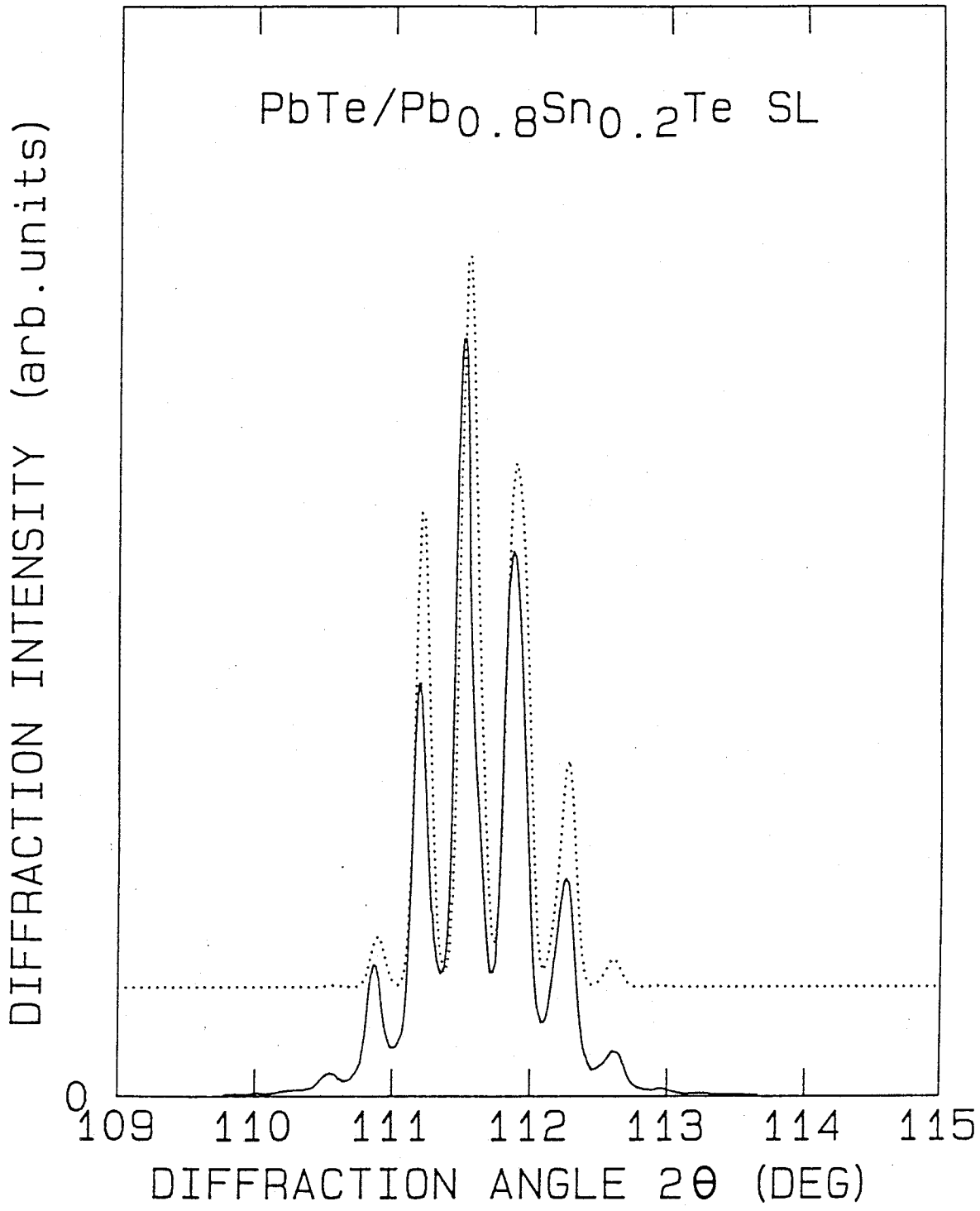

FIG. 7-5-1 Measured(solid line) and calculated(dotted line) X-ray diffraction patterns of the sample #5. Diffraction is around (444) reflection. From the calculation, the thicknesses of 300Å(80 PbTe layers) and 190Å(50 $Pb_{0.8}Sn_{0.2}Te$ layers) are obtained. The interdiffusion length is 95Å.

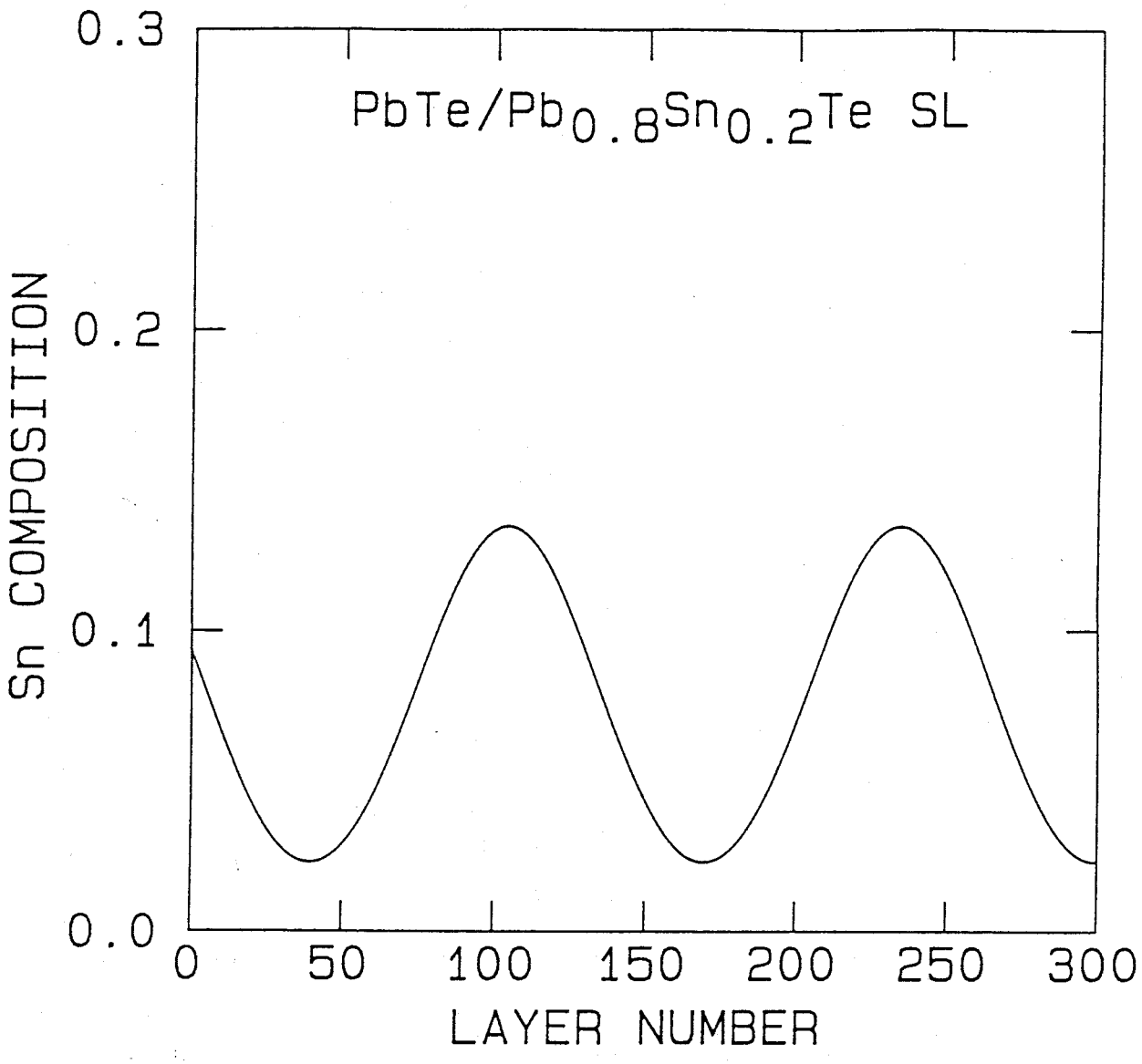

FIG. 7-5-2 Tin composition profile versus metallic atom layer numbers for the sample #5(300Å/190Å). The thickness of 100 molecular layers corresponds to 373Å.

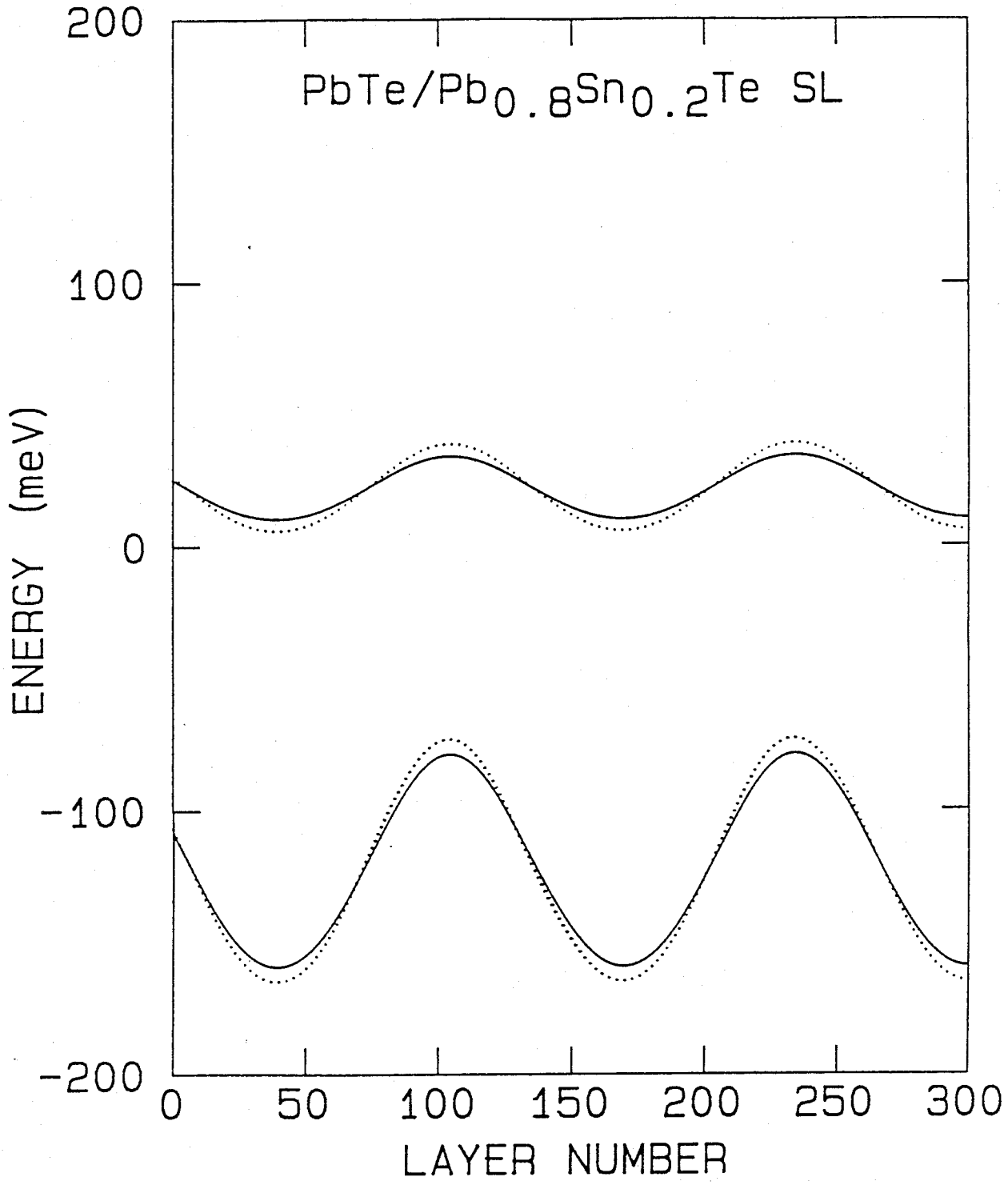

FIG. 7-5-3 Energy band diagrams of the singlet valley(solid lines) and triplet valleys(dotted lines) versus metallic atom layer numbers for the sample #5(300Å/190Å). The thickness of 100 molecular layers corresponds to 373Å. Energy bands shift by internal strain to accommodate the lattice mismatch between PbTe and $Pb_{0.8}Sn_{0.2}Te$ layers.

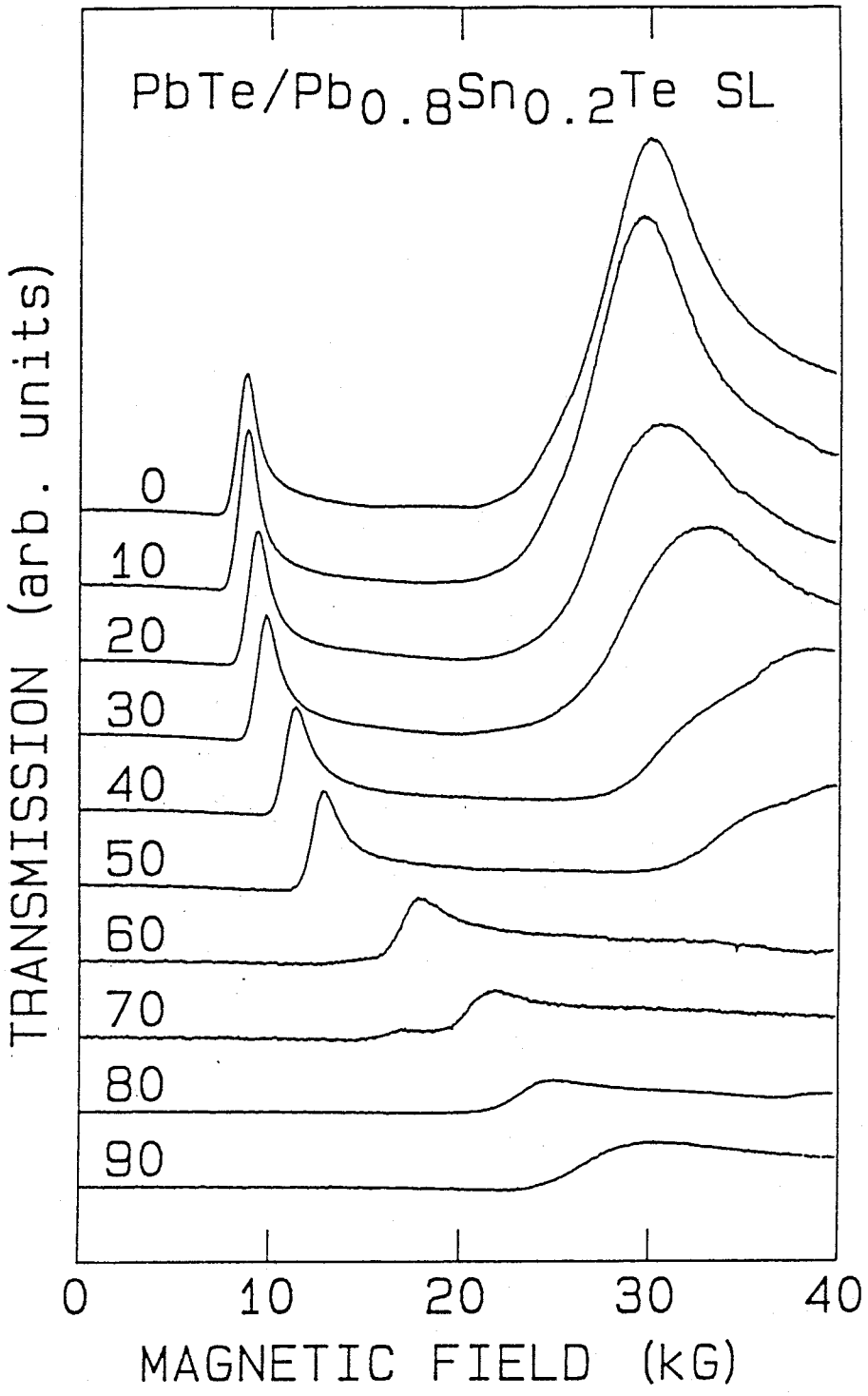

FIG. 7-5-4 Magnetoplasma transmission spectra with 337μm laser light at 4.2K for the sample #5(300Å/190Å). The magnetic field direction is changed from 0 deg along <111>(Faraday configuration) to 90 deg along <$\bar{1}\bar{1}$2>(Voigt configuration).

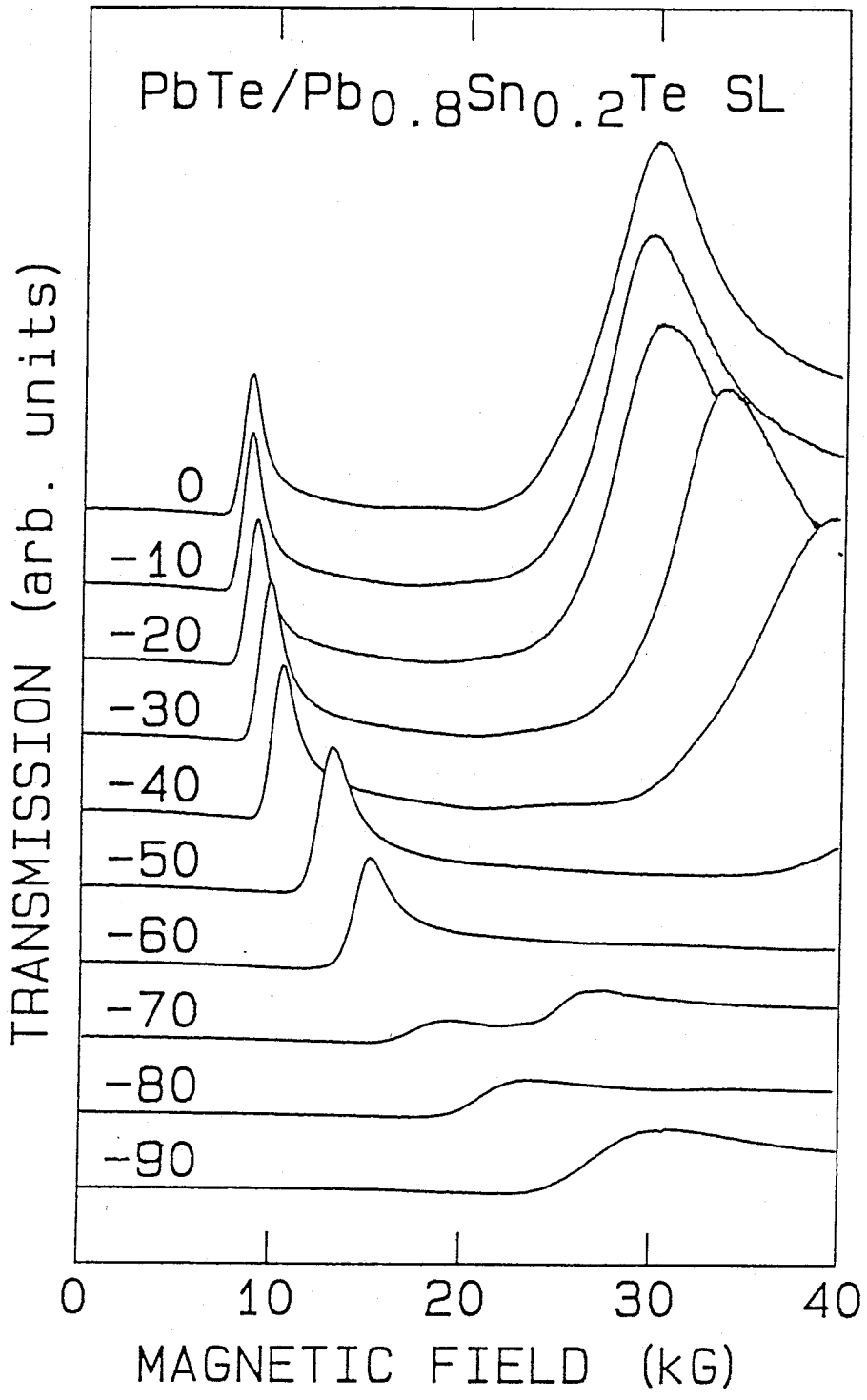

FIG. 7-5-5 Magnetoplasma transmission spectra with 337μm laser light at 4.2K for the sample #5(300Å/190Å). The magnetic field direction is changed from 0 deg along <111>(Faraday configuration) to at -90 deg along <11$\bar{2}$>(Voigt configuration).

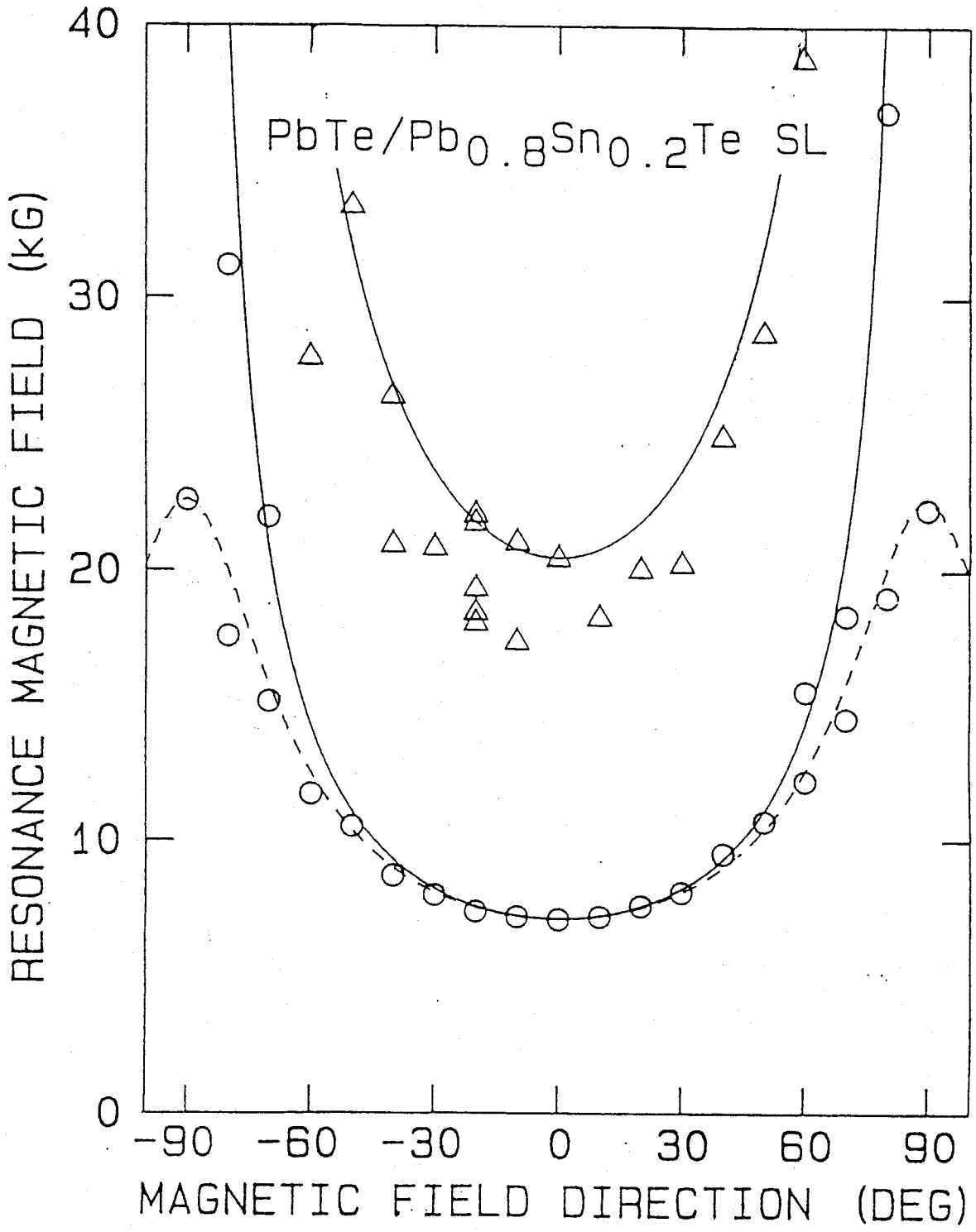

FIG. 7-5-6 Dip position as a function of the magnetic field direction for the sample #5(300Å/190Å). Solid lines are the cyclotron resonance field obtained from calculation based on the usual bulk Fermi surface.

§7-6 PbTe/$Pb_{1-x}Sn_xTe$ 180Å/231Å Superlattice(#6)

From the X-ray diffraction pattern(see Fig. 7-5-1), PbTe and $Pb_{1-x}Sn_xTe$ layer thicknesses, 180Å and 231Å are obtained. Total thickness is 4.32μm. Interdiffusion length is 70Å. Figure 7-6-2 shows Sn composition profile at interdiffusion length 70Å. Figure 7-4-3 shows energy diagram based on the model that indium level are taken as the energy origin. Figures 7-4-4 and 7-4-5 show the dependence of the magnetoplasma transmission spectra on magnetic field direction. In Voigt configuration(at 90 and -90 degree), transmission spectra is constant, so the electrons belonging to the singlet and triplet valleys are 2-dimensional. Comparing with the superlattice 180Å/231Å(in the previous section), low carrier density and small interdiffusion are the reason why 3-dimensional carrier can not be observed. The envelope function calculation was not carried out because of the same reason in section 7-5.

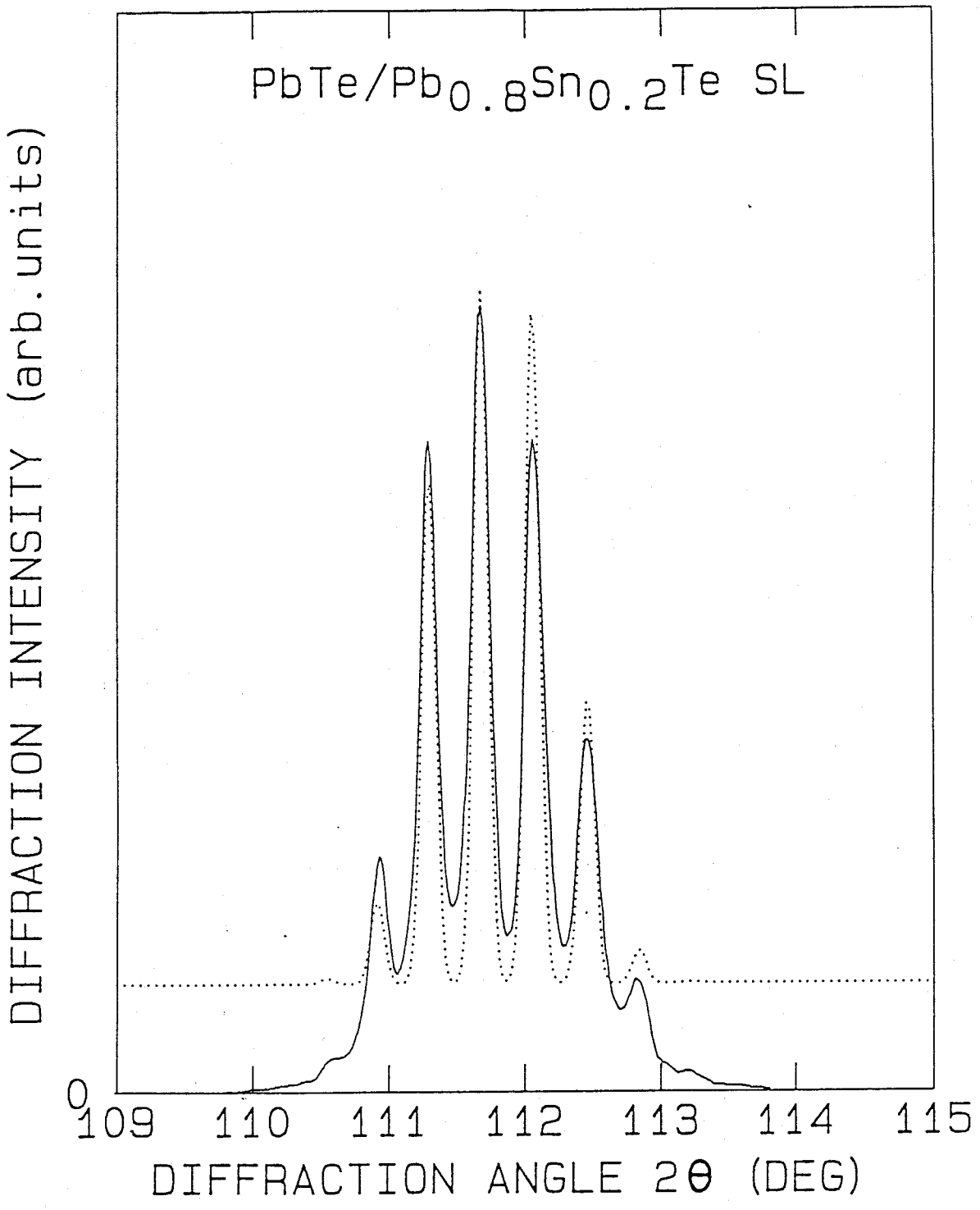

FIG. 7-6-1 Measured(solid line) and calculated(dotted line) X-ray diffraction patterns of the sample #6. Diffraction is around (444) reflection. From the calculation, the thicknesses of 180Å(48 PbTe layers) and 231Å(62 $Pb_{0.8}Sn_{0.2}Te$ layers) are obtained. The interdiffusion length is 70Å.

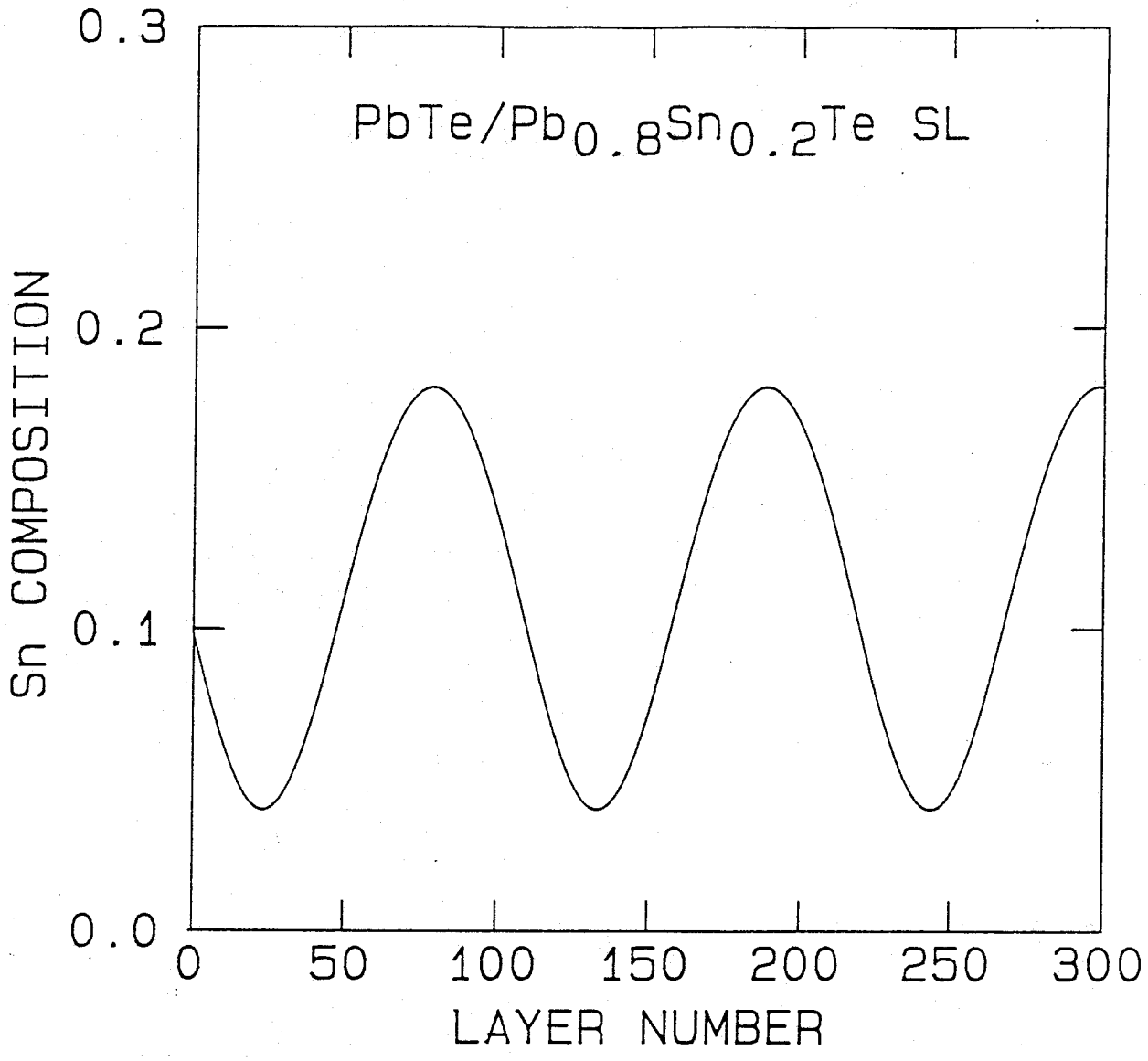

FIG. 7-6-2 Tin composition profile versus metallic atom layer numbers for the sample #6(180Å/231Å). The thickness of 100 molecular layers corresponds to 373Å.

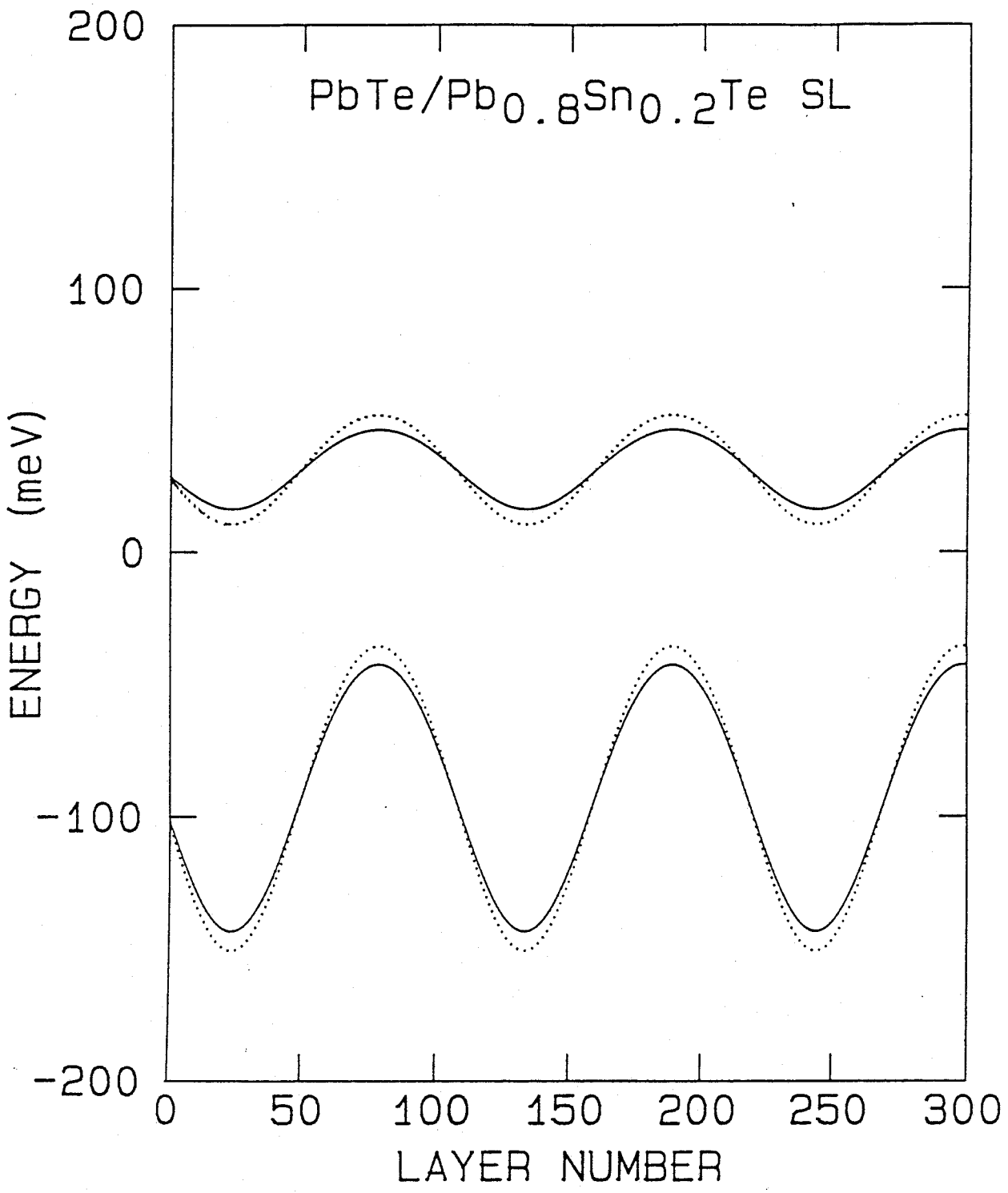

FIG. 7-6-3 Energy band diagrams of the singlet valley(solid lines) and triplet valleys(dotted lines) versus metallic atom layer numbers for the sample #6(180Å/231Å). The thickness of 100 molecular layers corresponds to 373Å. Energy bands shift by internal strain to accommodate the lattice mismatch between PbTe and $Pb_{0.8}Sn_{0.2}Te$ layers.

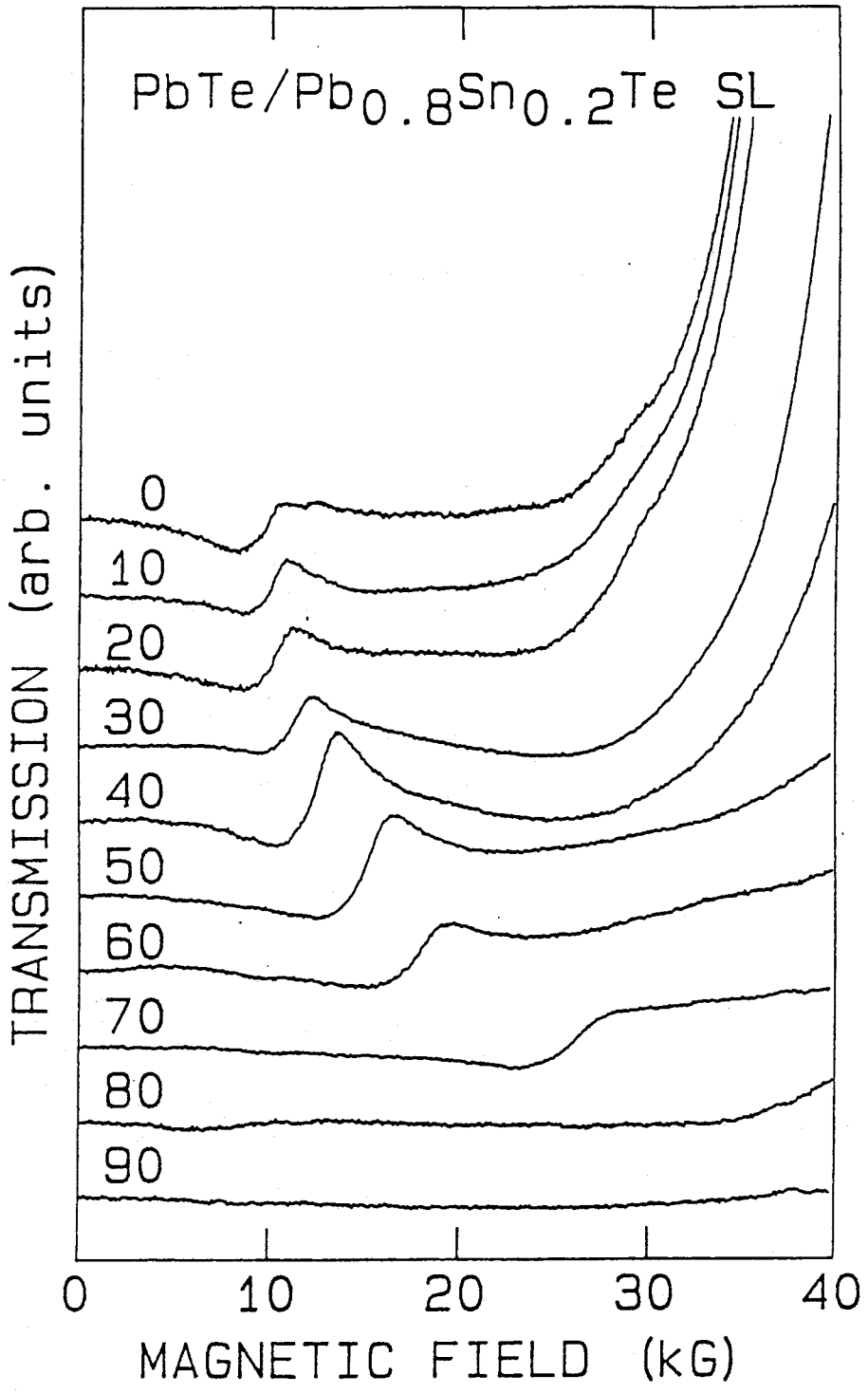

FIG. 7-6-4 Magnetoplasma transmission spectra with 337μm laser light at 4.2K for the sample #6(180Å/231Å). The magnetic field direction is changed from 0 deg along <111>(Faraday configuration) to 90 deg along <$\bar{1}\bar{1}$2>(Voigt configuration).

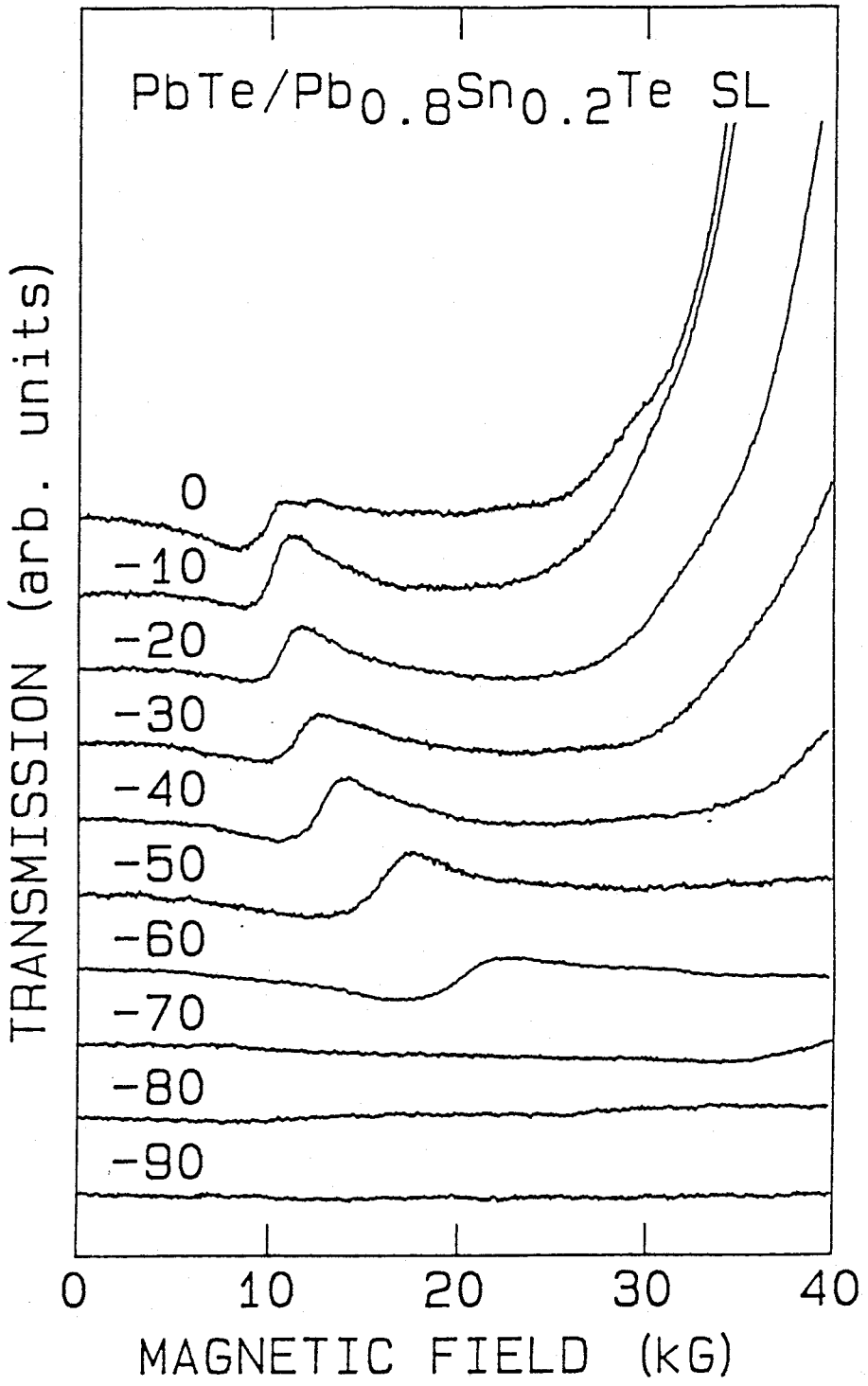

FIG. 7-6-5 Magnetoplasma transmission spectra with 337μm laser light at 4.2K for the sample #6(180Å/231Å). The magnetic field direction is changed from 0 deg along <111>(Faraday configuration) to -90 deg along <11$\bar{2}$>(Voigt configuration).

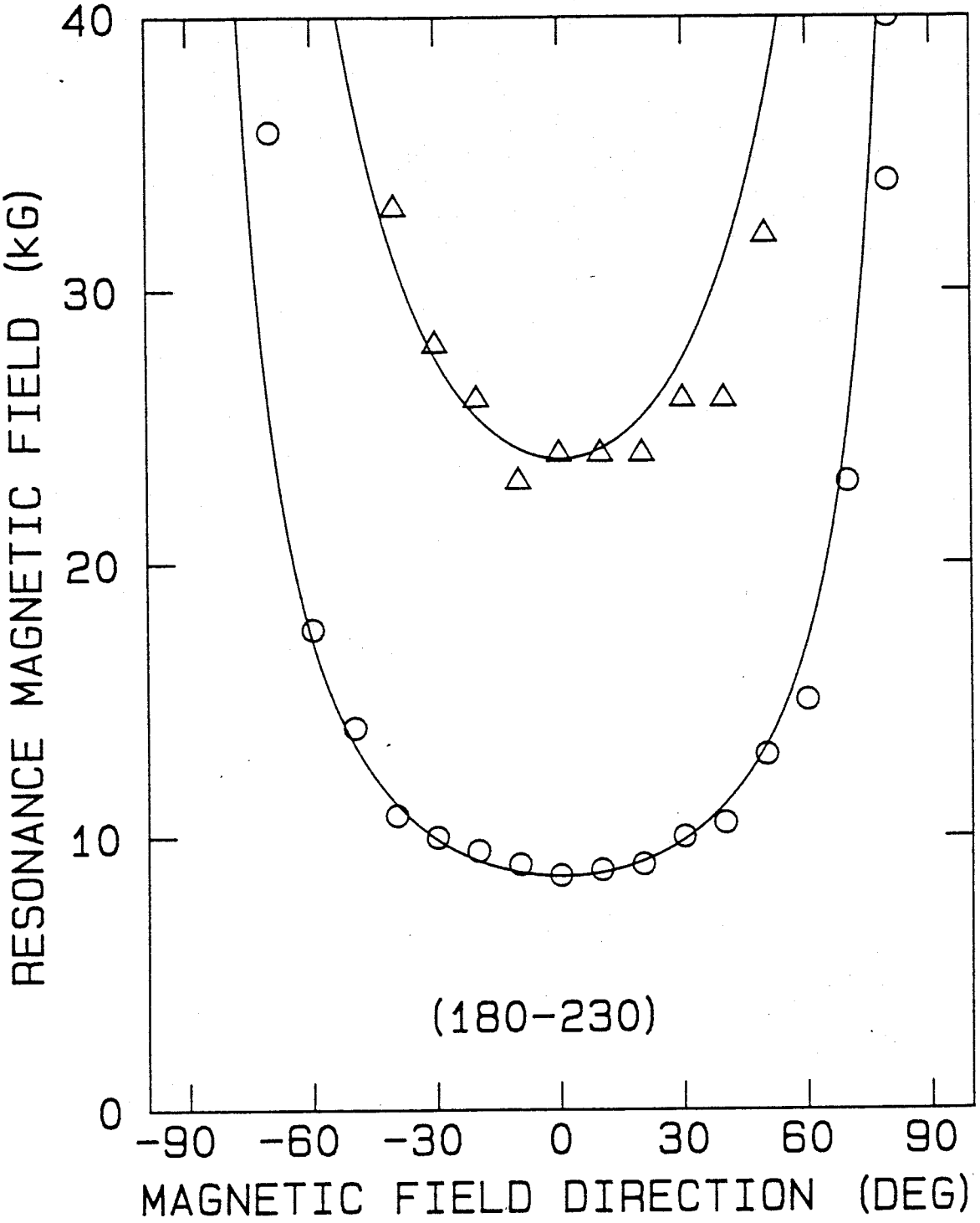

FIG. 7-6-6 Dip position as a function of the magnetic field direction for the sample #6(180Å/231Å). Solid lines are the cyclotron resonance field obtained from calculation based on the 2-dimensional Fermi Surface.

§7-7 PbTe/$Pb_{1-x}Sn_xTe$ 34Å/41Å Superlattice(#7)

From the X-ray diffraction pattern(see Fig. 7-7-1), PbTe and $Pb_{1-x}Sn_xTe$ layer thicknesses, 34Å and 41Å are obtained. Total thickness is 4.50μm. Interdiffusion length is below 16Å. To determine more precise interdiffusion length, intensity of the further satellites are required for the same reason in section 7-1. But they are very weak. Figure 7-7-2 shows Sn composition profile at interdiffusion length 16Å(worst case). Fig. 7-7-3 shows energy diagram based on the model that indium level are taken as the energy origin. In the worst case, it is the problem which the square well potential approximation is used safely or not. Figures 7-7-4 and 7-7-5 show the dependence of the magneto-plasma transmission spectra on magnetic field direction. The electrons belonging to the singlet and triplet valleys are 3-dimensional. Figure 7-7-6 shows resonance magnetic field versus magnetic field directions. The solid line in Fig. 7- 7-6 are calculated resonance magnetic field based on the envelope function approximation. In this sample, there are no data of SdH. Band parameters in calculation are given in Fig. 7-7-7. The energy dispersion curves are shown in Figs. 7-7-8 and 7-7-9.

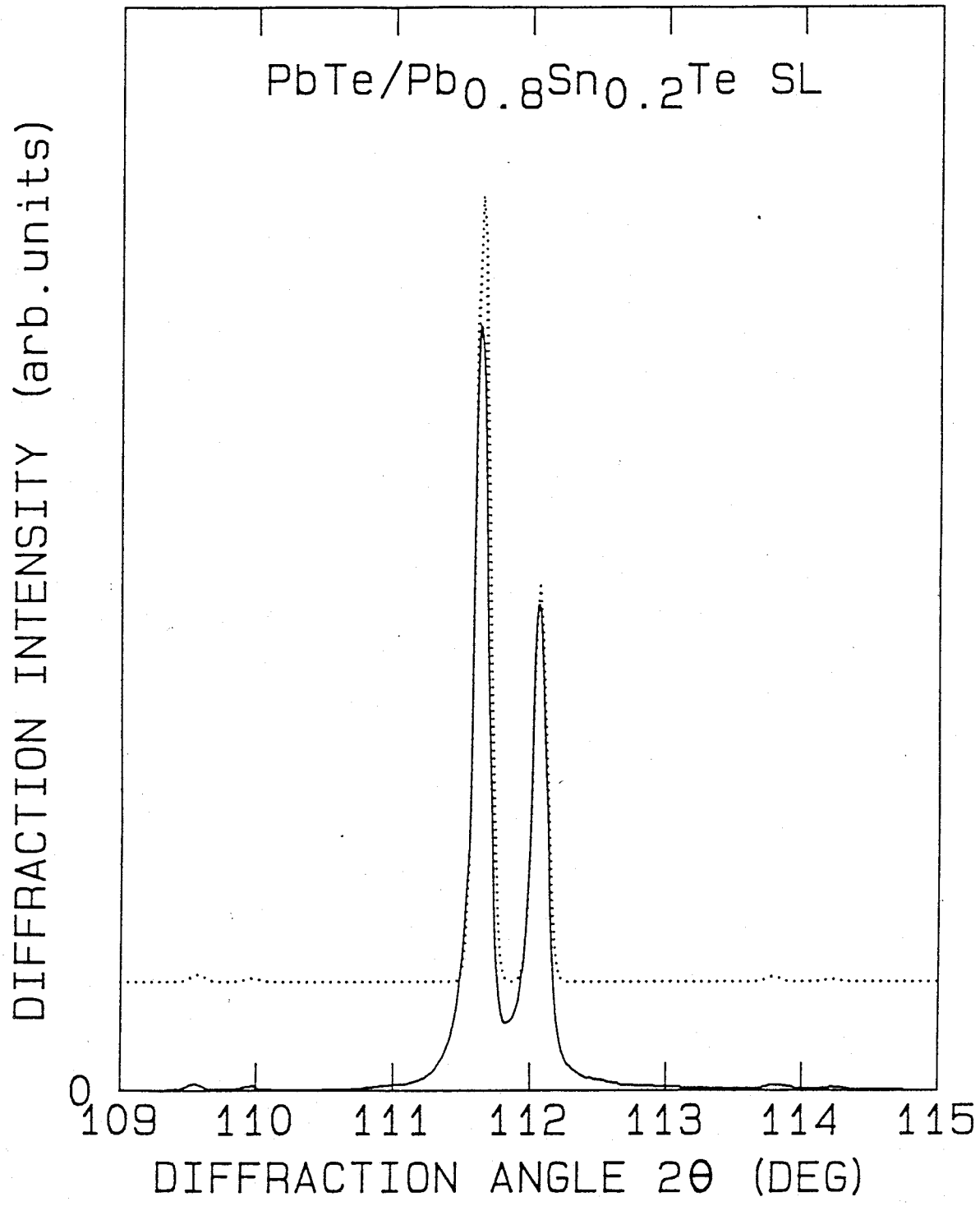

FIG. 7-7-1 Measured(solid line) and calculated(dotted line) X-ray diffraction patterns of the sample #7. Diffraction is around (444) reflection. From the calculation, the thicknesses of 34Å(9 PbTe layers) and 41Å(11 $Pb_{0.8}Sn_{0.2}Te$ layers) are obtained. The interdiffusion length is below 16Å.

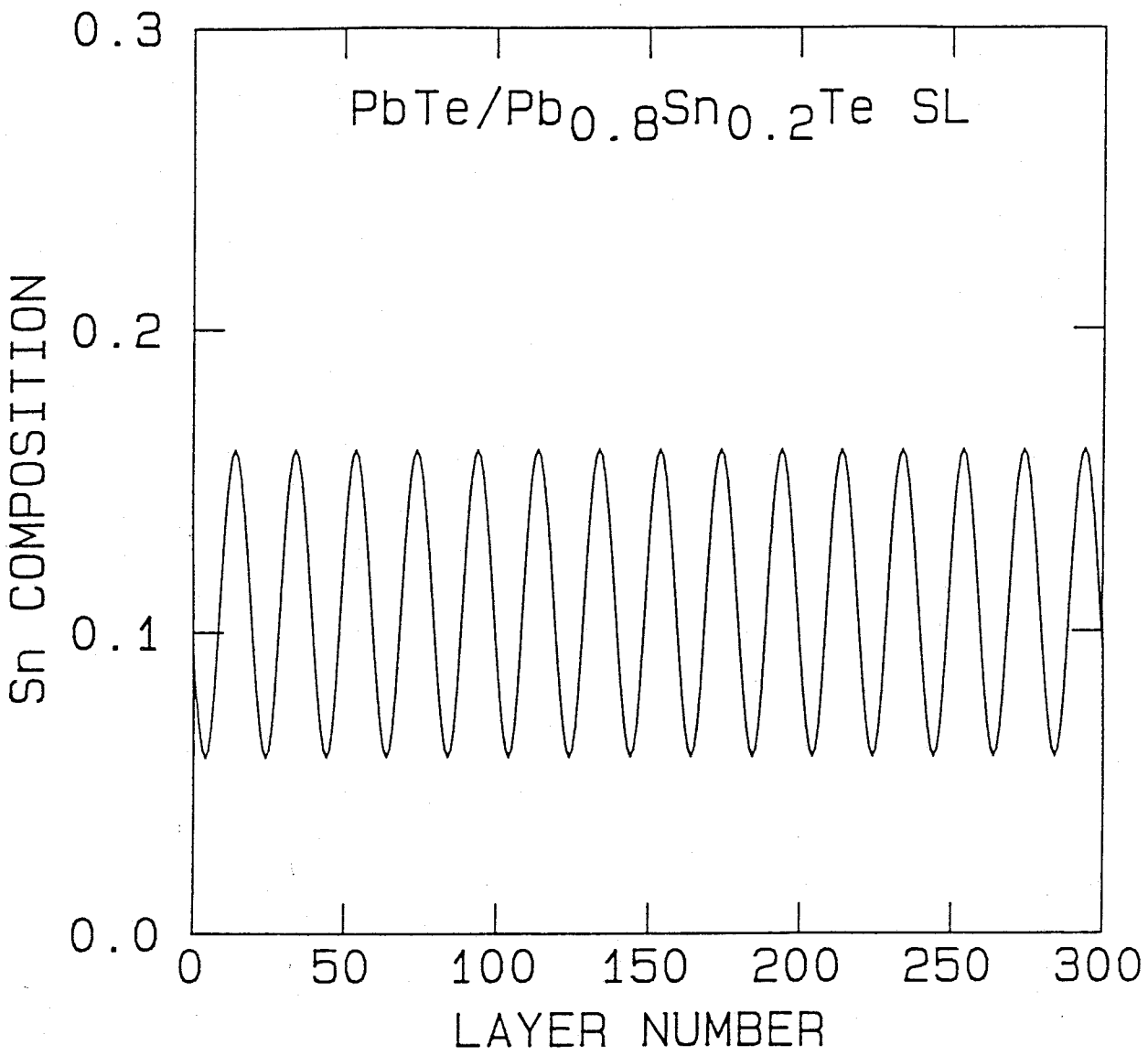

FIG. 7-7-2 Tin composition profile versus metallic atom layer numbers for the sample #7(34Å/41Å). The thickness of 100 molecular layers corresponds to 373Å.

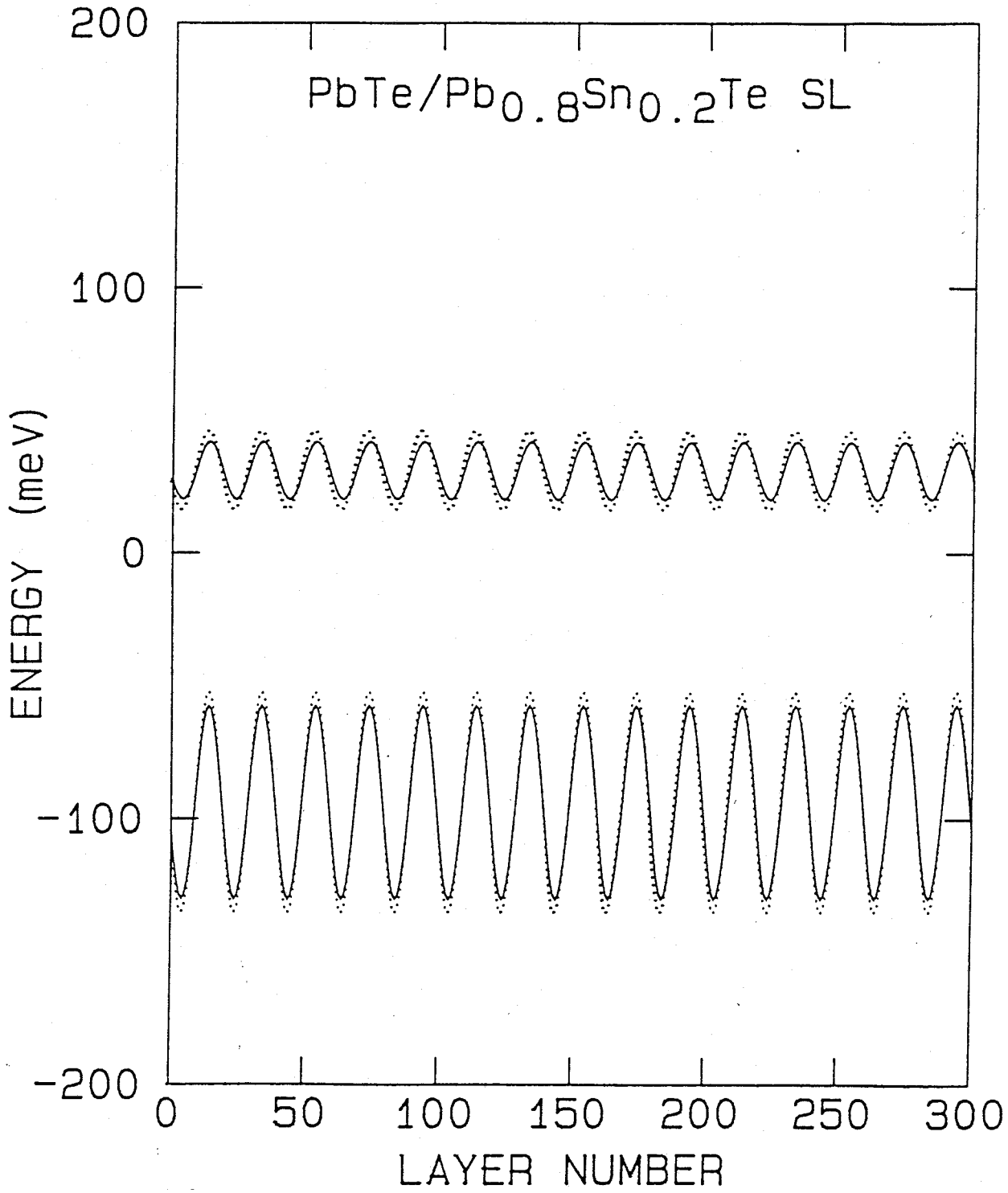

FIG. 7-7-3 Energy band diagrams of the singlet valley(solid lines) and triplet valleys(dotted lines) versus metallic atom layer numbers for the sample #7(34Å/41Å). The thickness of 100 molecular layers corresponds to 373Å. Energy bands shift by internal strain to accommodate the lattice mismatch between PbTe and $Pb_{0.8}Sn_{0.2}Te$ layers.

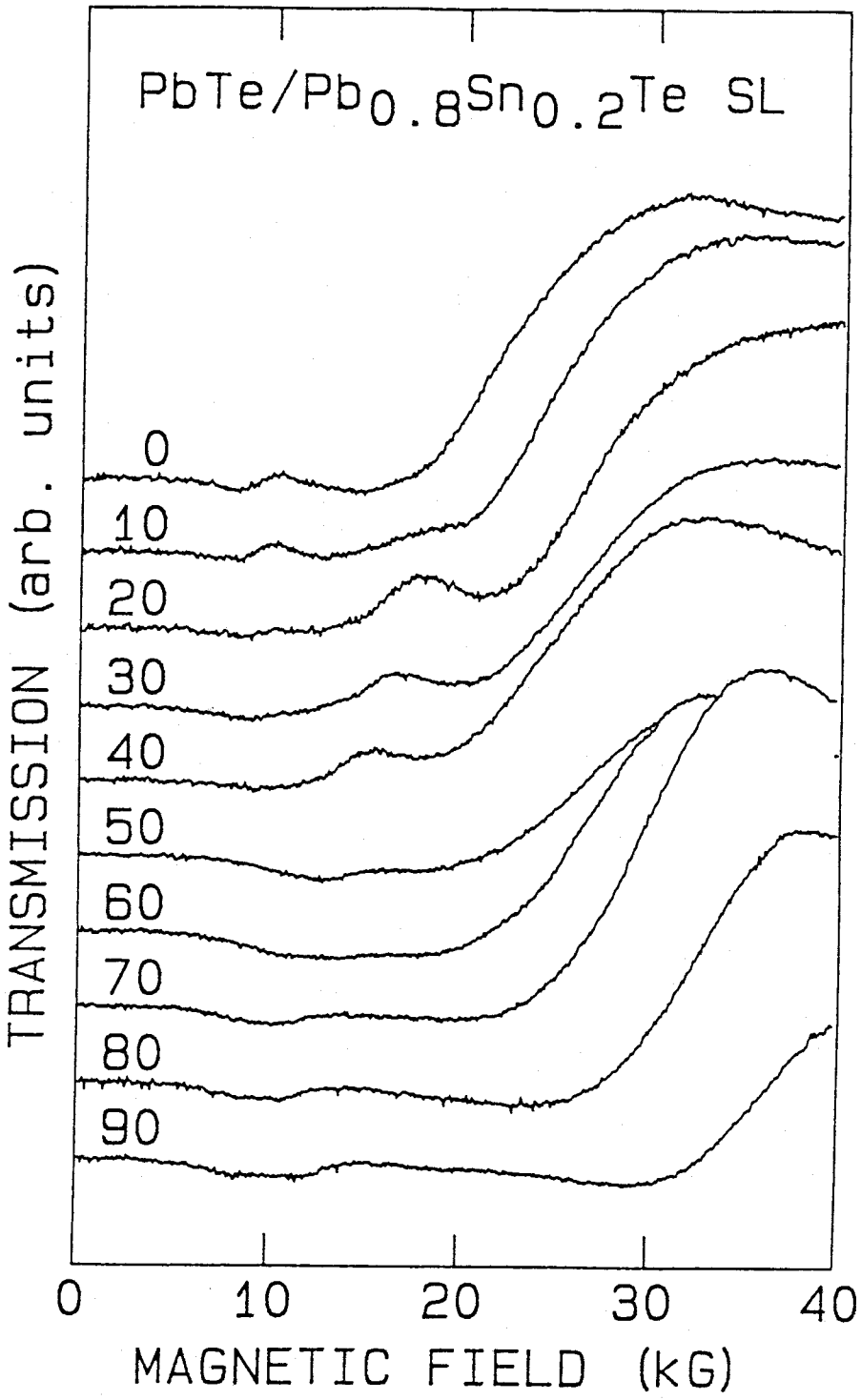

FIG. 7-7-4 Magnetoplasma transmission spectra with 337μm laser light at 4.2K for the sample #7(34Å/41Å). The magnetic field direction is changed from 0 deg along <111>(Faraday configuration) to 90 deg along <$\bar{1}\bar{1}$2>(Voigt configuration).

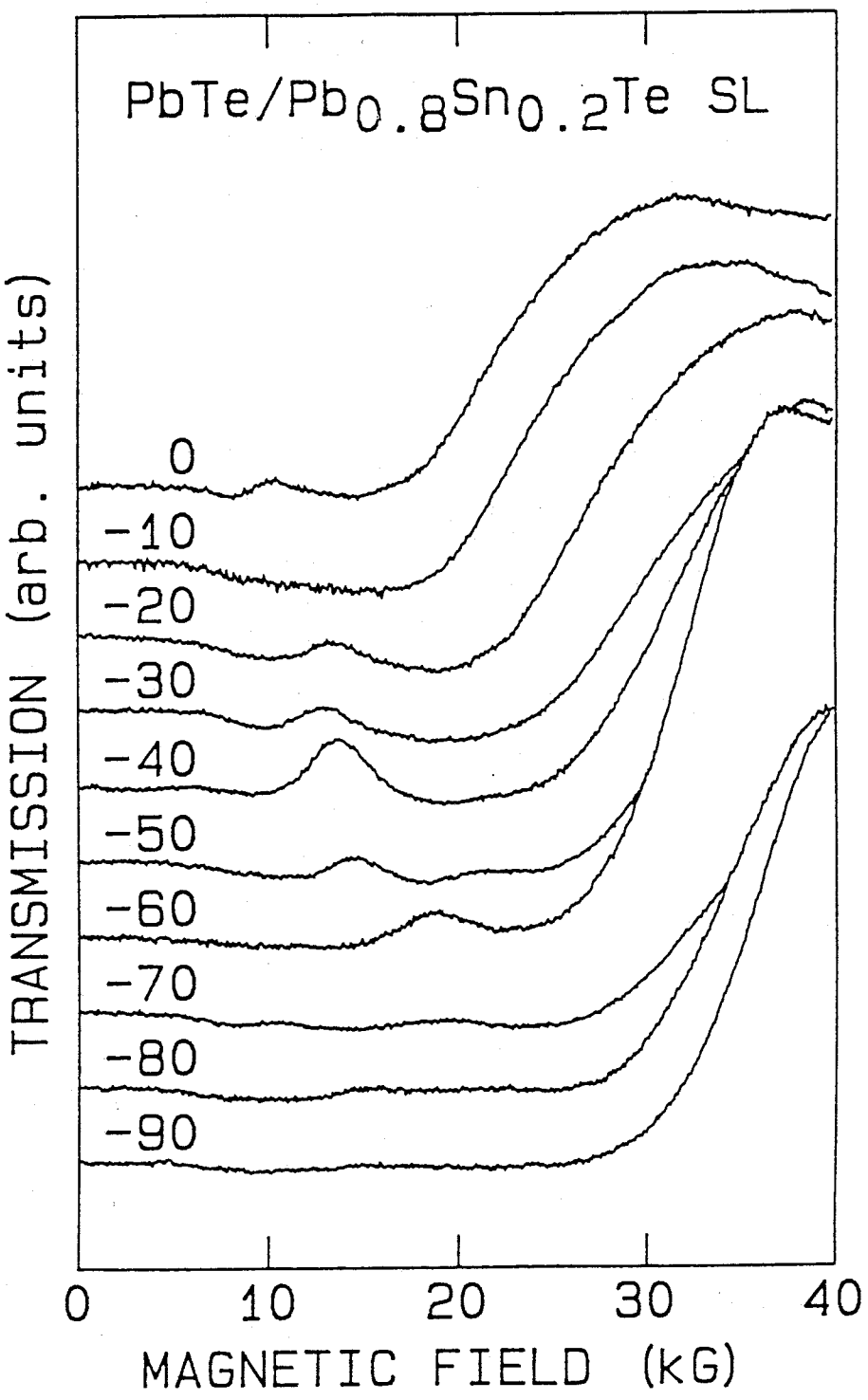

FIG. 7-7-5 Magnetoplasma transmission spectra with 337μm laser light at 4.2K for the sample #7(34Å/41Å). The magnetic field direction is changed from 0 deg along <111>(Faraday configuration) to -90 deg along <11$\bar{2}$>(Voigt configuration).

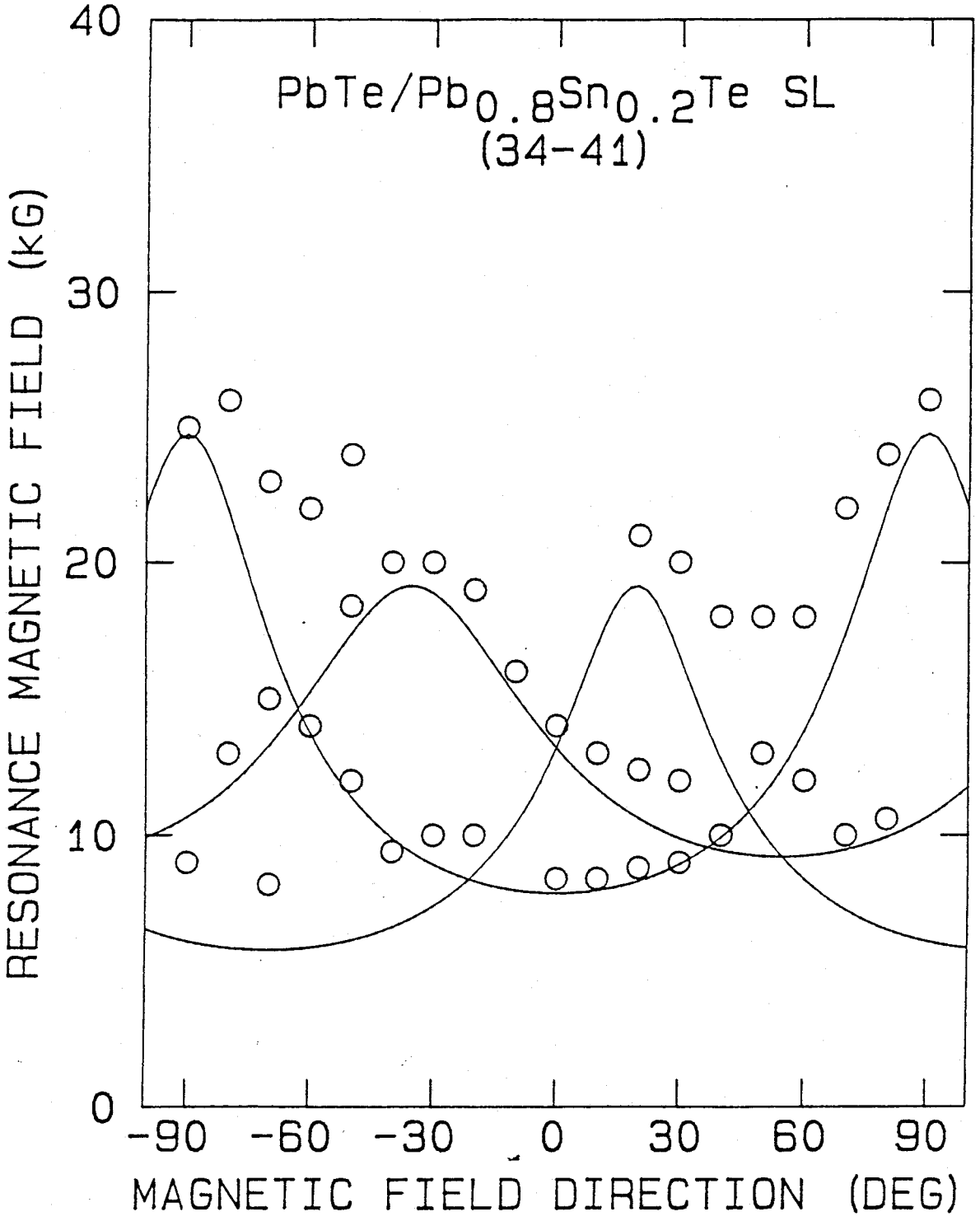

FIG. 7-7-6 Dip position as a function of the magnetic field direction for the sample #7(34Å/41Å). Solid lines are the cyclotron resonance field obtained from calculation based on the envelope function aproximation.

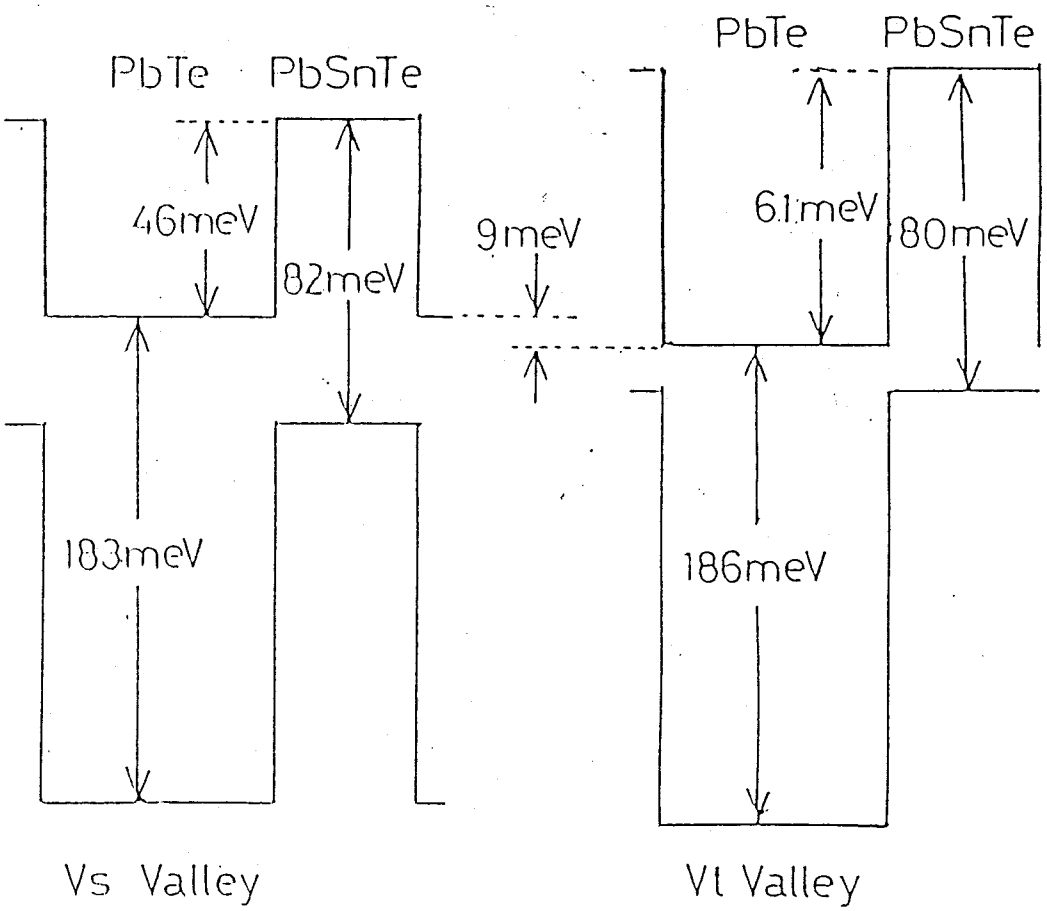

FIG. 7-7-7 Band parameters used in the calculation based on the envelope function approximation for the sample #7(34Å/41Å).

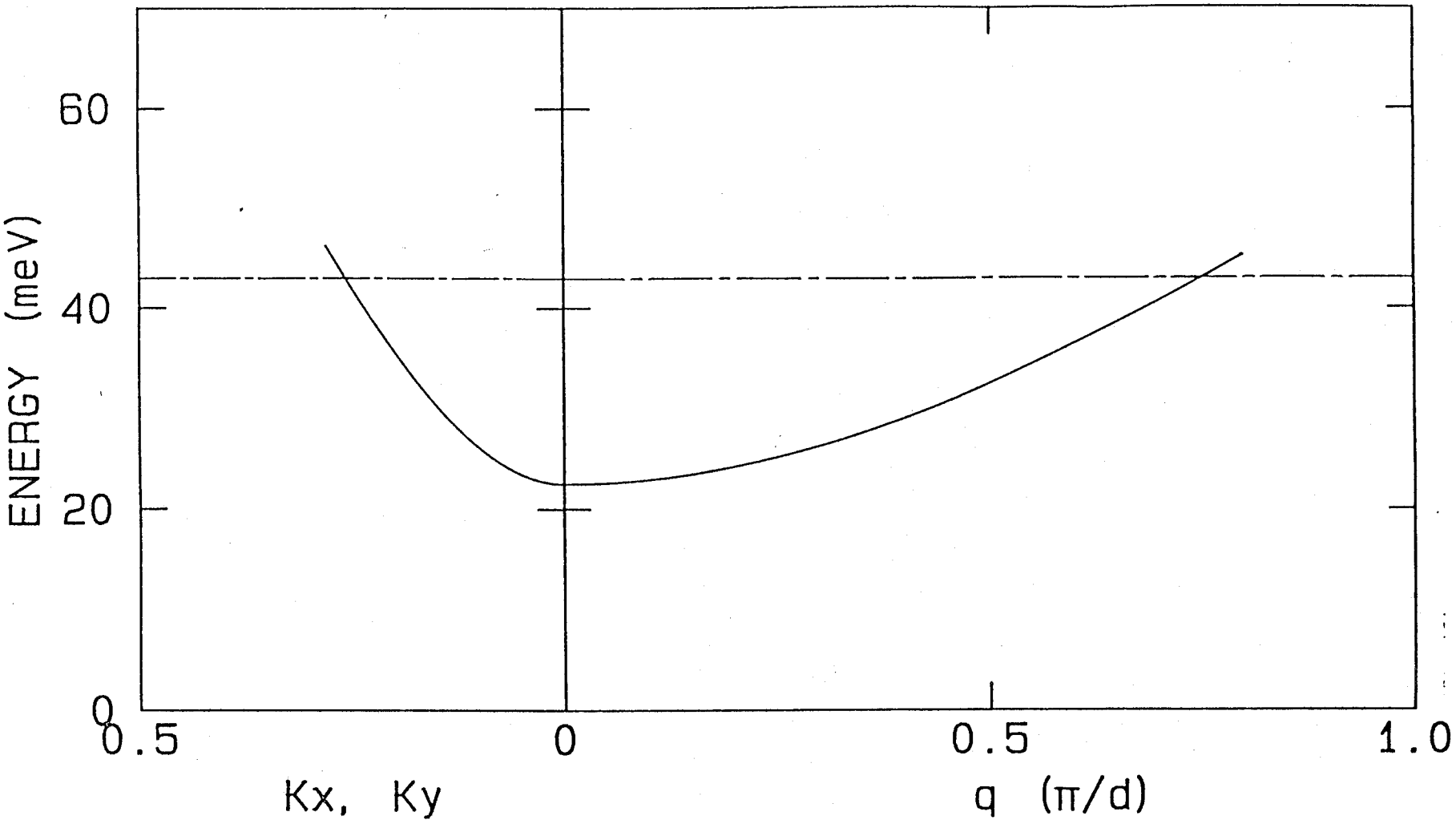

FIG. 7-7-8 Energy dispersion of the triplet valleys for the sample #7(34Å/41Å) obtained from the envelope function approximation.

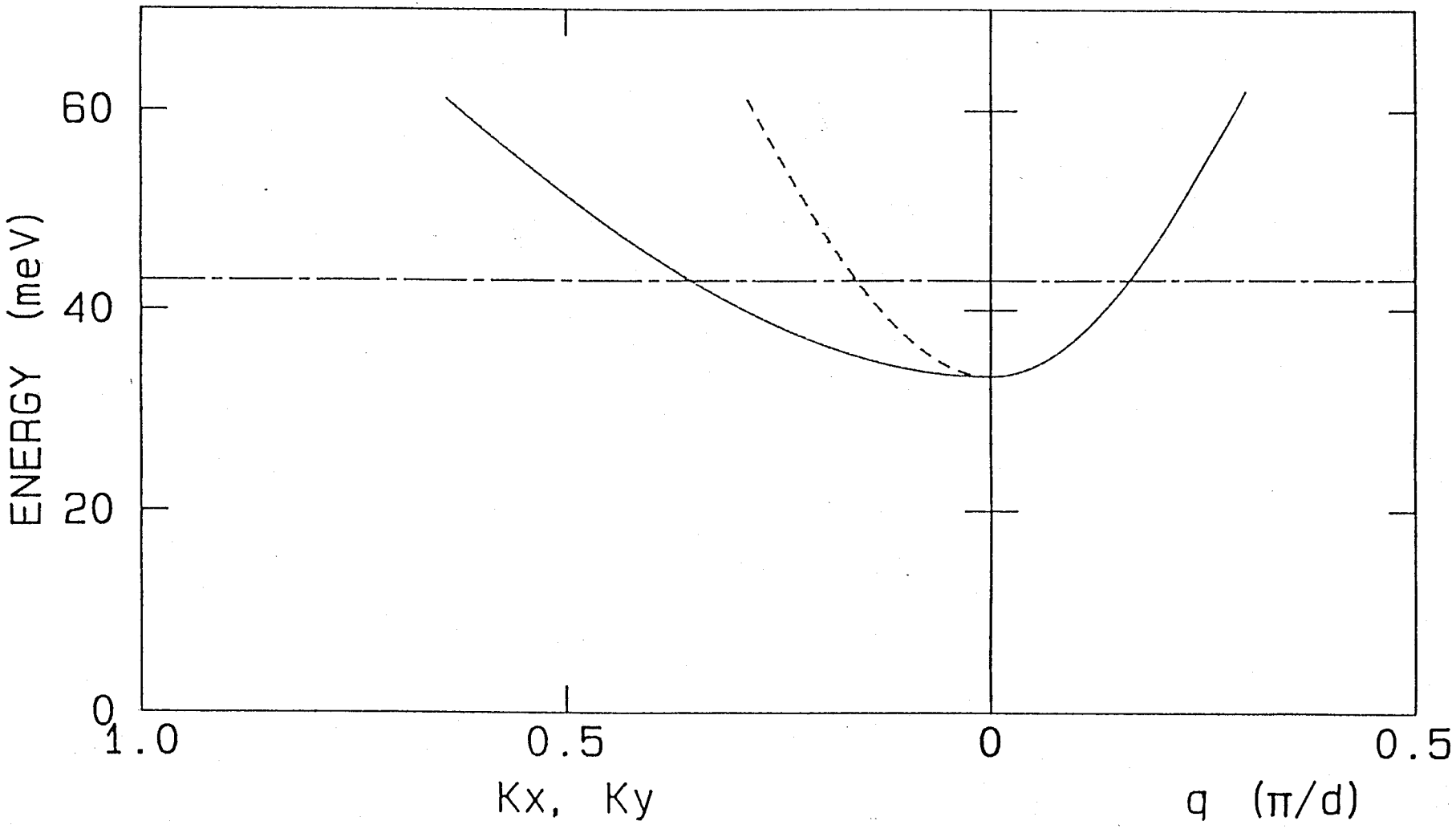

FIG. 7-7-9 Energy dispersion of the triplet valleys for the sample #7(34Å/41Å) obtained from the envelope function approximation.

§8 DISCUSSION FOR PbTe/$Pb_{1-x}Sn_xTe$ SUPERLATTICES

For 220Å/220Å, 260Å/150Å, 240Å/60Å, and 220Å/30Å superlattices with small interdiffusion, the dependence of band edge structure on the barrier layer($Pb_{1-x}Sn_xTe$ layer) thickness are observed by magnetoplasma transmission spectra(see sections 7-1, 7-2, 7-3, and 7-4). The electron system belonging to the singlet valleys is 2-dimensional for all these superlattices, even for the sample with the barrier layer thickness of 30Å. The electron system belonging to triplet valleys is 2-dimensional for the 220Å/220Å and 260Å/150Å superlattices, while for the 200Å/60Å superlattice, the electron systems belonging to triplet valleys are 3-dimensional due to electron tunneling across barrier layer. This coexistence of two dimensional and three dimensional bands is the first exapmple in IV-VI superlattices. The difference of dimensionality of electron systems between the singlet and triplet valleys comes from the fact that the singlet valley's electron mass along superlattice direction is ten times heavier than triplet ones. For the 220Å/30Å superlattices, the cyclotron resonance of electrons belonging to the triplet valleys is not observed, because the electrons do not exist due to valley splitting by tensile strain caused by the difference of thermal expansion coefficient between superlattice film and BaF_2 substrate.

Calculation of cyclotron masses is made using the envelope function approximation based on the two band model(see sections 2-1 and 3-2). For the band discontinuity, we use the model that

PbTe and $Pb_{1-x}Sn_xTe$ energy bands are connected in reference to the pinning level of the deep impurity indium. The measured and calculated cyclotron masses agree well with each other, where the measured carrier density and the cross section of Fermi surface are reproduced as good as possible. Also from the calculated energy dispersion curve, the relation of barrier thickness to dimensionality of electron system can be explained. Moreover it has been found that the band discontinuity model is consistent with the experimental results.

For the superlattices 300Å/190Å with large interdiffusion of Pb and Sn atoms across the interface, the resonance magnetic field due to the singlet valley's electrons splits into two with changing the magnetic field direction from Faraday configuration. This splitting comes from the fact that the higher subband of two lowest subbands is much more dispersive than the lower, because the large interdiffusion decreases the barrier potential and the dispersion of the higher subband becomes large.

§9 ANDERSON'S NEGATIVE U MODEL AND STATISTICS OF THREE CHARGED STATES

In this section let us consider a negative U potential model for double acceptor impurities. At first the model was proposed by Anderson to account for diamagnetism of localized states in gap in chalcogenide amorphous semiconductor[113]; generally impurity states in a covalent semiconductor shows Curie-Weiss paramagnetism due to repulsive Coulomb interactions. A large electron-phonon coupling incorporated in the model makes an impurity prefer two electron occupied state to single electron occupied one, though repulsive Coulomb interaction exists between localized electrons. The model also explains the Fermi level pinning, persistent photoconductivity, and metal-insulator transitions in $Pb_{1-x}Sn_xTe/In$. In Sec. 2-1 we show Anderson's negative U model. In Sec. 2-2 we give statistics of the three charged states derived from the model[114].

9-1 Anderson's negative U model

A starting Hamiltonian consists of the electron term, the phonon term, and the electron-phonon coupling term[113]:

$$\mathcal{H} = \mathcal{H}_{el} + \mathcal{H}_{ph} + \mathcal{H}_{el\text{-}ph} \cdot \qquad (9.1.1)$$

The electron term is given by

$$\mathcal{H}_{el} = \sum_i E_i(n_{i\uparrow} + n_{i\downarrow}) + U\sum_i n_{i\uparrow}n_{i\downarrow} , \qquad (9.1.2)$$

where $n_{i\uparrow}$ and $n_{i\downarrow}$ are number operators for a spin up electron and a spin down one, respectively. The energy, E_i, can be equal at any impurity site, i, or assumed to be distributed over a given range of energy. The energy U is the Coulomb repulsive energy between electrons at the same impurity. The phonon term is represented by

$$\mathcal{H}_{ph} = \sum_i (\tfrac{1}{2}m\dot{x}_i^2 + \tfrac{1}{2}cx_i^2) , \qquad (9.1.3)$$

where x_i is the Holstein coordinate; m the mass; c the force constant. The electron-phonon coupling term is

$$\mathcal{H}_{el\text{-}ph} = \sum_i - \lambda x_i(n_{i\uparrow} + n_{i\downarrow}) , \qquad (9.1.4)$$

where λ is the coupling constant. Replacing the parameters in these definition as follows

$$\Delta_i = \lambda x_i \qquad (9.1.5)$$

$$\Delta_o = \frac{\lambda^2}{c} \tag{9.1.6}$$

$$M = \frac{m}{\lambda^2} \quad , \tag{9.1.7}$$

the Hamiltonian becomes

$$\mathcal{H} = \sum_i E_i(n_{i\uparrow} + n_{i\downarrow}) + U \sum_i n_{i\uparrow}n_{i\downarrow}$$

$$+ \sum_i \{\frac{1}{2}M\dot{\Delta}_i^2 + \frac{1}{2\Delta_o}\Delta_i^2 - \Delta_i(n_{i\uparrow} + n_{i\downarrow})\} \quad , \tag{9.1.8}$$

where Δ_i and Δ_o have energy dimension of energy. Rewriting the Hamiltonian as follows:

$$\mathcal{H} = \sum_i (E_i - \frac{\Delta_o}{2})(n_{i\uparrow} + n_{i\downarrow}) + \sum_i (U - \Delta_o)n_{i\uparrow}n_{i\downarrow}$$

$$+ \sum_i [\frac{1}{2}M\dot{\Delta}_i^2 + \frac{1}{2\Delta_o}\{\Delta_i - \Delta_o(n_{i\uparrow} + n_{i\downarrow})\}^2] \quad , \tag{9.1.9}$$

we can obtain energy eigenstate. Defining U^{eff}, $E_i{}^{eff}$, and ω_o by

$$U^{eff} = U - \Delta_o \tag{9.1.10}$$

$$E_i{}^{eff} = E_i - \frac{\Delta_o}{2} \tag{9.1.11}$$

$$\omega_o{}^2 = (M\Delta_o)^{-1} \tag{9.1.12}$$

leads to diagonalized Hamiltonian involving quantized phonon term.

$$\mathcal{H} = \sum_i \{E_i^{eff}(n_{i\uparrow} + n_{i\downarrow}) + U^{eff} n_{i\uparrow} n_{i\downarrow}\}$$

$$+ \sum_i \hbar\omega_o (n + \frac{1}{2}) \ , \qquad (9.1.13)$$

where n is the phonon number operator. The Hamiltonian for each impurity is

$$\mathcal{H}_i = E_i^{eff}(n_{i\uparrow} + n_{i\downarrow}) + U^{eff} n_{i\uparrow} n_{i\downarrow}$$

$$+ \hbar\omega_o (n + \frac{1}{2}) \ . \qquad (9.1.14)$$

Under the low frequency limit that $\omega << \omega_o$, the last term is negligible and each impurity has three energy eigenstates, that is, three charged states. Unoccupied state $| 0 >$ is nondegenerate and has E=0.

$$\mathcal{H}_i | 0 > = 0 | 0 > \qquad (9.1.15)$$

Singly occupied state is twofold degenerate. One is a spin up state $| \uparrow >$, and the other is a spin down state $| \downarrow >$. They have $E=E_i^{eff}$;so that

$$\mathcal{H}_i | \uparrow > = E_i^{eff} | \uparrow > \qquad (9.1.16)$$

and

$$\mathcal{H}_i | \downarrow > = E_i^{eff} | \downarrow > . \qquad (9.1.17)$$

Doubly occupied state is nondegenerate and has $E=2E_i^{eff}$.

$$\mathcal{H}_i | \uparrow \downarrow > = (2E_i^{eff}+U^{eff}) | \uparrow \downarrow > \qquad (9.1.18)$$

Whether the U^{eff} is positive or negative is serious for this system. For example, consider the system which consists of N impurities and N electrons. While in the case of positive U^{eff} the lowest energy state is the one that all impurities are singly occupied, in the case of negative U^{eff} the lowest energy state is the one that N/2 impurities are unoccupied and N/2 impurities are doubly occupied. In next section we consider statistics of this system.

9-2 Statistics of three charged states

The character of the three charged states statistics depends on the sign of the U^{eff} greatly[114]. From eqs. (9.1.13), (9.1.15), (9.1.16), (9.1.17), and (9.1.18) the grand partition function for N_o impurities is

$$Z = \prod_i \{1+2\exp[-(E_i{}^{eff}-\varepsilon_F)/kT]+\exp[-(2E_i{}^{eff}+U^{eff}-2\varepsilon_F)/kT]\}. \tag{9.2.1}$$

If all E_i's are equal to E_o , defining $E_o{}^{eff}$ by

$$E_o{}^{eff} = E_o - \frac{\Delta_o}{2} \tag{9.2.2}$$

leads to

$$Z = \{1+2\exp[-(E_o{}^{eff}-\varepsilon_F)/kT]+\exp[-(2E_o{}^{eff}+U^{eff}-2\varepsilon_F)/kT]\}^{N_o} \tag{9.2.3}$$

The average number n of electrons per impurity site is given by

$$n(\varepsilon_F,T) = -kT\left(\frac{\partial \ln Z}{\partial \varepsilon_F}\right)_T$$

$$= \frac{2\{\exp[-(E_o{}^{eff}-\varepsilon_F)/kT]+\exp[-(2E_o{}^{eff}+U^{eff}-2\varepsilon_F)/kT]\}}{\{1+2\exp[-(E_o{}^{eff}-\varepsilon_F)/kT]+\exp[-(2E_o{}^{eff}+U^{eff}-2\varepsilon_F)/kT]\}}. \tag{9.2.4}$$

Solving (9.2.4) for the Fermi energy as a function of electronic concentration, we obtain

$$\varepsilon_F = E_o^{eff} - kT\ln\{(n^{-1}-1)^2+[(n^{-1}-1)+(2n^{-1}-1)\exp(-U^{eff}/kT)]\}^{1/2} \quad (9.2.5)$$

Consider the case that $U^{eff} > 0$ and $U^{eff}/kT >> 0$. The Fermi energy gradually rises with increasing the electronic concentration n from 0 to just before 1, abruptly rises near n=1, and gradually rises again with increasing n from just after 1 to 2 as shown in Fig 9-2-1. That is because $2I^+$ is more stable than $I^o + I^{2+}$. On the other hand, in the case that $U^{eff} < 0$ and $|U^{eff}/kT| >> 0$, the Fermi energy gradually increase and is almost constant value of $E_o^{eff} - U^{eff}/2$ with increasing n as shown in Fig. 9-2-2. That is why $I^o + I^{2+}$ has lower energy than $2I^+$ and I^+ does not almost exist all range of the n. Thus the negative U^{eff} pins the Fermi energy, where double acceptor impurities play a role of a reservoir of electrons. The concentration of I^o, I^+, and I^{2+} are denoted by $n_I o$, $n_I +$, and $n_I 2+$, respectively and they are given by

$$n_{Io}(\varepsilon_F,T) = \frac{\exp[-(2E_o^{eff}+U^{eff}-2\varepsilon_F)/kT]}{\{1+2\exp[-(E_o^{eff}-\varepsilon_F)/kT]+\exp[-(2E_o^{eff}+U^{eff}-2\varepsilon_F)/kT]\}}, \quad (9.2.6)$$

$$n_{I+}(\varepsilon_F,T) = \frac{2\exp[-(E_o^{eff}-\varepsilon_F)/kT]}{\{1+2\exp[-(E_o^{eff}-\varepsilon_F)/kT]+\exp[-(2E_o^{eff}+U^{eff}-2\varepsilon_F)/kT]\}}, \quad (9.2.7)$$

and

$$n_I 2+(\varepsilon_F, T) = \frac{1}{\{1+2\exp[-(E_o{}^{eff}-\varepsilon_F)/kT]+\exp[-(2E_o{}^{eff}+U^{eff}-2\varepsilon_F)/kT]\}}. \quad (9.2.8)$$

Figure 9-2-3 shows the I^+ concentration as a function of U^{eff}/kT. The temperature dependence of I^+ concentration is shown in Fig. 9-2-4.

In $Pb_{1-x}Sn_xTe/In$, the Fermi energy pinning occurs due to negative U^{eff} and the metal-insulator transitions are due to In level shift-down with increasing tin compositions.

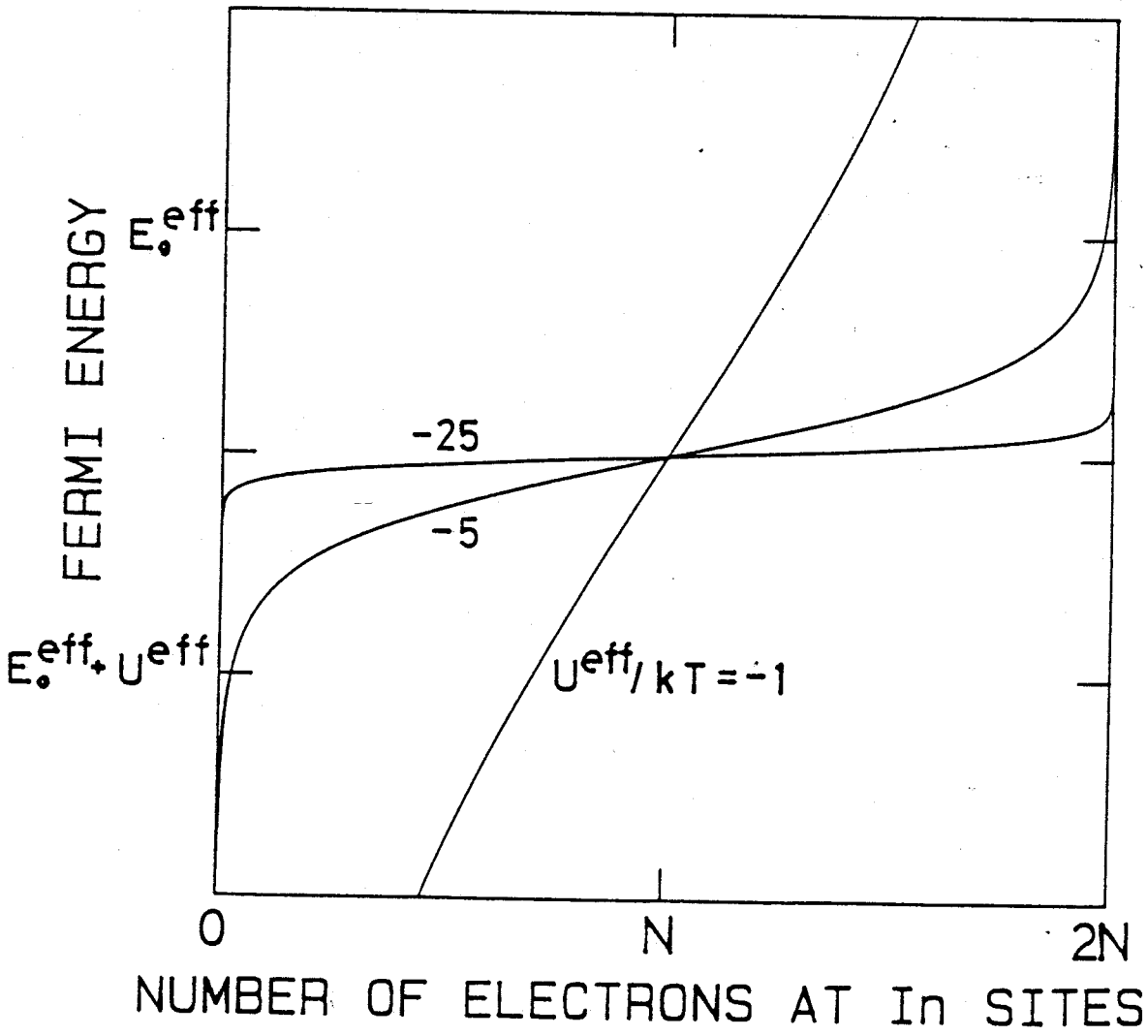

FIG. 9-2-1 Fermi energy versus number of electrons for the negative U^{eff}. The number of In atoms is denoted by N.

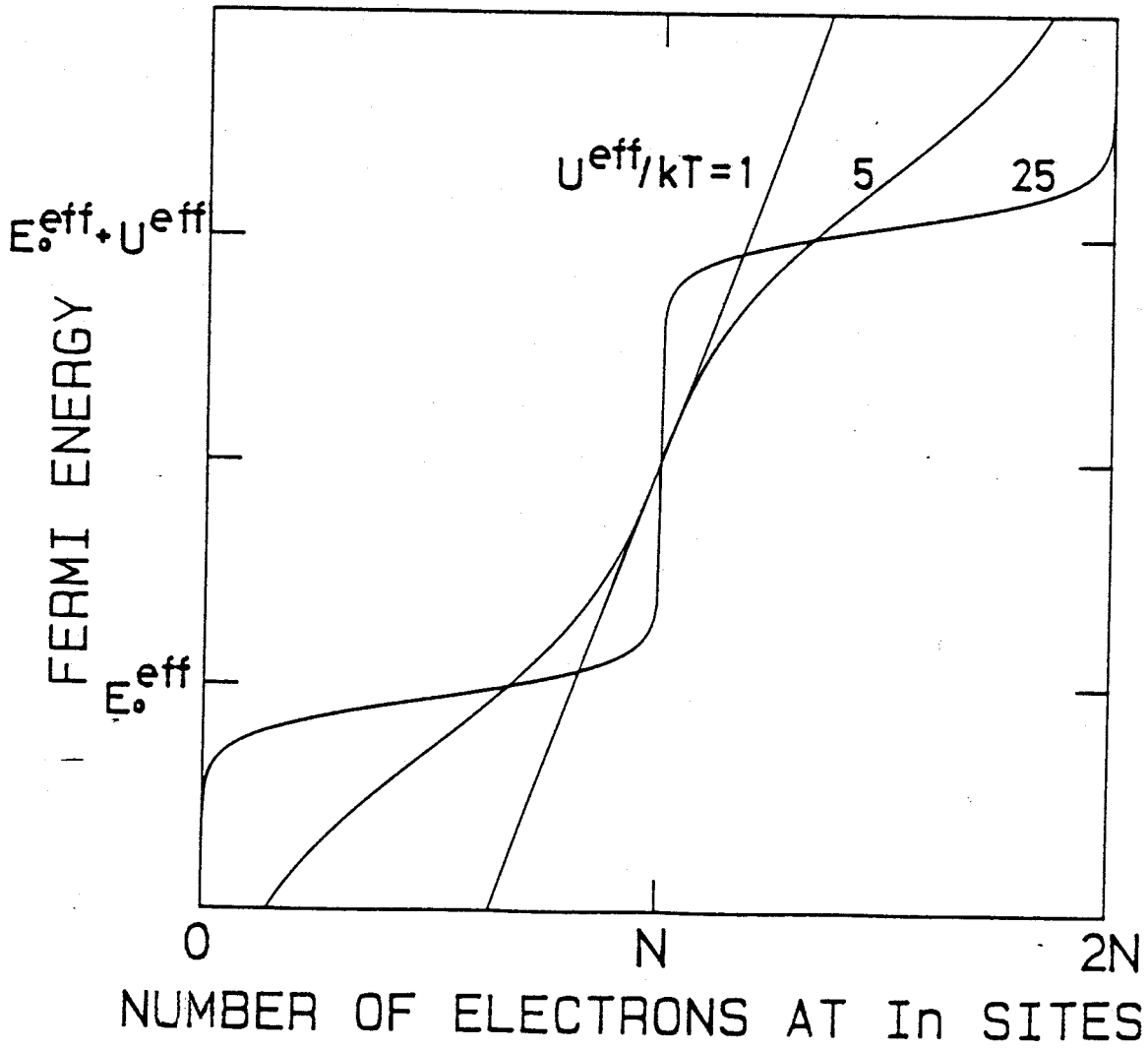

FIG. 9-2-2 Fermi energy versus number of electrons for the positive U^{eff}. The number of In atoms is denoted by N.

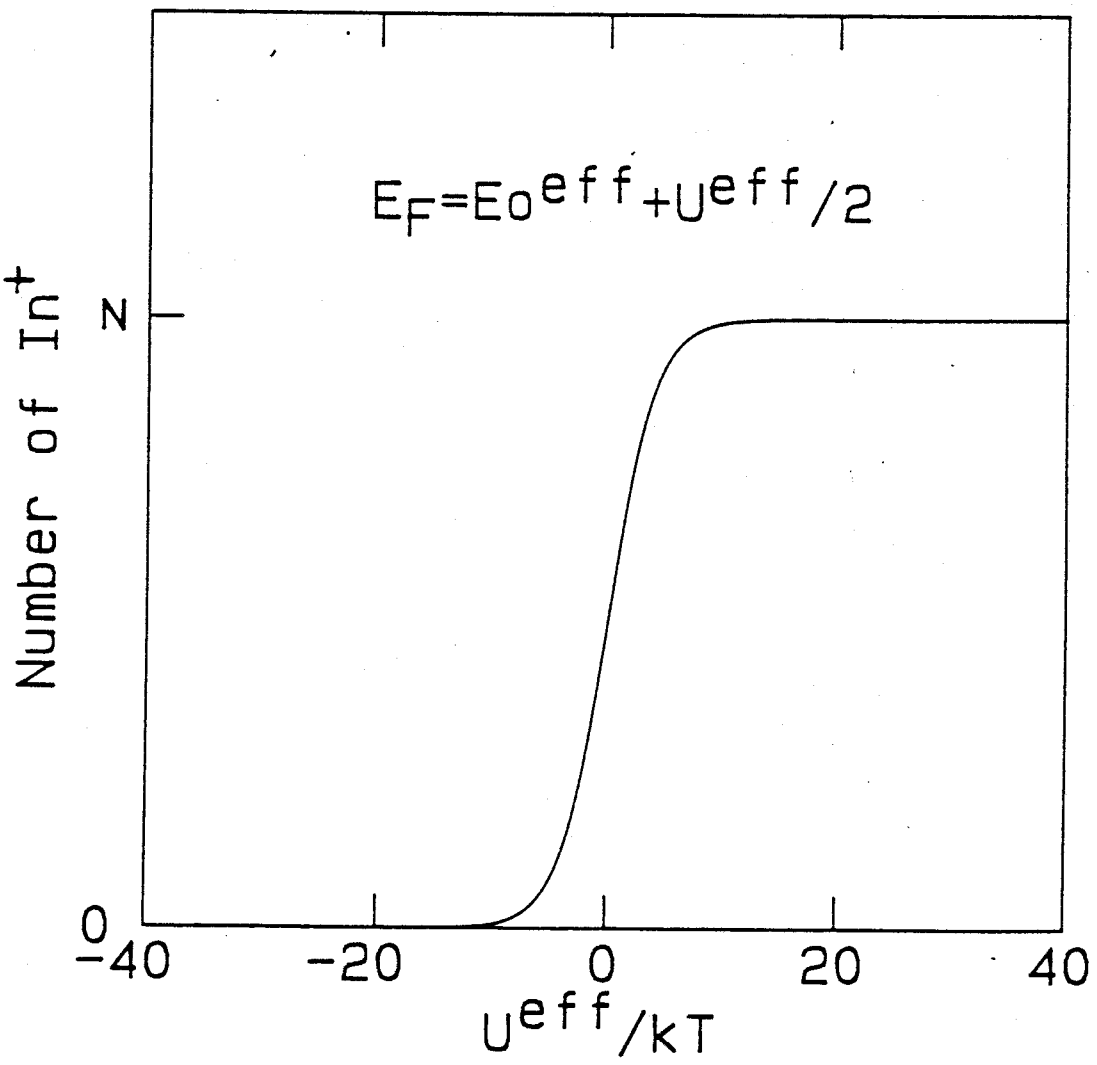

FIG. 9-2-3 Number of In^+ states as a function of U^{eff}/kT. The number of In atoms is N.

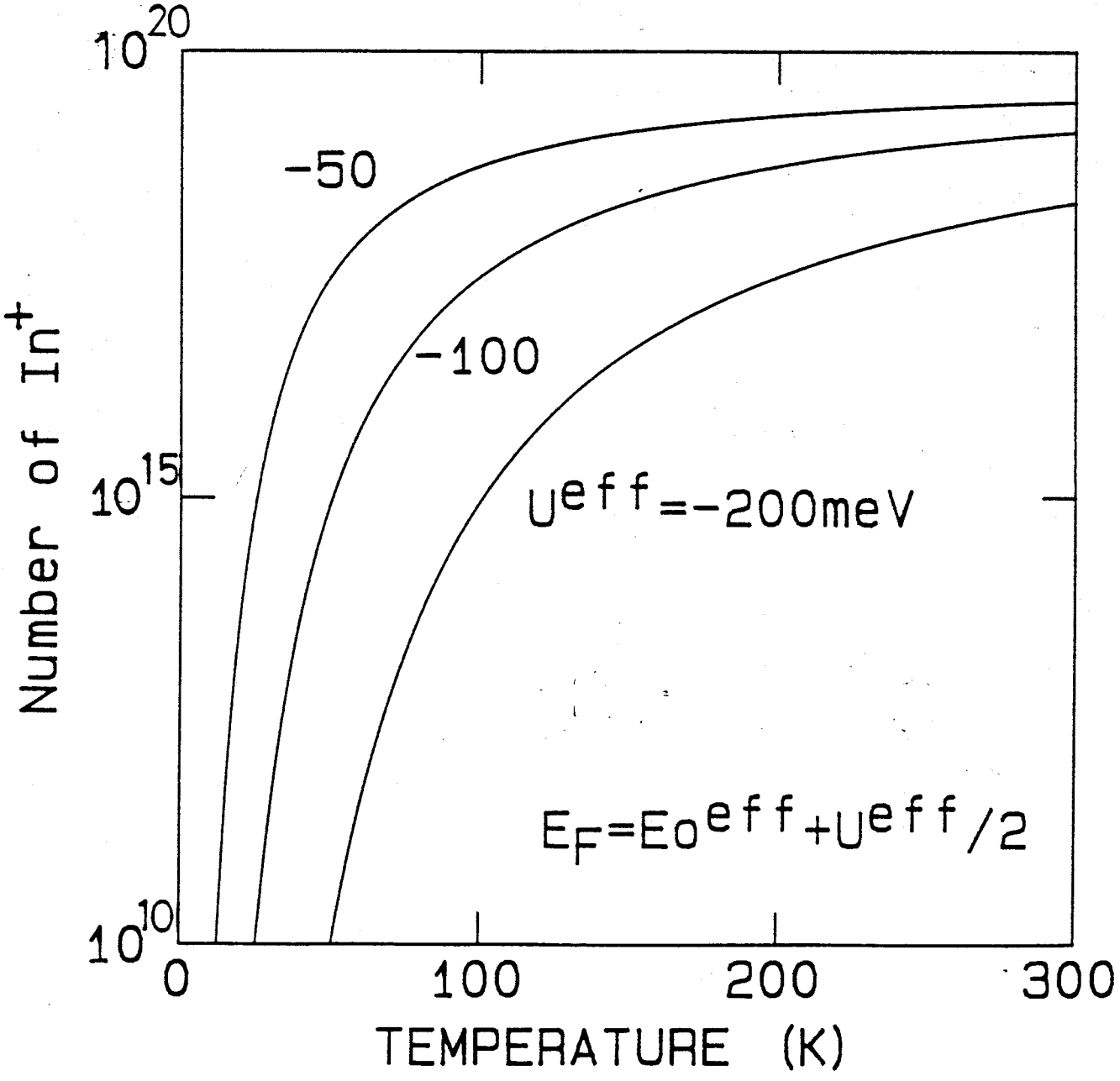

FIG. 9-2-4 Number of In^+ states as a function of temperature, where the number of In atoms is assumed to be $10^{20}cm^{-3}$.

§10 Magnetoplasma Dielectric Tensor of IV-VI Compounds

To analyze the stripline transmission spectra we need the dielectric tensor in the condition that q//H//<001>(Faraday configuration) and q//<001> H//<110>(Voigt configuration) . We name four valleys as follows:

<111> valley A,

<$\bar{1}\bar{1}$1> valley B,

<1$\bar{1}\bar{1}$> valley C,

and

<$\bar{1}$1$\bar{1}$> valley D.

We take the Cartesian coordinates as follows:

x <110>,

y <$\bar{1}$10>,

and

z <001>.

§10-1 Magnetoplasma dielectric tensor of IV-VI compounds in the Faraday configuration (q//H//<001>)

First, let us derive the dielectric tensor in Faraday configuration:

$$H \,//\, z,$$

and

$$q \,//\, z.$$

From Eq.(4.3.7), cyclotron masses of A,B,C,and D valleys, m_{ca}, m_{cb}, m_{cc}, and m_{cd}, are given by

$$m_{ca} = m_{cb} = m_{cc} = m_{cd} = m_c$$

and

$$m_c = \left\{ m_t^2 m_l / \left(\frac{2}{3} m_t + \frac{1}{3} m_l \right) \right\}^{1/2}. \qquad (10.1.1)$$

From Eq.(4.3.8), cyclotron frequency of A, B, C, and D valley, ω_{ca}, ω_{cb}, ω_{cc}, and ω_{cd} are given by

$$\omega_{ca} = \omega_{cb} = \omega_{cc} = \omega_{cd} = \omega_c$$

and

$$\omega_c = \frac{eH}{m_o m_c c}. \qquad (10.1.2)$$

Using Eqs.(4.1.12), (4.2.8), and (4.3.6), we obtain the component of the dielectric tensor as,

$$\varepsilon_{xx} = \varepsilon_l - \frac{4\pi n e^2}{m_o} \cdot \left\{ \frac{1}{2\omega(\omega + i\Gamma_{el} + \omega_c)} + \frac{1}{2\omega(\omega + i\Gamma_{el} - \omega_c)} \right\} \left\{ \frac{2}{3m_t} + \frac{1}{3m_l} \right\},$$

$$\varepsilon_{xy}=-\frac{4\pi ne^2}{m_o}\cdot\left\{\frac{1/i}{2\omega(\omega+i\Gamma_{el}+\omega_c)}-\frac{1/i}{2\omega(\omega+i\Gamma_{el}-\omega_c)}\right\}\left\{\frac{(2m_t+m_l)m_c}{3m_t^2m_l}\right\},$$

$$\varepsilon_{yx} = -\varepsilon_{xy},$$

$$\varepsilon_{yy} = \varepsilon_{xx},$$

$$\varepsilon_{yz} = \varepsilon_{zy} = 0,$$

$$\varepsilon_{zx} = \varepsilon_{xz} = 0,$$

and

$$\varepsilon_{zz}=\varepsilon_l-\frac{4\pi ne^2}{m_o}\cdot\frac{1}{\omega(\omega+i\Gamma_{el})}\cdot\left(\frac{2}{3m_t}+\frac{1}{3m_l}\right)^{-1}$$

$$-\frac{4\pi ne^2}{m_o}\cdot\left\{\frac{1}{2\omega(\omega+i\Gamma_{el}+\omega_c)}+\frac{1}{2\omega(\omega+i\Gamma_{el}-\omega_c)}\right\}$$

$$\cdot\left\{\left(\frac{2}{3m_t}+\frac{1}{3m_l}\right)-\left(\frac{2}{3m_t}+\frac{1}{3m_l}\right)^{-1}\right\}. \qquad (10.1.3)$$

Taking eigenvalue of Eq.(10.1.3), we obtain the effective dielectric constant of the cyclotron active mode

$$\varepsilon_{CRA}=\varepsilon_{xx}-i\varepsilon_{xy}$$

$$= \varepsilon_l - \frac{4\pi ne^2}{m_o} \cdot \frac{1}{\omega(\omega + i\Gamma_{el} - \omega_c)} \cdot \frac{1}{2} \left\{ \left(\frac{2}{3m_t} + \frac{1}{3m_l} \right) + \frac{(2m_t + m_l)m_c}{3m_t^2 m_l} \right\}$$

$$- \frac{4\pi ne^2}{m_o} \cdot \frac{1}{\omega(\omega + i\Gamma_{el} + \omega_c)} \cdot \frac{1}{2} \left\{ \left(\frac{2}{3m_t} + \frac{1}{3m_l} \right) - \frac{(2m_t + m_l)m_c}{3m_t^2 m_l} \right\} \qquad (10.1.4)$$

and the effective dielectric constant of the cyclotron inactive mode

$$\varepsilon_{CRI} = e_{xx} + i\varepsilon_{xy}$$

$$= \varepsilon_l - \frac{4\pi ne^2}{m_o} \cdot \frac{1}{\omega(\omega + i\Gamma_{el} + \omega_c)} \cdot \frac{1}{2} \left\{ \left(\frac{2}{3m_t} + \frac{1}{3m_l} \right) + \frac{(2m_t + m_l)m_c}{3m_t^2 m_l} \right\}$$

$$- \frac{4\pi ne^2}{m_o} \cdot \frac{1}{\omega(\omega + i\Gamma_{el} - \omega_c)} \cdot \frac{1}{2} \left\{ \left(\frac{2}{3m_t} + \frac{1}{3m_l} \right) - \frac{(2m_t + m_l)m_c}{3m_t^2 m_l} \right\} . \qquad (10.1.5)$$

'Controur map' of ε_{CRA} and ε_{CRI} is given in Fig. 10-1-1. Under the lossless limit situation, 0's of ε_{CRA} and ε_{CRI} correspond to the dips in the magnetoplasma reflection spectra. The effective dielectric constant ε_{CRA} and ε_{CRI}, and transmission versus magnetic field are shown in Fig. 10-1-2.

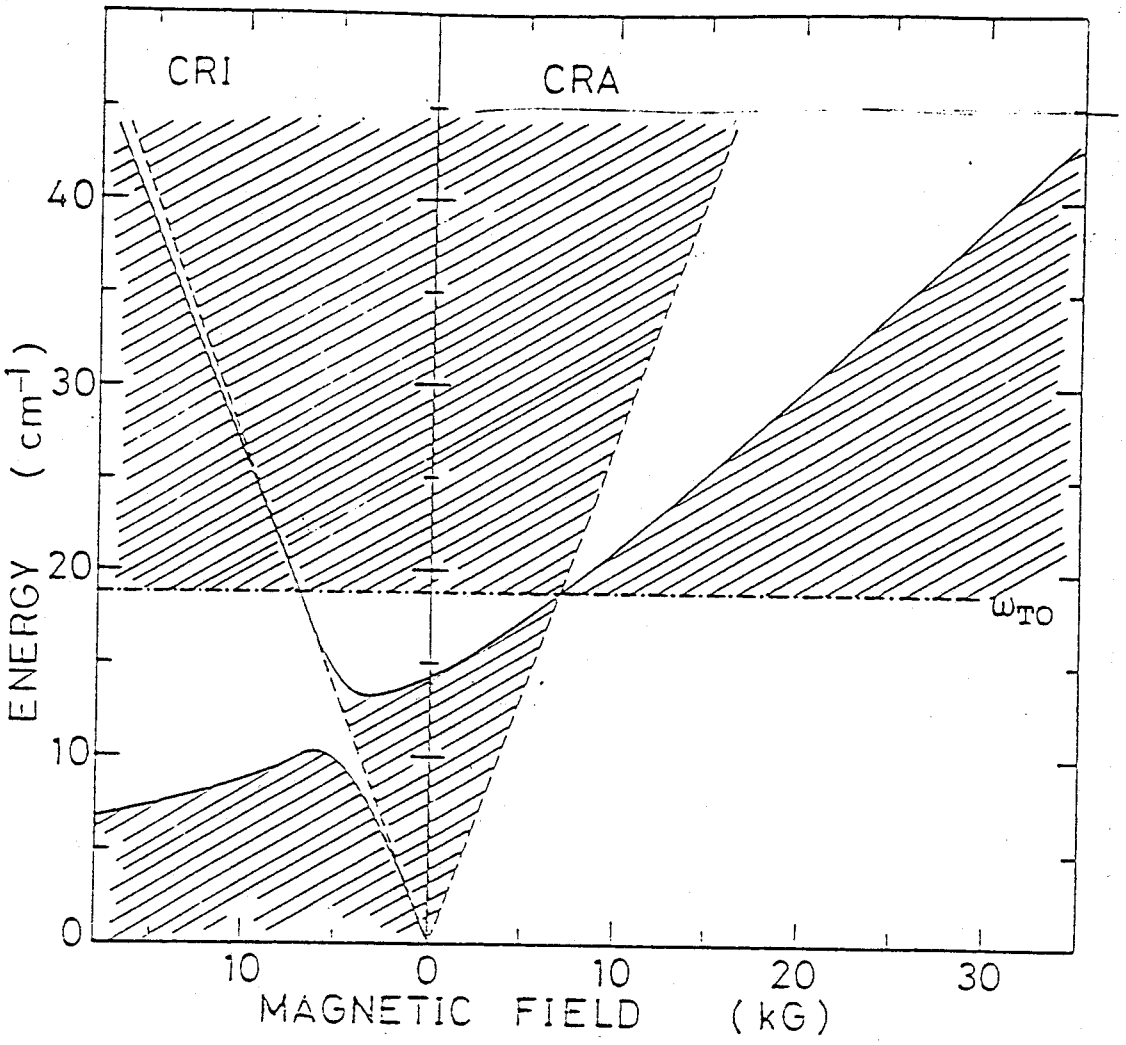

FIG. 10-1-1 Contour map of ε_{CRA} and ε_{CRI} for the Faraday configuration with H//<001>(by Ichiguchi). The solid and broken lines show the location of the dielectric anomalies and poles, respectively. Shaded areas represent regions of negative ε, where reflectivity is unity. The parameters used in calculation are: m_t = 0.0218m_o, K = 11, n = $2.0\times10^{17}cm^{-3}$, ω_{TO} = $18.8cm^{-1}$, ω_{LO} = $114cm^{-1}$ and ε_∞ = 34.(ref.115)

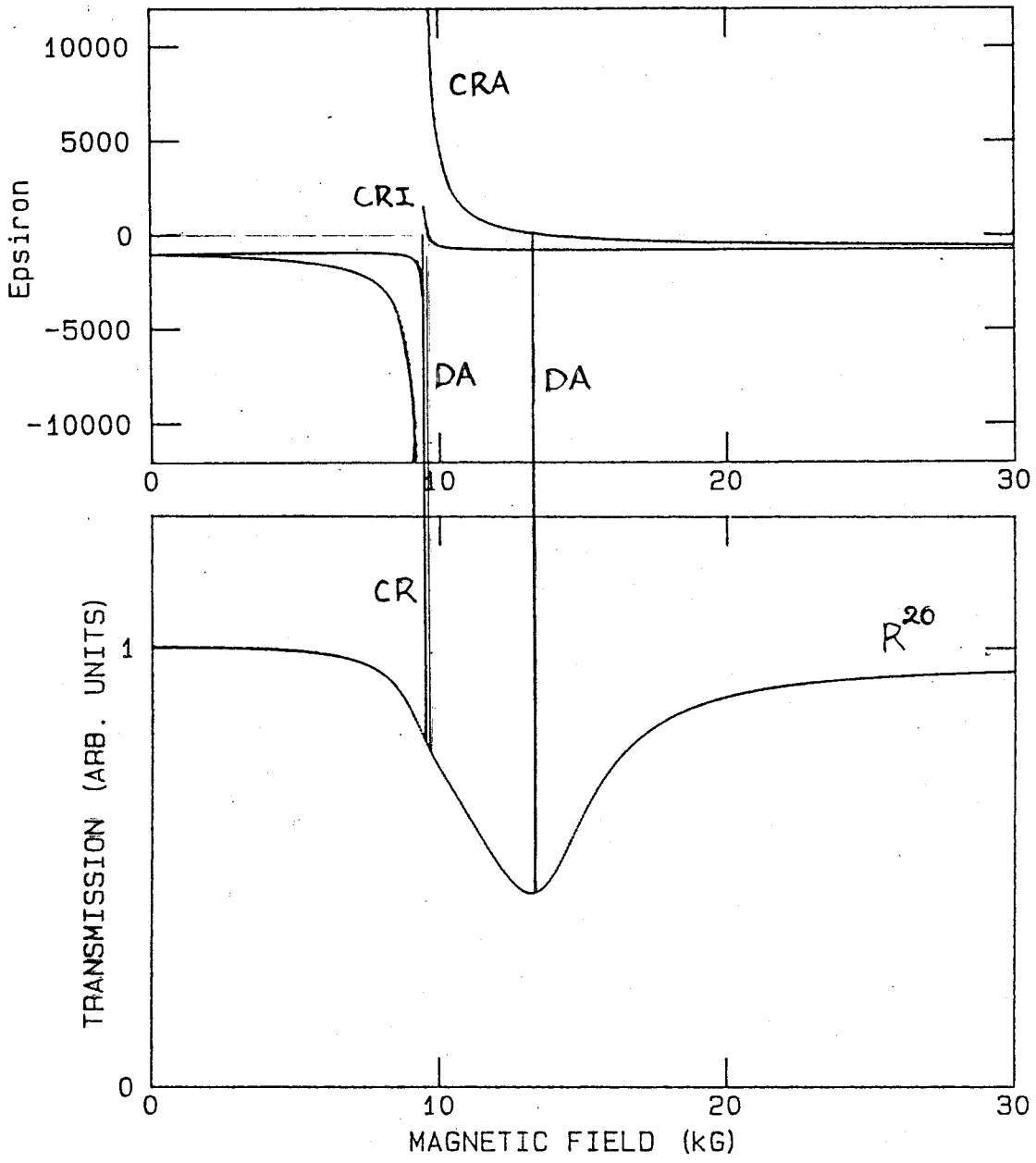

FIG. 10-1-2 Real parts of dielectric constant of ε_{CRA} and ε_{CRI}, and Transmissivity of stripline(R^{20}).

§10-2 Magnetoplasma dielectric tensor of IV-VI compounds in Voigt configuration

Let us derive the dielectric tensor in Voigt configuration

$H \parallel x$

$q \parallel z$

From Eq.(4.3.7), cyclotron masses of A, B, C, and D valleys, m_{ca}, m_{cb}, m_{cc}, and m_{cd}, are given by

$$m_{ca} = \left\{ m_t^2 m_l / (\tfrac{1}{3} m_t + \tfrac{2}{3} m_l) \right\}^{1/2},$$

$$m_{cb} = m_{ca},$$

$$m_{cc} = \sqrt{m_t m_l},$$

and

$$m_{cd} = m_{cc}.$$

(10.2.1)

From Eq.(4.3.8), cyclotron frequency of A, B, C, and D valley, ω_{ca}, ω_{cb}, ω_{cc}, and ω_{cd} are given by

$$\omega_{ca} = \frac{eH}{m_o m_{ca} c},$$

$$\omega_{cb} = \omega_{ca},$$

$$\omega_{cc} = \frac{eH}{m_o m_{cc} c},$$

and

$$\omega_{cd} = \omega_{cc}.$$

(10.2.2)

Using Eqs.(3.1.12), (3.2.8), and (3.3.6), we obtain the components of the dielectric tensor

$$\varepsilon_{xx}=\varepsilon_1$$

$$-\frac{2\pi ne^2}{m_o}\cdot\frac{1}{1(\omega+i\Gamma_{el})}\cdot\left\{\left(\frac{1}{3}m_t+\frac{2}{3}m_l\right)^{-1}+\frac{1}{m_t}\right\}$$

$$-\frac{2\pi ne^2}{m_o}\cdot\left\{\frac{1}{2\omega(\omega+i\Gamma_{el}+\omega_{ca})}+\frac{1}{2\omega(\omega+i\Gamma_{el}-\omega_{ca})}\right\}$$

$$\cdot\left\{\left(\frac{1}{3m_t}+\frac{2}{3m_l}\right)-\left(\frac{1}{3}m_t+\frac{2}{3}m_l\right)^{-1}\right\},$$

$$\varepsilon_{yy}=\varepsilon_1-\frac{2\pi ne^2}{m_o}\cdot\left\{\frac{1}{2\omega(\omega+i\Gamma_{el}+\omega_{ca})}+\frac{1}{2\omega(\omega+i\Gamma_{el}-\omega_{ca})}\right\}\frac{1}{m_t}$$

$$-\frac{2\pi ne^2}{m_o}\cdot\left\{\frac{1}{2\omega(\omega+i\Gamma_{el}+\omega_{cc})}+\frac{1}{2\omega(\omega+i\Gamma_{el}-\omega_{cc})}\right\}\left\{\frac{1}{3m_t}+\frac{2}{3m_l}\right\},$$

$$\varepsilon_{zz}=\varepsilon_1-\frac{2\pi ne^2}{m_o}\cdot\left\{\frac{1}{2\omega(\omega+i\Gamma_{el}+\omega_{ca})}+\frac{1}{2\omega(\omega+i\Gamma_{el}-\omega_{ca})}\right\}\left\{\frac{2}{3m_t}+\frac{1}{3m_l}\right\}$$

$$-\frac{2\pi ne^2}{m_o}\cdot\left\{\frac{1}{2\omega(\omega+i\Gamma_{el}+\omega_{cb})}+\frac{1}{2\omega(\omega+i\Gamma_{el}-\omega_{cb})}\right\}\left\{\frac{2}{3m_t}+\frac{1}{3m_l}\right\},$$

$$\varepsilon_{yz}=-\frac{4\pi n_a e^2}{m_o}\cdot\left\{\frac{1/i}{2\omega(\omega+i\Gamma_{el}+\omega_{ca})}-\frac{1/i}{2\omega(\omega+i\Gamma_{el}-\omega_{ca})}\right\}\frac{(1m_t+2m_l)m_{cb}}{3m_t{}^2m_l}$$

$$=-\frac{4\pi ne^2}{m_o}\cdot\left\{\frac{1/i}{2\omega(\omega+i\Gamma_{el}+\omega_{cb})}-\frac{1/i}{2\omega(\omega+i\Gamma_{el}-\omega_{cb})}\right\}\frac{1}{m_{cc}}\ ,$$

$$\varepsilon_{yx} = \varepsilon_{xy} = 0\ ,$$

$$\varepsilon_{zy} = -\varepsilon_{yz}\ ,$$

and

$$\varepsilon_{xz} = \varepsilon_{zx} = 0\ .$$

(10.2.3)

Taking eigenvalue of Eq.(3.1.17), we obtain the effective dielectric constant of the extra ordinary mode

$$\varepsilon_{EXT}=\varepsilon_{yy}-\frac{\varepsilon_{yz}\varepsilon_{zy}}{\varepsilon_{zz}} \qquad (10.2.4)$$

and the effective dielectric constant of the ordinary mode

$$\varepsilon_{ORD}=e_{xx}. \qquad (10.2.5)$$

'Controur map' of ε_{ORD} and ε_{EXT} is given in Fig. 10-2-1. Under the lossless limit situation, 0's of ε_{ORD} and ε_{EXT} correspond to the dips in the magnetoplasma reflection spectra. Fig. 10-2-2 shows the angular dependence of positions of poles and 0's.

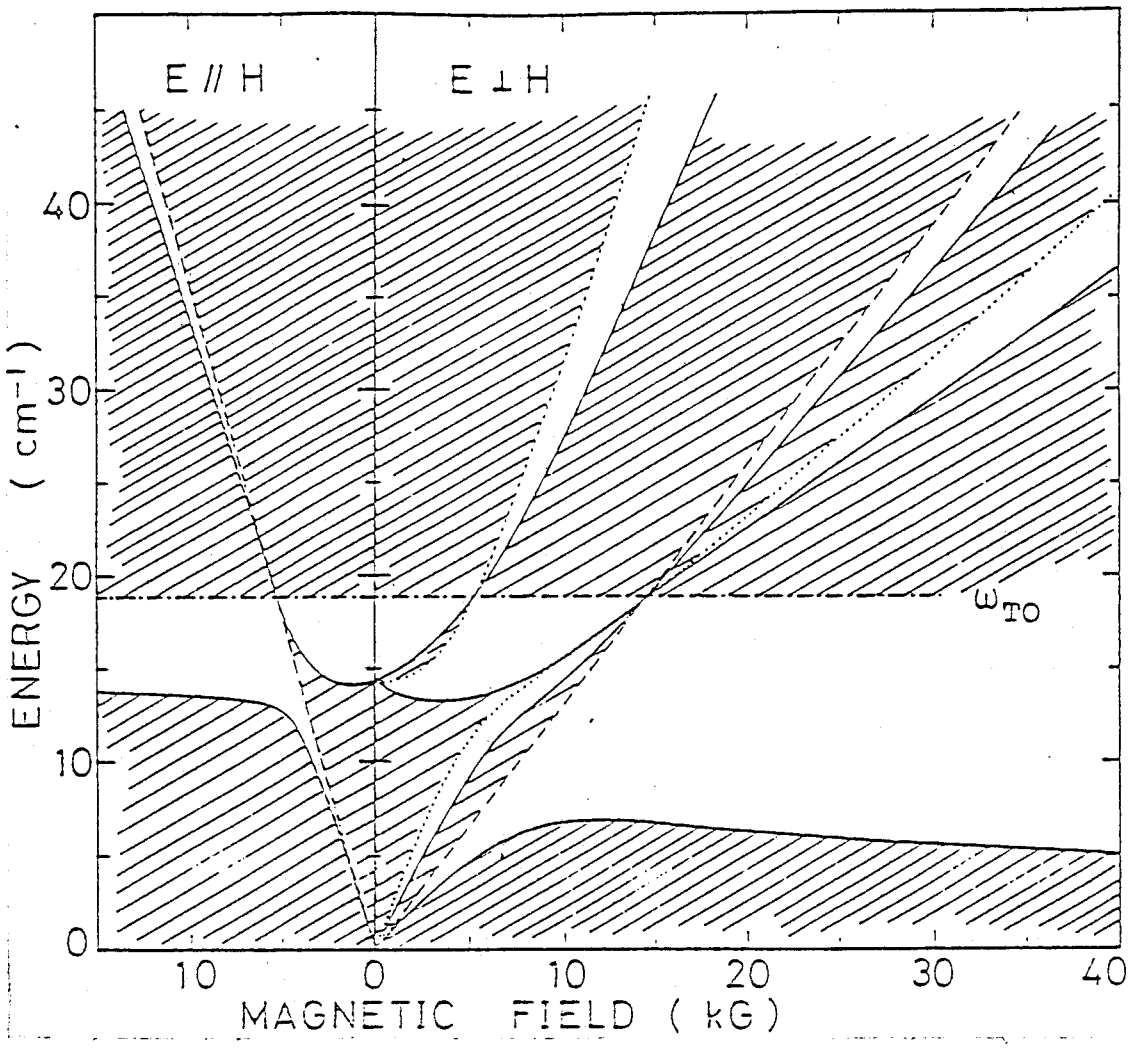

FIG. 10-2-1 Contour map of ε_{ORD} and ε_{EXT} for the Voigt configuration with H//<110>(by Ichiguchi ref. 115). The solid and dotted (or broken) lines denote the 0's and ∞'s of ε, respectively: the positions of dielectric anomalies and poles. The broken lines also show the cyclotron resonance positions. The shaded area indicate the regions where ε is negative. The parameters used in calculation are: $m_t = 0.0218m_0$, k = 11, $n = 2.0\times10^{17}cm^{-3}$, $\omega_{TO} = 18.8cm^{-1}$, $\omega_{LO} = 114cm^{-1}$ and $\varepsilon_\infty = 34$.(ref.115)

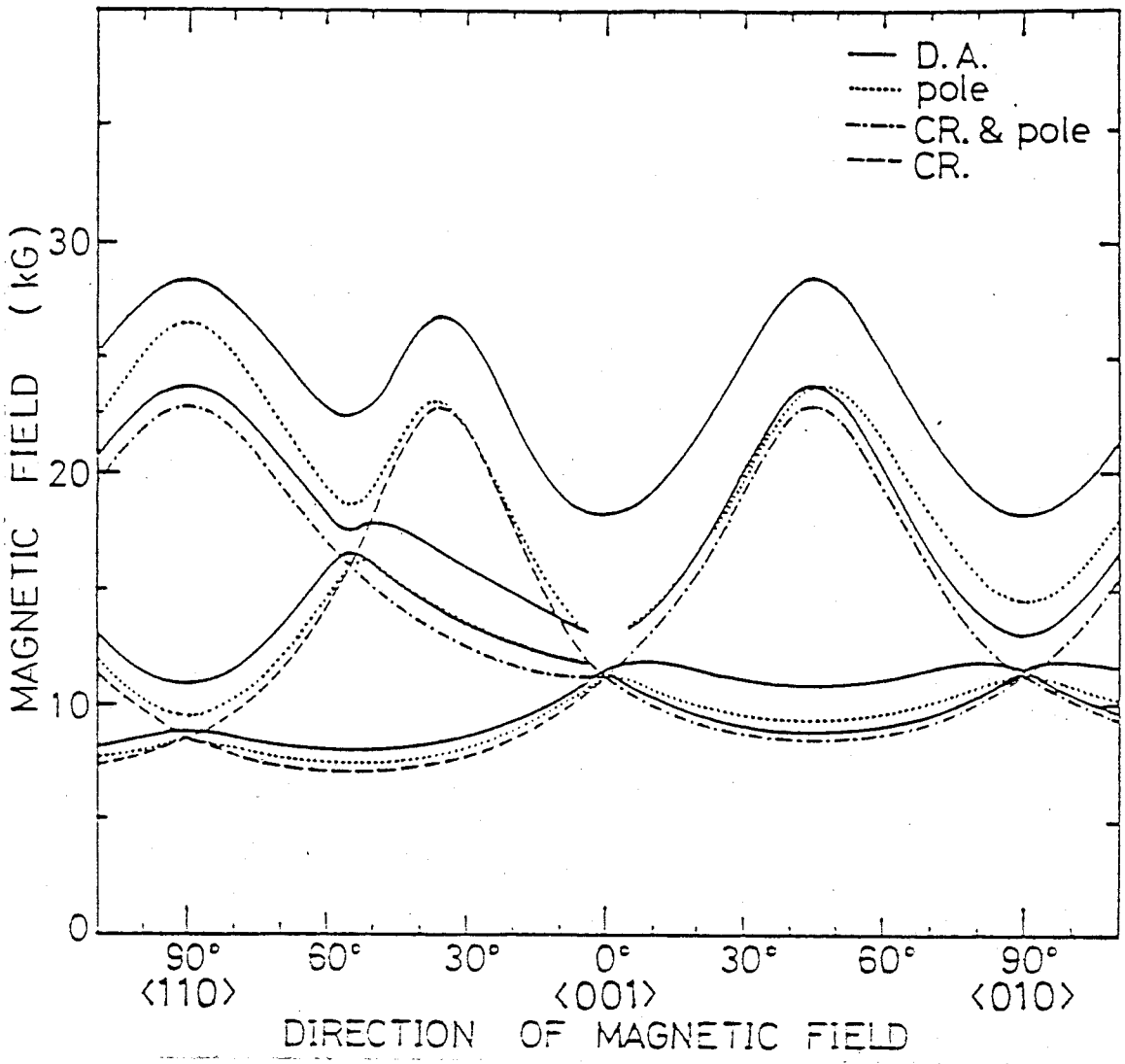

FIG. 10-2-2 Directional dependence of dielectric anomaly, pole, and uncoupled cyclotron resonance field in 337μm radiation(by Ichiguchi ref.115). Magnetic field is applied along (010) or ($\bar{1}$10) plane: left or right part. There are three kinds of cyclotron masses when magnetic field direction is in ($\bar{1}$10) plane while two kinds of cyclotron masses exist when magnetic field direction is in (010) plane. In general, there are four branches of dielectric anomaly(ε = 0) and four poles (ε = ∞). Parameters used in calculation are:m_t = 0.022m_o, K = 10.5, n = $1.7\times10^{17}cm^{-3}$ and $\varepsilon_l(\omega)$ = -820.

§11 EXPERIMENTAL PROCEDURE

§11-1 Sample preparation

Single crystal $Pb_{1-x}Sn_xTe$ has been made using the vapor transport method. Bridgeman method and the solution growth method make large differences in compositions between the source and the obtained sample because the solid phase line and liquid phase line separated from each other in phase diagram. But the difference in the vapor transport method is in the range of 1~2%. The preparation procedure is as follows.

First, Pb, Sn, and Te(their purity is six 9s) are cleaned by etching liquid. They are weighed in the atomic rate 1-x:x:1 taking into account buoyancy due to atmosphere and put into clean quartz ampoule. Next, we evacuate at 10^{-6} torr and raise temperature of the ampoule to 200°C to eliminate contaminants adsorbed at an inner surface of quartz ampoule and surfaces of Pb, Sn, and Te. After 2 hours, we seal the ampoule and put it into an electronic furnace and raise the temperature to 950°C which is higher by 30 degrees than the melting point of PbTe. The ampoule must be vibrated well once an hour to mix the molten materials. After 8 hours it is thrown into water cooled by crushed ice and quench the ampoule.

Next we take out the source and put it into another quartz ampoule. After evacuating to 10^{-6} torr and raise temperature of the ampoule to 200°C in 2 hours, we seal the ampoule and set in

an 840°C electronic furnace having a temperature gradient of 3 degrees between ends of ampoule. After one week a 1 cm^3 single crystal can be obtained. In this temperature the stoichiometry of the crystal shifts into side of Te excess and metal vacancies exist at 10^{19}~10^{20} cm^{-3}.

For doping In, the isothermal annealing has been used. After soaking the single crystal $Pb_{1-x}Sn_xTe$ in the etching liquid, (100) crystal face can be found out. We slice it into 1mm thickness wafer along the face. After etching the the sample, the wafer is put into quartz ampoule, with etched indium. After 2 hours taking gas out at 500°C, we seal the ampoule filled with 250Torr Ar gas and set it in an electric furnace. (Argon gas protect the sublimation of $Pb_{1-x}Sn_xTe$.) To get the uniform diffusion of indium atoms in $Pb_{1-x}Sn_xTe$, the ampoule temperature are controlled at 700°C in about ten days, at 650°C in about 7 days and at 600°C in about 8 days.

The samples prepared in this method have been characterized using chemical analysis and Auger electron spectroscopy analysis. Indium atoms exist much near surface (1~5%).

§11-2 Strip-line

Submillimeter magneto-optics is one of the most reliable methods to investigate the electronic structure near band edge and the plasma properties. Usually, the magnetic field dependence of transmissivity and reflectivity is measured in submillimeter magneto-spectroscopy. It is difficult to obtain thin samples from the bulk sample to get sufficient transmission through it, because their carrier density is large and wave length of probing light is in the reststrahlen region. Reflectivity is near 100% and its change due to applied magnetic field scanning is very small for the same reasons. In this case the strip-line method is effective. The strip-line method gives a strong contrast to change of reflection by using multiple reflection of the light through the narrow space between the bulk sample and metal(for example brass, copper). The spacing between the sample and metal must be set below half of wave length of the light(see Fig.11-2-1).

The strip-line method is applicable in various materials[116-119] and has been introduced in $Pb_{1-x}Sn_xTe$[115] by some authors. The transmission spectra of strip-line must be analyzed taking into account the mode problem as the same way in the wave guide problem. This problem has been solved and the transmission spectra obtained from the calculation is almost the same as that based on multiple reflection. Therefore we have carried out transmission spectra analysis by reproducing to nth order of reflectivity obtained from the dielectric function.

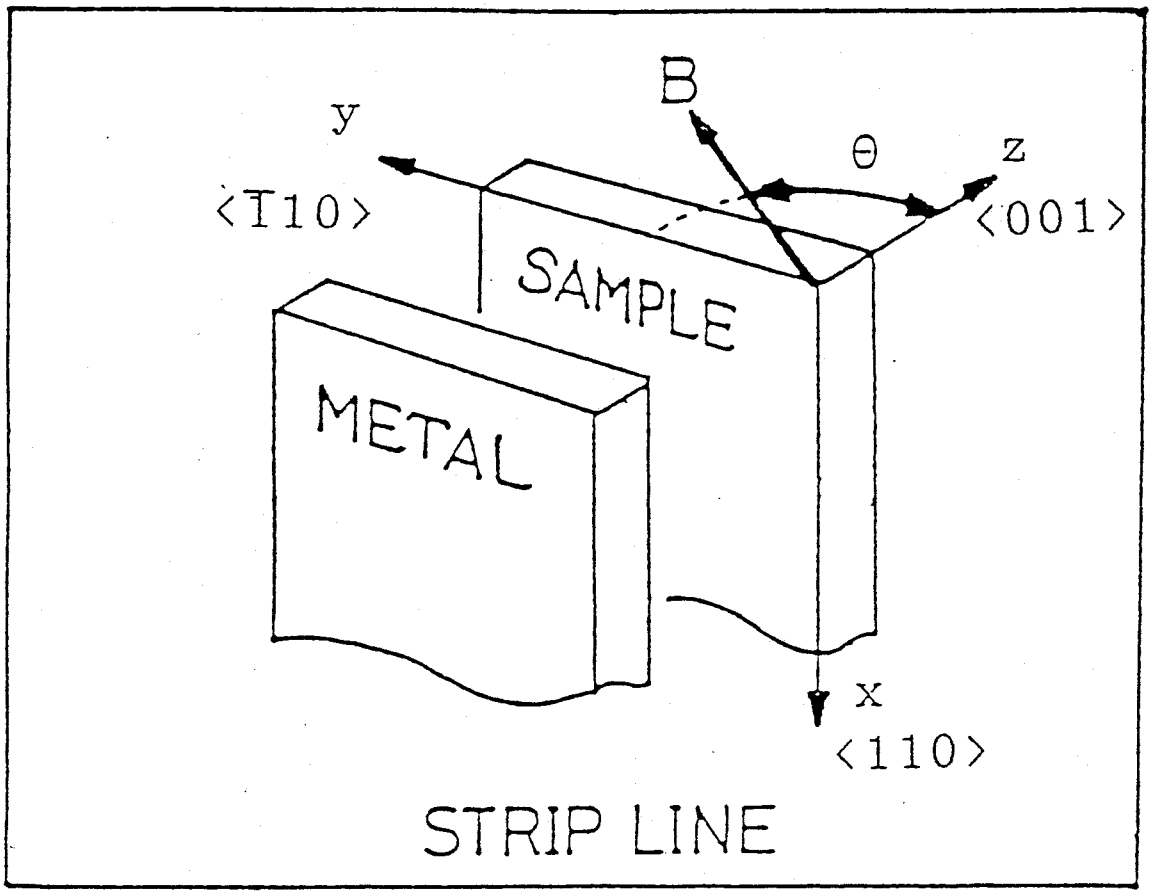

FIG. 11-2-1 Geometry of stripline.

§12 EXPERIMENTAL RESULTS AND ANALYSIS OF MAGNETOPLASMA EXCITAITON SPECTRA OF $Pb_{1-x}Sn_xTe$ DOPED WITH In

§12-1 Analysis in the case x=0.23

For $Pb_{0.77}Sn_{0.23}Te$/In, we obtained the dependence of magnetoplasma transmission spectra on the magnetic field directions(Fig. 12-1-1), temperatures(Figs. 12-1-2 and 12-1-3), and laser wave lengthes(Figs. 12-1-4 and 12-1-5). Each dip in spectra corresponds to dielectric anomaly. As shown in Figs. 12-1-2 and 12-1-3, the spectra changes abruptly flat ones and the magnetic field at dielectric anomaly makes toward low with increasing temperature from 15K to 20K. Above 20K, the field dependence disappears.

To obtain carrier density and mass of $Pb_{1-x}Sn_xTe$, we have made line shape fitting using the result of section 10. Carrier density, mass and ω_{TO} have been determined from the laser wavelength dependence and field direction dependence of spectra consistently. Next we have obtained the temperature dependence of carrier density by changing only a carrier density parameter (broken lines are calculated spectra in Figs. 12-1-2, 12-1-2, 12-1-3, 12-1-4, and 12-1-5).

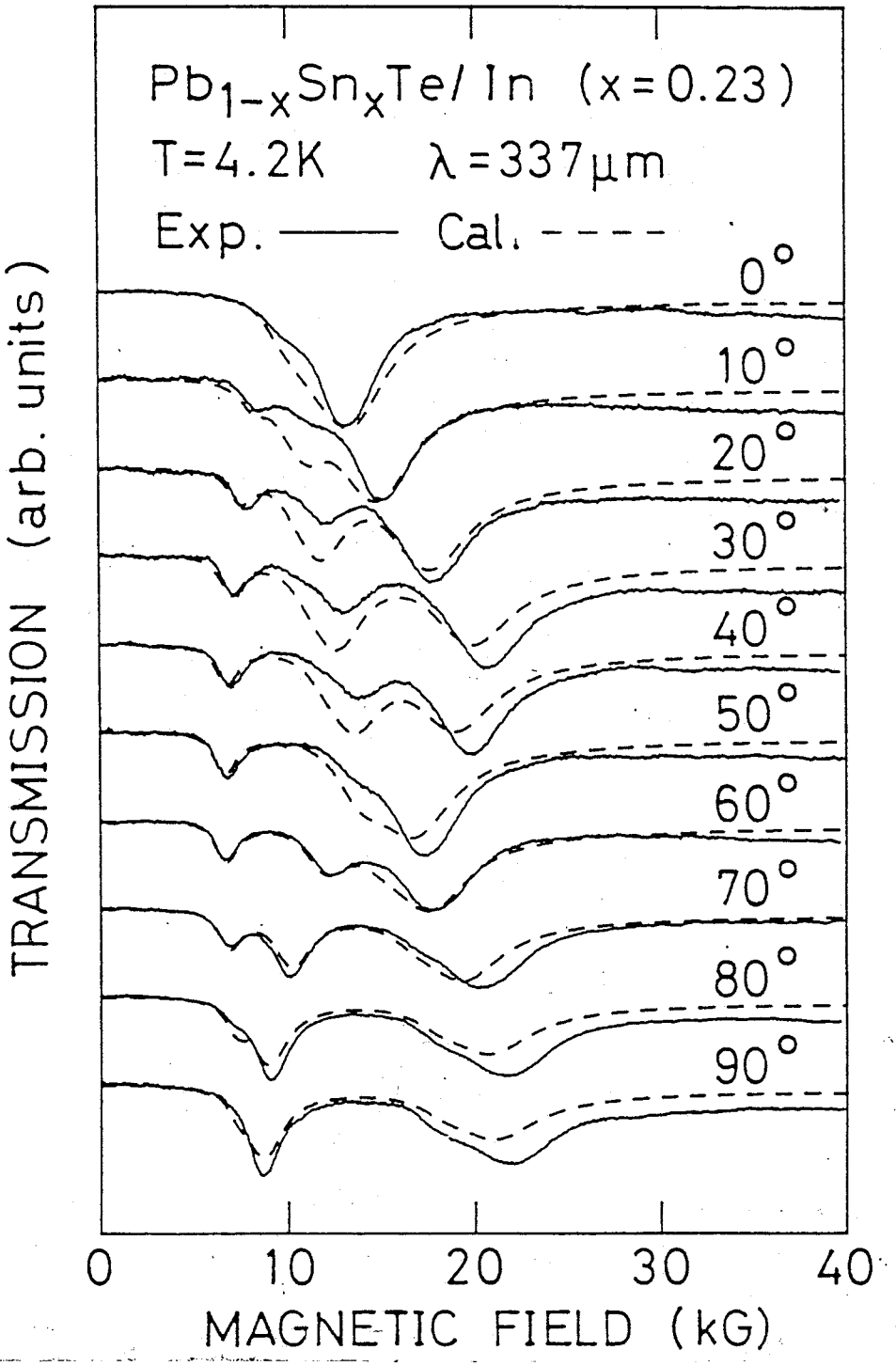

FIG. 12-1-1 Measured (solid lines) and calculated (dashed curves) magnetoplasma transmission spectra with 337μm laser light at 4.2K. The magnetic field direction is changed from 0 deg along <001>(the Faraday configuration) to 90 deg along <110>(the Voigt configuration).

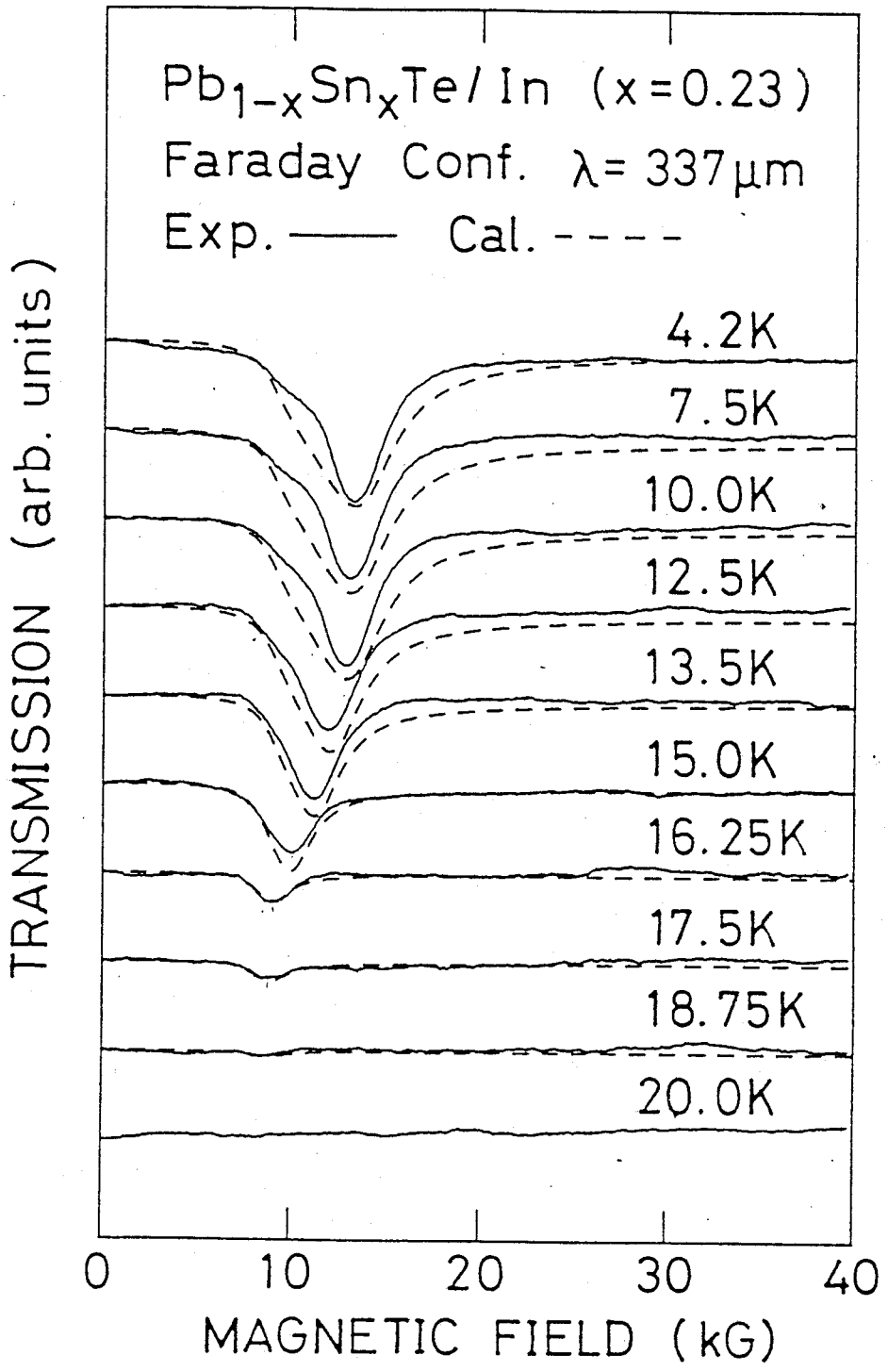

FIG. 12-1-2 Temperature dependence of magnetoplasma transmission spectra with 337μm laser light in the Faraday configuration.

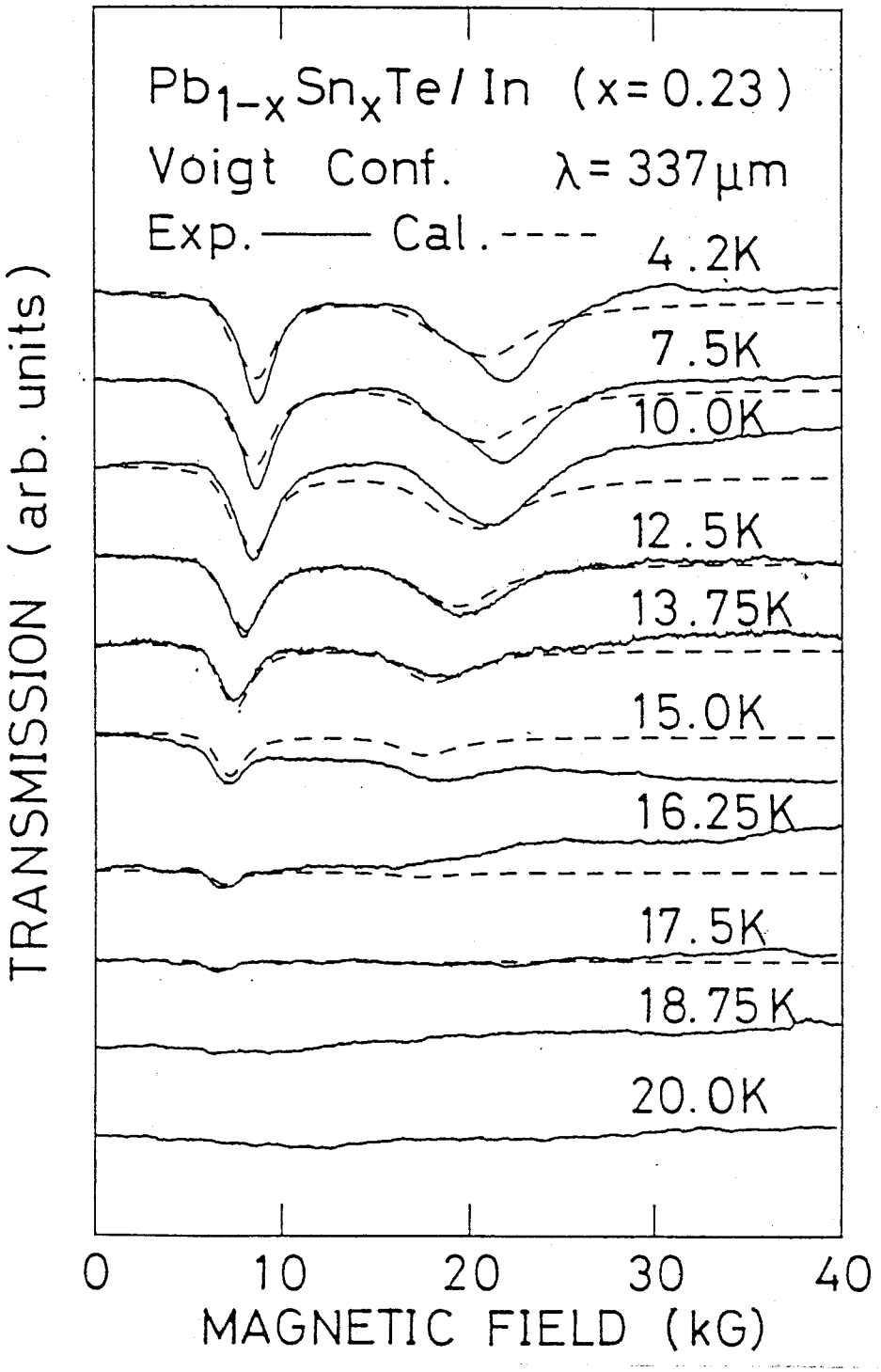

FIG. 12-1-3 Temperature dependence of magnetoplasma transmission spectra with 337μm laser light in the Voigt configuration.

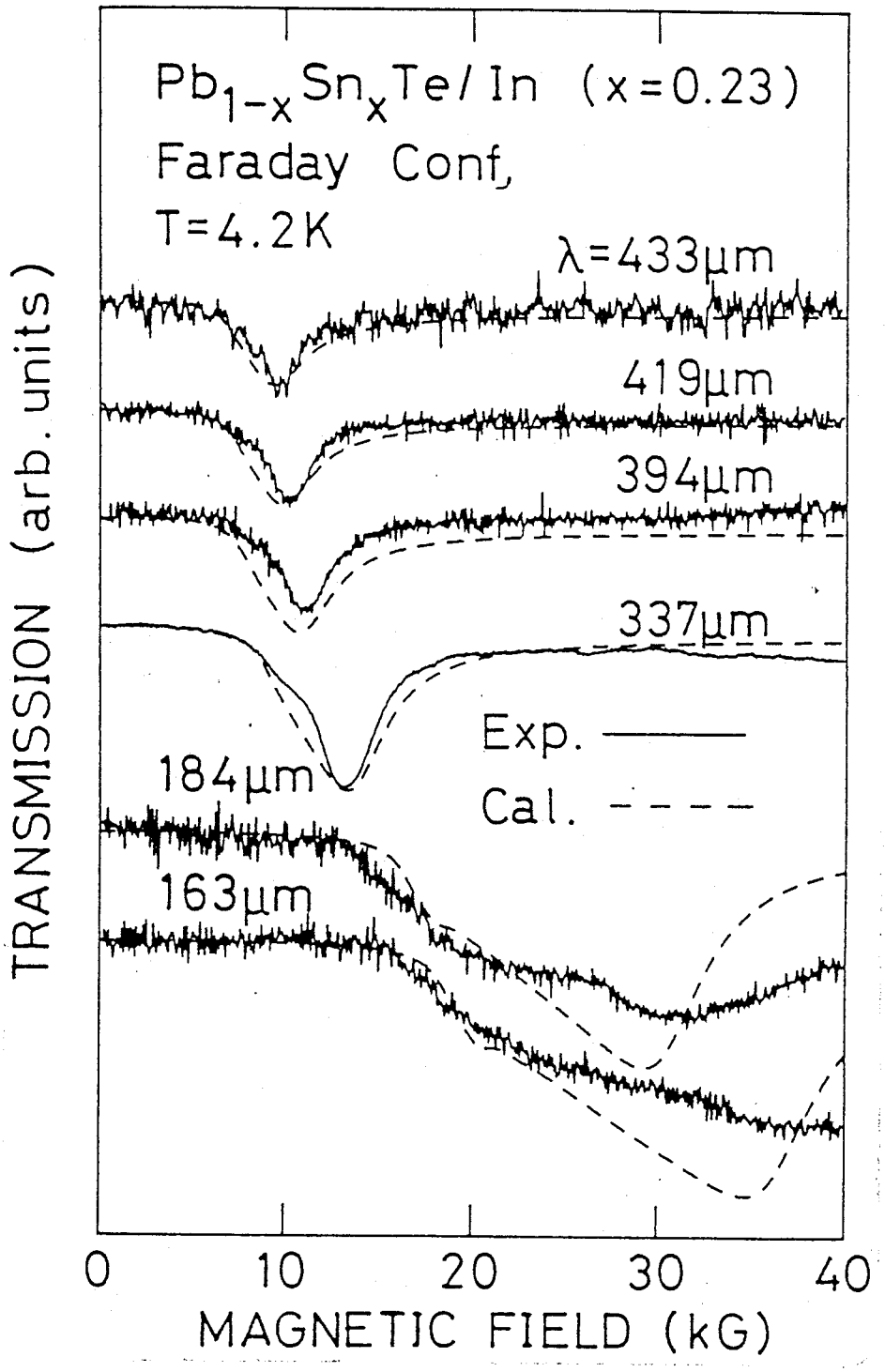

FIG. 12-1-4 Dependence of magnetoplasma transmission spectra on laser wave length in the Faraday configuration.

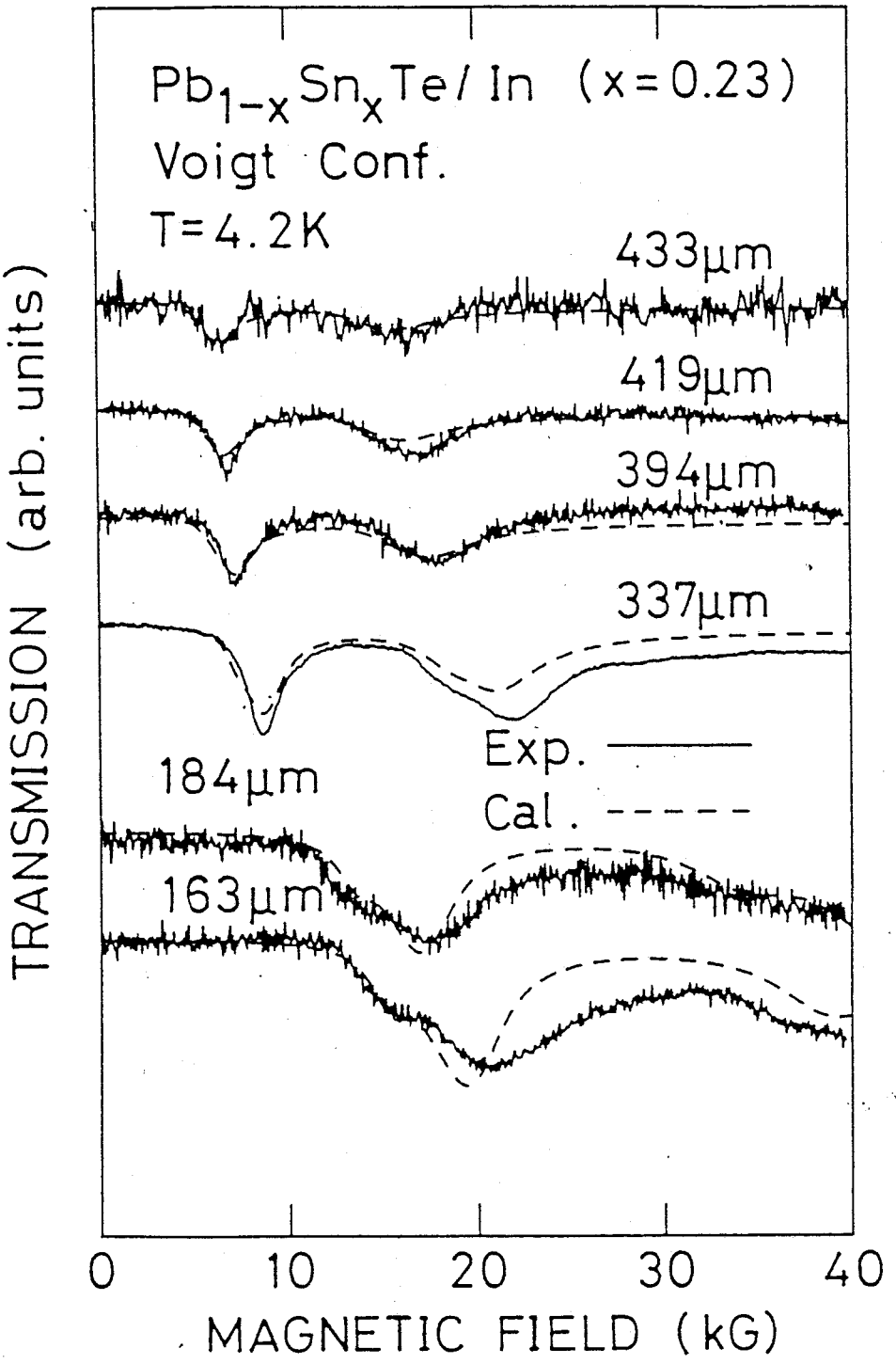

FIG. 12-1-5 Dependence of magnetoplasma transmission spectra on laser wave length in the Voigt configuration.

12-2 Temperature dependence of magnetoplasma spectra of x=0.21, 0.23, 0.25, 0.28, 0.35

For $Pb_{1-x}Sn_xTe$/In with various tin compositions, the temperature dependences of magnetoplasma spectra are shown in Figs. 12-2-1, 12-2-2, 12-2-3, 12-2-4, and 12-2-5. The changes of spectra are abrupt for all samples above 15K. For samples with tin composition of 0.21 and 0.35, the pinning Fermi energy situates in the conduction and valence band,respectively, so carriers do remain above 20K. Hence the spectra can be measured above 20K. The experimental results involve the dynamical process of photoconduction. In next section we will show this dependence well agree with the results of rate equations based upon the model that electrons relax from conduction or valence band to In levels by thermal activation process and tunneling process (which has no temperature dependence). This model are also understandable in terms of Anderson's negative U model. The dependence of ω_{TO} and band edge mass dependence on Sn composition is also discussed.

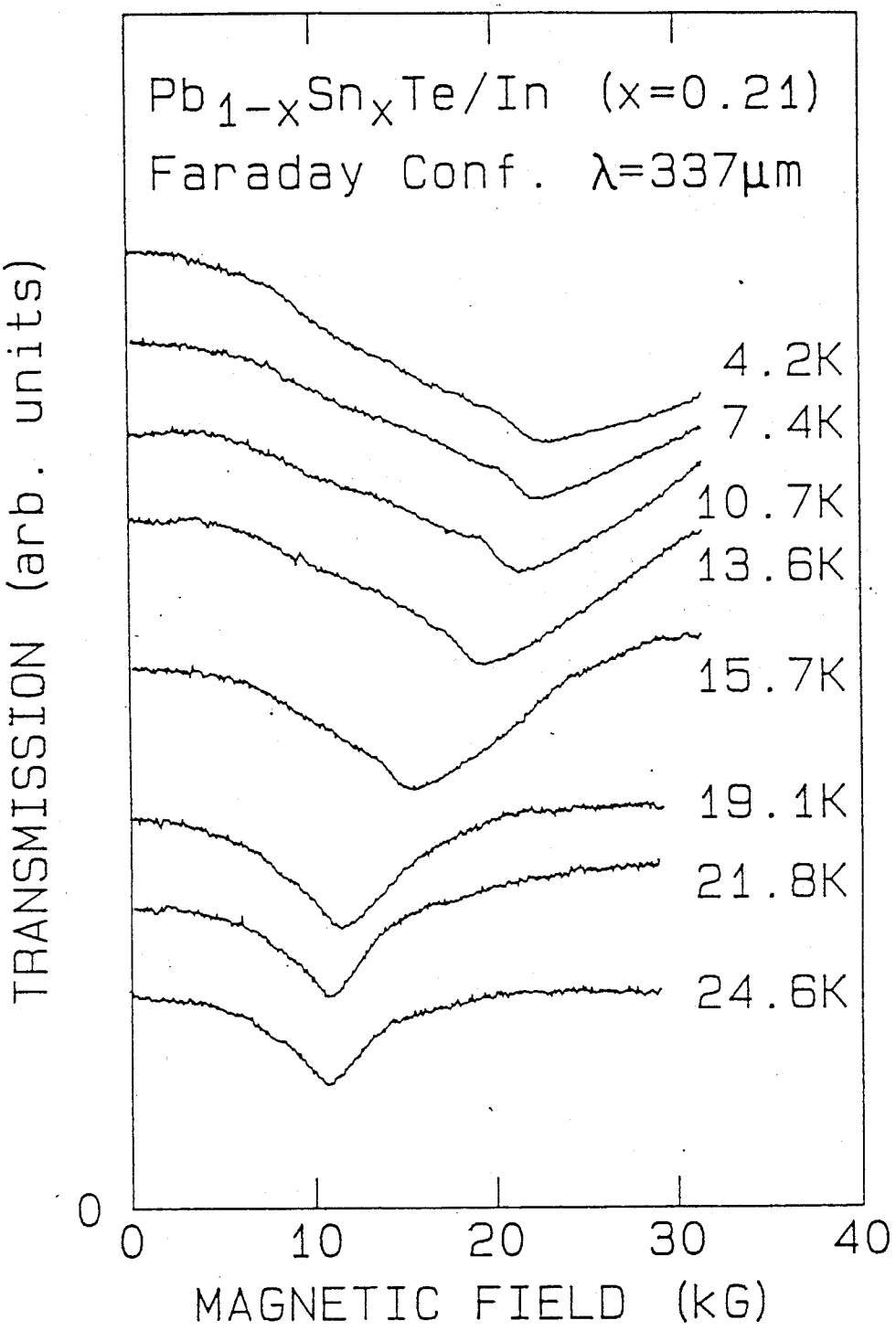

FIG. 12-2-1 Temperature dependence of magnetoplasma transmission spectra with 337μm laser light in the Faraday configuration.

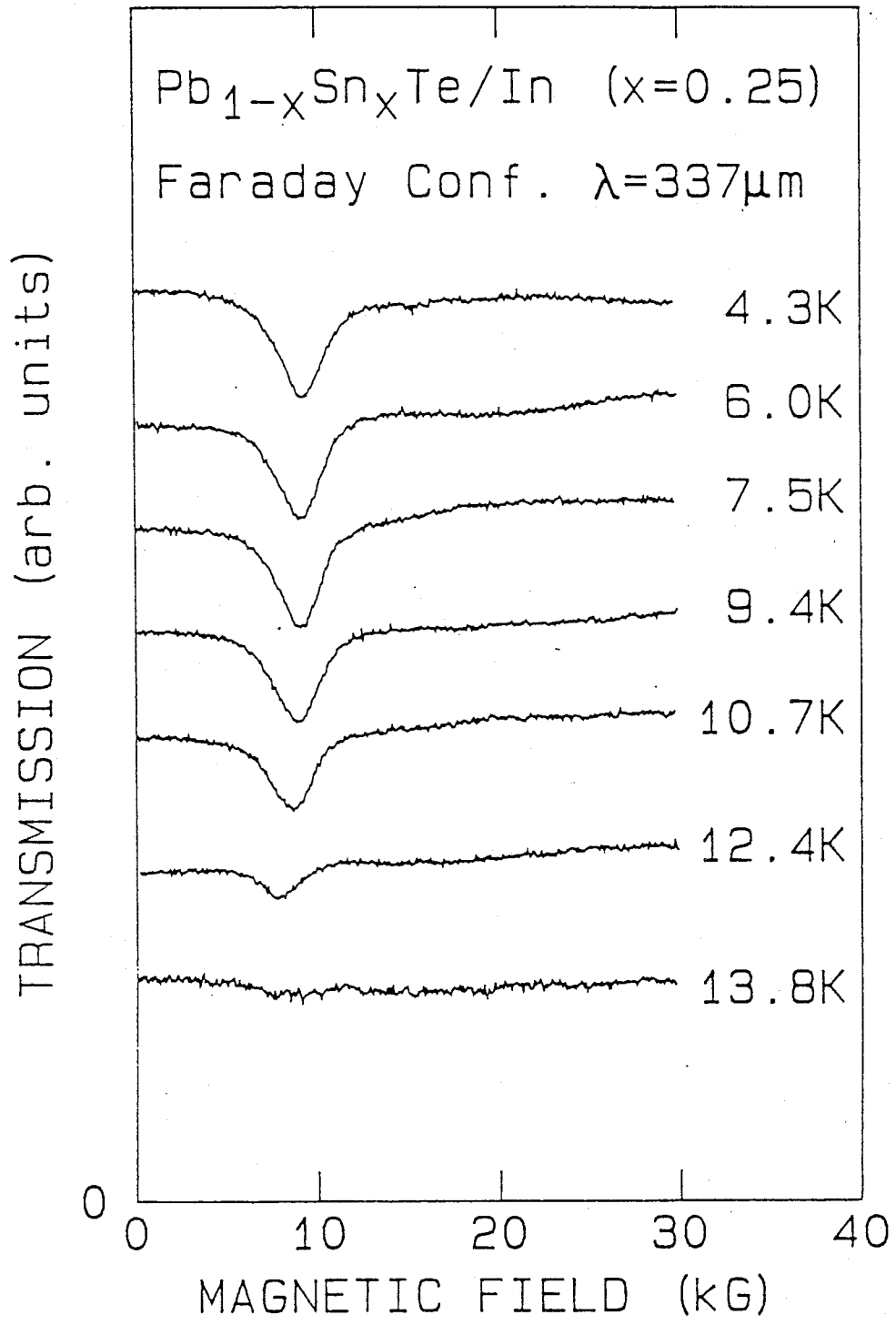

FIG. 12-2-2 Temperature dependence of magnetoplasma transmission spectra with 337μm laser light in the Faraday configuration.

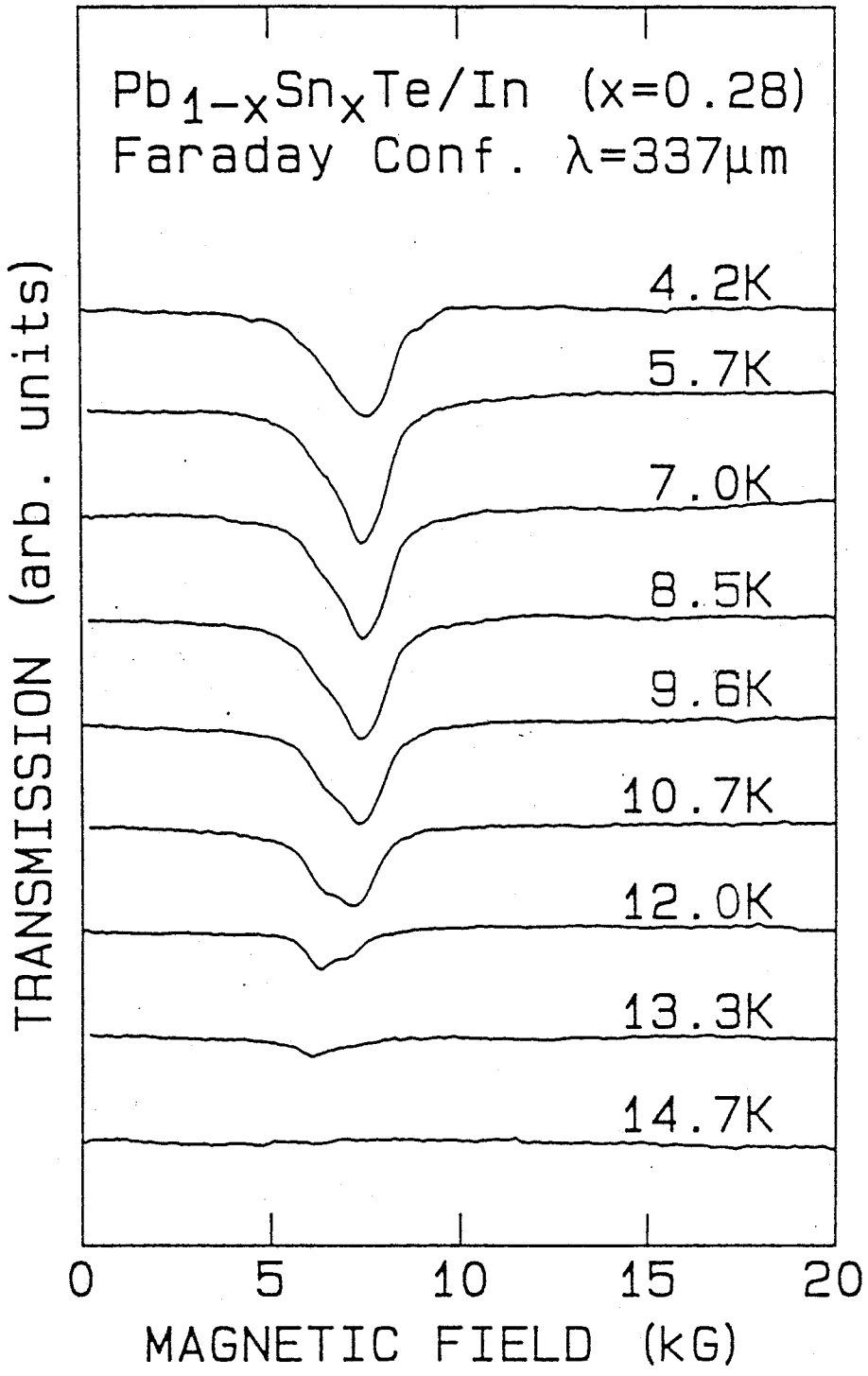

FIG. 12-2-3 Temperature dependence of magnetoplasma transmission spectra with 337μm laser light in the Faraday configuration.

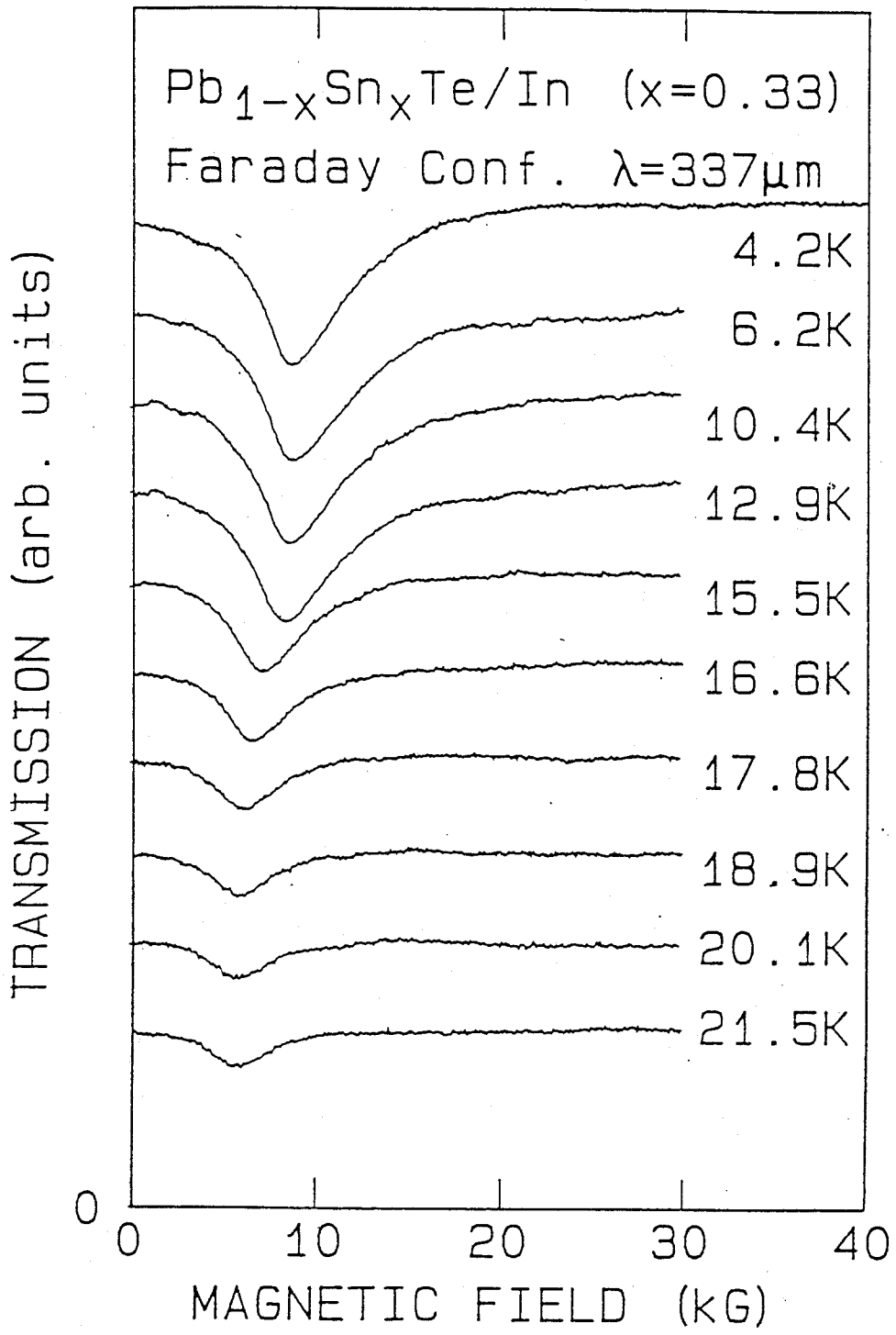

FIG. 12-2-4 Temperature dependence of magnetoplasma transmission spectra with 337μm laser light in the Faraday configuration.

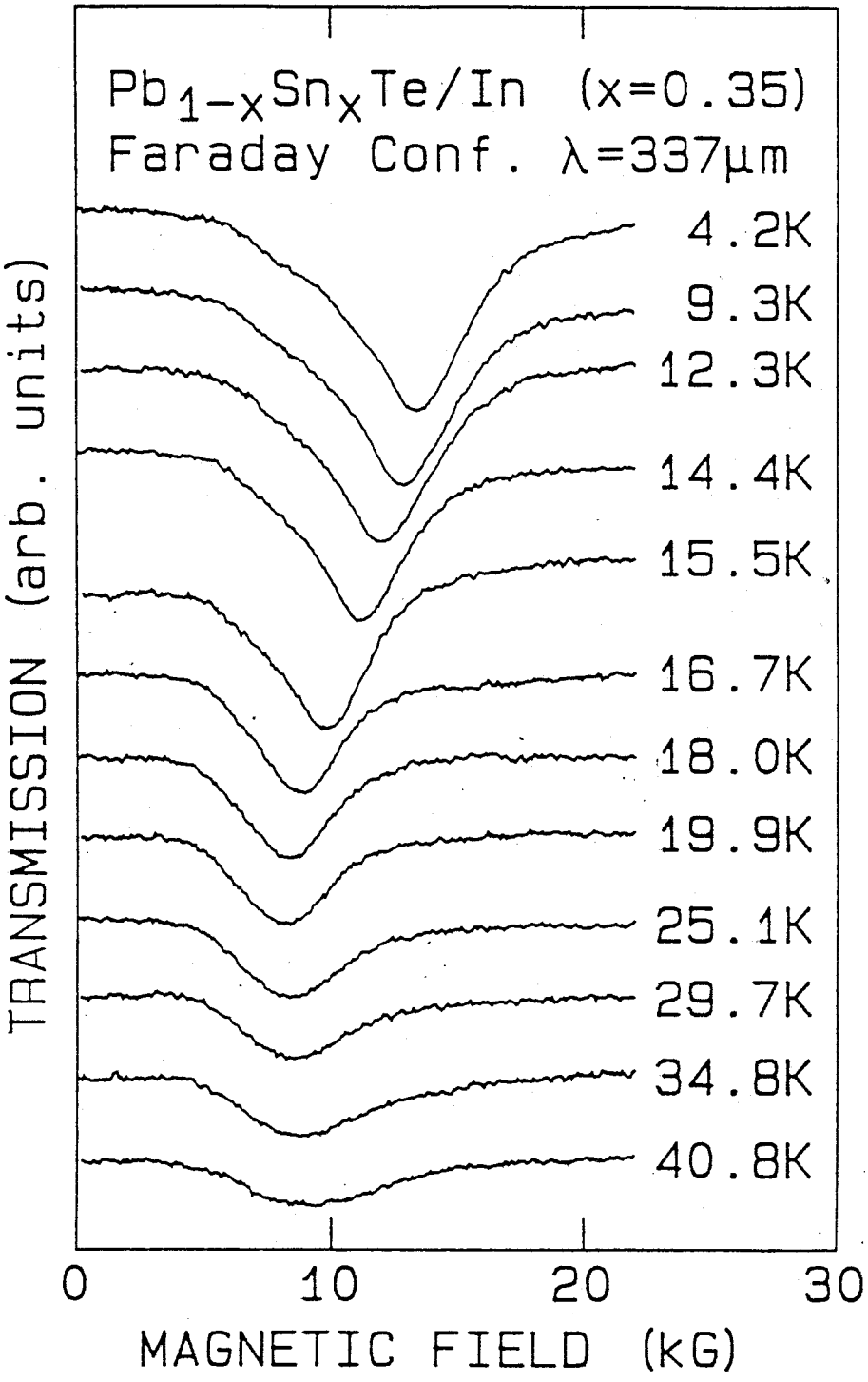

FIG. 12-2-5 Temperature dependence of magnetoplasma transmission spectra with 337μm laser light in the Faraday configuration.

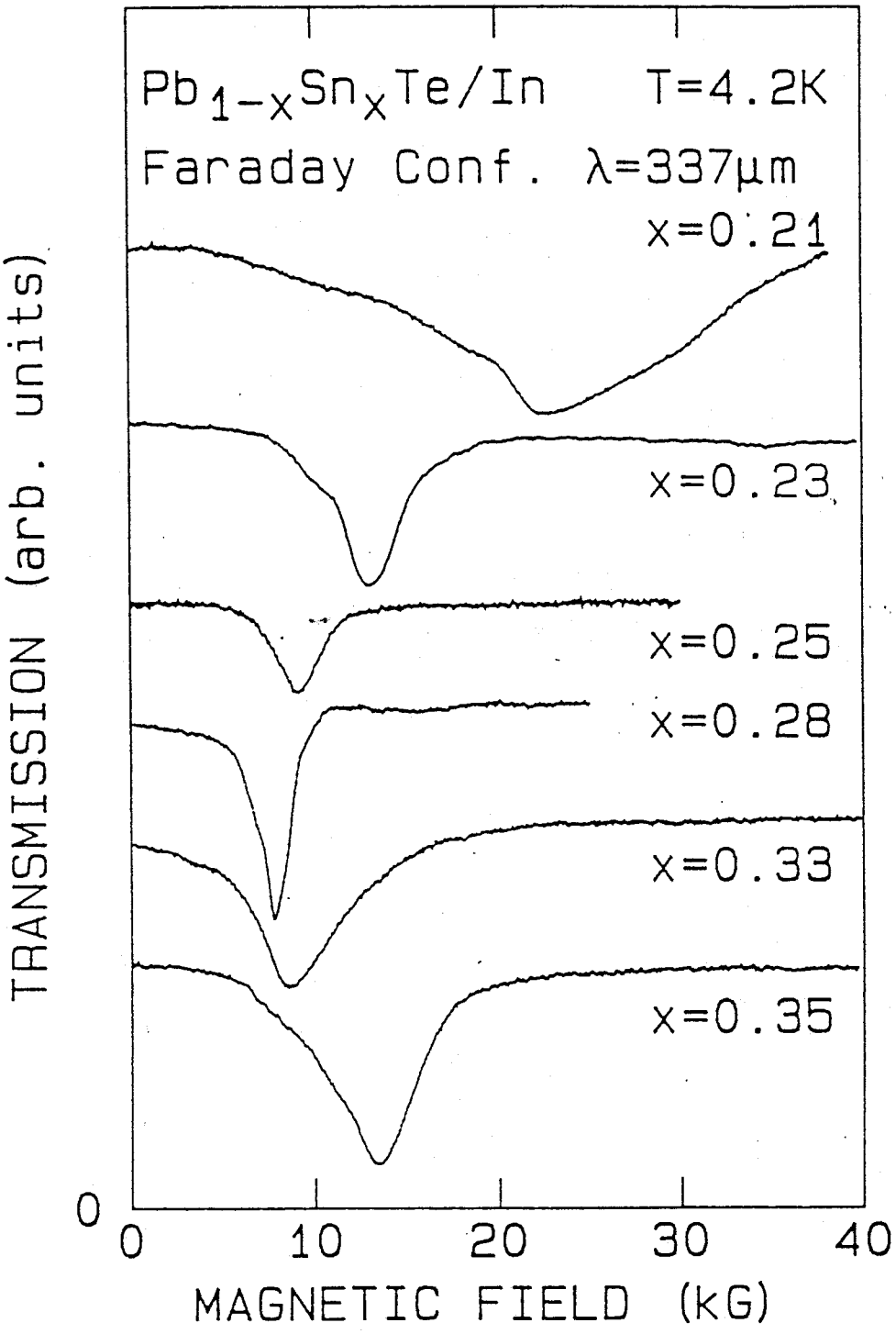

FIG. 12-2-6 Tin composition dependence of magnetoplasma transmission spectra with 337μm laser light in the Faraday configuration.

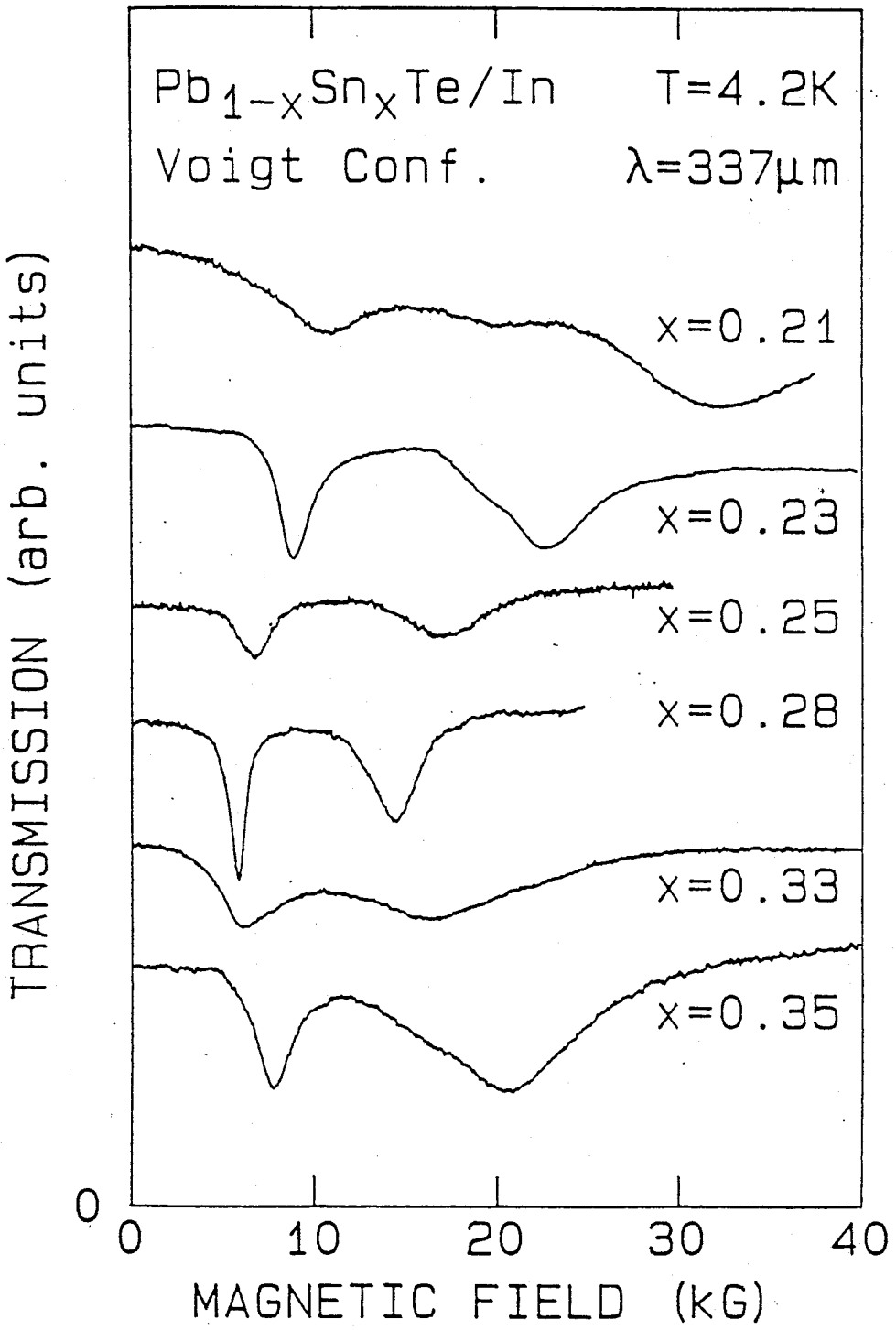

FIG. 12-2-7 Tin composition dependence of magnetoplasma transmission spectra with 337μm laser light in the Voigt configuration.

§13 DISCUSSION FOR PHOTOCARRIER DENSITY VERSUS TEMPERATURE AND MASS VERSUS Sn COMPOSITION OF In DOPED $Pb_{1-x}Sn_xTe$

§13-1 The temperature dependence of carrier density

The black body radiation of room temperature excites the electrons from localized In levels to conduction or valence band, and bring about photoconduction. We will discuss this photoconduction and its dynamical processes. Figures 13-1-1 and 13-1-2 shows the dependence of the carrier density on temperature in $Pb_{1-x}Sn_xTe$/In with various Sn composition. The carrier density is obtained by line shape fitting to the dependence of magnetoplasma in section 6. In all samples ,the carrier density remains constant below 15K, but it rapidly decreases down to below measuring limit with rising temperatures. The stabilizing energy level of the samples at Sn composition 21% and 35% are situated in the conduction or the valence band so that carriers remain with some density at more than 20K. On the other hand, since the stabilizing energy level of other samples is situated in the energy forbidden gap, carriers disappear at more than 20K. Qualitatively, this temperature dependence is recognized as follows. In stationary state(below 15K) electrons excited from In levels by black body radiation per unit time balanced with electrons relaxed to In levels. At low temperatures relaxation time does not depend on temperature, so that carrier concentration does not change in this temperature region. But, at above 15K, the relaxa-

tion time becomes short with increasing temperatures. We explain this dependence by the rate equation based upon the model that the electrons relax to In levels by thermal activation and tunneling process in next section.

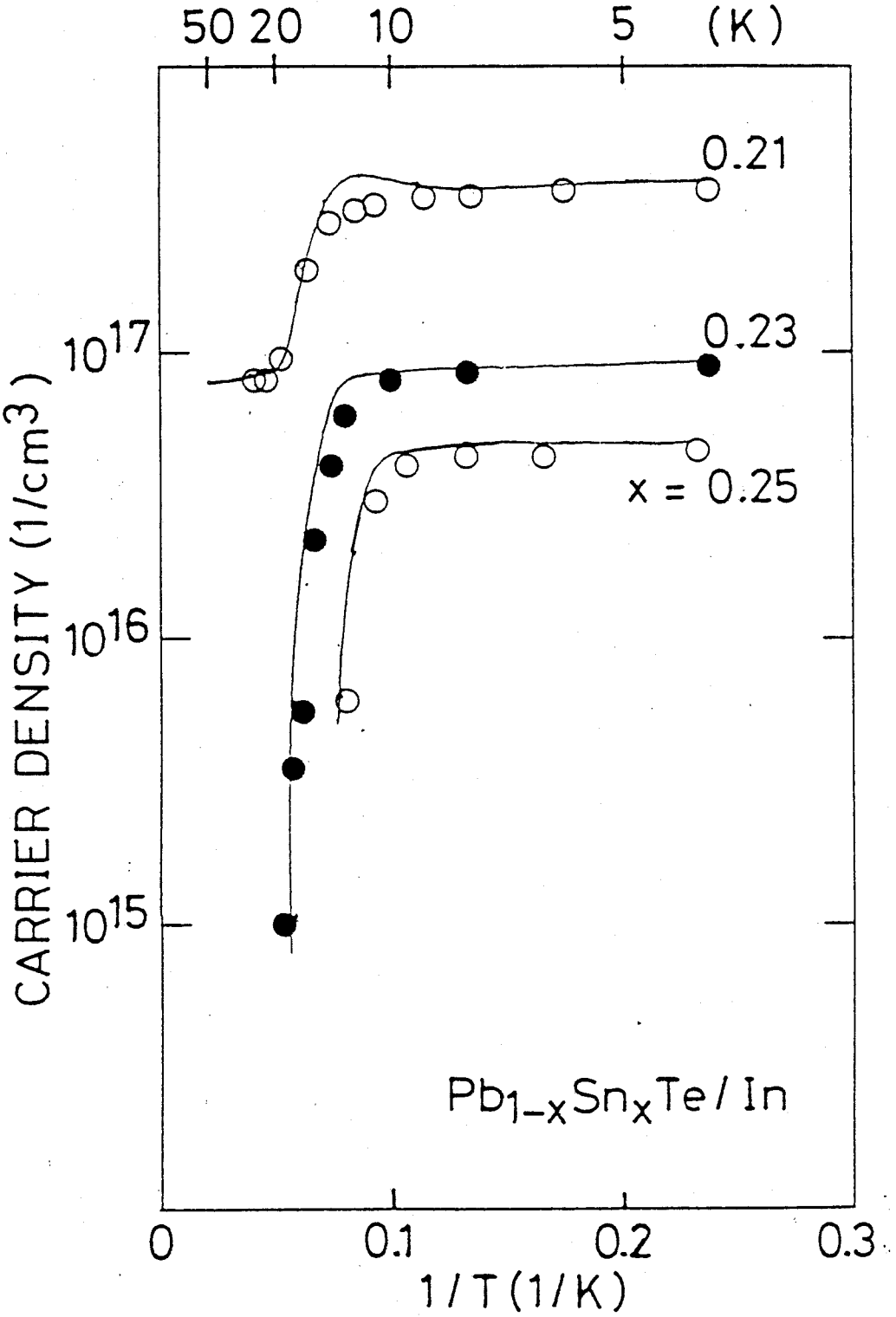

FIG. 13-1-1 Temperature dependences of the carrier density. Solid lines show the carrier density calculated from the model in which electrons relax from conduction band to In levels by tunneling and thermal activation processes(based on Anderson's negative U model).

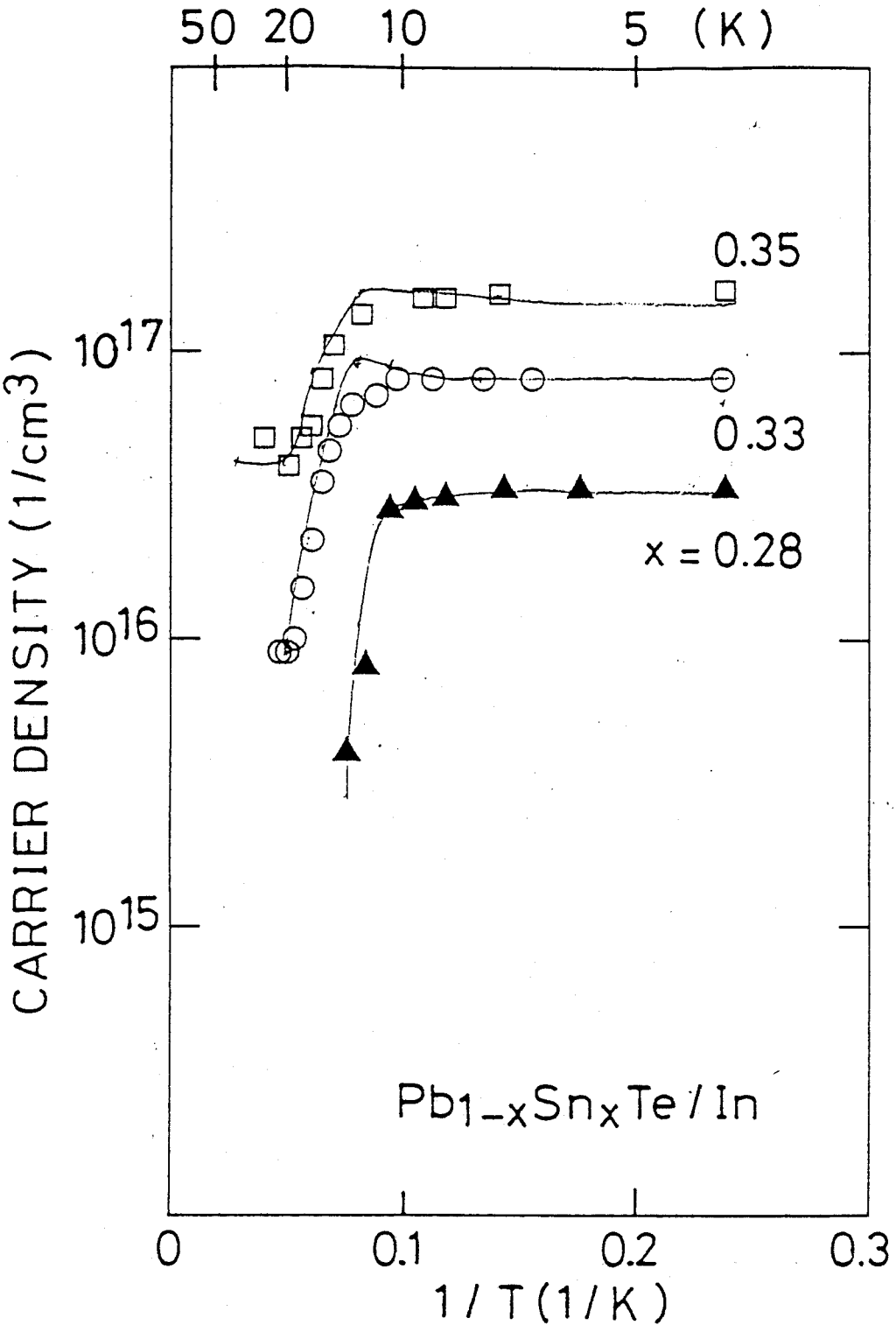

FIG. 13-1-2 Temperature dependences of the carrier density. Solid lines show the carrier density calculated from the model in which electrons relax from conduction band to In levels by tunneling and thermal activation processes(based on Anderson's negative U model).

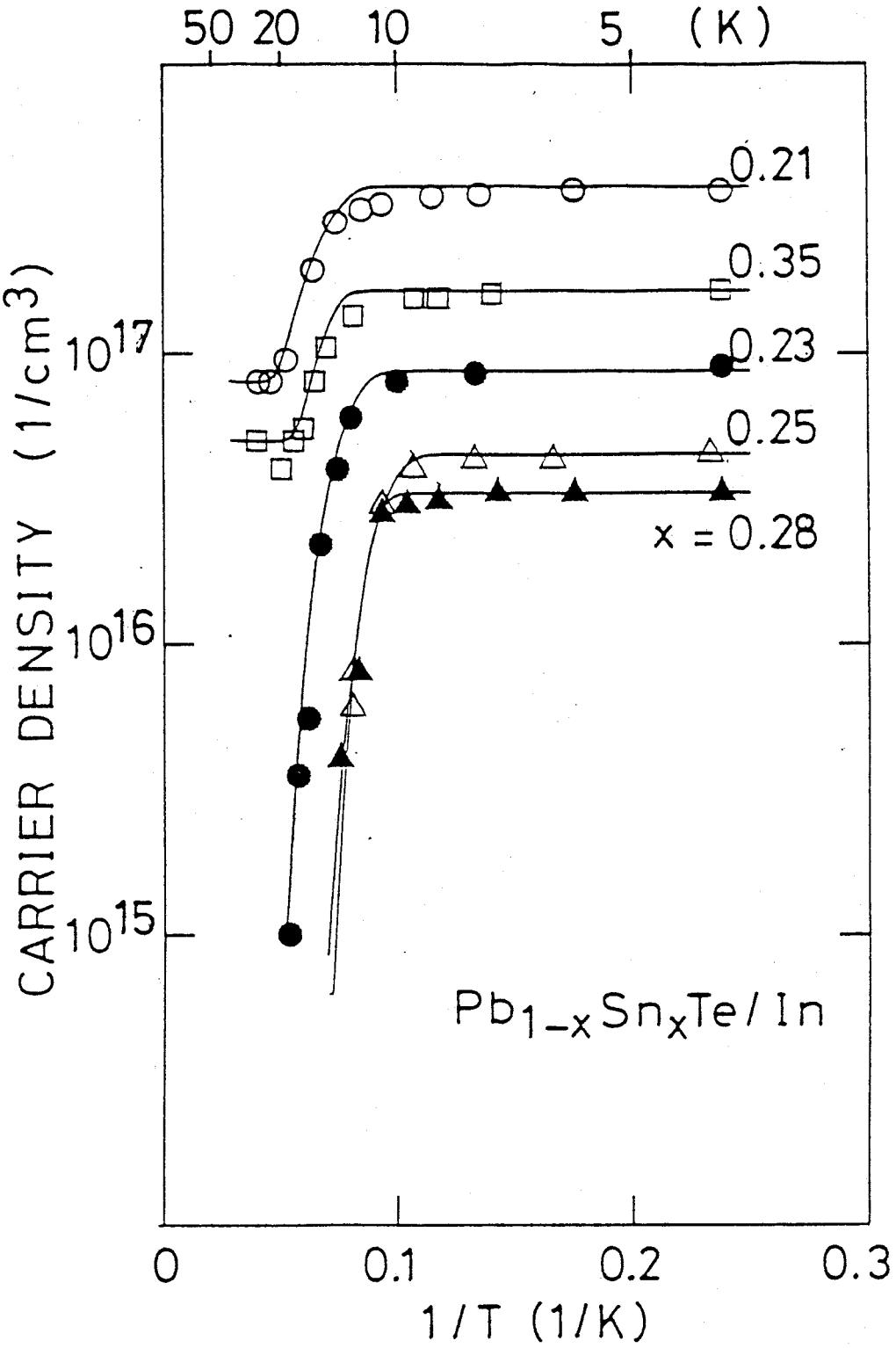

FIG. 13-1-3 Temperature dependences of the carrier density. Solid lines show the carrier density calculated from the model in which electrons relax from conduction band to In levels by tunneling and thermal activation processes(Single capture model).

13-2 Rate Equation and electron relaxation model

So far, the carrier concentrations of $Pb_{1-x}Sn_xTe$ are almost constant below 4.2K and rapidly decrease with increasing temperature above 15K at all these tin compositions. To interpret these experimental results, the processes of photoexcitation and thermal relaxation are considered microscopically within Anderson's negative U potential model. The negative U model has been successfully explaining the strong pinning of the Fermi energy, the negative photoconduction, and metal-insulator transitions versus Sn composition. This model is also consistent with the following experimental results;no observation of resonant scattering into the impurity band, the lack of ESR signal of In^+, and the lack of the impurity conduction. Only qualitative considerations are sufficient to understand these phenomena. But quantitative considerations are needed for the interpretation of the temperature dependence of carrier densities. And we will give the parameter values of this model.

In section 9, we explained Anderson's negative U model and gave the reason for the strong Fermi energy pinning by statistical thermodynamics. Now consider the photoexcitation and relaxation processes microscopically. By taking the proper position as the energy origin of the band electron, E_i in Eq.(9.1.2) can be defined by

$$E_i = \Delta_o - U/2 \ . \qquad (13.2.1)$$

From Eq.(9.2.6), the pinning level is zero, that is, the defini-

tion of Eq.(13.2.1) corresponds to taking the pinning energy level as the energy origin. Consider the case where the pinning level is above the conduction band edge, and the Fermi energy is coincident with the pinning level(equilibrium condition). Each term of Hamiltonian (9.1.8) as a function of lattice coordinate parameter Δ can be described in Fig. 13-2-1(a). The line 1 in this figure indicates the energy level of the electron in the singly occupied state of an In impurity; the line 2, the energy level of the second electron in the doubly occupied state; the line 3, the total energy level of the two electrons in the doubly occupied state; the line 4 is the lattice deformation energy. Adding this lattice energy to the levels indicated by line 1, 3, E_F^0, c.b. and v.b., the configurational coordinate diagram can be obtained(see Fig. 13-2-1(b)). In this figure, the line $E_F^0(In^0)$, $1(In^+)$ and $3(In^{2+})$ describe the total energies of the In^{2+} state and two electrons at the pinning level, the In^+ state and one electron at the pinning level, and the In^0, respectively. The stable points of these 3 states are 0, Δ_o, and $2\Delta_o$, respectively. The equilibrium state is characterized by the fact that the energy of In^{2+} and In^0 at the stable points coincide each other.

The transitions of the thermal excitations occur through the path as indicated by the arrows in Fig. 13-2-2. The activation energies from In^{2+} to In^+, from In^+ to In^{2+}, from In^+ to In^0, and In^+, U_{21}, U_{12}, U_{10}, and U_{01}, are defined by

$$U_{21} = \frac{(\Delta_o - U/2)^2}{2\Delta_o} , \qquad (13.2.2)$$

$$U_{12} = \frac{(U/2)^2}{2\Delta_o} , \qquad (13.2.3)$$

$$U_{10} = \frac{(U/2)^2}{2\Delta_o} , \qquad (13.2.4)$$

and

$$U_{01} = \frac{(\Delta_o - U/2)^2}{2\Delta_o} , \qquad (13.2.5)$$

respectively(see Fig. 13-2-2). In the equilibrium state considered now, the conditions

$$U_{21} = U_{01}$$

and

$$U_{12} = U_{10}$$

holds.

The photoexcitation processes are shown in Fig.13-2-2. The process where electrons are photoexcited from In impurities to the band is indicated by the vertical arrow A. The process where electrons in the bands are trapped by In impurities is indicated by the arrow B. These transitions occur vertically according to Frank-Condon principle. The transitions from In^+ are neglected because the population of In^+ is expected to be very small.

Next consider the case where the Fermi energy is situated above the pinning level. Define the Fermi energy by E_F. The total energy $E(In^{2+}+2e^-)$ of the In^{2+} state and the two electrons at the Fermi energy is given by

$$E(In^{2+}+2e^{-}) = \frac{\Delta^2}{2\Delta_o} + 2E_F. \qquad (13.2.5)$$

The total energy $E(In^{+}+e^{-})$ of the In^{+} state and one electron at the Fermi energy is

$$E(In^{+}+e^{-}) = \frac{1}{2\Delta_o}(\Delta-\Delta_o)^2 + \frac{\Delta_o}{2} - \frac{U}{2} + E_F. \qquad (13.2.6)$$

The total energy $E(In^{0})$ of the In^{0} is

$$E(In^{0}) = \frac{1}{2\Delta_o}(\Delta-2\Delta_o)^2 . \qquad (13.2.7)$$

From Eqs.(13.2.5), (13.2.6), and (13.2.7), the configurational coordinate diagram is given by Fig.13-2-3. In this situation, the condition

$$U_{21} < U_{01} \qquad (13.2.8)$$

holds so that the thermal transition from In^{2+} state to In^{0} arise more frequently than that from In^{0} to In^{2+} state. This nonequilibrium state returns to the equilibrium state. This relaxation has no exponential time dependence manner because activation energies are functions of E_F. On the other hand, when the Fermi energy is below the pinning level, the thermal transition from In^{0} to In^{2+} states overwhelms that from In^{2+} to In^{0} states.

The configurational coordinate diagram is show in Fig.13-2-4.

To obtain the transition rates from In^{2+} to In^{+}, etc., consider capture of an electron by In^{2+} center microscopically and precisely[120,121]. Firstly, the electron is in a free state of the conduction band or valence band and its state has an

energy E_{el}; we take the stabilized energy as the energy origin. Since In^{2+} has no trapped electron, it has only the lattice energy

$$\frac{\Delta^2}{2\Delta_o} \ . \qquad (13.2.9)$$

The total energy of the In 2+ and the free electron, $E(In^{2+}+e^-)$ is given by

$$E(In^{2+}+e^-) = \frac{\Delta^2}{2\Delta_o} + E_{el} . \qquad (13.2.10)$$

In this state the lattice vibrates sinusoidally about $\Delta = 0$ with amplitude Δ_Q, so

$$\Delta = \Delta_Q \sin\omega t \ . \qquad (13.2.11)$$

Secondly the free electron is captured by the In^{2+} and the In^+ is created. The In^+ state has the energy $E(In^+)$:

$$E(In^+) = \frac{1}{2\Delta_o}(\Delta-\Delta_o)^2 + \frac{\Delta_o}{2} - \frac{U}{2} \ . \qquad (13.2.12)$$

Figure 13-2-5 shows the configurational coordinate diagram. The transition from $In^{2+} + e^-$ to In^+ occurs mainly at or near the level crossing, that is, for $\Delta = \Delta_{21}$:

$$\Delta_{21} = \Delta_o - \frac{U}{2} - E_{el} \ . \qquad (13.2.13)$$

Hence when $\Delta_Q > \Delta_{21}$ the two state levels cross twice during each period of vibration and transition probability is finite. But when $\Delta_Q < \Delta_{21}$ the level crossing does not occur and the transi-

tion probability must be zero. Landau and Zener calculated the single crossing transition probability P_{21}:

$$P_{21} = 1 - \exp\left(-\frac{2\pi}{\hbar}\frac{|\langle In^{+}|\Delta V|In^{2+}+e^{-}\rangle|^{2}}{|\dot{E}_{dif}|}\right)$$

$$= \frac{2\pi}{\hbar}\frac{|\langle In^{+}|\Delta V|In^{2+}+e^{-}\rangle|^{2}}{|\dot{E}_{dif}|}, \qquad (13.2.14)$$

where $|In^{2+}+e^{-}\rangle$ and $|In^{+}\rangle$ are the electronic wave functions of the $In^{2+} + e^{-}$ and the In^{+} respectively; E^{dif} is defined by

$$\dot{E}_{dif} = \left|\frac{d}{dt}(E(In^{2+}+e^{-}) - E(In^{+})\right| \quad E(In^{2+}+e^{-}) \equiv E(In^{+}), \qquad (13.2.15)$$

From (13.2.9) and (13.2.10) we obtain

$$\dot{E}_{dif} = \dot{\Delta}_{\Delta=\Delta_o-E_{el}-\frac{U}{2}}$$

$$= (2\Delta_o(E_Q - U_{21}))^{1/2}, \qquad (13.2.16)$$

where E_Q is the vibration energy and U_{21} is expressed as

$$U_{21} = \frac{(\Delta_o - E_{el} - U/2)^2}{2\Delta_o}. \qquad (13.2.17)$$

We take the thermal average of P_{21} over phonon energy E_Q, $\langle P_{21}\rangle$:

$$\langle P_{21}\rangle = \int_{U_{21}}^{\infty} dE_Q \; P_{21} \exp[-E_Q/kT]/kT$$

$$= \frac{2}{\hbar}\frac{|\langle In^{+}|\Delta V|In^{2+}+e^{-}\rangle|^{2}}{\sqrt{2\Delta_o}} \exp[-U_{21}/kT](\pi/kT)^{1/2}. \qquad (13.2.18)$$

From similar manipulations, we obtain

$$\langle P_{12}\rangle = \frac{2}{\hbar}\frac{|\langle In^{+}|\Delta V|In^{2+}+e^{-}\rangle|^{2}}{\sqrt{2\Delta_o}}\exp[-U_{12}/kT](\pi/kT)^{1/2}\ , \tag{13.2.19}$$

$$\langle P_{01}\rangle = \frac{2}{\hbar}\frac{|\langle In^{0}|\Delta V|In^{+}+e^{-}\rangle|^{2}}{\sqrt{2\Delta_o}}\exp[-U_{01}/kT](\pi/kT)^{1/2}\ , \tag{13.2.20}$$

and

$$\langle P_{10}\rangle = \frac{2}{\hbar}\frac{|\langle In^{0}|\Delta V|In^{+}+e^{-}\rangle|^{2}}{\sqrt{2\Delta_o}}\exp[-U_{10}/kT](\pi/kT)^{1/2} \tag{13.2.21}$$

with

$$U_{12} = \frac{(E_{el}+U/2)^{2}}{2\Delta_o}\ , \tag{13.2.22}$$

$$U_{01} = \frac{(\Delta_o+E_{el}-U/2)^{2}}{2\Delta_o}\ , \tag{13.2.23}$$

and

$$U_{10} = \frac{(E_{el}-U/2)^{2}}{2\Delta_o}\ . \tag{13.2.24}$$

From these equations, the increments of the numbers of In^{0}, In^{2+}, and In^{+} by thermal relaxation in unit time, $\Delta N^{0}{}_{thermal}$, $\Delta N^{2+}{}_{thermal}$, and $\Delta N^{+}{}_{thermal}$, are given by

$$\Delta N^{0}{}_{thermal} = \int dE_{el}\rho(E_{el})f(E_{el}-E_f)P_{10}$$

$$-\int dE_{el}\rho(E_{el})[1-f(E_{el}-E_f)]P_{01} \quad , \qquad (13.2.25)$$

$$\Delta N^{2+}{}_{thermal}=\int dE_{el}\rho(E_{el})[1-f(E_{el}-E_f)]P_{12}$$

$$-\int dE_{el}\rho(E_{el})f(E_{el}-E_f)P_{21} \quad , \qquad (13.2.26)$$

and

$$\Delta N^{+}{}_{thermal}=-\Delta N^{0}{}_{thermal}-\Delta N^{2+}{}_{thermal} \qquad (13.2.27)$$

(see Fig. 13-2-5).

Assuming that the increment of the numbers of In^0, In^{2+}, and In^+ by photoexcitation in unit time, $\Delta N^0{}_{photo}$, $\Delta N^{2+}{}_{photo}$, and $\Delta N^+{}_{photo}$ are given by

$$\Delta N^0{}_{photo} = - I_0 \quad , \qquad (13.2.28)$$

$$\Delta N^{2+}{}_{photo} = - I_{2+} \quad , \qquad (13.2.29)$$

and

$$\Delta N^+{}_{photo} = I_0 + I_{2+} \quad . \qquad (13.2.30)$$

The total increment of the numbers of In^0, In^{2+}, and In^+ in unit time ΔN^0, ΔN^{2+}, and ΔN^+ are given by

$$\Delta N^0 = \Delta N^0{}_{thermal} + \Delta N^0{}_{photo} \quad , \qquad (13.2.31)$$

$$\Delta N^{2+} = \Delta N^{2+}{}_{thermal} + \Delta N^{2+}{}_{photo} \quad , \qquad (13.2.32)$$

and

$$\Delta N^{+} = - \Delta N^{0} - \Delta N^{2+} \ . \qquad (13.2.33)$$

Imposing stationary conditions that

$$\Delta N^{0} = 0 \qquad (13.2.34)$$

and

$$\Delta N^{2+} = 0 \ , \qquad (13.2.35)$$

the rate equations are obtained. Solving numerically these equation, the temperature dependence of the carrier density is obtained. In these equation the temperature independences of carrier density in the range from 4.2K to 15K are not obtained. This independence is explained by introducing tunnel relaxation in $\langle P_{12} \rangle$ and $\langle P_{10} \rangle$ by substitution of constant value into kT. Calculation curves are shown in Figs.13-2-1 and 13-2-2. From this calculation we obtained Δ_o=200meV in all samples.

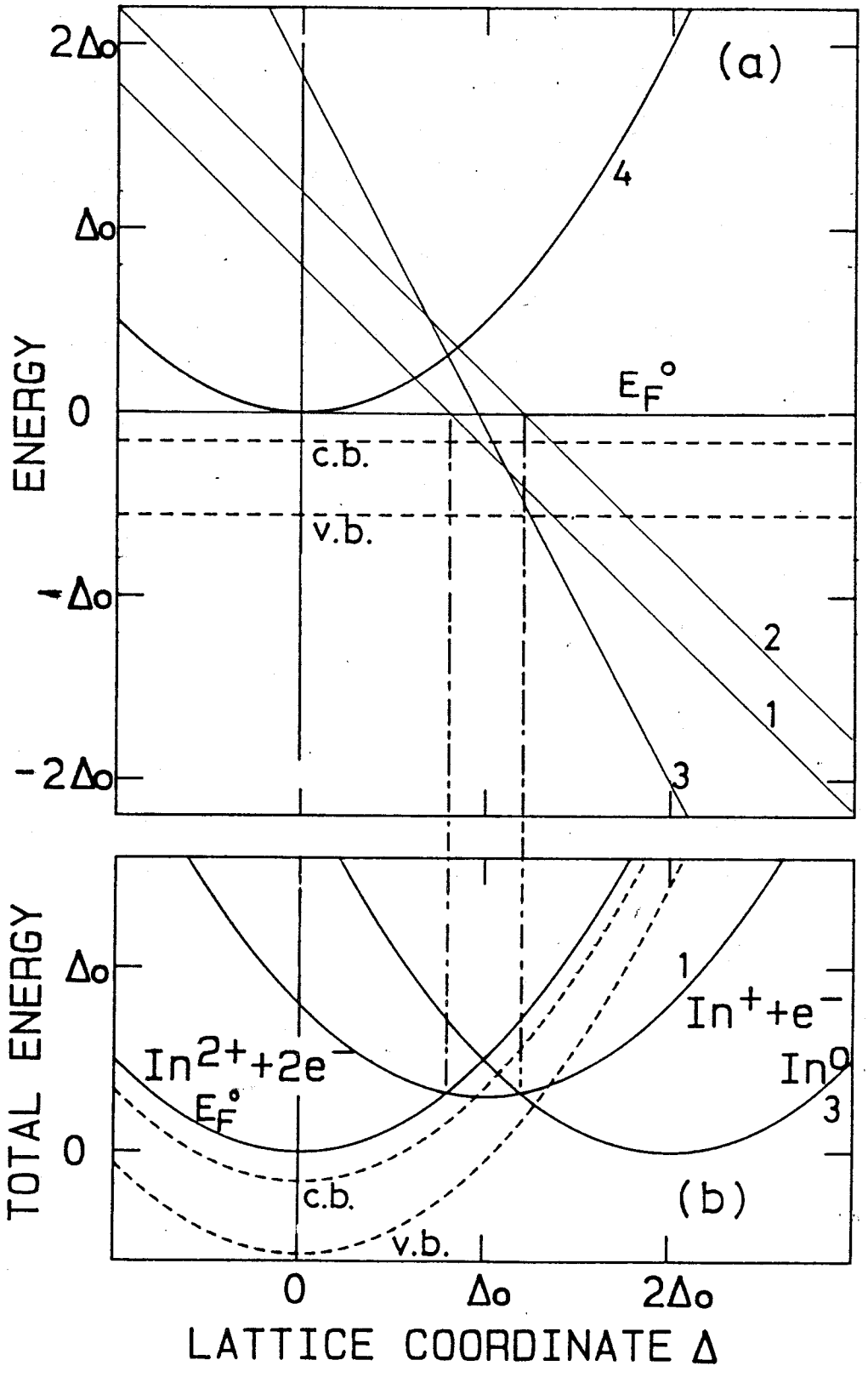

FIG. 13-2-1 (a) Electronic energy vs lattice coordinate Δ. (b)Configurational coordinate diagram: electric + lattice energy versus Δ.

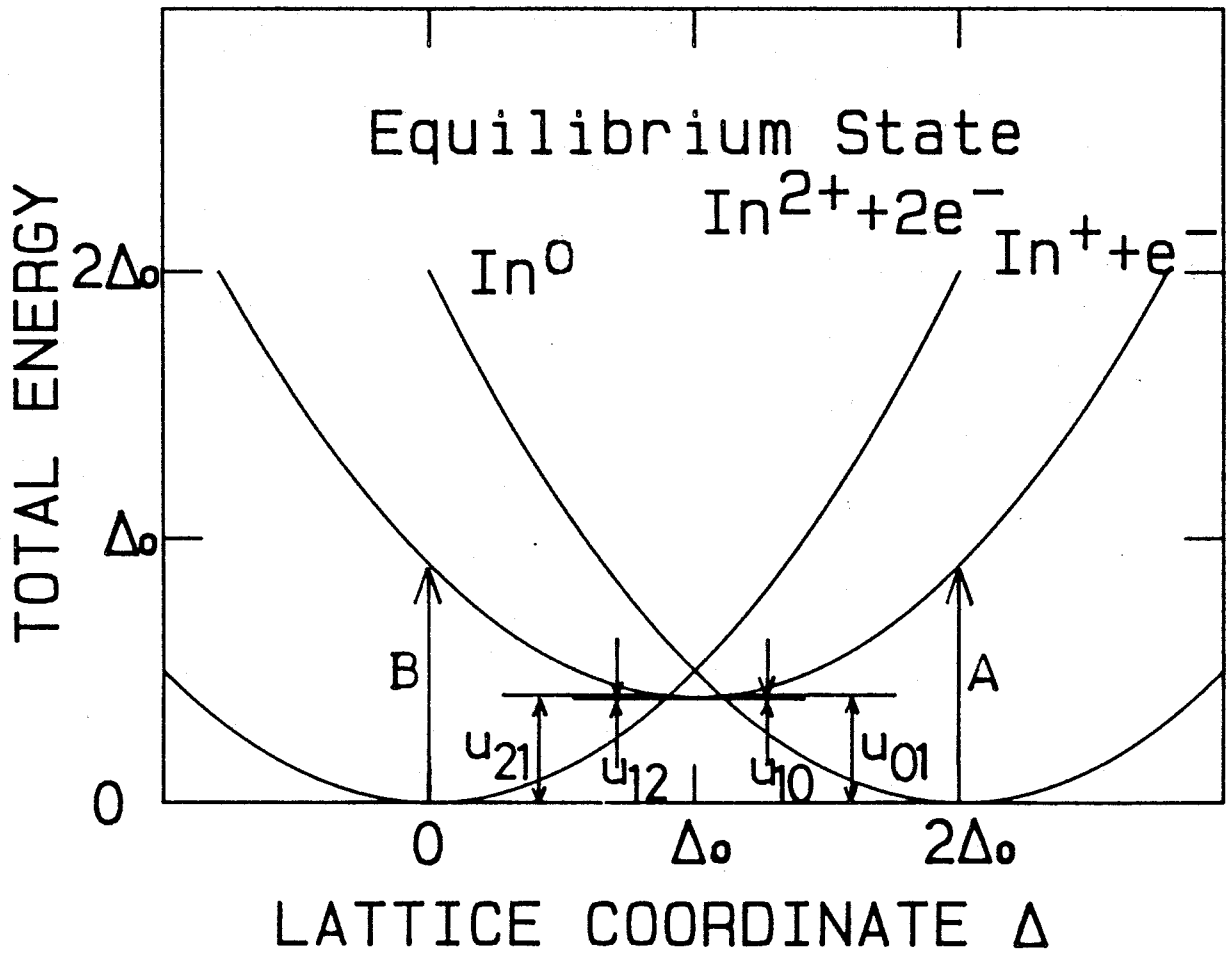

FIG. 13-2-2 Energy as a function of configurational coordinate in Anderson's Negative U potential model.

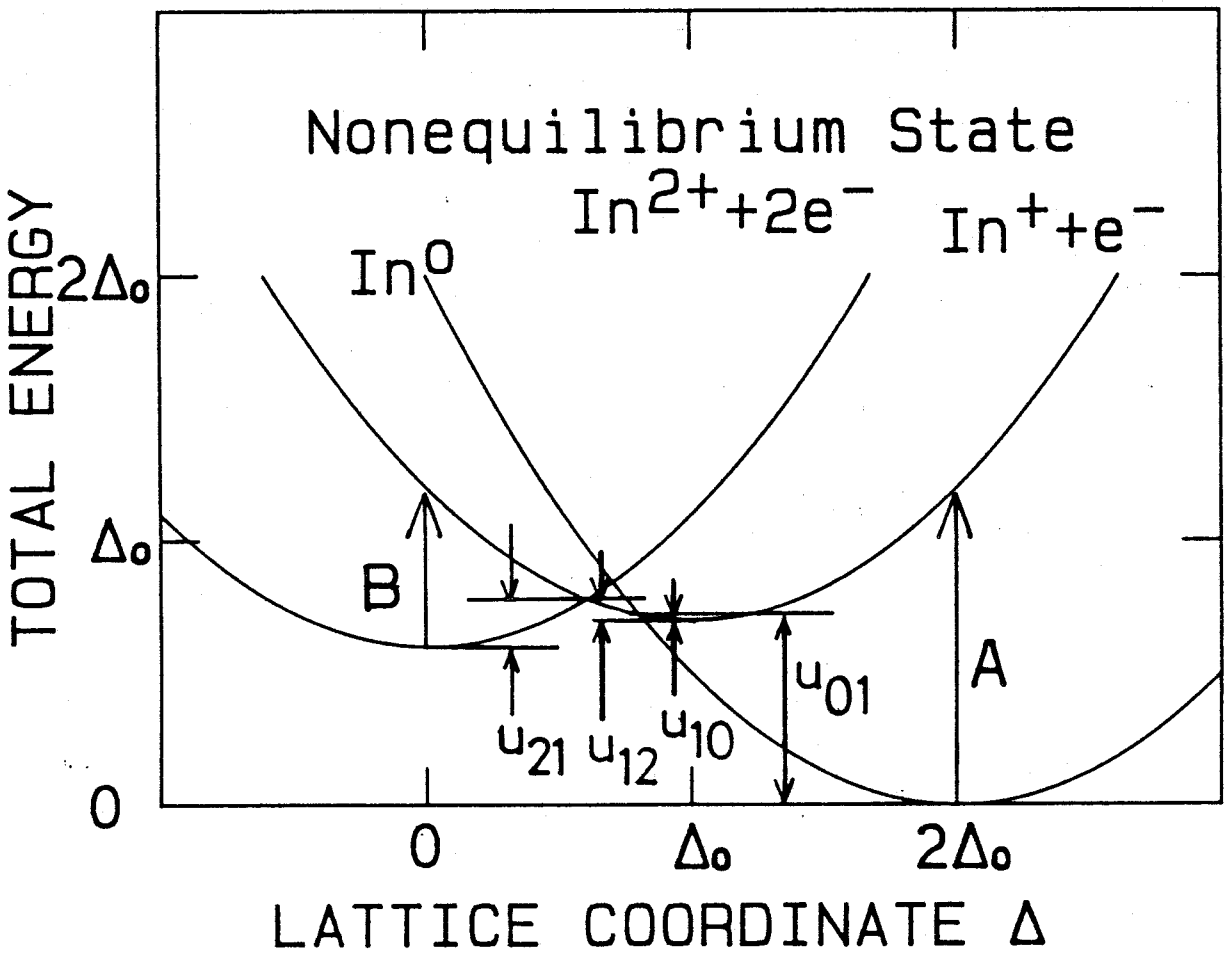

FIG. 13-2-3 Energy as a function of configurational coordinate in Anderson's Negative U potential model.

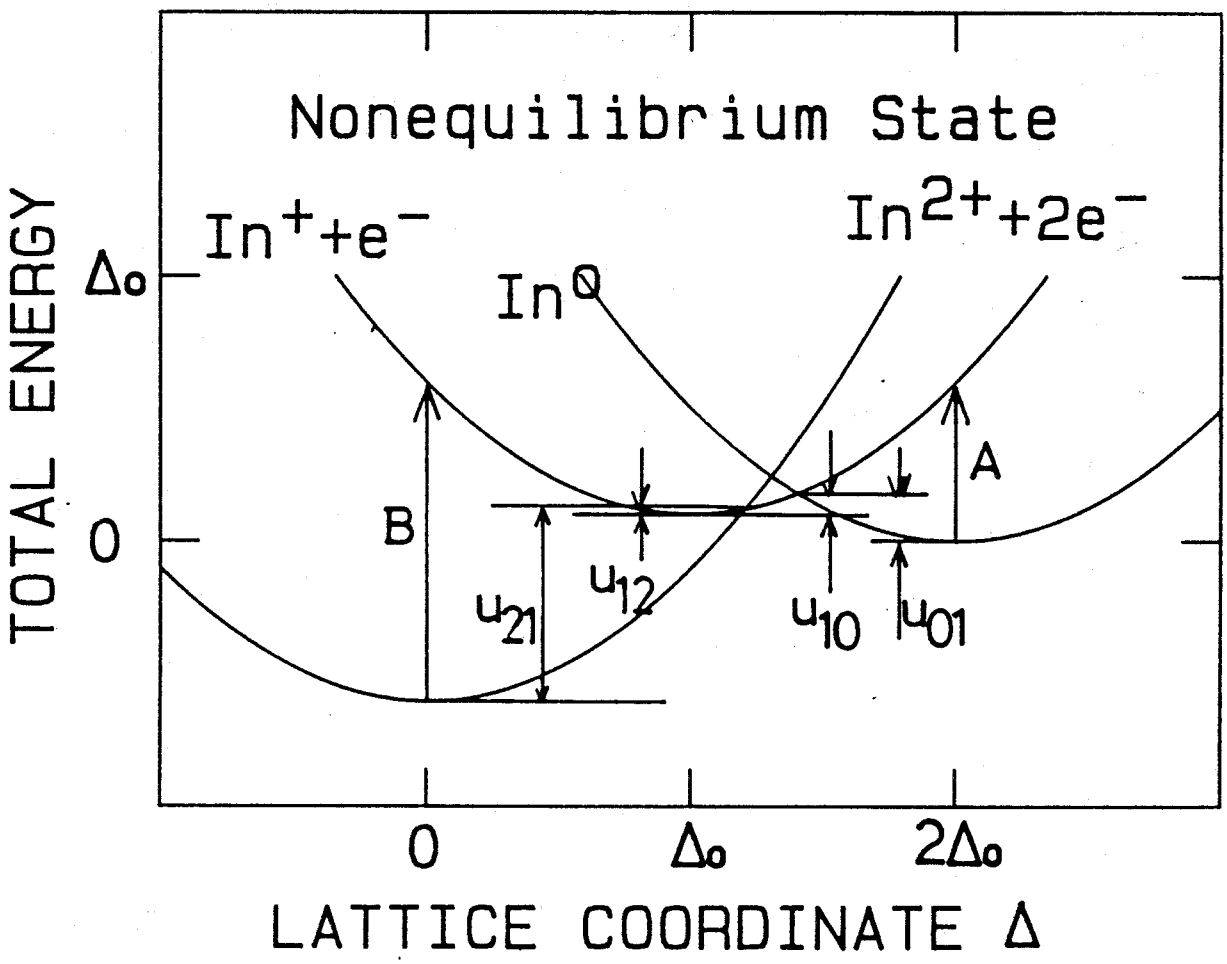

FIG. 13-2-4 Energy as a function of configurational coordinate in Anderson's Negative U potential model.

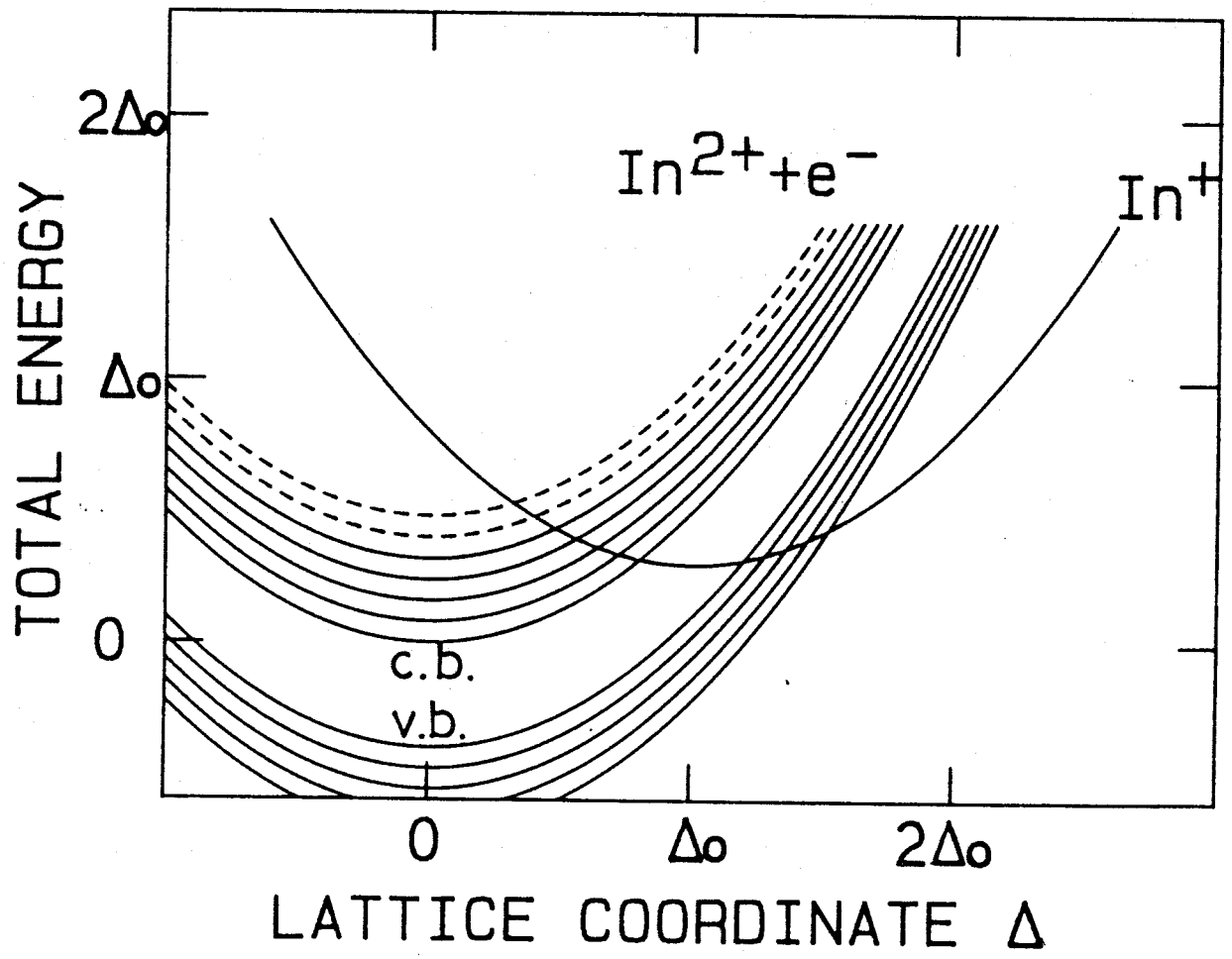

FIG. 13-2-5 Configurational coordinate diagram for indicating the thermal relaxation between $In^{2+} + e^-$ and In^+ states.

13-3 Band edge mass versus tin composition

The value of cyclotron mass is precisely determined by reproducing the measured magnetoplasma spectra by calculations using the dielectric constants(see sections 10-1 and 10-2). The band edge transverse masses of $Pb_{1-x}Sn_xTe/In$ with various Sn compositions were determined from the cyclotron masses in the case where the carrier densities are of the order of 10^{15} cm^{-3} near 20K(except for x=0.21 and 0.35). The nonparabolicity of the bands make the masses heavier by $2.46\times10^{-4}(m_o/meV)\times E_F(meV)$, where E_F is the Fermi energy measured from the band edge. In these small carrier density case, we can neglect the nonparabolic effect. Tin composition dependence of transverse band edge mass of $Pb_{1-x}Sn_xTe/In$ is given in Fig. 13-3-1. Considerably large mass enhancement is observed compared with masses measured in the $Pb_{1-x}Sn_xTe$. Various reasons for this rather constant mass enhancement can be considered in following ways. Some polaron effects that the local phonons of In atoms interact to band electrons change the conduction band dispersion and cause the polaron pinning. The usual Fröhlich type polaron effect[122-124] should be absent because carriers with considerably high concentration screen the electron-phonon interactions. Another possible reason for the mass enhancement is the breakdown of crystal symmetry by introducing the random potential due to the indium atoms. Under the perfect crystal symmetry, the energy level crossing of L_{61}^+ and L_{62}^- which corresponds to conduction and

valence band edge energies(see Fig. 2-2-1) occurs with increasing Sn composition. The random potential mixes the two wave functions and the level crossing does not occur. As a result, the energy gap becomes wide and the effective mass is enhanced. This may be related to the energy gap increase due to heavily doped In observed by Stafeev et al.[125].

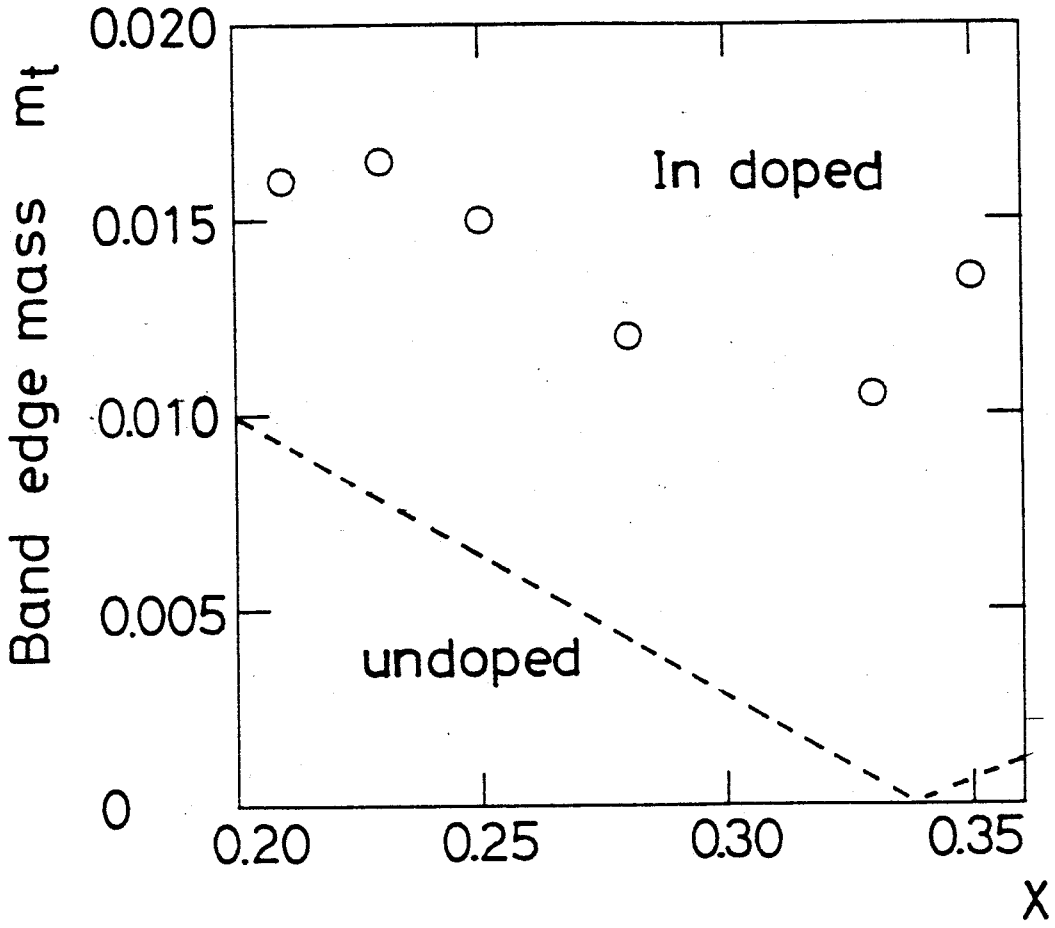

FIG. 13-3-1 Tin composition dependences of band edge mass of $Pb_{1-x}Sn_xTe/In$.

§14 SUMMARY AND CONCLUSIONS

Studies on $PbTe/Pb_{0.8}Sn_{0.2}Te$ superlattices and In doped $Pb_{1-x}Sn_xTe$ were made by magnetoplasma spectroscopy.

For the superlattices, we investigated the band edge structures from the dependence of the resonance magnetic fields on the magnetic field direction. The superlattices with various periodicities were prepared by a hot wall epitaxy system. The characterization of superlattice structures(layer thickness, interdiffusion of Sn and Pb atoms across the interfaces) was done by analyzing the satellite intensity of X-ray diffraction.

For 220Å/220Å, 260Å/150Å, 240Å/60Å, and 220Å/30Å superlattices with small interdiffusion, we observed the dependence of band edge structure on the barrier layer($Pb_{1-x}Sn_xTe$ layer) thickness. The electron system belonging to the singlet valley was 2-dimensional for all these superlattices, even for the samples with the barrier layer thickness of 30Å. The electron systems belonging to triplet valleys were 2-dimensional for the 220Å/220Å and 260Å/150Å superlattices. On the other hand, the electron systems belonging to triplet valleys were 3-dimensional due to electron tunneling across barrier layer for the 200Å/60Å superlattice. The difference of dimensionality of electron systems between the singlet and triplet valleys came from the fact that the singlet valley electron mass along the superlattice direction is ten times heavier than triplet ones. For the 220Å/30Å superlattices, we could not observe the cyclotron reso-

nance of electrons belonging to the triplet valleys, because the electrons are absent due to a valley splitting by tensile strain caused by the difference of thermal expansion coefficient between superlattice film and BaF_2 substrate.

Moreover we calculated cyclotron masses to examine the band discontinuity model in which PbTe and $Pb_{1-x}Sn_xTe$ bands are connected in reference to the pinning level of the deep impurity indium. The calculation were made by using the envelope function approximation based on two band model. The measured and calculated cyclotron masses agreed well with each other, it was found that this band discontinuity model is consistent with the experimental results.

For the superlattices 300Å/190Å with large interdiffusion of Pb and Sn atoms across the interface, we found the resonance magnetic field due to the singlet valley electrons splitted into two with changing magnetic field direction from the Faraday configuration. This splitting reflects the fact that the higher subband of the two was much more dispersive than the lower, because the large interdiffusion decreases the barrier potential and enlarges dispersion of the higher subband.

For $Pb_{1-x}Sn_xTe$(x=0.23, 0.25, 0.28, 0.33, 0.35) doped with indium, mechanism of photoexcitation and relaxation of electrons was investigated. From the magnetoplasma excitation spectra by a stripline method, the temperature dependence of photo-carrier density was obtained by the calculation to reproduce the measured

magnetoplasma spectra. It was found that the carrier density did not change in the temperature range from 4.2K to 15K, while it rapidly decreased above 15K for the all samples. We analyzed the temperature dependence of carrier density quantitatively within Anderson's negative U potential model.

It was also found that the band edge masses of In doped $Pb_{1-x}Sn_xTe$ were much heavier than those of undoped $Pb_{1-x}Sn_xTe$. Possible mechanisms of the mass enhancement have been discussed. Although some polaron effect due to the local phonon modes enhances the electron mass, usual Fröhlich polaron effects are absent due to screening by high density of carriers. Another cause is the static random potential introduced by In atoms. This random potential breaks the symmetry of the crystal potential and mixes the two band edge wave functions. As a result the energy gap spreads and the band edge mass becomes heavy. In composition dependence of the band edge mass should be investigated in detail to determining an essential mechanism for the mass enhancement.

It was found that the experimental results were consistent with the model that the band discontinuities at the heterojunctions between PbTe and $Pb_{1-x}Sn_xTe$ are determined by taking In level as the energy origin.

Many important developments are expected in these materials in future. For the superlattices, investigation of Sn composition dependence of the electronic structure is interesting. The energy gap of $Pb_{1-x}Sn_xTe$ decreases with increasing Sn compositions and

becomes zero at x=0.35. Above x=0.35, the band is inverted and the energy gap increases. For superlattices consisting of not inverted band and inverted band semiconductors, Korenman and Drew suggested that energy states like soliton states emerge in the energy gaps at the interfaces[126-128]. In our band offset, the gap states cannot be exist, because the band inversion superlattice belongs to type II. But Katnani et al.[129], Capasso et al.[130], and Niles et al.[131] have reported that the band discontinuities can be tuned by making dipole layer near or at the interface; that is, by putting another very thin material into the interface. If type I or I' superlattices can be realized by this method, the gap states in the band inversion superlattices will be observed. It is interesting to investigate electronic structures in PbTe/$Pb_{1-x}Sn_xTe$ superlattice with various lengths of interdiffusion of Pb and Sn across the interface. The interdiffusion length can be controlled by annealing temperature and time. If we could prepare the superlattices with various energy dispersions and mini gaps at will. The magnetic break down that is one of tunneling effect in k-space, should be observed by tuning the mini gaps. Indium doped PbTe/$Pb_{1-x}Sn_xTe$ superlattices are also attractive. Electronic properties, especially dimensionality, of superlattice is determined by the position of the Fermi level. If utilization of positive or negative photoconduction makes it possible to control the Fermi level, we can observe the electronic properties of the superlattice at various Fermi levels; i.e. metal insulator transitions.

REFERENCES

1) L. Esaki and R. Tsu, "Superlattice and Negative Differential Conductivity in Semiconductors", IBM J. Res. & Dev. 14, 1(1970).

2) R. Dingle, W. Wiegmann, and C. H. Henry, "Quantum State of Confined Carriers in Very Thin $Al_xGa_{1-x}As$-GaAs-$Al_{1-x}Ga_{1-x}As$ Heterostructures", Phys. Rev. Lett. 33, 823(1974).

3) R. Dingle, A. C. Gossard, and W. Wiegmann, "Direct Observation of Superlattice Formation in a Semiconductor Heterostructure", Phys. Rev. Lett. 34, 1327(1975).

4) J. P. van der Ziel, R. Dingle, R. C. Miller, W. Wiegmann, and W. A. Nordland Jr., "Laser Oscillation from Quantum States in Very Thin GaAs-$Al_{0.2}Ga_{0.8}As$", Appl. Phys. Lett. 29, 68(1975).

5) L. L. Chang, Armin Segmüller, and L. Esaki, "Smooth and Coherent Layers of GaAs and AlAs Grown by Molecular Beam Epitaxy", Appl. Phys. Lett. 28, 39(1976).

6) A. C. Gossard, P. M. Petroff, W. Weigmann, R. Dingle, and A. Savage, "Epitaxial Structure with Alternate-Atomic Layer Composition Modulation", Appl. Phys. Lett. 29, 323(1976).

7) L. L. Chang, G. Sakaki, C. A. Chang, and L. Esaki, "Shubnikov-de Haas Oscillations in a Semiconductor Superlattice", Phys. Rev. Lett. 38, 1489(1977).

8) R. Dingle, H. L. Störmer, A. C. Gossard, and W. Wiegmann, "Electron Mobilities in Modulation-Doped Semiconductor Heterojunction Superlattices", Appl. Phys. Lett. 33, 665(1978).

9) V. Narayanamurti, H. L. Störmer, M. A. Chin, A. C. Gossard, and W. Wiegmann, "Selective Transmission of High-Frequency Phonons by a Superlattice: The "Dielectric" Phonon Filter", Phys. Rev. Lett. 31, 2012(1979).

10) J. Yoshino, H. Sakaki, and T. Furuta, "Fermi Surface Study of a Semiconductor Superlattice".

11) W. T. Tsang, "Extremely Low Threshold(AlGa)As Modified Multiquantum Well Heterostructure Lasers Grown by Molecular-Beam Epitaxy", Appl. Phys. Lett. 39, 786(1981).
12) R. C. Miller, D. A. Kleinman, W. T. Tsang, and A. C. Gossard, "Observation of the Excited Level of Excitons in GaAs Quantum Wells", Phys. Rev. 24, 1134(1981).
13) T. Duffield, R. Bhat, M. Koza, F. DeRosa, D. M. Hwang, P. Grabbe, and S. J. Allen Jr., "Electron Mass Tunneling Along the Growth Direction of (Al,Ga)As/GaAs Semiconductor Superlattices", Phys. Rev. Lett. 56, 2724(1986).
14) K. Murase, S. Shimomura, S. Takaoka, A. Ishida, and H. Fujiyasu, Proc. 1st Intern. Conf. Superlattices, Microstructures and Microdevices, Aug. 13-16, 1984, Champaign-Urbana, "On the Type of Superlattice in Lead-Tin-Telluride System", Proc. 1st Intern. Conf. Superlattices, Microstructures and Microdevices, Aug. 13-16, 1984, Champaign-Urbana, Superlattices and Microstructures 1, 177(1985).
15) Chin-An Chang, R. Ludeke, L. L. Chang, and L. Esaki, "Molecular-Beam Epitaxy (MBE) of $In_{1-x}Ga_xAs$ and $GaSb_{1-y}As_y$", Appl. Phys. Lett. 31, 759(1977).
16) G. A. Sai-Halasz, R. Tsu, and L. Esaki, "A New Semiconductor Superlattice", Appl. Phys. Lett. 30, 651(1977).
17) H. Sakaki, L. L. Chang, R. Ludeke, Chin-An Chang, G. A. Sai-Halasz, and L. Esaki, "$In_{1-x}Ga_xAs$-$GaSb_{1-y}As_y$ Heterojunctions by Molecular Beam Epitaxy", Appl. Phys. Lett. 31, 211(1977).
18) G. A. Sai-Halasz, L. Esaki, and W. A. Harrison, "InAs-GaSb Superlattice Energy Structure and Its Semiconductor-Semimetal Transition", Phys. Rev. B18, 2812(1978).
19) H. Sakaki, L. L. Chang, G. A. Sai-Halasz, C. A. Chang, and L. Esaki, "Two-Dimensional Electronic Structure in InAs-GaSb Superlattices", Solid State Commun. 26, 589(1978).

20) L. L. Chang, N. Kawai, G. A. Sai-Halasz, R. Ludeke, and L. Esaki, "Observation of Semiconductor-Semimetal Transition in InAs-GaSb Superlattices", Appl. Phys. Lett. 35, 939(1979).

21) H. Bluyssen, J. C. Maan, P. Wyder, L. L. Chang, and L. Esaki, "Cyclotron Resonance in an InAs-GaSb Superlattice", Solid State Commun. 31, 35(1979).

22) H. J. A. Bluyssen, J. C. Maan, P. Wyder, L. L. Chang, and L. Esaki, "Cyclotron Resonance and Shubnikov-de Haas Experiments in a n-InAs-GaSb Superlattice", Phys. Rev. B25, 5364(1982).

23) T. Ando and S. Mori, "Effective-Mass Theory of Semiconductor Heterojunctions and Superlattices", Surf. Sci. 113, 124(1982).

24) S. R. White and L. J. Sham, "Electronic Properties of Flat-Band Semiconductor Heterostructures", Phys. Rev. Lett. 47, 879(1981).

25) G. Bastard, "Superlattice Band Structure in the Envelope-Function Approximation", Phys. Rev. B24, 5693(1981).

26) G. Bastard, "Theoretical Investigation of Superlattice band Structure in the Envelope-Function Approximation", Phys. Rev. B25, 7584(1982).

27) P. Voisin, G. Bastard, and M. Voos, "Optical Selection Rules in Superlattice in the Envelope-Function Approximation", Phys. Rev. B29, 935(1984).

28) C. Mailhiot and D. L. Smith, "k·p Theory of Semiconductor Superlattice Electronic Structure II. Application to $Ga_{1-x}In_xAs$-$Al_{1-y}In_yAs$ [100] Superlattice", Phys. Rev. B33, (1986).

29) M. Kriechbaum, K. E. Ambrosch, E. J. Fantner, H. Clemens, and G. Bauer, "Electronic Structure of PbTe/$Pb_{1-x}Sn_xTe$ Superlattices", Phys. Rev. B30, 3394(1984).

30) P. Pichler, E. J. Fantner, G. Bauer, H. Clemens, H. Pascher, and M. von Ortenberg, "Magnetooptical Investigation of PbTe/$Pb_{1-x}Sn_xTe$ Superlattices", Superlattices and Microstructures 1, 1(1985).

31) T. Fukui and Y. Horikoshi, "InAsSbP-InAs Superlattice Grown by Organometallic VPE Method", Jpn. J. Appl. Phys. 19, L551(1980).

32) S. V. Gopanov, Sov. Tech. Phys. Lett. 5, 210(1979).

33) K. Murase, S. Shimomura, S. Takaoka, A. Ishida, and H. Fujiyasu, Proc. 1st Intern. Conf. Superlattices, Microstructures and Microdevices, Aug. 13-16, 1984, Champaign-Urbana, "On the Type of Superlattice in Lead-Tin-Telluride System", Proc. 1st Intern. Conf. Superlattices, Microstructures and Microdevices, Aug. 13-16, 1984, Champaign-Urbana, Superlattices and Microstructures 1, 177(1985).

34) K. Murase, S. Ishida, S. Takaoka, and T. Okumura, Yamada Conference XIII on Electronic Properties of Two-Dimensional Systems, Kyoto, Japan, 9-13 Sept. 1985, "Superconducting Behavior in PbTe-SnTe Superlattices", Yamada Conference XIII on Electronic Properties of Two-Dimensional Systems, Kyoto, Japan, 9-13 Sept. 1985.

35) P. A. Wolff, "Matrix Elements and Selection Rules for the Two-Band Model of Bismuth", J. Phys. Chem. Solids 25, 1057(1964).

36) J. O. Dimmock and G. B. Wright, "Band Edge Structure of PbS, PbSe, and PbTe", Phys. Rev. 135, A821(1965).

37) M. Yoshikawa, K. Shinohara, and R. Ueda, "Continuous Operation Over 1500h a PbTe/PbSnTe Double-Heterostructure Laser at 77K", Appl. Phys. Lett. 31, 699(1977).

38) D. L. Partin and W. Lo, "Low Threshold Current Lead-Telluride Diode Lasers Grown by Molecular Beam Epitaxy", J. Appl. Phys. 52, 1579(1981).

39) D. L. Partin, J. P. Heremans, and C. M. Thrush, "Side Optical Cavity, Single Quantum Well Diode Laser", Superlattices and Microstructures 2, 459(1987).
40) K. Murase, S. Ishida, S. Takaoka, and T. Okumura, Yamada Conference XIII on Electronic Properties of Two-Dimensional Systems, Kyoto, Japan, 9-13 Sept. 1985, "Superconducting Behavior in PbTe-SnTe Superlattices", Yamada Conference XIII on Electronic Properties of Two-Dimensional Systems, Kyoto, Japan, 9-13 Sept. 1985.
41) A. Ishida, S. Matsuura, H. Fujiyasu, H. Ebe, and K. Shinohara, "Properties of PbTe/EuTe Short Period Superlattices and Their Application to Laser Diodes", Superlattices and Microstructures 2, 575(1986).
42) L. S. Kim, H. D. Drew, R. E. Doezema, J. P. Heremans, and D. L. Partin, "Cyclotron-Resonance Determination of Band Offset in a PbTe Quantum Well", Phys. Rev. B35, 2521(1987).
43) H. Kinoshita, T. Sakashita, and H. Fujiyasu, "(p/n)PbTe Multiple-Layer Films Prepared by a Hot Wall Technique", J. Appl. Phys. 52, 2869(1981).
44) P. Pichler, G. Bauer, and H. Clemens, "Magnetooptical Properties of PbTe Doping Superlattices", Z. Phys. B-Condensed Matter 67, 475(1987).
45) M. Kriechbaum, G. Bauer, E. J. Fantner, P. Pichler, H. Clemens, K. E. Ambrosch, H. Pascher, and M. v. Ortenberg, "Intra- and Interband Magnetooptical Investigation of PbTe/$Pb_{1-x}Sn_xTe$ Superlattices".
46) K. E. Ambrosch, H. Clemens, E. J. Fantner, and G. Bauer, "Structural and Electronic Properties of PbTe/$Pb_{1-x}Sn_xTe$ Superlattices".
47) H. Kinoshita, H. Fujiyasu, A. Ishida, and H. Kuwabara, "Optical Properties of PbTe-$Pb_{1-x}Sn_xTe$ Superlattices Prepared by a Hot Wall Technique", Physics of Narrow Gap Semiconductors(Springer-Verlag, Berlin Heidelberg, 1982) p.368.

48) H. Fujiyasu, A. Ishida, H. Kuwabara, S. Shimomura, S. Takaoka, and K. Murase, Proc. 5th Intern. Conf. on Electronical Properties of 2-Dimensional Systems, Sept. 5-9, 1983, Oxford, "Optical and Electrical Properties of PbTe-$Pb_{1-x}Sn_xTe$ Superlattice Prepared on KCl by a HWE", Proc. 5th Intern. Conf. on Electronical Properties of 2-Dimensional Systems, Sept. 5-9, 1983, Oxford, Surface Science 142, 579(1984).

49) H. Pascher, G. Bauer, and H. Clemens, "Spin Resonant Optical Four Wave Mixing in $Pb_{1-x}Sn_xTe$ Epitaxial Layer and in $Pb_{1-x}Sn_xTe$/PbTe Superlattices", Solid State Commun. 55, 765(1985).

50) A. J. Rosenberg and F. Wald, "Massive Heterovalent Substitutions in Octahedrally Coordinated Semiconductors", J. Phys. Chem. Solids 26, 1079(1965).

51) Z. Feit, D. Eger, and A. Zemel, "Quasilocal Impurity States in $Pb_{1-x}Sn_xTe$ and $PbSe_{0.08}Te_{0.92}$ Liquod-Phase Epitaxial Layers with Group-III Elements", Phys. Rev. B31, 3903(1985).

52) B. A. Akimov, V. P. Zlomanov, L. I. Ryabova, S. M. Chudinov, and O. B. Yatsenko, "Semiconductor-Metal-Semiconductor Transitions in $Pb_{1-x}Sn_xTe$:In Alloys under Pressure", Fiz. Tekh. Poluprovodn. 13, 1293(1979)[Sov. Phys. Semicond. 13, 759(1979)].

53) B. A. Akimov, R. S. Vadkhva, V. P. Zlomanov, L. I. Ryabova, and S. M. Chudinov, "Pressure-Induced Transition to Gapless State in In-Doped $Pb_{1-x}Sn_xTe$ Alloy", Fiz. Tekh. Poluprovodn. 11, 1077(1977)[Sov. Phys. Semicond. 11, 637(1977)].

54) K. Murase, S. Takaoka, T. Itoga, and S. Ishida, Proceeding of the Application of High Magnetic Fields in Semiconductor Physics, Sept. 13-17, 1982, Grenoble, "Evidence of Fermi Level Pinning in $Pb_{1-x}Sn_xTe$/In at High Magnetic Fields", Proceeding of the Application of High Magnetic Fields in Semiconductor Physics, Sept. 13-17, 1982, Grenoble.

55) S. Takaoka, T. Itoga, and K. Murase, "Quantum Oscillation of Carrier Concentration Due to Fermi Level Pinning by Doped Indium Impurities in $Pb_{1-x}Sn_xTe$", Solid State Commun. 46, 287(1983).

56) Claude M. Penchina, A. Klein, and K. Weiser, Proc. 15th Int. Conf. Physics of Semiconductors. Kyoto, 1980, "Negative Photoconductivity and Large Lattice Relaxation in Indium Doped Lead-Tin Telluride", Proc. 15th Int. Conf. Physics of Semiconductors. Kyoto, 1980, J. Phys. Soc. Japan 49 sup, A783(1980).

57) V. I. Kaidanov, R. B. Mel'nik, and I. A. Chernik, "Investigation of Indium-Doped Lead Telluride", Fiz. Tekh. Poluprovodn. 7, 522(1973).

58) I. I. Zasavitsky, B. N. Matsonashvili, and G. V. Flusov, Physics of narrow gap Semiconductros Proceedings, Linz, Austria, 1981, "Photoluminescence of $Pb_{1-x}Sn_xTe$ Crystals Doped with Cd and In", Physics of narrow gap Semiconductros Proceedings, Linz, Austria, 1981, Lecture Notes in Physics 152, 449(1981).

59) I. I. Zasavitskii, A. V. Matveenko, B. N. Matsonashvili, and V. T. Trofimov, "Kinetics of the Photoconductivity of $Pb_{1-x}Sn_xTe$:In", Fiz. Tekh. Poluprovodn. 17, 2184(1983)[Sov. Phys. Semicond. 17, 1396(1983)].

60) I. I. Zasavitskii, A. V. Matveenko, B. N. Matsonashvili, and V. T. Trofimov, "Kinetics of the Photoconductivity of $Pb_{1-x}Sn_xTe$:In", Fiz. Tekh. Poluprovodn. 17, 2184(1983)[Sov. Phys. Semicond. 17, 1396(1983)].

61) I. I. Zasavitskii, A. V. Matveenko, B. N. Matsonashvili, and V. T. Trofimov, "Negative Photoconductivity in $Pb_{1-x}Sn_xTe$:In", Pis'ma Zh. Eksp. Teor. Fiz. 17, 1864(1983)[Sov. Phys. Semicond. 17, 1190(1983)].

62) B. A. Akimov, N. B. Brandt, L. I. Ryabova, and V. V. Sokovishin, "Long-Term Relaxation Processes Induced by a Quantizing Magnetic Field in the Metallic Phase of $Pb_{1-x}Sn_xTe$(In) Alloys", Zh. Eksp. Teor. Fiz. 87, 1349(1984)[Sov. Phys. JETP 60, 774(1984)].

63) B. A. Akimov, L. I. Ryabava, O. B. Yatsenko, and S. M. Chudinov, "Modifications in the Energy Spectrum of In-doped $Pb_{1-x}Sn_xTe$ Alloys Due to Charges in Composition and Application of Pressure", Fiz. Tekh. Poluprovodn. 13, 752(1979)[Sov. Phys. Semicond. 13, 441(1979)].

64) H. A. Alperin, S. T. Pickart, J. J. Phyne, and V. J. Minkiewicz, "Softening of the Transverse-Optic Mode in PbTe", Phys. Lett. 40A, 295(1972).

65) G. S. Pawley, W. Cockran, R. A. Cowley, and G. Dolling, "Diatomic Ferroelectrics", Phys. Rev. Lett. 17, 753(1966).

66) S. Sugai, K. Murase, S. Katayama, S. Takaoka, S. Nishi, and H. Kawamura, "Carrier Density Dependence of Soft TO-Phonon in SnTe by Raman Scattering", Solid State Commun. 24, 407(1977).

67) C. R. Hewes, M. S. Adler, and S. D. Senturia, "Nuclear-Magnetic-Resonance Studies in PbTe and $Pb_{1-x}Sn_xTe$: an Experimental Determination of k·p Band Parameters and Magnetic Hyperfine Constants", Phys. Rev. B7, 5195(1973).

68) L. E. Johnson, J. B. Conklin, Jr., and G. W. Pratt, Jr., "Relativistic Effects in the Band Structure of PbTe", Phys. Rev. Lett. 11, 538(1963).

69) J. B. Conklin, Jr., L. E. Johnson, and G. W. Pratt, Jr., "Energy Bands in PbTe", Phys. Rev. 137, A1282(1965).

70) P. J. Lin and L. Kleinman, "Energy Bands of PbTe, PbSe and PbS", Phys. Rev. 142, 478(1966).

71) F. Herman, R. L. Kortum, I. Ortenburger, and J. P. Van Dyke, J. Phys. (Paris) Suppl. 29, C4-62(1968).

72) S. Rabii, "Investigation of Energy-Band Structure and Electronic Properties of PbS and PbSe", Phys. Rev. 173, 918(1968).
73) S. Rabii, "Energy-Band Structure and Electronic Properties of SnTe", Phys. Rev. 182, 821(1969).
74) Y. W. Tung and M. L. Cohen, "Relativistic Band Structure and Electronic Properties of SnTe, GeTe, and PbTe", Phys. Rev. 180, 823(1969).
75) H. Overhof and U. Rössler, "Electronic Structure of PbS, PbSe, and PbTe", Phys. Status Solidi 37, 691(1970).
76) R. L. Bernick and L. Kleinman, "Energy Bands, Effective Masses and g-factors of the Lead Salts and SnTe", Solid State Commun. 8, 569(1970).
77) S. E. Kohn, P. Y. Yu, Y. Petroff, Y. R. Shen, Y. Tsang, and M. L. Cohen, "Electronic Band Structure and Optical Properties of PbTe, PbSe, and PbS", Phys. Rev. B8, 1477(1973).
78) G. Martinez, M. Schlüter, and M. L. Cohen, "Electronic Structure of PbSe and PbTe.I. Band Structures, Densities of States, and Effective Masses", Phys. Rev. B11, 651(1975).
79) F. R. McFeely, S. Kowalczyk, L. Ley, R. A. Pollak, and D. A. Shirley, "High-Resolution X-Ray Photoemission Spectra of PbS, PbSe, and PbTe Valence Bands", Phys. Rev. B7, 5228(1973).
80) M. Cardona, D. W. Langer, N. J. Shevchik, and J. Tejeda, "Photoelectric Properties of the Lead Chalcogenides", Phys. Stat. Sol.(b) 58, 127(1973).
81) E. O. Kane, "Band Structure of Indium Antimonide", J. Phys. Chem. Solids. 1, 249(1956).
82) J. M. Luttinger, "Quantum Theory of Cyclotron Resonance in Semiconductor: General Theory", Phys. Rev. 102, 1030(1956).
83) J. O. Dimmock and G. B. Wright, "Band Edge Structure of PbS, PbSe, and PbTe", Phys. Rev. 135, A821(1965).

84) D. L. Mitchell and R. F. Wallis, "Theoretical Energy-Band Parameters of the Lead Salts", Phys. Rev. 151, 581(1966).
85) J. O. Dimmock, "k·p Theory of the Conduction and Valence Band of $Pb_{1-x}Sn_xTe$ and $Pb_{1-x}Sn_xSe$ Alloys", The Physics of Semimetals and Narrow-Gap Semiconductors, Edited by L. L. Carter and R. T. Bate, Pergamon, Oxford, p.319(1971).
86) M. S. Adler, C. R. Hewes, and S. D. Senturia, "k·p Model for the Magnetic Energy Levels in PbTe and $Pb_{1-x}Sn_xTe$", Phys. Rev. B7, 5186(1973).
87) B. A. Volkov, O. A. Pankratov, and A. V. Sazonov, "Band Structure of Solid Solution Based on IV-VI Compounds", Fiz. Tverd. Tela 26, 255(1984)[Sov. Phys. Solid State 26, 255(1984)].
88) I. Kasai, "Band Inversion Semiconductor", Oyo Buturi 41, 377(1972).
89) R. C. Miller, D. A. Kleinman, and A. C. Gassard, "Energy Gap Discontinuities and Effective Masses for GaAs-$Al_xGa_{1-x}As$ Quantum Wells", Phys. Rev. B29, 7085(1984).
90) R. Dingle, Festkörper Probleme XV, 21(1975).
91) R. S. Bauer and G. Margaritondo, "Probing Semiconductor-Semiconductor Interfaces", Physics Today 40, Jan.27(1987).
92) W. A. Harrison, "Elementary Theory of Heterojunctions", J. Vac. Sci. Technol. 14, 1016(1977).
93) W. A. Harrison, "Theory of Band Line-Ups", J. Vac. Sci. Technol. B3, 1231(1985).
94) J. Tersoff, "Reference Levels for Heterojunctions and Schottky Barriers", Phys. Rev. Lett. 56, 675(1986).
95) J. G. Mavroides, "Magneto-Optical Properties", Optical Properties of Solids Edited by F. Abeles.
96) M. Born and K. Haung, "Dynamical Theory of Crystal Lattice", Dynamical Theory of Crystal Lattice, p82(Oxford. U.P.).

97) D. T. Hodges, "A Review of Advances in Optically Pumped Far-Infrared Lasers", Infrared Phys. 18, 375(1978).
98) K. Nagasaka, "Far-Infrared Cyclotron Resonance in Solids", Oyo Buturi 41, 574(1972).
99) M. Yamanaka, "Submillimeter-Wave Lasers and Their Applications", Oyo Buturi 49, 813(1980).
100) A. Yariv, Optical Electronics 3rd ed. p211(Holt Sanuders).
101) T. Y. Chang and T. J. Bridges, Opt. Commun. 1, 423(1970).
102) T. Yoshida, K. Kuba, K. Sakaki, and S. Fujita, "Frequency Stabilization of a CO_2 Laser for Sub-mm Laser Pumping by the Stark Modulated Lamb Dip Signal", Oyo Buturi 53, 52(1984).
103) P. Jongsuck, K. Mizuno, S. Ono, and K. Sagae, "A Method of Stabilizing the Output of a CO_2 Laser for Use in Submillimeter-Wave Laser", Oyo Buturi 51, 734(1981).
104) S. Okajima, "Stabilization of Far-Infrared Gas Laser", Kogaku 13, 190(1984).
105) Y. Tsunawaki, G. Takaharu, A. Tanimoto, and H. Yoshinaga, "Relative Response of Tunable InSb Detector in Far-Infrared", Japan. J. Appl. Phys. 11, 1746(1972).
106) R. F. Bis and J. R. Dixon, "Applicability of Vegard's Law to the $Pb_{1-x}Sn_xTe$ Alloy System", J. Appl. Phys. 40, 1918(1969).
107) A. Segmuller, P. Krishna, and L. Esaki, "X-ray Diffraction Study of a One-Dimensional GaAs-AlAs Superlattice", J. Appl. Cryst. 10, 1(1977).
108) R. M. Fliming, D. B. McWhan, A. C. Gossard, W. Wiegmann, and R. A. Logan, "X-ray Diffraction Study of Interdiffusion and Growth in $(GaAs)_n(AlAs)_m$ Multilayers", J. Appl. Phys. 51, 357(1979).
109) E. J. Fantner, B. Oetner, W. Ruhs, and A. Lopez-Otero, "Misfit Strain in Epitaxial IV-VI Semiconduction Films", Lecture Notes in Physics Vol. 152, Physics of Narrow Gap Semiconductor, Springer-Verlag Berlin Heidelberg, New York p.59-63.

110) A. Ishida, M. Aoki, and H. Fujiyasu, "Sn Diffusion Effects on X-ray Diffraction Patterns of $Pb_{1-x}Sn_xTe$-$PbSe_yTe_{1-y}$ Superlattices", J. Appl. Phys. 58, 797(1985).
111) A. J. Miller, G. A. Saunders, and Y. K. Yogurtçu, "Pressure Dependences of the Elastic Constants of PbTe, SnTe and $Ge_{0.08}Sn_{0.92}Te$", J. Phys. C 14, 1569(1981).
112) A. Ishida, Ph. D. Thesis (Shizuoka Univ. 1986).
113) P. W. Anderson, "Model for the Electronic Structure of Amorphous Semiconductors", Phys. Rev. Lett. 14, 953(1975).
114) D. Adler and E. J. Yoffa, "Electronic Structure of Amorphous Semiconductors", Phys. Rev. Lett. 36, 1197(1976).
115) T. Ichiguchi, Ph. D. Thesis(Osaka Univ. 1981).
116) G. Nimtz and B. Schlicht, "Narrow-Gap Lead Salts(Chap.2 The Crystal)", Narrow-Gap Semiconductor, p.11(Springer-Verlag Berlin Heidelberg New York Tokyo).
117) H. D. Drew and A. J. Sievers, "Far-Infrared Absorption in Superconducting and Normal Lead", Phys. Rev. Lett. 19, 697(1967).
118) U. Strom, H. D. Drew, and J. F. Koch, "Quantum Aspects of the Azbel'-Kaner Resonance in Bismuth", Phys. Rev. Lett. 26, 1110(1971).
119) U. Storm, A. Kamgar, and J. F. Koch, "Quantum Aspects and Electrodynamics of High-Frequency Cyclotron Resonances in Bismuth", Phys. Rev. B7, 2435(1973).
120) L. D. Landau and I. Lifshitz, "Chap.11 Diatomic Molecule", Quantum Mechanics(nonrelativistic theory).
121) C. H. Henry and D. V. Lang, "Nonradiative Capture and Recombination by Multiphonon Emission in GaAs and GaP", Phys. Rev. B15, 989(1977).
122) H. Fröhlich, "Introduction to the Theory of the Polaron", Polaron and Excitons p.1, Edited by C. G. Kuper and G. D. Whitfield.

123) G. Ascarelli, "Seminars on Experimental Work, 1. Polarons in Cyclortron Resonance", Polaron and Excitons p.357, Edited by C. G. Kuper and G. D. Whitfield.

124) D. H. Dickey, E. J. Johnson, and D. M. Larsen, "Polaron Effects in the Cyclotron-Resonance Absorption of InSb", Phys. Rev. Lett. 18, 599(1967).

125) V. I. Stafeev, E. Yu. Salaev, Kh. D. Dzhalilova, E. I. Kurbanova, and T. S. Mamedov, "Optical Absorption Spectra and Photoconductivity of Epitaxial $Pb_{1-x}Sn_xTe$:In Films", Fiz. Tekh. Poluprovodn. 17, 1864(1983)[Sov. Phys. Semicond. 17, 1190(1983)].

126) R. E. Doezma and D. Drew, "Motionally Dependent Bound States in Semiconductor Quantum Wells", Phys. Rev. Lett. 57, 762(1986).

127) B. A. Volkov and O. A. Pankratov, ""Heavy Fermion" in a Supersymmetric Ferroelectric Domain Wall", Pis'ma Zh. Eksp. Teor. Fiz. 43, 99(1986)[Sov. Phys. JETP Lett. 43, 130(1986)].

128) E. Fradkin, E. Dagotto, and D. Voyanovsky, "Physical Realization of the Parity Anomaly in Condensed Matter Physics", Phys. Rev. Lett. 57, 2967(1986).

129) A. D. Katnani, P. Chiaradia, Y. Cho, P. Mahowald, P. Pianetta, and R. S. Bauer, "Effect of an Al Interlayer on the GaAs/Ge(100) Heterojunction Formation", Phys. Rev. B32, 4071(1985).

130) F. Capasso, A. Y. Cho, K. Mohammed, and P. W. Foy, "Doping Interface Dipoles: Tunable Heterojunction Barrier Heights and Bandedge Discontinuities by Molecular Beam Epitaxy", Appl. Phys. Lett. 46, 664(1985).

131) D. W. Niles, G. Margaritondo, P. Perfetti, C. Quaresima, and M. Capozi, "Hetrojunction Band Discontinuity Contronl by Ultrathin Intralayers", Appl. Phys. Lett. 47, 1092(1985).